

FEDERAL UNIVERSITY OF PELOTAS
Center for Chemical, Pharmaceutical and Food Sciences
Chemistry Postgraduate Program



Thesis

**Functionalization strategies of *Luffa cylindrica* for the
adsorption of pharmaceutical contaminants from water**

Juliê Silveira da Costa

Pelotas, RS
2025

Juliê Silveira da Costa

**Functionalization strategies of *Luffa cylindrica* for the adsorption of
pharmaceutical contaminants from water**

Thesis presented to the Postgraduate Program in Chemistry of the Universidade Federal de Pelotas (UFPel, Brazil), as partial requirement for obtaining the Ph.D. in Science.

Supervisor: Prof. Dr. André Ricardo Fajardo

Pelotas, RS

2025

Universidade Federal de Pelotas / Sistema de Bibliotecas
Catalogação da Publicação

C837f Costa, Juliê Silveira da

Functionalization strategies of *Luffa cylindrica* for the adsorption of pharmaceutical contaminants from water [recurso eletrônico] / Juliê Silveira da Costa ; André Ricardo Fajardo, orientador. — Pelotas, 2025. 232 f.

Tese (Doutorado) — Programa de Pós-Graduação em Química, Centro de Ciências Químicas, Farmacêuticas e de Alimentos, Universidade Federal de Pelotas, 2025.

1. Vegetal biomass. 2. Functionalization. 3. Bioadsorbents. 4. Adsorption. 5. Pharmaceuticals. I. Fajardo, André Ricardo, orient. II. Título.

CDD 620.8

UNIVERSIDADE FEDERAL DE PELOTAS
CENTRO DE CIÊNCIAS QUÍMICAS, FARMACÊUTICAS E DE ALIMENTOS

Programa de Pós-Graduação em Química


A Comissão Examinadora, abaixo assinada, aprova a
Tese de Doutorado

**Functionalization strategies of Luffa Cylindrica for the adsorption of
pharmaceutical contaminants from water**


Elaborada por
Juliê Silveira da Costa

Como requisito parcial para a obtenção do grau de
Doutora em Ciências


COMISSÃO EXAMINADORA:

Documento assinado digitalmente
 **ANDRE RICARDO FAJARDO**
Data: 03/10/2025 13:31:23-0300
Verifique em <https://validar.iti.gov.br>


Prof. Dr. André Ricardo Fajardo (Presidente/Orientador) - PPGQ/UFPel

Documento assinado digitalmente
 **DENISE FREITAS SIQUEIRA PETRI**
Data: 02/10/2025 14:31:58-0300
Verifique em <https://validar.iti.gov.br>

Prof^a. Dr^a. Denise Freitas Siqueira Petri – USP

Documento assinado digitalmente
 **DANIEL PASQUINI**
Data: 02/10/2025 18:46:50-0300
Verifique em <https://validar.iti.gov.br>

Prof. Dr. Daniel Pasquini – UFU

Documento assinado digitalmente
 **ROBSON DA SILVA OLIBONI**
Data: 03/10/2025 10:15:09-0300
Verifique em <https://validar.iti.gov.br>

Prof. Dr. Robson da Silva Oliboni – PPGQ/UFPel

Dedicate this thesis to all the strong
women who have helped me reach
this point, especially my mother,
Maria Luiza, my sister, Leizi,
and my godmother, Maria Julia.

Acknowledgements

To CAPES for the doctoral scholarship and the internship scholarship.

To the Federal University of Pelotas, for the infrastructure and opportunities for growth.

To God, who, when I thought I wouldn't make it this far, gave me strength and wisdom.

To my mother, Maria Luiza, my godmother, Maria Julia, and my sister Leizi, who are the women responsible for raising me and for the person I've become today. They are my greatest emotional and psychological support, my greatest role models, and the ones who believe most in my potential.

To my husband, Ayel, who gives me the security and peace of mind to pursue my dreams, makes all my dreams his own, and never lets me give up.

To my advisor, Prof. Dr. André Fajardo, who often believes in my potential more than I do, and who always encouraged me to overcome barriers in the academic world.

To my eternal friends who have been with me since graduation, my soul sister, Nichole, and my friends Marinalva and Cassiane.

To the special friends I made during my internship at CERMAV, especially Steve, Dorcas, Maelle, Hong Li, and Sakshi, who warmly welcomed me into the group, always believed in my potential, and supported me in every way.

To my Brazilian/Portuguese friends who Grenoble gave me, especially Madalena, Mari, Marcia, Kauã, and Gustavo, thank you for all the exchanges.

To my friends from Paraná that Grenoble brought into my life, Flavia, and Elisangela, you were true gifts from France and inspiring examples of women researchers.

To my friends in the LaCoPol group, who have shared knowledge, joys, and frustrations with me for so long.

To the many friends I made in the halls of the Federal University of Pelotas, who were always willing to talk, listen to my tears, or lend a hand, especially Andressa N., Diego O., and Laura A.

To Dr. Sami Halila, thank you for the experience of being part of his research group at CERMAV/Fr.

I thank everyone who helped me get here.

*“Eu sou a continuação de um sonho
Da minha mãe, do meu pai
De todos que vieram antes de mim
Eu sou a continuação de um sonho
Da minha vó, do meu vô
Quem sangrou pra gente poder sorrir” – BK’*

Abstract

Title: Functionalization strategies of *Luffa cylindrica* for the adsorption of pharmaceutical contaminants from water

Author: Juliê Silveira da Costa

Supervisor: Prof. Dr. André Ricardo Fajardo

Luffa cylindrica (LF) is an abundant plant-based biomass with a highly porous three-dimensional structure, offering great potential for environmental applications. However, the low density and predominantly hydrophilic nature of its active sites limit its adsorption capacity for pharmaceutical contaminants. This thesis hypothesizes that chemical functionalization of LF fibers can enhance their adsorption performance by introducing specific functional groups while preserving the native 3D architecture. To test this hypothesis, three complementary functionalization strategies were developed and systematically evaluated. The grafting of polyethyleneimine (PEI) introduced nitrogen-rich groups, significantly improving reactivity and enabling stable removal of antibiotics and antivirals with confirmed reusability. The coating of LF with polypyrrole and stearic acid increased fiber hydrophobicity, thereby enhancing interactions with less polar pharmaceuticals such as diclofenac, and further demonstrated feasibility under continuous-flow conditions relevant for scale-up. Finally, grafting with β -cyclodextrin (β -CD) created selective host–guest complexation sites, producing an efficient fixed-bed column adsorbent capable of removing non-steroidal anti-inflammatory drugs (NSAIDs) from large volumes of water. Collectively, these results demonstrate that distinct modifications routes can be applied to LF without compromising its structural integrity, while tailoring surface chemistry for adsorption of pharmaceuticals with diverse chemical properties. By correlating functionalization strategies with adsorption outcomes, this thesis advances the understanding of structure–function relationships in lignocellulosic adsorbents, provides new insights into the sustainable valorization of agricultural residues, and establishes a framework for designing scalable biomass-based materials for water treatment technologies.

Keywords: Vegetal biomass; functionalization; bioadsorbents; adsorption; pharmaceuticals.

Resumo

Título: Estratégias de funcionalização da *Luffa cylindrica* para a adsorção de contaminantes farmacêuticos da água

Autora: Juliê Silveira da Costa

Orientador: Prof. Dr. André Ricardo Fajardo

Luffa cylindrica (LF) é uma biomassa vegetal abundante, com uma estrutura 3D altamente porosa, com grande potencial para aplicações ambientais. No entanto, a baixa densidade e a natureza hidrofílica de seus sítios ativos limitam sua capacidade de adsorção de contaminantes farmacêuticos. Esta tese parte da hipótese de que a funcionalização química das fibras de LF pode aprimorar seu desempenho adsorptivo, por meio da introdução de grupos funcionais específicos, preservando ao mesmo tempo a arquitetura 3D nativa. Para isso, três estratégias complementares de funcionalização foram desenvolvidas e avaliadas sistematicamente. A graftização da polietilenimina (PEI) introduziu grupos ricos em nitrogênio, melhorando significativamente a reatividade e permitindo a remoção estável de antibióticos e antivirais, com reutilização confirmada. O revestimento da LF com polipirrol e ácido esteárico aumentou a hidrofobicidade das fibras, intensificando as interações com fármacos menos polares, como o diclofenaco, além de demonstrar viabilidade em condições de fluxo contínuo, relevantes para escalonamento. Por fim, a graftização com β -ciclodextrina (β -CD) criou sítios de complexação hospedeiro-hospede, resultando em um adsorvente eficiente em coluna de leito fixo, capaz de remover anti-inflamatórios não esteroides (AINEs) de grandes volumes de água. Coletivamente, esses resultados demonstram que rotas de modificação distintas podem ser aplicadas à LF sem comprometer sua integridade estrutural, ao mesmo tempo em que permitem ajustar a química superficial para a adsorção de fármacos com propriedades químicas diversas. Ao correlacionar estratégias de funcionalização com os resultados de adsorção, esta tese avança na compreensão das relações estrutura-função em adsorventes lignocelulósicos, oferece novos insights sobre a valorização de resíduos agrícolas e estabelece um referencial para o design de materiais de biomassa escalonáveis voltados a tecnologias de tratamento de água.

Palavras-chave: Biomassa vegetal; funcionalização; bioadsorventes; adsorção; fármacos.

List of Figures

Figure 1: Photographic image of in natura LF highlighting its characteristic three-dimensional fibrous network.	23
Figure 2: Components of lignocellulosic materials (CARAFA; FOUCHER; SACRIPANTE, 2023).	23
Figure 3: Different routes of chemical modification through the grafting method (THAKUR et al., 2020).	26
Figure 4: Chemical structure of PEI (linear and branched forms).	26
Figure 5: Polymerization mechanism for the synthesis of PPy.	29
Figure 6: Chemical structure of stearic acid.	29
Figure 7: Chemical structure of β -CD.	31
Figure 8: Routes of PhCs contaminants (SAMAL; MAHAPATRA; HIBZUR ALI, 2022).	38
Figure 3-1.1: FTIR spectra of LF, PEI, LF-Glut, LF-PEI, and LF-g-PEI.	60
Figure 3-1.2: Images obtained by SEM images (at different magnifications) for (a,b) LF and (c,d) LF-g-PEI.	62
Figure 3-1.3: Adsorption capacity of (a) NTZ and (b) AMP on LF and LF-g-PEI as a function of time (Other experimental conditions: C_0 50 mg/L, amount of adsorbent 30 mg, volume 30 mL, r.t., pH not adjusted, stirring 100 rpm).	69
Figure 3-1.4: (a) FTIR spectra of AMP, LF-g-PEI, and LF-g-PEI loaded with AMP (LF-g-PEI/AMP), and (b) Scheme of AMP adsorption on LF-g-PEI.	77
Figure 3-1.5: (a) FTIR spectra of NTZ, LF-g-PEI, and LF-g-PEI loaded with NTZ (LF-g-PEI/NTZ), and (b) Scheme of NTZ adsorption on LF-g-PEI.	79

Figure 3-1.6: Adsorption capacity at equilibrium (bars) and reduction in the adsorption efficiency (line + symbol) for (a) NTZ and (b) AMP after consecutive reuse cycles using LF-g-PEI as the adsorbent.....	80
Figure 3-1.S1: (a) TGA and (b) DTG curves for LF, LF-g-PEI, and PEI.....	91
Figure 3-1.S2: Effect of the amount of adsorbent on the adsorption of (a) NTZ and (b) AMP (Other experimental conditions: C_0 50 mg/L, volume 30 mL, r.t., pH not adjusted, stirring 100 rpm).....	92
Figure 3-1.S3: Effect of initial concentration on the adsorption of (a) NTZ and (b) AMP (Other experimental conditions: Amount of adsorbent 30 mg, volume 30 mL, r.t., pH not adjusted, stirring 100 rpm).....	92
Figure 3-1.S4: Effect of the pH on the adsorption of (a) NTZ and (b) AMP (Other experimental conditions: Amount of adsorbent 30 mg, C_0 50 mg/L, volume 30 mL, r.t., stirring 100 rpm).....	92
Figure 3-1.S5: ΔpH vs pH_i curves for LF and LF-g-PEI.....	93
Figure 3-1.S6: Kinetic plots for the adsorption of (a) NTZ and (b) AMP on LF and LF-g-PEI.....	94
Figure 3-1.S7: (a) Freundlich, (b) Temkin, (c) DR, and (d) Sips isotherm plots for the adsorption of NTZ and AMP on LF and LF-g-PEI at 25 °C.....	95
Figure 3-2.1: (a) FTIR spectra and (b) XRD pattern of raw LF, LF-PPy, and LF-PPySAC.....	107
Figure 3-2.2: Photographic and SEM images (at different magnifications) obtained for (a) raw LF, (b) LF-PPy, and (c) LF-PPySAC.....	110
Figure 3-2.3: WCA measurements for raw LF, LF-PPy, and LF-PPySAC. Inset: Water droplet photographs on each sample.....	112

Figure 3-2.4: Batch adsorption kinetics of DCF on (a) raw LF, (b) LF-PPy, and (c) LF-PPySAC (Experimental conditions: $C_0 = 10\text{--}50$ mg/L, adsorbent dosage 40 mg, pH ~ 5.5 , r.t., stirring 100 rpm, contact time 60 min).....	115
Figure 3-2.5: Continuous adsorption kinetics of DCF on (a) raw LF, (b) LF-PPy, and (c) LF-PPySAC (Experimental conditions: $C_0 = 50$ mg/L, flow rate 0.5 mL/min, adsorbent dosage 40 mg, pH ~ 5.5 , r.t.).....	122
Figure 3-2.6: FTIR spectra of DCF, LF-PPySAC (before adsorption) and LF-PPySAC/ DCF (after adsorption).....	124
Figure 3-2.7: Schematic illustration of the adsorption mechanism of DCF on LF-PPySAC.....	125
Figure 3-2.8: Adsorption capacity of LF-PPySAC as a function of the reuse cycles. (a) Batch adsorption (Experimental conditions: $C_0 = 50$ mg/L, adsorbent dosage 40 mg, pH ~ 5.5 , r.t., stirring 100 rpm, contact time 60 min) and (b) continuous adsorption (Experimental conditions: $C_0 = 50$ mg/L, flow rate 0.5 mL/min, adsorbent dosage 40 mg, pH ~ 5.5 , r.t.).....	127
Figure 3-2.S1: (a) TGA and (b) DTG curves of LF, LF-PPy, and LF-PPySAC...	142
Figure 3-2.S2: Compression of the (a) LF, (b) LF-PPy, and (c) LF-PPySAC samples with a load.....	143
Figure 3-2.S3: Effect of adsorbent dosage on the DCF adsorption capacity (Other experimental conditions: Solution volume 20 mL, C_0 50 mg/L, pH ~ 5.5 , r.t., stirring 100 rpm, contact time 60 min).....	144
Figure 3-2.S4: (a) Effect of initial pH on the DCF adsorption capacity (Other experimental conditions: C_0 50 mg/L, adsorbent dosage 40 mg, volume 20 mL, r.t., stirring 100 rpm, contact time 60 min). (b) pH_{PZC} values determined for LF, LF-PPy, and LF-PPySAC.....	146

Figure 3-2.S5: PFO plots for the adsorption of DCF onto (a) LF, (b) LF-PPy, and (c) LF-PPySAC samples (Experimental conditions: $C_0 = 10\text{--}50$ mg/L, adsorbent dosage 40 mg, pH ~ 5.5 , r.t., stirring 100 rpm, contact time 60 min).....	147
Figure 3-2.S6: PSO plots for the adsorption of DCF on (a) LF, (b) LF-PPy, and (c) LF-PPySAC samples (Experimental conditions: $C_0 = 10\text{--}50$ mg/L, adsorbent dosage 40 mg, pH ~ 5.5 , r.t., stirring 100 rpm, contact time 60 min).....	148
Figure 3-2.S7: Intraparticle diffusion plots for the adsorption of DCF on (a) LF, (b) LF-PPy, and (c) LF-PPySAC samples (Experimental conditions: $C_0 = 10\text{--}50$ mg/L, adsorbent dosage 40 mg, pH ~ 5.5 , r.t., stirring 100 rpm, contact time 60 min).....	149
Figure 3-2.S8: (a) Langmuir, (b) Freundlich, (c) Temkin, and (d) D-R isotherm plots for the adsorption of DCF on LF, LF-PPy and LF-PPySAC at 25 °C (Experimental conditions: $C_0 = 1\text{--}50$ mg/L, adsorbent dosage 40 mg, pH ~ 5.5 , r.t., stirring 100 rpm, contact time 60 min).....	151
Figure 3-2.S9: (a) Effect of adsorbent dosage on the DCF adsorption capacity (Other experimental conditions: Flow rate 0.5 mL/min, C_0 50 mg/L, pH ~ 5.5 , r.t.). (b) Effect of flow rate on DCF adsorption capacity (Other experimental conditions: Adsorbent dosage 40 mg, C_0 50 mg/L, pH ~ 5.5 , room temperature).....	153
Figure 3-2.S10: Adsorption capacity at equilibrium of DCF on LF, LF-PPy, and LF-PPySAC using tap water as medium (Other experimental conditions: C_0 50 mg/L, adsorbent dosage 40 mg, volume 20 mL, room temperature, stirring 100 rpm, contact time 60 min).....	154
Figure 3-2.S11: Images obtained by SEM from LF-PPySAC after the 5th adsorption/desorption cycle at different magnifications. (a) Mag x100 and (b) Mag x1000.....	155

Figure 3-3.1: FTIR spectra of (a) raw LF and LF(NaOH) and (b) LF(NaOH), β -CD and LF(NaOH)- β CD.....	175
Figure 3-3.2: Images obtained by SEM from (a,b) LF(NaOH) and (c,d) LF(NaOH)- β CD at two different magnifications (x200 and x1000).....	179
Figure 3-3.3: FTIR spectra of pure NIM, LF(NaOH)- β CD, and LF(NaOH)- β CD after NIM adsorption (denoted as LF(NaOH)- β CD/NIM).....	194
Figure 3-3.4: (a) Adsorption capacity (q_e) and removal efficiency of NIM by LF(NaOH)- β CD during ten consecutive adsorption-desorption cycles in batch mode; (b) desorption efficiency of LF(NaOH)- β CD in batch mode using MeOH:HCl (0.15 mol/L) as eluent; (c) removal efficiency of NIM by LF(NaOH)- β CD over three consecutive adsorption–desorption cycles in fixed-bed column experiments.....	198
Figure 3-3.S1: UV-Vis absorption spectra of phenolphthalein in aqueous solution: (a) measured in the presence of LF, LF(NaOH), and LF(NaOH)- β CD; (b) measured with varying amounts of LF(NaOH)- β CD.....	214
Figure 3-3.S2: (a) TGA and (b) DTG curves for raw LF, LF(NaOH), and LF(NaOH)- β CD.....	215
Figure 3-3.S3: (a) Variation of final pH as a function of initial pH (pH_i) for the determination of the point of zero charge (pH_{PZC}) of LF(NaOH) and LF(NaOH)- β CD. (b) Equilibrium adsorption capacity (q_e) of NIM onto LF(NaOH)- β CD as a function of solution pH.....	215
Figure 3-3.S4: Adsorption capacity (q_t) of NIM onto LF(NaOH)- β CD as a function of time. Experimental data (dots) are compared with nonlinear fits of the PFO, PSO, and Elovich kinetic models.....	216

Figure 3-3.S5: Equilibrium adsorption capacity (q_e) of NIM onto LF(NaOH)- β CD as a function of initial NIM concentration. Experimental data (dots) are compared with nonlinear fits of the Sips, Hill, and Redlich-Peterson (RP) isotherm models.....	216
Figure 3-3.S6: Breakthrough curves for NIM adsorption onto LF(NaOH)- β CD as a function of time, varying (a) flow rate, (b) initial NIM concentration, and (c) column height.....	217
Figure 3-3.S7: 3D contour plots of NIM adsorption onto LF(NaOH)- β CD (a) flow rate, (b) initial NIM concentration, and (c) column height; and percentage removal.....	217

List of Tables

Table 1. Examples of LF modifications and their applications.....	24
Table 2: Physicochemical properties and molecular structures of the selected PhCs.	40
Table 3: Summary of treatment processes applied for PhCs removal.	42
Table 3-1.1: Elemental analysis for LF and LF-g-PEI.....	60
Table 3-1.2: Density and porosity values for LF and LF-g-PEI.....	63
Table 3-1.3. Kinetic parameters calculated for NTZ and AMP adsorption on LF and LF-g-PEI.....	70
Table 3-1.4. Isotherms parameters calculated for NTZ and AMP adsorption on LF and LF-g-PEI at 25 °C.....	72
Table 3-1.S1: Kinetic and isotherm mathematical models and error-function...	93
Table 3-1.S2: Thermodynamic parameters for NTZ and AMP adsorption on LF and LF-g-PEI	95
Table 3-2.1: Kinetic parameters calculated for DCF adsorption on LF, LF-PPy, and LF-PPySAc.....	116
Table 3-2.2: Isotherms parameters calculated for DCF adsorption LF, LF-PPy, and LF-PPySAc at 25 °C.....	120
Table 3-2.3: Comparison between adsorption capacities (q_e) of some adsorbents tested in the removal of DCF from aqueous media.....	126
Table 3-2.S1: Intraparticle diffusion parameters calculated for DCF adsorption on LF, LF-PPy, and LF-PPySAc.....	149
Table 3-2.S2: Thermodynamic parameters for DCF adsorption on LF samples at various temperatures.....	152
Table 3-3.1: Density and porosity values for LF _(NaOH) and LF _(NaOH) - β CD.....	180

Table 3-3.2: Kinetic parameters calculated for NIM adsorption onto LF _(NaOH) -βCD.....	182
Table 3-3.3: Isotherms parameters calculated for NIM adsorption onto LF _(NaOH) -βCD at 25 °C.....	184
Table 3-3.4: Parameters of the breakthrough curve for NIM adsorption onto LF _(NaOH) -βCD.....	187
Table 3-3.5: Breakthrough curve modellings calculated for NIM adsorption onto LF _(NaOH) -βCD at 25 °C.....	190
Table 3-3.6: Comparison between adsorption capacities (q_e) of some adsorbents tested in the removal of NIM from water.....	200
Table 3-3.S1: Kinetic, isothermal, and breakthrough models, along with the associated error function used for modeling the adsorption of NIM ions on LF _(NaOH) -βCD.....	212
Table 3-3.S2: Thermodynamic parameters for NIM adsorption on LF _(NaOH) - βCD at various temperatures.....	213
Table 3-3.S3: Estimated production cost of LF _(NaOH) -βCD under laboratory-scale conditions.....	214
Table 4: Summary of LF modification strategies, characterization results, and adsorption performances for each study.	216

List of Abbreviations and Acronyms

Abs:	Absorbance
AMP:	Ampicillin
β -CD:	β -Cyclodextrin
CA:	Citric acid
C ₀ :	Initial analyte concentration
C _e :	Analyte concentration at equilibrium
C _t :	Analyte concentration at a specific time
DCF:	Sodium diclofenac
D-R:	Dubinin–Radushkevich isotherm
EC:	Emerging contaminant
FTIR:	Fourier-transform infrared spectroscopy
Glut:	Glutaraldehyde
LF:	<i>Luffa cylindrica</i>
NIT:	Nitazoxanide
PEI:	Polyethylenimine
pH _{PZC} :	pH of point of zero charge
PFO:	Pseudo-first-order kinetic model
PPy:	Polypyrrole
PSO:	Pseudo-second-order kinetic model
q _e :	Amount of contaminant adsorbed per gram of sponge at equilibrium
q _t :	Amount of contaminant adsorbed per gram of sponge at a specific time
rpm:	Rotations per minute
r.t.:	Room temperature
SAC:	Stearic acid
SEM:	Scanning electron microscopy
TGA:	Thermogravimetric analysis
WCA:	Water contact angle
XRD:	X-ray diffraction
χ^2 :	Chi-square

Summary

Chapter 1 – General introduction and objectives	18
1.1. Introduction.....	18
1.2. Objective	21
1.2.1. <i>General objective</i>	21
1.2.2. <i>Specific objectives</i>	21
Chapter 2 – Literature review	22
2.1. Luffa cylindrica (LF)	22
2.2. Modification of agricultural residue	24
2.2.1. Polyethyleneimine (PEI)	26
2.2.2. Polypyrrole (PPy).....	27
2.2.3. Stearic acid (SAc).....	29
2.2.4. β -cyclodextrin (β -CD).....	30
2.3. Adsorption: Fundamentals and applications	32
2.3.1. Batch adsorption.....	34
2.3.2. Fixed-bed column adsorption	35
2.4. Pharmaceuticals as emerging contaminants	36
Chapter 3 – Research developed	44
3.1. Article – Synthesis and characterization of polyethyleneimine grafted lignocellulosic fibers for improved removal of nitazoxanide and ampicillin from water	45
3.2. Article – Polypyrrole/stearic acid-coated Luffa cylindrica for enhanced removal of sodium diclofenac from water: Batch and continuous adsorption studies	95
3.3. Article – Efficient fixed-bed removal of the emerging contaminant nimesulide using β-cyclodextrin-grafted Luffa biomass	156
Chapter 4 – Final remarks.....	216
5. References.....	219

Chapter 1 – General introduction and objectives

1.1. Introduction

The disposal of untreated agricultural residues contributes significantly to environmental contamination, yet their valorization offers a sustainable alternative. Agricultural residues such as *Luffa cylindrica* (LF), a subtropical Cucurbitaceae plant, have attracted increasing attention due to their abundance, biodegradability, non-toxicity, and low cost (DA COSTA et al., 2024). Its lignocellulosic composition, mainly made up of cellulose, hemicellulose, lignin, and extractives, offers valuable structural characteristics such as high porosity, mechanical strength, toughness, lightness, and rigidity (KHADIR et al., 2021). In addition, the abundance of hydroxy groups enables diverse modifications, such as ring-opening polymerization, esterification, grafting, and step-growth polymerization, thereby expanding its potential applications (AKAY et al., 2021).

Despite these advantages, raw LF fibers contain relatively few active sites, predominantly hydrophilic hydroxy groups, which limit interactions with hydrophobic contaminants (AKAY et al., 2022; PREMALATHA et al., 2021). Although LF has been tested as an adsorbent for dyes, metal ions, and certain pharmaceuticals (IGHALO et al., 2020), its modification remains underexplored. Tailoring LF fibers through functionalization can increase the density of active sites and enhance affinity toward emerging contaminants (KHADIR; NEGARESTANI; MOLLAHOSSEINI, 2020). Thus, the valorization of this abundant natural resource for high-value environmental applications promotes the sustainable use of biomass within the framework of green chemistry and materials science.

The development of adsorbents from natural residues directly aligns with several United Nations Sustainable Development Goals (SDGs) (MOHANRASU et al., 2025). Specifically, SDG 6 (Clean Water and Sanitation) is addressed by contributing to affordable water treatment technologies; SDG 12 (Responsible Consumption and Production) is advanced through the conversion of agricultural waste into functional materials; and SDG 14 (Life Below Water) is supported by mitigating pharmaceutical pollution in aquatic ecosystems. These connections highlight the societal and environmental relevance of this research, situating it within a global agenda of sustainable development.

The urgency of new treatment strategies is reinforced by growing concerns over emerging contaminants (ECs), a heterogeneous group of micropollutants that includes pharmaceuticals, personal care products, hormones, and agrochemicals originating mainly from urban, industrial, agricultural, and healthcare activities (BASHEER, 2018; SHAMSUDIN; AZHA; ISMAIL, 2022). Pharmaceuticals (PhCs) are of particular concern due to their frequent detection in aquatic systems, either as residues or metabolites, often at trace levels. Each class of PhCs has a specific mode of action that complicates detection, analysis, and removal in conventional treatment plants (SOPHIA A.; LIMA, 2018). Given the risks associated with these compounds, their effective removal from water is critical to protect both human health and biodiversity (FEIZI; SARMAH; RANGSIVEK, 2021).

Various treatment methods have been investigated for PhCs removal, including biodegradation, photodegradation, electrochemical processes, ozonation, and adsorption (FINKBEINER et al., 2015; JANG et al., 2020; PRASETYA et al., 2023). However, most are costly, non-selective, inefficient at

trace concentrations, or generate harmful by-products (SHEARER; PAP; GIBB, 2022). By contrast, adsorption stands out for its high efficiency, operational simplicity, cost-effectiveness, and the absence of toxic secondary products (HUANG; SHEN; SHUAI, 2021; SHEARER; PAP; GIBB, 2022). Its efficiency depends on the chemical properties of both contaminant and adsorbent, which determine the underlying interactions and mechanisms (SHAMSUDIN et al., 2022). Accordingly, the rational design of biomass-based adsorbents with tailored surface properties emerges as an urgent scientific and technological challenge.

Based on these considerations, the central hypothesis of this thesis is that modification of LF fibers can significantly enhance their adsorption capacity for pharmaceuticals by introducing additional functional groups and strengthening interactions with diverse classes of contaminants. Although LF has recognized potential as an adsorbent, the effects of specific modification strategies on its structure, surface chemistry, and adsorption behavior remain poorly understood, particularly under environmentally relevant conditions. This thesis seeks to address these gaps by developing and systematically evaluating different modification approaches for LF, with emphasis on the relationships between functionalization, fiber structure, and adsorption efficiency. The original contribution lies in advancing the sustainable design of biomass-based adsorbents for water treatment, providing effective strategies to tailor LF fibers for improved removal of pharmaceutical contaminants, and establishing a framework to guide future developments in lignocellulosic adsorbent modification.

1.2. Objective

1.2.1. General objective

To develop functionalized LF fibers with enhanced adsorption capacity for pharmaceuticals in aqueous media, establishing relationships between fiber functionalization, structural properties, and adsorption performance.

1.2.2. Specific objectives

- Develop efficient, reproducible, and robust methodologies for modification of LF fibers;
- Characterize the physicochemical, structural, thermal, and morphological properties of modified fibers to understand the effects of functionalization on LF fibers;
- Evaluate the adsorption performance of modified fibers toward selected pharmaceuticals under controlled aqueous conditions;
- Apply mathematical modeling to elucidate adsorption kinetics, isotherms, and mechanistic pathways;
- Assess the stability, recyclability, and reusability of the developed adsorbents for practical water treatment applications.

Chapter 2 – Literature review

2.1. *Luffa cylindrica* (LF)

LF, also known as loofah sponge or sponge gourd, is an agricultural biomass product (**Figure 1**). It is cultivated in several Asian and African countries, and is also commonly found in India, Japan, China, as well as in Central and South America (SANTOS et al., 2024). This subtropical plant belongs to the *Cucurbitaceae* family, which comprises several species, including *L. acutangula*, *L. cylindrica* (*L. aegyptiaca*), *L. echinata*, *L. graveolens*, *L. hermaphrodita*, *L. operculata*, *L. tuberosa*, and *L. umbelatta* (AKINYEMI; DAI, 2022). Fresh *L. cylindrica* is consumed as a vegetable and has applications in traditional medicine. Its sponge form is widely used to produce packaging materials, bath sponges, soundproof linings, and as a support matrix for immobilizing plants, algae, bacteria, and yeasts. LF has a plant growth yield achieving 62,000 sponge gourd fruits/ha (20–25 fruits/plant), that is, one mature sponge gourd produces more than 30 seeds (ANASTOPOULOS; PASHALIDIS, 2020). Structurally, LF is a lignocellulosic material whose fibers are microcellular and arranged with macropores of approximately 10–20 μm in diameter, forming a fibrous vascular network that results in a three-dimensional reticulated structure (SANTOS et al., 2024). Chemically, its fibers are composed of approximately 60% cellulose, 30% hemicellulose, and 10% lignin, although this composition may vary depending on the geographical and environmental conditions at which the plant was cultivated (ADEYANJU et al., 2021; KAMRAN et al., 2022).



Figure 1: Photographic image of *in natura* LF highlighting its characteristic three-dimensional fibrous network.

The fibers of LF are rich in hydroxy ($-OH$) groups, from the lignocellulosic composition, which enable surface functionalization (**Figure 2**). This modification can alter its chemical and physical properties, thereby enhancing its ability for different applications (SANTOS et al., 2024). Based on **Table 1**, it can be observed that LF has been widely used in the development of various materials and across diverse application areas, such as solid-phase extraction, plastic and biocomposites reinforcement, etc. However, the good structural properties, LF have attracted increasing attention as a potential adsorbent (ANASTOPOULOS; PASHALIDIS, 2020; KAMRAN et al., 2022).

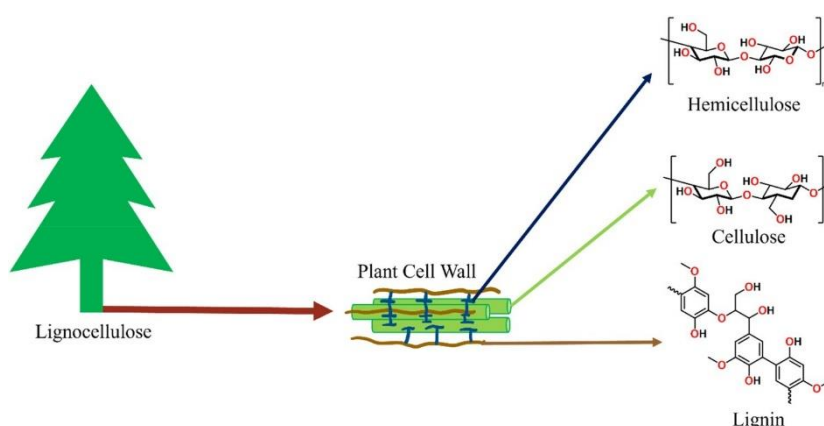


Figure 2: Components of lignocellulosic materials (CARAFA; FOUCHER; SACRIPANTE, 2023).

Table 1. Examples of LF modifications and their applications.

Type of modification	Application	Main results	Ref.
Quaternization	Solid-phase extraction for selective enrichment of phosphopeptides	Improved the removal of phosphate ions (QA ~77% and QB ~89%)	(DAI; SUN; ZHOU, 2019)
Alkali treatment	Prevention of postoperative adhesion bands	Reduction of inflammatory cells and adhesions one week after fiber implantation.	(JAMSHIDI-ADEGANI et al., 2021)
Modification with silver nanoparticles	Removal of ibuprofen from aqueous solutions	Increase adsorption capacity (71 mg/g) and removal efficiency (92%)	(JOODAKI; MOLLAHOSSEINI, 2023)
Fibrillation and incorporation into recycled polystyrene matrix	Production of reinforced plastic composites with LF	Improved rigidity and impact strength of composites	(ADENIYI et al., 2023)
Alkali treatment	Reinforcement of biocomposites based on poly(butylene succinate-co-lactate)/starch	Increased rigidity and impact strength of biocomposites	(LAI et al., 2016)
Grafting of poly(ϵ -caprolactone) via ring-opening polymerization	Biodegradable bioplastics	Degradation more pronounced under enzymatic conditions	(AKAY et al., 2022)
Hydrophobic modification	Oil/water separation	Demonstrated high oil absorption capacity and selectivity	(ZHANG et al., 2024)
Incorporation of phase change materials (PCM) into LF matrix with styrene-isoprene-styrene copolymer	Thermal protection and wearable thermal management	Developed a flexible PCM composite with high latent heat storage capacity (up to 160 J/g)	(HE et al., 2024)
Crosslinking with polyethyleneimine and loading with biochar	Ecological remediation of oligotrophic water	Achieved high removal efficiencies for COD, $\text{NH}_4^+\text{-N}$, Ca^{2+} , and $\text{PO}_4^{3-}\text{-P}$	(CAO et al., 2024)
Carbonization followed by modification with ZIF-67 and KOH	Biodiesel production from waste edible oil	Developed a heterogeneous catalyst (ACL/ZIF-67/KOH) that achieved biodiesel yield of 98.31%.	(FOROUTAN et al., 2022)

2.2. Modification of agricultural residue

The presence of hydroxy groups in the chemical structure of agricultural residues facilitates alterations in their chemical composition through various

modification processes (YUAN; LI; PENG, 2023). Physicochemical properties, like their hydrophilic/hydrophobic characteristics, surface area and porosity, reactive functional groups, resistance to microbiological attack, and thermal stability, are improving in the resulting material (TAN et al., 2024). These modifications can be classified into physical, chemical, biological, mechanical, etc. Among these approaches, chemical modification is noteworthy for producing materials with enhanced physicochemical properties. Methods such as alkalization, acidification, esterification, etherification, carbonization, magnetization, and graft copolymerization are commonly employed chemical techniques for modifying agricultural residues (LIU et al., 2022a).

The graft copolymerization method is highly versatile, allowing the grafting not only of different functional groups but also of long functional chains. This method, which involves grafting monomers, polymers, or other functional species onto the surface of agricultural residues, is noteworthy because the resulting material exhibits the characteristics of the polymer or species attached to the residue structure (YUAN; LI; PENG, 2023). The grafting process can occur through three approaches: grafting to, where the terminal functional group of the species is attached to the residue structure; grafting from, in which monomers polymerize directly on the residue surface; and grafting through, which involves the preparation of macromolecular monomers (**Figure 3**) (LIU et al., 2022a). Among these methodologies, grafting from is the most commonly employed approach for attaching polymers onto the surface of agricultural residues. In this context, the use of polymers or molecules with specific functional groups and properties becomes important to obtain a material exhibiting desirable characteristics for the intended application (YUAN; LI; PENG, 2023).

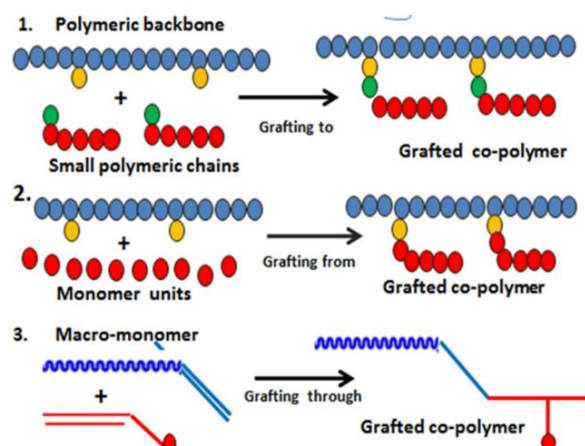


Figure 3: Different routes of chemical modification through the grafting method (THAKUR et al., 2020).

2.2.1. Polyethyleneimine (PEI)

PEI is a polymer that exists in both linear and branched forms (**Figure 4**). It is a water-soluble polymer with a high density of amine groups in its structure. PEI is biocompatible, cationic, commercially available, and environmentally friendly (KANI et al., 2022).

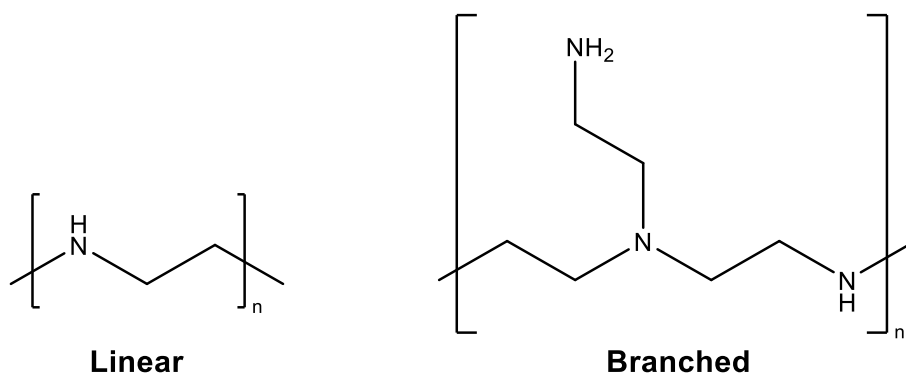


Figure 4: Chemical structure of PEI (linear and branched forms).

The high density of amine groups present in the structure of polyethyleneimine (PEI) allows its grafting onto various materials (e.g. MOFs (WANG et al., 2024), silica nanoparticles (AL-ARAJI; AL-ANI; ALSALHY, 2023), polymers (HU et al., 2023; WU et al., 2021), etc.). In this context, PEI has been reported to be grafted onto cellulose fibers to enhance the material's performance

in adsorption processes (BETTAIEB et al., 2025; WU; WANG, 2024). The main rationale for incorporating PEI into the chemical matrix of an adsorbent is the introduction of amine groups, which can significantly improve adsorption efficiency (WANG et al., 2024). Furthermore, PEI modification offers additional advantages, as it is a low cost approach that does not compromise the inherent benefits of using natural agricultural residues, such as availability, biodegradability, environmental friendliness, efficiency, renewability, and reusability (KANI et al., 2022).

The modification of biomass with PEI can be carried out through crosslinking or grafting processes. In these cases, the biomass is chemically modified via the formation of irreversible covalent bonds (RIVA; FIORATI; PUNTA, 2021). Most grafting and crosslinking processes used to produce PEI-modified materials occur by chemical reactions (CHEN et al., 2021). Biomass modification with PEI can be performed using linking agents (e.g., epichlorohydrin), organic solvents (e.g., *N,N*-dimethylformamide and thionyl chloride, SOCl_2), or crosslinking agents (e.g., glutaraldehyde) (KANI et al., 2022). When glutaraldehyde is used to crosslink PEI onto cellulose, the main constituent of LF, a Schiff base and a hemiacetal are formed. This modification is straightforward and can be conducted in a single vessel at room temperature (r.t.) (RIVA; FIORATI; PUNTA, 2021).

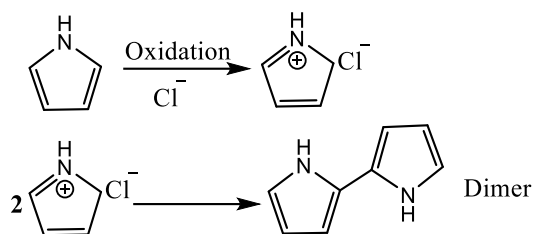
2.2.2. Polypyrrole (PPy)

PPy is a conductive polymer formed through the oxidation of the pyrrole monomer via a pseudo-polycondensation mechanism (SASSO et al., 2011). This polymer has been widely investigated for various applications due to its redox

properties, high electrical conductivity, strong environmental stability, and ease of processing (MAITY; DUBEY; CHAKRABORTY, 2021). The presence of nitrogen atoms in the PPy backbone endows the material with significant potential as an adsorbent (MUHAMMAD EKRAMUL MAHMUD; HUQ; YAHYA, 2016).

The use of PPy to coat natural adsorbent materials has emerged as an important strategy, as the resulting composite exhibits enhanced removal capacity while maintaining low cost (WANG et al., 2022b). Coating natural fibers, such as LF, with PPy can be achieved via *in situ* chemical polymerization in the presence of an oxidant and a dopant. When FeCl_3 is employed as the oxidant, the initial stage of polymerization involves the oxidation of pyrrole monomers into radical cations, which combine to form bipyrrrole. Chain growth occurs during the propagation stage, leading to the formation of PPy, which is insoluble in water (**Figure 5**) (MAITY; DUBEY; CHAKRABORTY, 2021). Consequently, the polymer precipitates and is adsorbed onto the fibers through hydrogen-bond interactions between the amine groups of PPy and the hydroxy groups of the natural fibers (SASSO et al., 2011).

Initiation



Propagation

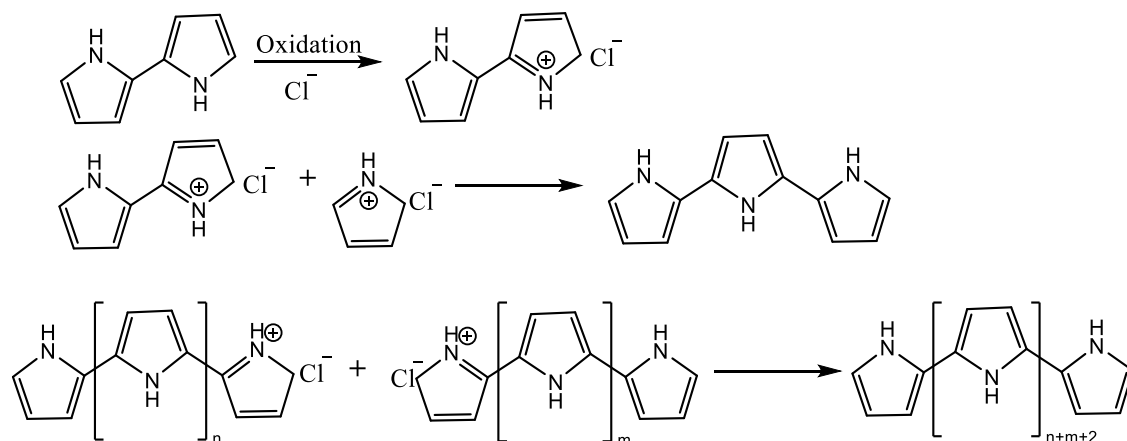


Figure 5: Polymerization mechanism for the synthesis of PPy.

2.2.3. Stearic acid (SAc)

Stearic acid or octadecanoic acid is a saturated fatty acid consisting of an 18-carbon chain, widely found in both animal and vegetable fats (**Figure 6**) (BANGAR et al., 2024). Due to its low cost and low chemical toxicity, SAc has been increasingly employed in various fields of application (KHATTAB; MOHAMED; HASSABO, 2020).

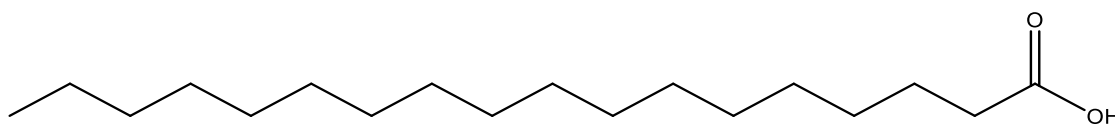


Figure 6: Chemical structure of stearic acid.

Pharmaceutical compounds often exhibit a certain degree of hydrophobicity or low water solubility in their neutral structural form, which can influence the adsorption process (KAUR et al., 2018; SUNTISUKASEAM;

WESCHAYANWIWAT; SABATINI, 2007). HE; XU; ZHANG, (2013) used stearic acid to create a moisture barrier, as this compound has a carboxyl group in its molecular structure capable of reacting with the hydrophilic hydroxy groups of cellulose fibers. Modifying the surface of the fibers resulted in increased roughness and water resistance.

2.2.4. β -cyclodextrin (β -CD)

β -CD is a cyclic oligosaccharide composed of seven D-glucopyranoside units linked by $\alpha(1\rightarrow4)$ glycosidic bonds, **Figure 7** (AHMADI et al., 2025; UROOJ; MISHRA; PANDEY, 2024). The external surface is formed by hydroxy groups, which impart a hydrophilic character, whereas the internal cavity is lined with ether-like oxygen atoms, providing a hydrophobic microenvironment. Despite this hydrophobic nature, the cavity can accommodate a limited number of water molecules without compromising its intrinsic characteristics or structural arrangement (AHMADI et al., 2025). This phenomenon occurs because the confined water molecules establish hydrogen bonds both among themselves and with the inner walls of β -CD. Consequently, the internal cavity endows β -CD with the crucial ability to form inclusion complexes with hydrophobic guest molecules (UROOJ; MISHRA; PANDEY, 2024).

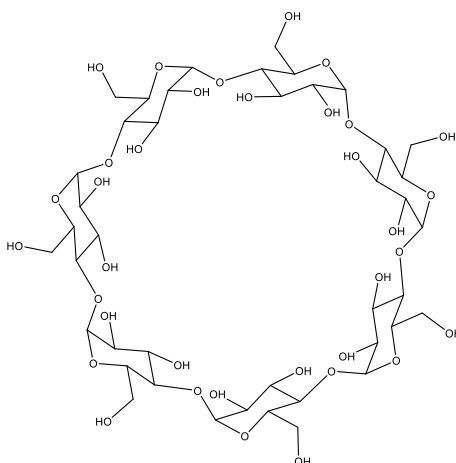


Figure 7: Chemical structure of β -CD.

β -CD exhibits several advantageous characteristics, including an intermediate cavity size, stable crystalline structure, low cost, and a strong ability to establish hydrogen bonding (TIAN et al., 2021). Its internal cavity has an average diameter ranging from 7 to 8 Å, which is particularly suitable for host–guest interactions (ABU RAHIM et al., 2023). This capability distinguishes β -CD as an effective material for the adsorption of pollutants in aqueous systems. Inclusion complexes can be formed through different mechanisms, such as hydrogen bonding, electrostatic attraction, hydrophobic interactions, and van der Waals forces (ABU RAHIM et al., 2023). Owing to these properties, the use of β -CD has been extensively reported in the literature, both for the modification of various materials and for the removal of different contaminants from water. For example, LIU et al. (2022) made a rice husk modified by synergistic effects of β -CD grafting and Fe_3O_4 loading for the removal of Pb(II) and Bisphenol A. BHATTACHARJEE et al. (2022) developed graphene oxide functionalized with β -cyclodextrin (BCDGO) for an efficient and faster removal of atenolol from water.

2.3. Adsorption: Fundamentals and applications

Adsorption is a surface phenomenon that consists of separating one or more substances from a gas or liquid phase and concentrating them onto the surface of another phase (BHUYAN; AHMARUZZAMAN, 2023). The substances present in the gas or liquid are referred to as the adsorbate, while the surface onto which they accumulate is called the adsorbent. The efficiency of the transfer process from the adsorbate to the adsorbent surface depends on the interactive forces established between the two species (PÉREZ-BOTELLA; VALENCIA; REY, 2022). The type and strength of interaction occurring between the contaminants (adsorbate) and the adsorbent are determined by the intrinsic surface properties and the degree of functionalization of the adsorbent material (ALOMAR et al., 2023).

The interaction between the adsorbent and the adsorbate can occur through two main mechanisms: Chemical or physical interaction. When adsorption takes place via chemical interactions, the process is referred to as chemisorption. In this case, stronger electrostatic forces, such as covalent or ionic bonding, dominate adsorption. Since these interactions are characterized by shorter bond lengths and higher bond energies, chemisorption is generally considered an irreversible process (PATEL, 2019). In contrast, when adsorption occurs through weaker interactions, it is known as physisorption. This process is governed by weaker electrostatic forces, including dipole-dipole interactions, dispersion forces, and hydrogen bonding. Physisorption is reversible, as these interactions are associated with relatively low enthalpy values (BHUYAN; AHMARUZZAMAN, 2023; PÉREZ-BOTELLA; VALENCIA; REY, 2022). It is important to emphasize, however, that the nature of the adsorption process

depends exclusively on the intrinsic properties of both the adsorbent and the adsorbate (PATEL, 2019).

Several sources have been employed for the development of adsorbents. Synthetic adsorbents are produced in laboratories and generally exhibit high porosity, which results in a high adsorption capacity. However, their main drawback is the elevated cost of production (COSTA et al., 2022; LETSOALO et al., 2023). To illustrate, TEE et al. (2023) developed a 3D heteroatom-doped graphene for adsorb dyes, heavy metals, pharmaceuticals, oils, and solvents; DONG et al. (2021) developed a novel biochar-based iron oxide composite (FeYBC) for simultaneous Cr(VI) and phenol adsorption. Natural adsorbents, on the other hand, are derived from plant roots, leaves, and agricultural residues. These materials undergo physical pretreatment without chemical interference and are subsequently applied as adsorbents. Their major advantage is the low cost, although they typically suffer from a relatively low adsorption capacity (PATEL, 2019). *Moringa oleifera* seeds are an example of a natural adsorbent. VIEIRA et al. (2010) utilize these seeds for dairy industry wastewater, and RAJI et al. (2023) prepared activated carbon from these seeds to remove crystal violet. Semi-synthetic adsorbents have been developed to combine the benefits of both categories. These materials are based on a natural substrate that is chemically or physically modified to enhance performance in the adsorption process. Semi-synthetic adsorbents stand out due to their low cost, high efficiency, reduced generation of chemical or biological sludge, and the possibility of adsorbent regeneration (KRASNOPEEVA; PANOVA; YAKIMANSKY, 2022). Owing to these advantages, the use and application of semi-synthetic adsorbents have grown significantly in recent years. ARABKHANI and ASFARAM (2022) utilized a

combination of sugarcane bagasse ash, polyvinyl alcohol, and pine cone-derived tannin to prepare a bio-based ceramic/organic xerogel for removing antibiotics from water; in the same way, XIA et al. (2021) prepared an adsorbent by the electrostatic-interaction-driven self-assembly of lignosulfonate, tannic acid, and cationic polyacrylamide for efficient removal of boron.

The contact between the adsorbent and the adsorbate can be established through different treatment configurations, including batch systems, continuous fixed-bed systems (with upward or downward flow), continuous moving-bed systems, continuous fluidized-bed systems, and pulsed-bed systems. Among these approaches, batch and fixed-bed methods are the most widely applied, as they avoid disadvantages such as the requirement of large operational areas, high costs, excessive adsorbent consumption, feed channeling, the need for adsorbent storage before use, and non-uniform residence times (PATEL, 2022).

2.3.1. Batch adsorption

Batch adsorption treatment is the most widely applied adsorption method among researchers, as it is a traditional and effective approach for the removal of contaminants from different types of water. In batch adsorption processes, parameters such as agitation speed, solution pH, contaminant concentration, adsorbent dosage, temperature, contact time, and particle size (in the case of particulate materials) are evaluated regarding their influence on adsorption performance (CHOUCHANE et al., 2023). This method is commonly employed to assess the feasibility of the adsorbent–adsorbate interaction. Batch adsorption offers advantages such as simplicity, ease of operation, and low cost. However, its main drawback is that only small volumes of contaminants can be treated,

which limits the applicability of this technique for large-scale industrial systems (PATEL, 2022). ALKHATHAMI et al. (2023) employed the batch adsorption process to evaluate the adsorption capacity of a zirconium-based metal-organic framework (Zr-MOF) functionalized with tryptophan (Zr-MOF-NH₂) for the removal of ibuprofen, achieving an adsorption capacity of 371 mg/g. Similarly, XU et al. (2023) utilized biochar synthesized from algal biomass for the efficient removal of tetracycline through batch adsorption, where, under optimized conditions, an adsorption capacity of 376.878 mg/g was obtained.

2.3.2. Fixed-bed column adsorption

Column treatment, also known as fixed-bed adsorption, is a process in which the contaminated solution is continuously passed through a column packed with the adsorbent material. Fixed-bed adsorption can be divided into two operational modes: downflow, in which the contaminated solution flows through the adsorbent in the same direction as gravity, and upflow, in which the solution flows in the opposite direction to gravity (PATEL, 2019). Similar to batch adsorption, several parameters are evaluated in fixed-bed systems to assess their influence on adsorption performance, including flow rate, contaminant concentration, bed height (adsorbent dosage), and pH. Fixed-bed adsorption is particularly noteworthy due to its ability to treat large volumes of contaminated water, making it highly suitable for industrial-scale applications. However, this method also presents disadvantages such as adsorbent exhaustion, feed channeling, and uncontrolled movement of adsorbent particles within the column (RICHARD et al., 2025). PUGA et al. (2022) utilized the fixed-bed column for the adsorption of a multicomponent mixture of Venlafaxine (VLX), Trazodone (TRZ)

and Fluoxetine (FLX), which was studied in a biochar, and obtained the maximum experimental uptake of 2.07, 2.89, and 7.71 mg/g for VLX, FLX, and TRZ, respectively. Magnetic tyre char, activated tyre char (ATC), and commercial activated carbon were used as packing materials in a lab-scale column by FEIZI, SARMAH, and RANGSIVEK, (2021) to investigate the adsorption of propranolol, ciprofloxacin, and clomipramine from aqueous solution. The authors concluded that the column packed with ATC exhibited a higher adsorption capacity (25.32 mg/g) compared to MTC.

2.4. Pharmaceuticals as emerging contaminants

Emerging contaminants (ECs) are substances that have been recently detected in the environment and are not commonly monitored but have the potential to pose risks to human health and ecosystems. Products such as pesticides, PhCs, personal hygiene products, disinfectants, surfactants, household materials, nanomaterials, and illicit drugs are considered ECs because they are found in low concentrations in water bodies and are not regulated by current environmental laws (MADDELA et al., 2022). The persistence and bioaccumulation potential of ECs, combined with their complex chemical structures, make them challenging to remove through conventional water treatment processes. This has led to increased attention on developing advanced treatment technologies and monitoring strategies to mitigate their impact (KUMAR et al., 2022). Among these, PhCs and personal care products (PPCPs) are among the main groups of emerging contaminants, due to their increasing use in recent years (OSUOHA; ANYANWU; EJILEUGHA, 2023).

PhCs are biologically active compounds used for the treatment or prevention of diseases in humans and animals. These can be sold with or without a prescription, which further increases the presence of this group of contaminants in the environment, especially in aquatic environments (LETSOALO et al., 2023). Drugs can be classified into different groups depending on their mechanism of action, mode of action, chemical structures, and disease treatment. Considering the use of the drug, it can be classified as analgesics and anti-inflammatories, antidepressants, antibiotics, antivirals, anticoagulants, sedatives, cardiovascular drugs, etc. (SAMAL; MAHAPATRA; HIBZUR ALI, 2022).

The main sources of PhCs pollution in the environment include hospital effluents, industrial discharges from PhCs manufacturing, agricultural runoff (pesticides and fertilizers), and human and animal excreta originating from households and sewage systems (**Figure 8**) (LETSOALO et al., 2023). The consumption of medicines results in the direct release of a portion of the active PhC ingredient, since only part of the compound is metabolized by the body, while the remainder is excreted either unchanged or in its metabolized form (SAMAL; MAHAPATRA; HIBZUR ALI, 2022).

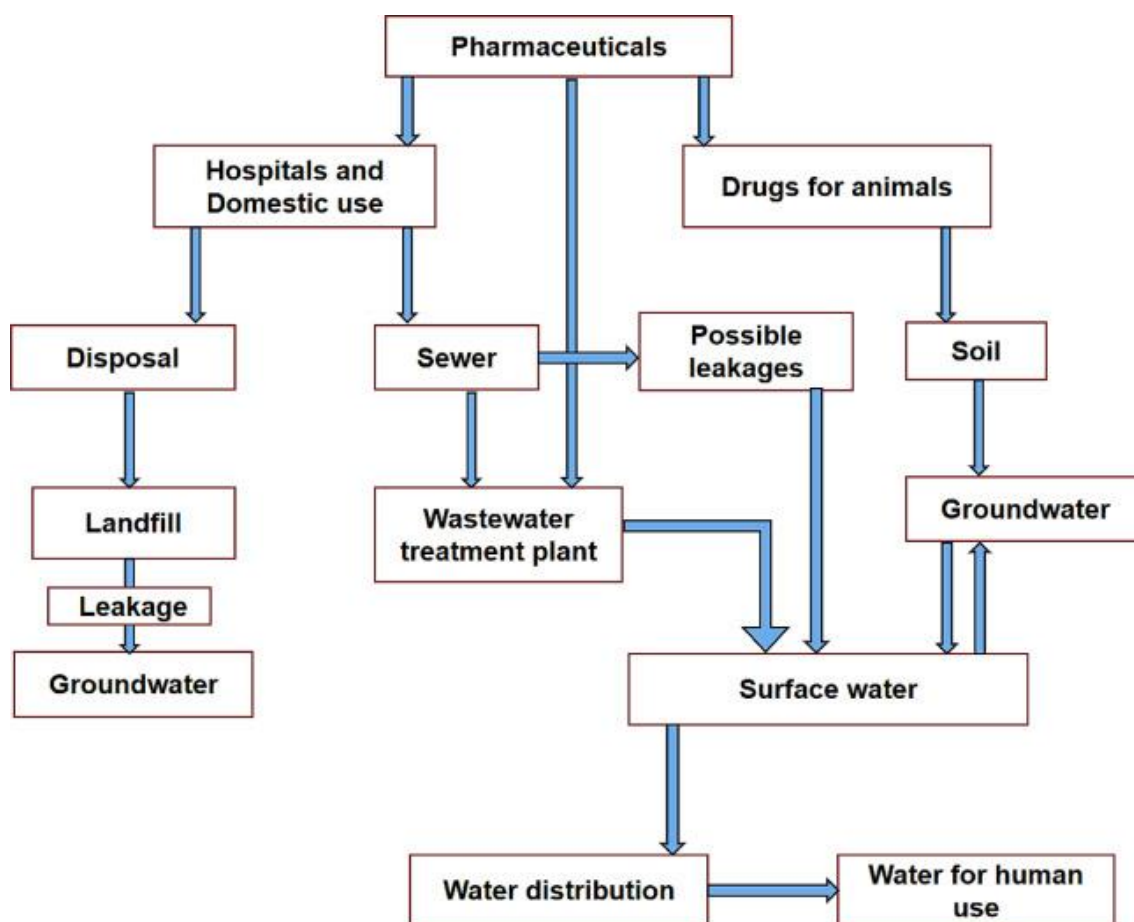


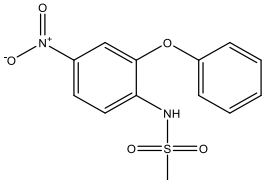
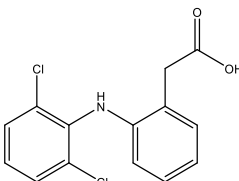
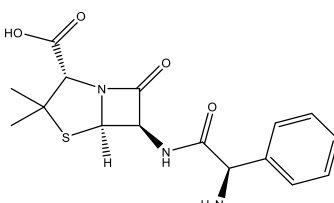
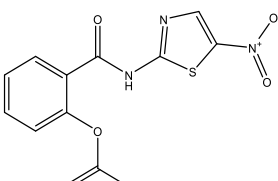
Figure 8: Routes of PhCs contaminants (SAMAL; MAHAPATRA; HIBZUR ALI, 2022).

Although the concentrations of PhCs detected in the environment are relatively low, typically in the range of ng to μg per litre, their structural diversity and ability to interact with and be absorbed by living organisms allow them to persist in the environment for long periods (HUSSAIN et al., 2023). For example, nimesulide (NIM), which is a non-steroidal anti-inflammatory drug (NSAID) has been quantified in surface waters in Brazil at concentrations up to $0.05 \mu\text{g/L}$ (50 ng/L), with additional detections of around 12 ng/L in other Brazilian rivers and up to 3.581 ng/L in Greek wastewater treatment plant (WWTP) effluents (CALDAS et al., 2018; KOLTSAKIDOU et al., 2019). Diclofenac (DCF) is another NSAID that has been reported in Indian rivers at concentrations ranging from 100 to 2000 ng/L , with frequent occurrences above $0.1 \mu\text{g/L}$ in various regions worldwide

(PLACOVA et al., 2023). The NSAIDs present chronic ecotoxic effects to aquatic organisms and are a potential endocrine disruptor in human health (SAMAL; MAHAPATRA; HIBZUR ALI, 2022). Given the stable chemical structure and bioactive nature of these contaminants, even when found in small concentrations, they can promote resistance to biodegradation, toxicity, persistence in food chains and even lead to the disintegration of physiological processes in vertebrates and invertebrates (LETSOALO et al., 2023).

Ampicillin (AMP) is an antibiotic, another group of pharmaceuticals of concern, this is β -lactam antibiotic, being detected in spring and groundwater in Tokyo at concentrations of 0.30–87 ng/L (KURODA; KOBAYASHI, 2021). Even at low levels, the presence of antibiotics in water bodies intensifies antimicrobial resistance, resulting in interference in the structure of the microbial community, thus affecting the microbial population and the ecological function of the aquatic ecosystem, increasing oxidative stress and blocking the electron chain of photosynthesis II (LETSOALO et al., 2023; SAMAL; MAHAPATRA; HIBZUR ALI, 2022). Nitazoxanide (NTZ) belongs to a different class of pharmaceuticals, the antiparasitics. It is rapidly transformed into its metabolite tizoxanide (TZ) in aquatic systems (SOKOŁOWSKI et al., 2023). This class of pharmaceuticals is suspected to be persistent and potentially toxic to aquatic organisms, highlighting the need for more targeted monitoring (HAMMAD et al., 2022). The physicochemical properties and chemical structures of the selected PhCs are summarized in **Table 2**.

Table 2: Physicochemical properties and molecular structures of the selected PhCs.

PhC	Molecular formula	Molecular weight (g/mol)	Solubility in water (25 °C)	pKa	Log P (Octanol–Water)	Chemical Structure
Nimesulide	C ₁₃ H ₁₂ N ₂ O ₅ S	308.3	0.002 g/mL	6.5	0.7	
Diclofenac	C ₁₄ H ₁₁ Cl ₂ NO ₂	296.1	0.002 g/mL	4.0	4.51	
Ampicillin	C ₁₆ H ₁₉ N ₃ O ₄ S	349.4	0.3 g/mL	2.5 (carboxyl), 7.3 (amine)	−0.85	
Nitazoxanide	C ₁₂ H ₉ N ₃ O ₅ S	307.3	0.005 g/mL	6.2	1.63	

In addition to direct discharge into water bodies, PhCs are also present in the environments because conventional wastewater treatment plants are not designed to efficiently remove them, enabling their penetration into soils and subsequent contamination of groundwater (OSUOHA; ANYANWU; EJILEUGHA, 2023). Considering that even at low concentrations, PhCs can cause adverse effects on aquatic life, the development and implementation of effective strategies for their removal from the environment has become an urgent necessity (AHAMMAD et al., 2022). **Table 3** shows the application of different techniques for the treatment of pharmaceutical-contaminated water, as well as their efficiency. Among these techniques, adsorption has gained increasing attention

from researchers, as it represents an efficient method for wastewater treatment (AHAMMAD et al., 2022). This is mainly due to its advantages, including low cost, wide variety of available adsorbent materials, ease of operation, regeneration and reuse potential of the adsorbents, high efficiency, and the absence of sludge formation as a secondary by-product (KHAN et al., 2022). In addition to these advantages, FURLAN et al. (2010) and HUANG et al. (2019) reported the combined use of adsorption with coagulation/flocculation, the most commonly applied technique in water treatment. Both studies demonstrated that the integration of these processes overcomes the individual limitations and enhances the purification efficiency of treated water.

Table 3: Summary of treatment processes applied for PhCs removal.

Treatment process	Description	Characteristics	Efficiency for PhCs removal	Ref.
Anaerobic biotechnological treatment	Biodegradation of PhCs under anaerobic microbial activity	Low energy demand, potential for biogas recovery, but slow degradation of some PhCs	Moderate to high, depending on PhC type and conditions	(WANG et al., 2022a)
Advanced oxidation process (AOPs)	Oxidation of pollutants via reactive oxygen species (e.g., $\bullet\text{OH}$, O_3 , H_2O_2)	High degradation efficiency, non-selective, can mineralize pollutants	High efficiency, but costly and may generate by-products	(IQBAL et al., 2024)
Photodegradation	Decomposition of PhCs under light irradiation (UV/solar, often photocatalysts)	The green process relies on renewable energy; efficiency depends on the catalyst and the light source	Variable to high, dependent on conditions	(MOHAPATRA et al., 2023)
Electrochemical removal	Oxidation or reduction of PhCs at electrodes	No chemical addition, controllable, but energy-intensive	High efficiency for certain PhCs	(SOARES et al., 2022)
Constructed wetlands	Use of plants, substrates, and microbes for pollutant removal	Eco-friendly, low cost, large area required, slower treatment	Moderate, depending on design and climate	(AL-MASHAQBEH et al., 2024)
Membrane treatment	Separation based on size/charge exclusion (e.g., NF, RO, UF)	High removal, compact system, but membrane fouling is a limitation	Very high	(FANG et al., 2023)
Microalgae-based treatment	Uptake and biodegradation of PhCs by microalgae	Sustainable, CO_2 capture potential requires light and nutrients	Moderate, species and condition-dependent	(MORILLAS-ESPAÑA et al., 2025)
Adsorption	Removal via physical/chemical interaction with adsorbent surfaces	Low cost, wide range of adsorbents, simple operation, reusable, and no sludge formation	High efficiency, cost-effective, and versatile	(FRAIHA et al., 2024)

Although a variety of techniques have been proposed for the removal of pharmaceuticals, adsorption has emerged as one of the most effective approaches. This is primarily because its performance can be tailored by the appropriate selection of the adsorbent material, thereby enabling the efficient

removal of a broad spectrum of pharmaceutical compounds. Moreover, the versatility of adsorption allows the application of different adsorbent materials to maximize removal efficiency.

Chapter 3 – Research developed

The results of this thesis are organized into three chapters, each presented in the form of a scientific article. Each article contains the sections Introduction, Materials and Methods, Results and Discussion, References, and Supporting Information, structured in accordance with the standards of scientific journals.

3.1. Article – Synthesis and characterization of polyethyleneimine grafted lignocellulosic fibers for improved removal of nitazoxanide and ampicillin from water

The results of this article of the thesis were published in Journal Colloids and Surfaces A: Physicochemical and Engineering Aspects, v. 693, p. 134063, jul. 2024.

Synthesis and characterization of polyethyleneimine grafted lignocellulosic fibers for improved removal of nitazoxanide and ampicillin from water

Juliê S. da Costa^a, Débora R. S. dos Santos^a, Marcela B. Alvarez^b, Márcio S. Silva^b, and André R. Fajardo^{a}*

Abstract

The COVID-19 pandemic has led to increased usage of various drugs, impacting both human and environmental health. Detecting these drugs and their metabolites in water sources has become common, presenting challenges for water treatment. Adsorption processes, particularly using vegetal biomass as an adsorbent, offer an environmentally friendly solution. In this study, we chemically grafted polyethyleneimine (PEI) onto *Luffa cylindrica* (LF) to enhance its adsorption capacity, enabling effective removal of nitazoxanide (NTZ) and ampicillin (AMP), two drugs used in COVID-19 treatment, from water. Characterization analyses confirmed that PEI grafting induced changes in the

chemical, thermal, and morphological properties of LF. The resulting grafted material (LF-g-PEI) exhibited improved adsorption capacity compared to unmodified LF for both drugs. Specifically, the adsorption capacity of LF-g-PEI increased by 59 % for NTZ and 43 % for AMP. Removal rates of these drugs from water using LF-g-PEI reached 59 % for NTZ and 23 % for AMP within 60 min. The adsorption of NTZ and AMP on LF-g-PEI demonstrated higher spontaneity and a physisorption nature, primarily due to enhanced adsorbent-adsorbate interactions facilitated by PEI. LF-g-PEI showed excellent potential for reuse, enhancing its practical applicability for adsorption processes. Overall, this study illustrates that grafting PEI onto LF is a dependable strategy to boost the adsorption capacity of this vegetal biomass. The resulting adsorbent material holds promise for efficiently removing drugs commonly used in COVID-19 treatment from water sources.

Keywords: Vegetable sponge; surface modification; emerging contaminants; wastewater treatment; ampicillin; nitaxozanide.

1. Introduction

In March 2020, the World Health Organization (WHO) declared a global pandemic in response to the potentially lethal effects of the new coronavirus (COVID-19) [1]. As a result, there has been a surge in the production and consumption of chemical compounds, particularly pharmaceuticals, aimed at addressing the consequences of the pandemic and even preventing or mitigating virus transmission [2]. The increased consumption, misuse, and abuse of drugs during the COVID-19 outbreak have significantly amplified the release of these

chemical compounds and their metabolites into various environments. This has been substantiated by multiple surveillance studies [3–5].

The presence of pharmaceuticals is most perceptible in waterways, posing a threat to diverse organisms and endangering both ecosystems and human health [4]. Unfortunately, conventional wastewater treatment plants can not eliminate these types of contaminants, leading to their continuous introduction into aquatic systems and resulting in various adverse impacts. Consequently, there is an urgent need to enhance existing processes or develop novel ones with greater efficiency. In this sense, adsorption is a well-established method for water and wastewater treatment, known for its advantageous characteristics [6]. The effectiveness of this separation process is closely tied to the capacity of the adsorbent material to interact with the targeted contaminants. Over time, the use of bio-based adsorbents has gained traction due to their eco-friendly and cost-effective attributes. *Luffa cylindrica* (LF), a vegetal biomass primarily composed of cellulose, hemicellulose, and varying amounts of lignin [7,8], has been adopted for the removal of diverse pollutants from water. LF shows attractive features such as mechanical and chemical stability, a substantial surface area, and a distinctive porous structure formed by interconnected hollow microchannels [9]. Besides, hydroxy groups are widely distributed across the surface of LF, facilitating pretreatment or chemical modification of the fibers to enhance their adsorption capabilities, particularly toward compounds with limited hydrophilicity [10,11]. Overall, the chemical modification of lignocellulosic materials like LF yields adsorbents with new functionalities, such as additional adsorption sites, consequently amplifying their potential to adsorb target contaminants [10].

In this context, various chemical compounds and polymers can serve as modifiers of LF [12,13]. Herein, we employed branched polyethyleneimine (PEI), a cationic synthetic polymer featuring multiple primary, secondary, and tertiary amine groups in its structure [14], to modify and enhance the adsorption capacity of the LF fibers. Past research has applied this strategy to modify cellulose-based materials with PEI to bolster their adsorption capabilities. For instance, Zhang et al. [15] modified microcrystalline cellulose with PEI and Fe_2O_4 , obtaining an adsorbent with a high capacity to remove Congo red from water. Chen et al. [16] combined cellulose and PEI to produce an aerogel capable of adsorbing sodium diclofenac. However, the application of this polymer to modify LF fibers and enhance their adsorption capacity towards water contaminants has not been previously reported. We hypothesize that the chemical nature of PEI, combined with the natural three-dimensional structure of LF, may result in a material with superior adsorption performance for removing pharmaceuticals from aqueous systems.

To evaluate this hypothesis, we grafted PEI onto LF, and the resulting material was applied to the adsorption of two different drugs, nitazoxanide (NTZ) and ampicillin (AMP). NTZ, primarily an anti-parasitic drug, exhibits potent antiviral properties and is commonly used for treating protozoa, various helminths, and viral infections [17,18]. Within the human body, NTZ undergoes hydrolysis in plasma, resulting in the formation of its metabolite, tizoxanide [19]. It is important to highlight that approximately one-third of the oral dose is excreted in urine, while two-thirds are excreted in feces [20]. Remarkably, in sources of contamination, only the metabolite has been detected. In a study conducted by Sanches-Neto et al. [21], the toxicity of NTZ and its metabolite in aquatic

environments was evaluated. It was observed that, based on the criteria outlined in European Union (EU) and Chinese regulations, tizoxanide is more toxic than NTZ when assessing the impact on various organisms, including fish, daphnia, and green algae. AMP, on the other hand, is a widely used antibiotic for the treatment of bacterial infections affecting humans and animals, particularly those involving the respiratory system [2]. Its chemical composition is inherently unstable, with the β -lactam ring being highly susceptible to hydrolysis. Consequently, detecting these molecules in water bodies poses a significant challenge [22]. While AMP is not directly harmful to humans, its presence in water can foster the development of antibiotic-resistant organisms, thus impeding the growth of aquatic life and adversely affecting various human production activities [23]. Given these considerations, it is imperative to prioritize the removal of these two drugs from aquatic environments to safeguard and preserve the environment. To the best of our knowledge, the utilization of LF grafted with PEI as an adsorbent to remove NTZ and AMP from water has not been reported in the literature.

2. Materials and methods

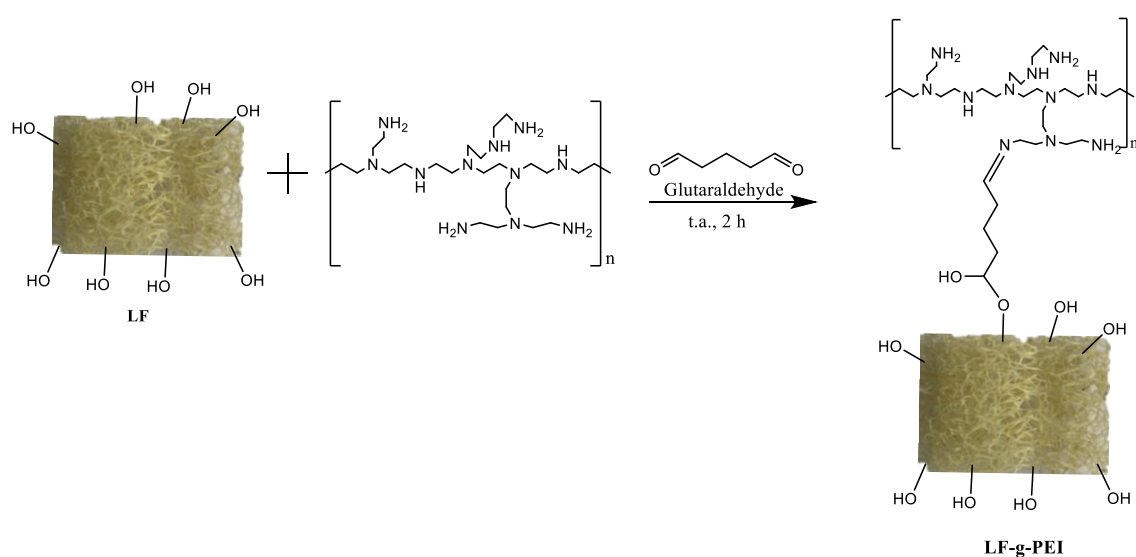
2.1 Materials

Luffa cylindrica (LF) was obtained from a plantation localized in Perola, Paraná, Brazil. Hydrochloric acid (HCl, 35%), sodium hydroxide (NaOH, P.A.), and ethanol (EtOH, P.A.) were purchased from Synth (Brazil). Glutaraldehyde (Glut) and branched polyethyleneimine (PEI, MW 25.000 g/mol) were purchased from Sigma-Aldrich (USA). Nitazoxanide (NTZ, 99%) was purchased from

Althaia® (Brazil), and ampicillin (AMP, 98%) was purchased from Prati® (Brazil). All commercial chemicals of reagent grade were used as received.

2.2 Grafting of LF with PEI (LF-g-PEI)

The synthesis of LF-g-PEI was adapted from a methodology previously reported by Batool and Valiyaveetil [24]. Firstly, the raw LF was cut into small pieces (cubic shape, 1 cm³), cleaned three times with an EtOH/H₂O solution (70:30 v/v), and oven-dried at 50 °C for 24 h. Next, LF (1.30 g) was added to a beaker filled with distilled water (200 mL) and stirred vigorously. PEI (0.65 g or 26.0 μmol) was dissolved in distilled water (65 mL) and dripped into the aqueous dispersion of LF. The mixture was stirred for 5 h at 50 °C and then cooled to r.t. (approximately 20 °C). After that, Glut (0.33 g or 3.3 mmol) was added to the mixture, which was stirred for 2 h. The LF-g-PEI sample was recovered, washed abundantly with distilled water, oven-dried (50 °C for 24 h), and stored for later characterization and use. Scheme 1 summarizes the experimental steps done to synthesize LF-g-PEI and the proposed chemical structure.



Scheme 1. Grafting reaction of PEI on LF backbone.

A similar reaction between LF and PEI was carried out using the same experimental conditions described before except for the addition of Glut. The resulting material from this reaction was labeled as LF-PEI, respectively. Also, a third reaction was performed in the absence of PEI keeping the other experimental conditions, to examine the interaction between Glut and LF. Herein, the obtained material was labeled as LF-Glut.

2.3 Materials characterization

FTIR analyses were performed from 4000 to 400 cm^{-1} at a resolution of 4 cm^{-1} (Shimadzu IR-Affinity-1 spectrometer, Japan). Before the spectra acquisition, the samples were cut and held between two KBr pellets. Elemental analyses were performed to determine the amount of carbon (C), hydrogen (H), and nitrogen (N) on the samples (PerkinElmer, model PE 240, USA). TGA analyses were run from 30 to 500 $^{\circ}\text{C}$ at a heat ramp of 10 $^{\circ}\text{C}/\text{min}$ and an $\text{N}_2(\text{g})$ flow rate of 20 mL/min (Shimadzu, DTG60 analyzer, Japan). Before the TGA analysis, the samples were ground using a pestle and liquid N_2 . SEM was conducted in an FEI Quanta 250 FEG-SEM microscope (USA). The samples were sputter-coated with gold before SEM visualization. The pH of the point of zero charges (pH_{PZC}) values were determined as follows: The samples (30 mg) were placed in falcon tubes filled with NaCl solution (0.1 mol/L, 30 mL), and then, the initial pH value was adjusted (2–10) with HCl (0.1 mol/L) or NaOH (0.1 mol/L) solutions using a pHmeter (Hannah Instruments, model HI2211, USA). All tubes were orbitally stirred (100 rpm) for 24 h at 25 $^{\circ}\text{C}$. Next, the final pH of each solution was measured again. The variation between the final and initial pH values (ΔpH)

was then plotted against the initial pH values. Therefore, pH_{PZC} values were estimated from the points where the initial pH at which ΔpH is zero [25].

2.4. Density and porosity measurement

The density of the LF samples was determined using the liquid pycnometer method [79]. The densities of LF samples were determined by measuring the weight of dry LF samples (m_1), of the pycnometer empty (m_2), of the pycnometer with ethylene glycol (m_3), and of the pycnometer with ethylene glycol and LF sample (m_4). The relative density (g/cm³) can be calculated using Equation (1).

$$Density = \frac{m_1 / (m_3 - m_2) - (m_4 - m_2 - m_1)}{\rho_{ethylene\ glycol}} \quad (1)$$

Where the absolute density of ethylene glycol ($\rho_{ethylene\ glycol}$) is about 1.11 g/cm³ at 18 °C.

The porosity of the LF samples was determined using a method previously described for Singh and Jelinek [26]. To determine the porosity, an LF sample of measured weight (m_i) was immersed in a vial containing 30 mL of ethanol and soaked for 24 h to allow the liquid to penetrate the pores of the sample. The final weight of the wet sponge was noted as m_f . The total porosity (%) can be calculated using Eq. (2), where $\rho_{ethanol}$ is the ethanol density at 25 °C (0.789 g/cm³).

$$\%Porosity = \frac{(m_f - m_i)}{\rho_{ethanol} \times lwh} \times 100 \quad (2)$$

2.5. Adsorption experiments

Batch experiments were performed to evaluate the capacity of LF and LF-g-PEI to adsorb NTZ and AMP from the aqueous media. The effect of the initial drug concentration (20–50 mg/L), adsorbent amount (30–50 mg), and initial pH of the solution (4–10) on the adsorption capacity were evaluated first. For these experiments, the following conditions were utilized: specific amounts of each adsorbent (LF or LF-g-PEI) were placed in a 100 mL Erlenmeyer flask containing 30 mL of NTZ or AMP solutions at fixed initial concentrations (C_0). Next, the flasks were orbitally stirred (100 rpm) for 3 h at approximately 25 °C. After this while, aliquots of the solutions were analyzed by UV-Vis spectrophotometer (PerkinElmer Lambda 25, USA) to determine the residual concentrations of drugs in the solution. Absorbance measurements were done at $\lambda = 345$ nm for NTZ and at 230 nm for AMP and the collected data were converted to concentration using calibration curves ($R^2 > 0.940$). The adsorption capacity at equilibrium (q_e) was calculated using Eq. (3):

$$q_e = \frac{(C_0 - C_e)}{m} \times V \quad (3)$$

where C_0 (mg/L) is the initial drug concentration, C_e (mg/L) is the residual concentration at equilibrium, m (g) is the mass of the adsorbent, and V (L) is the volume of the solution. For the kinetic analysis a similar experimental procedure was conducted; however, aliquots were collected from the Erlenmeyers flaks at pre-determined intervals. Eq. (4) was utilized to calculate the adsorption capacity at each time (q_t):

$$q_t = \frac{(C_0 - C_t)}{m} \times V \quad (4)$$

2.6. Thermodynamics analysis

Batch adsorption experiments were conducted at different temperature (293–323 K) to investigate the thermodynamics of the adsorption of NTZ and AMP on the LF samples. The other experimental conditions were set to 30 mg of adsorbent; initial drug concentration of 50 mg/L; 30 mL of solution volume; and pH 7.0. The study on the effect of temperature on adsorption will extend the knowledge of thermodynamic parameters, such as standard Gibbs free energy of adsorption (ΔG°), the heat of the adsorption (ΔH°), and standard entropy changes (ΔS°) [27]. Thermodynamic equations used for these calculations are given in Eqs. (5), (6), and (7):

$$K = \frac{q_e}{C_e} \quad (5)$$

$$\ln K = \frac{\Delta S^\circ}{R} - \frac{\Delta H^\circ}{RT} \quad (6)$$

$$\Delta G^\circ = -RT \ln K \quad (7)$$

where K is the equilibrium constant, R is the universal gas constant (8.314 J/mol K), and T is the absolute temperature. ΔH° and ΔS° can be determined from the slope and intercept of the plot between $\ln (q_e/C_e)$ versus $1/T$ (not shown). ΔG° can be calculated from Eq. (7).

2.7 Reuse experiments

After the adsorption experiments, the post-utilized LF-g-PEI samples (30 mg) were recovered and soaked in a NaOH solution (0,1 mol/L, 40 mL) for 2 h at

25 °C for desorption. After the desorption process, the regenerated LF-g-PEI was washed with distilled water, oven-dried (50 °C for 24 h), and then, reused in new adsorption experiments. For the adsorption step, the following conditions were utilized: initial drug concentration of 50 mg/L, 30 mL of solution, pH ~ 7, 25 °C, and 3 h of contact. After each reuse run, the q_e values were (re)calculated using Eq. (3). The adsorption/desorption processes were repeated eight times consecutively. Each reuse experiment was conducted in triplicate, and the results are expressed as mean \pm standard deviation.

3. Results and discussion

3.1 Characterization of LF and LF-g-PEI

The chemical nature of LF, PEI, LF-Glut, LF-PEI, and LF-g-PEI was investigated through FTIR analysis (Figure 1). The FTIR spectrum of LF closely resembled that which had been previously reported and discussed by Costa and Fajardo [28]. In the PEI spectrum, the broadband in the range of 3560–3100 cm^{-1} was observed, which corresponds to the N–H stretching of primary and secondary amine groups. The bands associated with the C–H stretching of CH_2 groups (ethylene portion), which are typically observed in the 2930–2800 cm^{-1} range, were not clearly discernible. Hijazi et al. [29] have previously described this trend. The bands at 1655 and 1601 cm^{-1} were attributed to the N–H bending of amine groups [30]. In the case of LF-g-PEI, the spectrum exhibited bands from both LF and PEI with some shifts and the appearance of new bands attributable to the grafting reaction. Notably, the broadband at 3447 cm^{-1} , attributed to the O–H stretching of hydroxy groups in LF, shifted to 3349 cm^{-1} , and its intensity was lower compared to other bands in the same spectrum. This observation may be

related to the partial consumption of these groups due to the grafting and the increment of interactions via H-bonding with PEI. The band associated with the N–H stretching of amine groups from PEI appeared to overlap with the O–H stretching [31]. The bands associated with the C–H stretching of the CH_x groups (2925 and 2855 cm⁻¹) exhibited increased intensity, and a new band at 800 cm⁻¹, corresponding to C–H bending, was noticed [32]. According to Zhang et al. [33], these findings confirm the success of the grafting process. Furthermore, the band at 1050 cm⁻¹, related to the C–O–C stretching of pyranose and furanose rings in the LF, shifted to a higher wavenumber (1060 cm⁻¹). This shift can be attributed to a new ether bond formed through aldolization between the aldehyde group of Glut and the hydroxy groups of LF [32]. The presence of the Schiff base structure (C=N bond) was confirmed by the appearance of a new band at 1642 cm⁻¹, because of the grafting of the amine groups of PEI with the aldehyde group of Glut [34,35]. Furthermore, the band related to the N–H bending of PEI shifted to a lower wavenumber (1567 cm⁻¹) after grafting, and a band at 1163 cm⁻¹, corresponding to the C–N stretching of PEI, was observed [33]. Considering these data, it can be inferred that the grafting of PEI onto LF using Glut as a crosslinker was successful.

To gain a deeper understanding of the grafting reaction, we analyzed the FTIR spectra of LF-Glut and LF-PEI. The LF-Glut spectrum displayed the characteristic bands of LF with noticeable changes. For instance, the broadband centered at 3447 cm⁻¹, attributed to O–H stretching, exhibited a decrease in intensity compared to other bands in the same spectrum after the reaction with Glut. This decrease suggests that the hydroxy groups of LF were consumed in the process. Additionally, the intensity of the bands at 2925 and 2855 cm⁻¹,

associated with the C–H stretching of the CH_x groups, increased due to the binding of Glut to LF fibers. A new band around 1106 cm⁻¹ appeared, which can be related to the C–O stretching of the hemiacetal group formed following the reaction. This observation provides evidence that the interaction between LF and Glut occurs through chemical bonds [36]. The presence of this band had also been reported by Hou et al. [37], who explored the significance of crosslinked Glut and poly(vinyl alcohol) in cellulose membranes to optimize pore sizes and stability.

The LF-PEI spectrum was examined to assess the interaction forces between LF and PEI in the absence of Glut. In comparison to the LF and PEI spectra, the LF-PEI spectrum did not reveal any new bands. However, it did show changes and shifts in the characteristic bands of LF and PEI. The broadband related to the combined O–H and N–H stretching was centered at a lower wavenumber region, around 3349 cm⁻¹. This shift suggests an increase in interactions through H-bonding between the hydroxy groups of LF and the amine groups of PEI. As a result of this interaction, the bands related to the N–H bending of PEI shifted to lower wavenumbers (1649 and 1593 cm⁻¹). Finally, the intensity of the bands associated with C–H stretching (2930–2800 cm⁻¹) increased due to the aliphatic CH_x groups of PEI. These findings demonstrate that the grafting of PEI onto LF only requires the mediation of Glut. Without the crosslinker, only physical interactions occur between them.

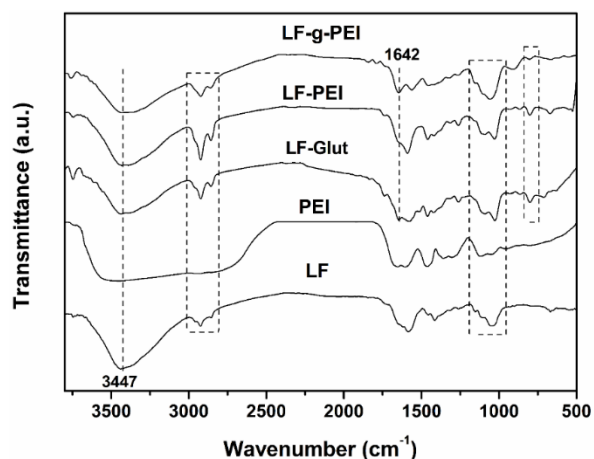


Figure 3-1.1. FTIR spectra of LF, PEI, LF-Glut, LF-PEI, and LF-g-PEI.

The elemental analysis results are summarized in Table 1. After the grafting process, the content of the N element in LF-g-PEI increased significantly compared to LF (approximately 4.5 times). In raw LF, the presence of N can be caused by the proteins present in the fibers. The increment of the N content in LF-g-PEI is due to the amine groups proceeding from PEI. According to Guerra et al. [38], materials based on PEI that show a high N content usually have a high concentration of this polymer.

Table 3-1.1: Elemental analysis for LF and LF-g-PEI.

Sample	Element		
	C (%)	H (%)	N (%)
LF	43.64 ± 0.37	6.61 ± 0.07	0.29 ± 0.01
LF-g-PEI	43.82 ± 0.14	6.66 ± 0.06	1.30 ± 0.02

TGA/DTG analyses revealed that LF and LF-g-PEI exhibited three weight loss stages, while PEI exhibited only two within the temperature range of 30–500 °C (Figures S1a and S1b). For all samples, the first stage, occurring from 30 to 100 °C, resulted in less than a 5 % weight loss, attributed to the evaporation of

water molecules and other volatile compounds. In the case of LF, the second weight loss stage (from 230 to 300 °C) was associated with the thermal depolymerization of its hemicellulose portion, while the third stage (from 320 to 400 °C) corresponds to the depolymerization of cellulose [39]. The combination of these two stages contributed to the highest weight loss observed for LF, approximately 65 %.

In the case of PEI, the second weight loss stage occurred between 290 and 410 °C, attributed to the thermal decomposition of its side chains and backbone structure [40]. Conversely, the TGA/DTG curves of LF-g-PEI closely resembled those of LF, with some variations. Notably, the grafting of PEI onto LF resulted in a shift of the temperature ranges associated with the thermal degradation of the LF structure to higher values. This shift indicates that the grafting process conferred increased thermal stability to LF-g-PEI. The enhanced thermal stability of LF fibers can be attributed to the formation of new chemical bonds during the grafting reaction mediated by Glut [24]. Sehaqui et al. [41] also observed an improvement in the thermal stability of oxidized nanofibrillated cellulose foams after grafting with PEI. Furthermore, the H-bonding interactions between LF and PEI, as revealed by the FTIR analysis, may have contributed to the increment in thermal stability. It is worth noting that the absence of new weight loss stages in comparison to LF may indicate that the grafting process occurred primarily on the surface of the fibers, having a limited impact on their internal structure [42].

The surface morphology and texture of the LF and LF-g-PEI fibers were examined through SEM analysis. As depicted in Figure 2a and b, the raw LF fibers exhibited incrustations and particle cluster-like structures, which could be

attributed to residual waxy and gummy substances not completely removed during the cleaning process [43]. Furthermore, the surface of the raw LF fibers appeared rough, compacted, with aligned structures, and irregular micropores that were unevenly distributed [44]. In contrast, the fibers grafted with PEI displayed dendritic wrinkles on their surface and were notably devoid of pores. However, the overall morphology of the fibers remained compact [45]. By examining Figure 2c and d, it is evident that the grafting process occurred uniformly across the entire surface of the LF fibers, as the described morphology was consistently observed along the entire length of the analyzed fibers [34].



Figure 3-1.2: Images obtained by SEM images (at different magnifications) for (a,b) LF and (c,d) LF-g-PEI.

3.2. Density and total porosity

The density and total porosity of the LF samples were assessed and are outlined in Table 2. Following grafting with PEI, a decrease in the density of LF was observed alongside an increase in total porosity. This phenomenon can be attributed to the potential blocking of micro-mesopores during the grafting process, leading to a decrease in density [46]. Conversely, the presence of macropores in LF suggests that porosity remains unaffected. Additionally, the observed increase in total porosity is likely attributed to the enhanced roughness induced by PEI grafting, as evidenced in the SEM images [47].

Table 3-1.2: Density and porosity values for LF and LF-g-PEI.

Samples	Density (g/cm ³)	Porosity (%)
LF	1.8442 ± 0.041	2.269 ± 0.351
LF-g-PEI	0.4453 ± 0.002	2.613 ± 0.353

3.3 Adsorption of NTZ and AMP

3.3.1 Effect of amount of adsorbent, initial drug concentration, and solution pH

The investigation of the dependence on the amount of adsorbent is crucial in understanding the cost-effectiveness of adsorption processes [48]. Herein, adsorption experiments using different amounts of LF and LF-g-PEI (ranging from 30 to 50 mg) were conducted to assess the effect of this variable on the adsorption capacity of NTZ and AMP. The q_e values determined for these experiments are shown in Figures S2a and S2b, respectively. As observed, the ability of LF and LF-g-PEI to adsorb NTZ and AMP decreased as the amount of adsorbent increased from 30 to 50 mg. The q_e values for NTZ adsorption decreased from 22.74 to 6.08 mg/g for LF-g-PEI and from 6.63 to 2.53 mg/g for LF. Similarly, the q_e values decreased from 19.41 to 5.91 mg/g for LF-g-PEI and

from 3.05 to 0.24 mg/g for LF in AMP adsorption. The influence of increasing the amount of adsorbent can be explained by the reduction in the available surface area, which may occur due to aggregation of adsorbent molecules [49,50]. Furthermore, when comparing the q_e values of both LF and LF-g-PEI, it was observed that for LF-g-PEI the q_e values were 70 % higher in NTZ adsorption and 84 % higher in NTZ adsorption when 30 mg of samples were evaluated. This difference in adsorption capacity between the two adsorbents can be attributed to the fact that LF has a smaller number of active sites compared to LF-g-PEI, where the presence of PEI and Glut results in an increased number of active sites available for the adsorption process. Based on these results, subsequent adsorption tests were conducted using 30 mg of LF or LF-g-PEI.

In addition to the amount of adsorbent, the initial drug concentration in the solution has a direct relationship with adsorption capacity [51]. To evaluate the effect of this parameter, adsorption studies were conducted by varying the initial concentration of the two drugs. According to the data presented in Figure S3a, it is evident that an increase in NTZ concentration from 20 to 50 mg/L led to an increase in adsorption capacity of 98 % for LF-g-PEI and 571 % for LF. A similar trend can be observed in Figure S3b, where an increase in AMP concentration from 20 to 50 mg/L resulted in an increase in adsorption capacity of 194 % for LF-g-PEI and 173 % for LF. This increase in adsorption capacity can be explained by the greater driving force that exists when the concentration is higher, causing the contaminants in the solution to overcome the resistance to mass transfer from the aqueous phase to the surface of the adsorbent [46]. This effect can also be justified by the presence of more drug molecules in the solution, which compete with the active sites of the adsorbent [46,52]. The lower q_e values at lower

concentrations (20 mg/L) can be explained by the fact that the active sites of the adsorbent are unsaturated, as there are not enough contaminant molecules to compete with these sites [52]. Therefore, based on the results obtained at medium concentrations, an initial concentration of 50 mg/L was chosen for the subsequent experiments with both pharmaceuticals (NTZ and AMP).

The pH of the medium in which the adsorption process occurs can also directly influence the process by affecting changes on the surface of the adsorbent and/or adsorbate [46]. In this study, the pH of the NTZ and AMP solutions was adjusted using HCl (0.1 mol/L) or NaOH (0.1 mol/L) before the adsorption experiments. As shown in Figures S4a and S4b, increasing the pH from 4 to 7 resulted in an increase in adsorption capacity for both drugs on LF and LF-g-PEI adsorbents. However, when the pH is in alkaline conditions (pH 10), the adsorption capacity decreases for both drugs. To further understand these results, the pH_{PZC} values for LF and LF-g-PEI were determined. In general terms, pH_{PZC} defines the pH condition at which the components of the surface charge on the solid (adsorbent) are equal to zero ($[H^+] = [OH^-]$) [53]. At pH conditions below these values ($pH < pH_{PZC}$), the surface of the LF samples is positively charged ($[H^+] > [OH^-]$), while pH conditions above pH_{PZC} denote surfaces negatively charged ($[H^+] < [OH^-]$). The pH_{PZC} value (Figure S5) computed for LF was 3.95 and 5.23 for LF-g-PEI. The increase in the pH_{PZC} value after the grafting process is associated with the amine groups from PEI that can be protonated, leaving the surface of LF-g-PEI more positively charged, thus increasing this parameter [32].

Changes in solution pH can also affect the drugs. For instance, the behavior of NTZ molecules at different pH levels can be explained by their pK_a ,

which is approximately 6.18. At $\text{pH} < 7$, the NTZ molecules are positively charged and can interact favorably with the negatively charged surface of LF, leading to adsorption. However, at $\text{pH} 4$, both LF-g-PEI and NTZ have positively charged surfaces, resulting in repulsion between them, and the need for other interaction forces to promote the adsorption of this drug [32]. As the pH increases and gets closer to a neutral pH , the adsorption is favored due to the electrostatic interactions between the neutral NTZ and the negatively charged surface of LF and LF-g-PEI. Consequently, the highest q_e values for this drug are computed at $\text{pH} 7$ (Figure S4a). On the other hand, at pH levels higher than 7, both the surface of LF and LF-g-PEI and the NTZ molecules are negatively charged, leading to electrostatic repulsion, which decreases the adsorption capacity [31].

For AMP, when the pH of the solution is less than 7, the drug molecules are in their zwitterionic form (with pK_a between 2.4 and 7.3). At $\text{pH} < 7$, there is an attractive interaction between the negatively charged surface of LF, with an excess of negative charge, and the positively charged portion of the zwitterionic AMP molecule. However, there is a repulsion interaction with the negatively charged portion of AMP. At $\text{pH} 7$, repulsion forces between the negatively charged surface of the adsorbent and AMP dominate the interaction process [54]. The same principles apply to LF-g-PEI, albeit with a different pH_{PZC} value. At $\text{pH} 4$ or 5, there is an attractive interaction between the negatively charged portion of AMP and the surface of this adsorbent, which mostly has a positive charge. At $\text{pH} 6$ or 7, repulsion forces between the negatively charged surface of LF-g-PEI and AMP are likely to dominate the interaction. At $\text{pH} > 7$, both AMP molecules and adsorbents present an excess of negative charges, leading to repulsion between them and a decrease in adsorption capacity. The highest q_e values

observed for both adsorbents towards AMP were at pH 7, suggesting that the AMP adsorption mechanism on LF and LF-g-PEI may involve electrostatic interactions, as well as other interactions such as hydrogen bonds, π - π interactions, or hydrophobic interactions [2].

Considering that the highest adsorption capacity values for NTZ and AMP on LF and LF-g-PEI were determined for solutions with a pH close to neutrality, further adsorption experiments were conducted without adjusting this parameter. It is important to note that the solutions of NTZ and AMP prepared at a concentration of 50 mg/L in distilled water had initial pH values of approximately 7.8 and 7.3, respectively.

3.3.2 Kinetics analysis

Kinetic studies were carried out to evaluate the adsorption capacity of LF and LF-g-PEI as a function of time considering both drugs (NTZ and AMP). Figure 3 shows that the adsorption kinetics of NTZ and AMP on the tested adsorbents have similar behavior, where the q_t values increased as the experiment time went on. It is observed that the adsorption of the drugs occurs quickly in the first 10 min, and this may be associated with the fact that there is a greater number of free active sites on the adsorbent. Over time, the activation sites are occupied, and the adsorption rate decreases until equilibrium is reached (plateau). For the NTZ and AMP adsorption on LF, the equilibrium was achieved at 60 min and 150 min, respectively. On the other hand, solutions treated with LF-g-PEI reached the adsorption equilibrium at 60 min for both drugs. These results suggest that the grafting process increased the number of adsorption sites in the LF-g-PEI adsorbent and, consequently, this process reached equilibrium in a short period.

Furthermore, it is important to consider that as the number of adsorbed molecules increases, the repulsion energy between them in the solution decreases. Consequently, the remaining molecules in the solution exhibit greater resistance to adsorption, leading to a deceleration in the adsorption kinetics until equilibrium is achieved.

The highest adsorption capacity for NTZ at equilibrium was 18.66 mg/g for LF and 29.59 mg/g for LF-g-PEI. This indicates that the adsorption capacity was improved by 59 % for LF-g-PEI compared to LF. In terms of removal efficiency, LF was able to remove approximately 37.32 % of the total NTZ content in the solution, while LF-g-PEI removed more than 59.18 % of this drug. For AMP, the highest adsorption capacities were 8.00 mg/g for LF and 11.46 mg/g for LF-g-PEI. Comparatively, the adsorption capacity for AMP was improved by 43 % for the sample grafted with PEI. Additionally, the removal efficiency for AMP increased from 16 % for LF to 23 % for LF-g-PEI. By analyzing these results, it becomes clear that grafting PEI onto the LF structure not only altered the chemical and morphological characteristics of the material but also led to an increase in its adsorption capacity. This is consistent with findings reported by Lu et al. [55], who grafted PEI onto chitosan beads to enhance sodium diclofenac adsorption. The presence of amines in the PEI structure introduces new adsorption sites on LF-g-PEI. Depending on the pH of the medium, these sites can interact with the drugs through electrostatic or H-bonding interactions. Additionally, the carbon aliphatic moieties of PEI provide additional options for interaction, as weak forces such as van der Waals and hydrophobic interactions can be established between LF-g-PEI and the drugs.

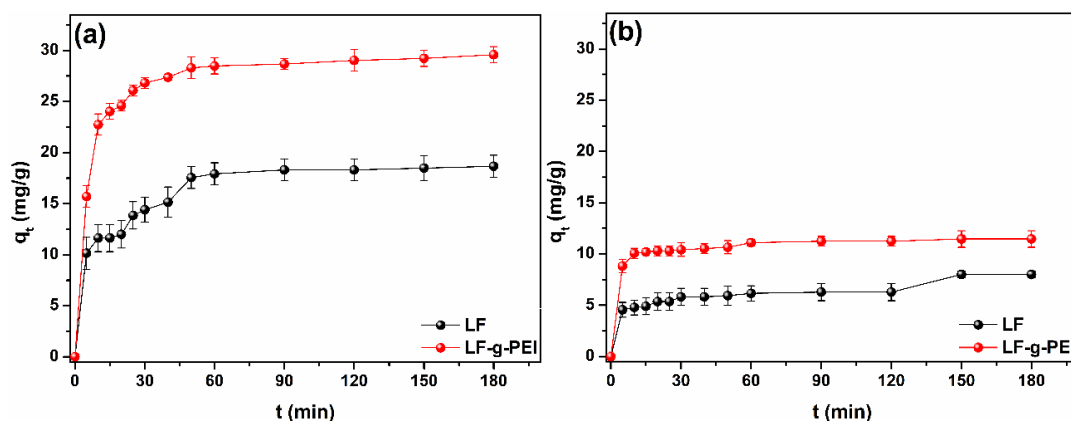


Figure 3-1.3: Adsorption capacity of (a) NTZ and (b) AMP on LF and LF-g-PEI as a function of time (Other experimental conditions: C_0 50 mg/L, amount of adsorbent 30 mg, volume 30 mL, r.t., pH not adjusted, stirring 100 rpm).

The adsorption data summarized in Figure 3a and b were fitted using the pseudo-first order (PFO), pseudo-second order (PSO), and Elovich kinetic models, which are expressed in the Supporting Information (Table S1). The kinetic parameters were determined from the non-linear regression of the data depicted in the plot of q_t versus t (Figure S6). To evaluate the best-fit model, the values of the correlation coefficient (R^2) and Chi-square (χ^2) values were used. Table 3 also shows kinetic parameters including the R^2 and χ^2 values.

Table 3-1.3. Kinetic parameters calculated for NTZ and AMP adsorption on LF and LF-g-PEI.

PFO										
Sample	NTZ					AMP				
	$q_{e(exp)}$	$q_{e(calc)}$	k_1 ($\times 10^{-2}$)	R^2	χ^2	$q_{e(exp)}$	$q_{e(calc)}$	k_1 ($\times 10^{-2}$)	R^2	χ^2
LF	18.6	19.1	0.7	0.946	$>>0.1$	8.0	6.3	14.7	0.781	0.46
LF-g-PEI	29.6	28.1	14.6	0.979	>0.1	11.4	10.8	31.8	0.976	$>>0.1$
PSO										
Sample	NTZ					AMP				
	$q_{e(exp)}$	$q_{e(calc)}$	k_2 ($\times 10^{-4}$)	R^2	χ^2	$q_{e(exp)}$	$q_{e(calc)}$	k_2 ($\times 10^{-2}$)	R^2	χ^2
LF	18.6	19.1	0.7	0.936	$>>0.1$	8.0	6.9	2.9	0.877	0.17
LF-g-PEI	29.6	26.2	5.9×10^3 9	0.766	0.44	11.4	11.2	6.0	0.992	$>>0.1$
Elovich										
Sample	NTZ			AMP						
	α	β	R^2	α	β	R^2				
LF	15.6	0.35	0.968	15.6	1.1	0.950				
LF-g-PEI	284.3	0.31	0.960	22.4×10^4	1.5	0.995				

Units: C_0 (mg/L); $q_{e(exp)}$ (mg/g); $q_{e(calc)}$ (mg/g); k_1 (1/min); and k_2 (g mg/min).

The kinetic analysis indicates that the adsorption of NTZ onto LF and LF-g-PEI is best described by the PFO model. This choice is supported by the highest R^2 values and the lowest χ^2 values obtained for this model. Indeed, the low χ^2 values indicate a good agreement between the experimental and theoretical values of q_e , which strengthens the suitability of the PFO model for describing the adsorption kinetics of NTZ on LF and LF-g-PEI. According to the PFO model, the rate-limiting step is the diffusion process, and the reaction rate depends solely on the concentration of the adsorbate in a single adsorbate system. This indicates that the kinetic model is primarily controlled by physisorption, where weak interaction forces are involved [52]. Finally, by

comparing the k_1 constants, it is noticed that the adsorption of NTZ on LF-g-PEI is faster than on LF, which aligns with the experimental observations.

It is worth noting that the Elovich model yielded high R^2 values, indicating its adequacy for explaining the adsorption of NTZ on the evaluated adsorbents. The Elovich model, although not providing specific insights into the adsorption mechanism, is particularly suitable for processes occurring on heterogeneous surfaces [56]. This model assumes that activation energy is distributed non-uniformly across the adsorbent surface and may vary with surface coverage [57]. As seen in Table 3, the Elovich model was also the most suitable for explaining the adsorption of AMP on LF and LF-g-PEI, as indicated by the highest R^2 values obtained for this model. The kinetic parameters derived from the Elovich model provide valuable insights into the adsorption process. The significantly higher α value compared to the β value suggests a rapid AMP adsorption onto the adsorbents. Moreover, the notably higher α value for LF-g-PEI, exceeding the β value, is consistent with the presence of a greater number of active sites on the LF surface after the grafting process, in line with the findings of Geng et al. [58]. This implies that LF-g-PEI exhibits enhanced adsorption capacity and efficiency for AMP removal compared to unmodified LF.

3.3.3 Adsorption isotherms

The experimental adsorption data were also subjected to fitting with various isotherm models to provide insights into the mechanism of the adsorption process. The non-linear forms of the Freundlich, Temkin, Dubinin-Radushkevich (DR), and Sips isotherm models were employed. These models were used to estimate the respective isotherm parameters and constants by performing non-

linear regression on the data represented as q_e versus C_e , as shown in Figure S7. The summarized results are provided in Table 4.

Table 3-1.4: Isotherms parameters calculated for NTZ and AMP adsorption on LF and LF-g-PEI at 25 °C.

Isotherm	Parameter	NTZ		AMP	
		LF	LF-g-PEI	LF	LF-g-PEI
Freundlich	$1/n$	1.625	2.118	1.312	0.763
	n	0.615	0.472	0.762	1.309
	K_F (mg/g(L/mg) $^{1/n}$)	0.008	0.006	0.066	0.615
	R^2	0.978	0.895	0.811	0.847
	χ^2	0.035	1.731	1.460	0.822
Temkin	K_T (L/mg)	0.071	0.076	0.078	0.205
	b_T	778.765	223.343	340.506	540.309
	R^2	0.967	0.802	0.920	0.767
	χ^2	0.052	3.290	0.615	1.252
DR	q_{mDR} (mg/g)	5.294	23.099	11.175	9.810
	E (J/mol)	1.303	1.230	1.552	2.917
	K_{DR} (mol 2 /J 2)	0.294	0.330	0.207	0.058
	R^2	0.958	0.896	0.933	0.596
	χ^2	0.065	1.726	0.517	2.172
Sips	q_{mS} (mg/g)	15.910	82.713	21.076	5982.385
	n_S	5.280	9.157	133.939	0.763
	K_S (L/mg)	0.070	0.123	3.598	6.026x10 $^{-3}$
	R^2	0.981	0.883	0.866	0.816
	χ^2	0.030	1.938	1.035	0.986

The analysis of the calculated data suggests that the adsorption of AMP and NTZ on LF occurs through different mechanisms. The adsorption of AMP on LF was well-described by the DR isotherm since this model exhibited the highest R^2 values and lowest χ^2 values. The DR isotherm suggests a pore-filling mechanism for the adsorption process, applicable to both homogeneous and

heterogeneous surfaces [59]. By using the isothermal constant of the DR model (K_{DR}), it is possible to estimate the free energy (E) and, through this parameter, determine the type of adsorption process [60]. For AMP adsorption on LF, the low value of E (1.5×10^{-3} KJ/mol) confirms that the adsorption process occurs through physisorption, which is consistent with the work of Al-Musawi et al. [2], who described the adsorption of AMP on activated carbon derived from *Azolla filiculoides* fern (ACAF) as a physisorption mechanism.

In contrast, the Sips isotherm provided the best description for the NTZ adsorption mechanism on LF. The Sips model is a combination of the Langmuir and Freundlich models, suitable for describing adsorption processes over a wide concentration range, accounting for the heterogeneity of the adsorbent surface [61]. The Sips equation can be reduced to the Freundlich isotherm at low concentrations and to the Langmuir isotherm at high concentrations [62]. When the value of the Sips exponent (n_s) is close to or equal to 1, it indicates that the adsorption process is homogeneous and follows a pattern like the Langmuir model. However, in the current study, the value of n_s was determined to be 5.28, suggesting that the adsorption process occurred on a heterogeneous surface and exhibited behavior similar to the Freundlich isotherm. This finding supports a complex and heterogeneous adsorption process for NTZ on LF and agrees with the kinetic analysis [63,64].

According to the data in Table 4, the adsorption of AMP and NTZ on LF-g-PEI exhibited different mechanisms than LF, which can be ascribed to the grafting process. For AMP adsorption on LF-g-PEI, the Freundlich isotherm model provided the best fit to the experimental data, while the DR model was the most suitable for describing the adsorption of NTZ on this adsorbent. The

Freundlich model is used to characterize non-ideal, multilayer adsorption on heterogeneous adsorbent surfaces. This isotherm model assumes that there is an initial number of active sites available for adsorption, and over time, these sites are consumed, leading to a decrease in activity [65]. The parameters of the Freundlich isotherm provide insights into the adsorption process. In particular, the value of n indicates how favorably the adsorption process occurred, and an n value between 1 and 10 suggests favorable adsorption. For AMP adsorption onto LF-g-PEI ($n = 1.309$), it can be inferred that the process occurred favorably [66]. Additionally, the $1/n$ value, which characterizes the heterogeneity of the adsorption process, was between 0 and 1, indicating a more heterogeneous adsorption process. As for NTZ adsorption on LF-g-PEI, the DR model was the most adequate to fit the experimental data. The low value of E (1.2×10^{-3} KJ/mol) calculated from this isotherm indicates that the adsorption of the NTZ molecules on LF-g-PEI occurred through physisorption, corroborating the kinetic analysis.

3.3.4 Thermodynamic analysis

The thermodynamic parameters, including ΔG° , ΔH° , and ΔS° , for the adsorption of NTZ and AMP on LF and LF-g-PEI were calculated and are summarized in Table S2. The thermodynamics of NTZ adsorption on LF differed slightly from that observed for LF-g-PEI. For NTZ adsorption on LF, the ΔG° value at r.t. (approximately 293 K) was negative, indicating that the adsorption process occurs spontaneously [67]. However, as the temperature increases, the spontaneous nature of the NTZ adsorption process on LF diminishes. In contrast, after PEI grafting (LF-g-PEI), the NTZ adsorption process occurs spontaneously at all evaluated temperatures, as indicated by the negative values of ΔG° .

Moreover, the ΔG° values increase with rising temperature, suggesting that the NTZ adsorption process is more spontaneous at lower temperatures [68]. The negative ΔH° values for both LF and LF-g-PEI imply that the adsorption of NTZ was an exothermic process [69]. These negative ΔH° values are lower than 40 kJ/mol, indicating that the adsorption of this drug primarily occurs through physisorption [70]. The negative ΔS° value reflects a decrease in randomness during the NTZ adsorption process on LF samples [68].

In the case of AMP adsorption on LF samples, the process is not spontaneous because the ΔG° values are positive at all temperatures [71]. The negative ΔH° values (-54.26 kJ/mol for LF and -14.45 kJ/mol for LF-g-PEI) indicate that the AMP adsorption on both adsorbents was exothermic and has a physisorption nature. The negative ΔS° values in the AMP adsorption process suggest a decrease in randomness. Overall, these thermodynamic results align with the findings from the kinetic and isothermal models, supporting the conclusion that the adsorption process occurs primarily through physisorption. Furthermore, the ΔG° results explain why the adsorbents performed better in removing NTZ compared to AMP, as the spontaneity of the NTZ adsorption process contributes to higher removal efficiency, while the AMP adsorption is not spontaneous.

3.3.5 Adsorption mechanism

Spectroscopic analysis was conducted to investigate the potential interactions between the NTZ and AMP molecules and the surface of LF-g-PEI. This analysis focused solely on LF-g-PEI due to its high adsorption capacity. Upon comparing the FTIR spectra (Figure 4a), it is evident that following AMP

adsorption, the broadband associated with the combination of O–H and N–H stretching ($3650\text{--}3050\text{ cm}^{-1}$ range) in LF-g-PEI becomes broader and shifts to higher wavenumber regions. These observations suggest an H-bonding interaction between the adsorbent and AMP molecules. The absence of the band at 1582 cm^{-1} , related to the deformation of N–H in AMP, further indicates the presence of H-bonding interactions [72]. Changes within the $1770\text{--}1600\text{ cm}^{-1}$ wavenumber range may be attributed to H-bonds formed with electronegative atoms in the AMP structure (e.g., O, N, and S) [73]. Additionally, changes observed between $1670\text{--}1550\text{ cm}^{-1}$ range may be associated with $\pi\text{--}\pi$ interactions involving the phenyl ring of AMP and electron donor groups (--NH_2) in LF-g-PEI. Indeed, the amino groups of PEI are suggested to engage in a $\pi\text{--}\pi$ donor-acceptor interaction with the benzene ring of AMP [74]. As observed, the band at 1567 cm^{-1} attributable to the N–H bending of amino groups in LF-g-PEI shifted to a lower wavenumber region, indicating the aforementioned interaction [75].

As discussed previously, electrostatic interactions were ruled out as the primary adsorption mechanism based on the pH results. However, under the experimental conditions in this study, the pH of the AMP solution exhibited only minimal variation ($\Delta\text{pH} \approx 0.25$) after the adsorption process, suggesting a slight influence of electrostatic interactions between AMP and LF-g-PEI. Nevertheless, both the adsorbate and adsorbent were negatively charged under these conditions, indicating a repulsive interaction between them. In this context, Oba et al. [76] suggest that hydrophobic interactions become more pronounced. Considering the observed repulsion energy between AMP and LF-g-PEI, along with the broadening of the band between 2925 and 2855 cm^{-1} , associated with

the stretching of C–H bonds from the CH_x groups in LF-g-PEI, it is proposed that hydrophobic interactions play a significant role in the adsorption of AMP on LF-g-PEI. Additionally, the carbon backbone of Glut may contribute to this type of interaction. Figure 4b illustrates the possible interactions between AMP and LF-g-PEI.

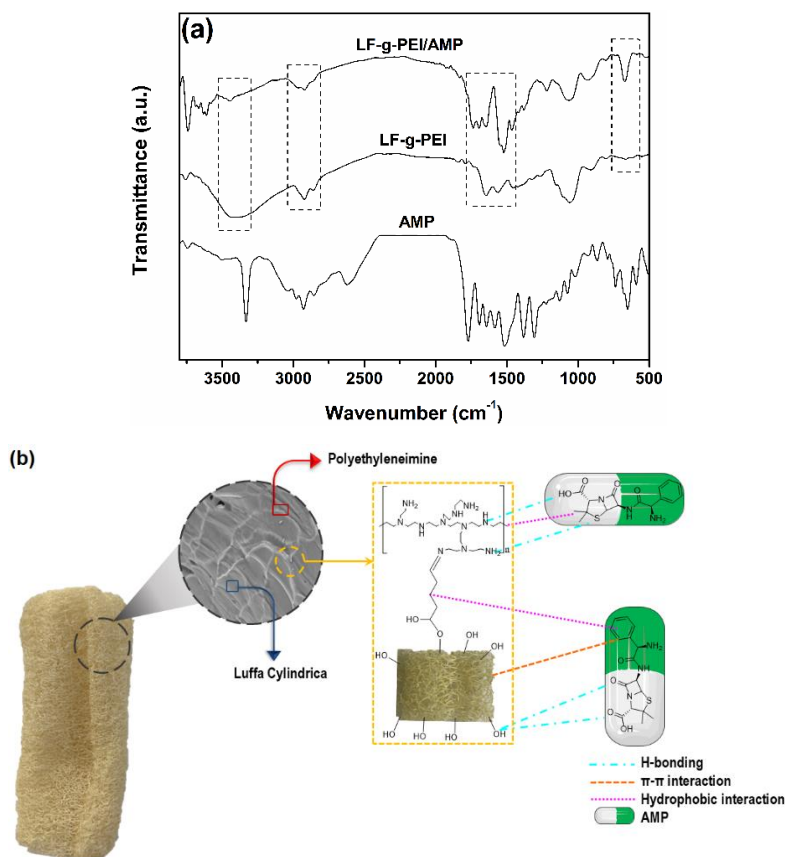


Figure 3-1.4: (a) FTIR spectra of AMP, LF-g-PEI, and LF-g-PEI loaded with AMP (LF-g-PEI/AMP), and (b) Scheme of AMP adsorption on LF-g-PEI.

Following the adsorption of NTZ, the FTIR spectrum of LF-g-PEI/NTZ (Figure 5a) exhibits changes similar to those previously observed in the LF-g-PEI/AMP spectrum. Notably, the broadband in the 3650–3050 cm⁻¹ range, associated with the combination of O–H and N–H stretching of LF-g-PEI, shifts to a lower wavenumber after NTZ adsorption, indicating the formation of H-bonds between the adsorbent and the adsorbate. Furthermore, the absence of the band

at 3078 cm^{-1} , associated with the stretching of aromatic C–H bonds in NTZ, suggests evidence of hydrophobic interactions [17]. The broadening of the band between 2925 and 2855 cm^{-1} provides additional evidence of hydrophobic interactions akin to what was observed in the LF-g-PEI/NTZ system. The additional contribution of this kind of interaction aids in explaining the greater affinity between NTZ and LF-g-PEI. Khalid et al. [77] note that the bands located at 1775 and 1530 cm^{-1} are associated with the C=O and N=O stretching of functional groups of NTZ. After the adsorption process, these characteristic bands of NTZ shift to lower wavenumber regions (1737 and 1512 cm^{-1}), indicating the formation of H-bonds with LF-g-PEI. The decrease in intensity of the band at 1643 cm^{-1} can be attributed to π - π interactions between the aromatic rings from lignin in LF-g-PEI and the C=C group in the aromatic ring of NTZ [17]. Based on these observed changes in the LF-g-PEI spectrum, it can be proposed that the adsorption mechanism of NTZ involves H-bonds, hydrophobic interactions, and π - π interactions. A schematic representation of the interaction forces between NTZ and LF-g-PEI is provided in Figure 5b.

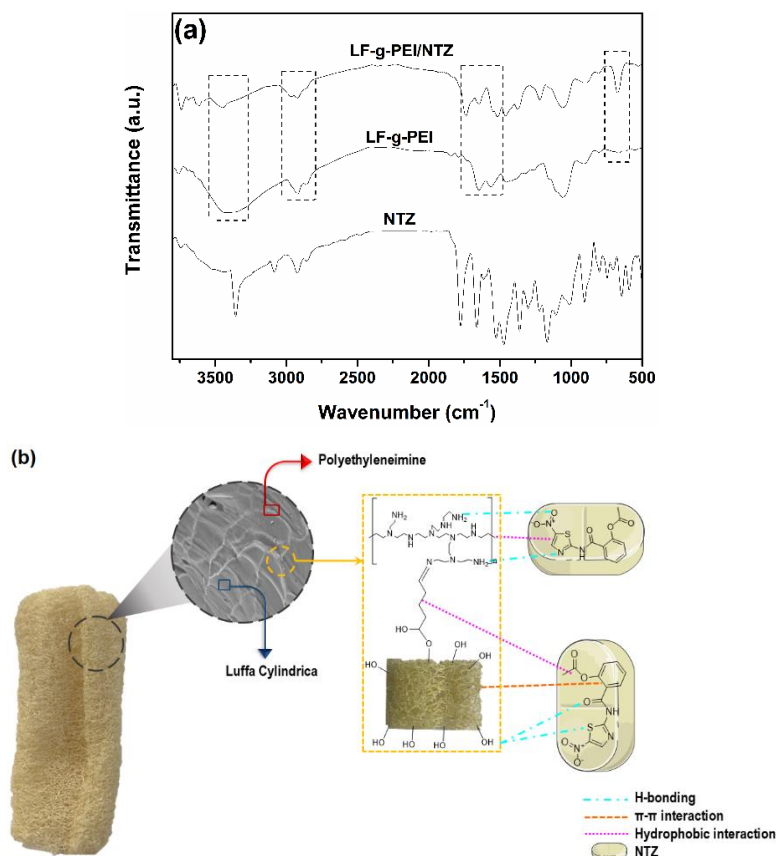


Figure 3-1.5: (a) FTIR spectra of NTZ, LF-g-PEI, and LF-g-PEI loaded with NTZ (LF-g-PEI/NTZ), and (b) Scheme of NTZ adsorption on LF-g-PEI.

3.3.6 Reuse experiments

It is essential to evaluate the reusability of the adsorbent to improve the economic viability of the adsorption process. Fan et al. [78] emphasize the significance of assessing the adsorbent's reusability, as it directly impacts its feasibility for practical water treatment applications. Given the superior adsorption performance of LF-g-PEI compared to LF, the regeneration and reuse potential of this adsorbent was. In this context, the adsorption capacity at equilibrium (q_e) of LF-g-PEI was determined for eight consecutive adsorption/desorption cycles and analyzed. The computed data are presented in Figure 6.

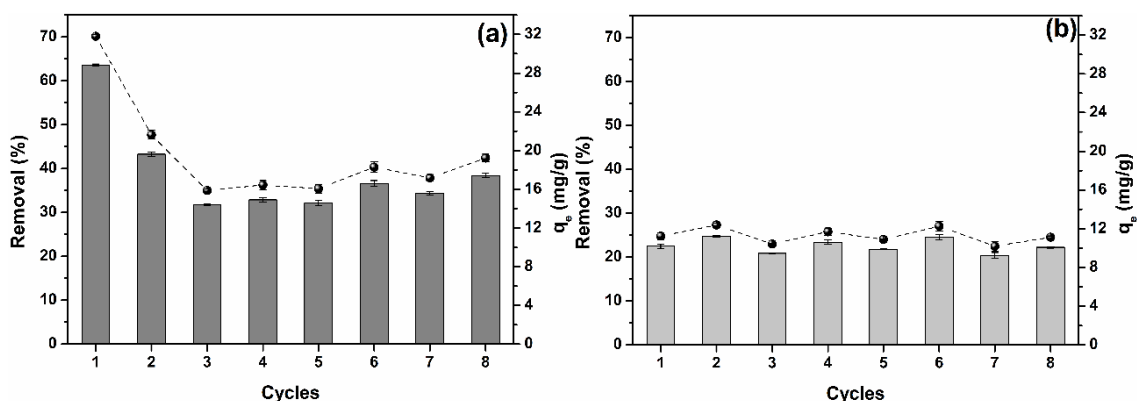


Figure 3-1.6: Adsorption capacity at equilibrium (bars) and reduction in the adsorption efficiency (line + symbol) for (a) NTZ and (b) AMP after consecutive reuse cycles using LF-g-PEI as the adsorbent.

As shown in Figure 6a, the adsorption capacity for NTZ was significantly impacted after consecutive reuse cycles. Overall, the q_e values exhibited a 25% decrease from the first to the last cycle. In contrast, for AMP adsorption (Figure 6b), the q_e values showed a much smaller variation of 0.24 %, indicating that the capacity of LF-g-PEI to adsorb this drug is minimally affected by reuse. The decrease in q_e values for NTZ adsorption can be attributed to the fact that NTZ adsorption follows a pore-filling mechanism, as described by the DR isotherm. Consequently, the desorption solution may only remove NTZ molecules adsorbed on the surface of LF-g-PEI, leaving those within the pores of the adsorbent unaffected. Future studies should investigate improved mediums and conditions for regenerating LF-g-PEI after its utilization for NTZ adsorption. Despite of this, it is noteworthy that in the last adsorption/ desorption cycle, more than 30 % of NTZ was still removed from the water.

In the case of AMP adsorption on LF-g-PEI, the q_e values remained consistent between the first and last cycles. This observation aligns with the isotherm results, as the adsorption process is better described by the Freundlich isotherm, which indicates a heterogeneous surface. Therefore, the desorption

process is believed to occur more efficiently in this case. In the last adsorption/desorption cycle, more than 20 % of AMP was still removed from the water. These findings suggest that LF-g-PEI, a chemically modified vegetal biomass, can be regarded as a stable and recyclable adsorbent for the removal of NTZ and AMP from aqueous solutions, with the potential to be employed in practical processes.

4. Conclusions

In this study, polyethyleneimine (PEI) was successfully grafted onto the fibers of LF to enhance its performance as an adsorbent. The presence of PEI was confirmed through elemental analysis, which revealed an increased percentage of the element nitrogen (N) after the grafting process. This modification led to significant changes in the physicochemical and morphological properties of LF, as evident from the FTIR, TGA, and SEM data. Importantly, this grafting process resulted in an improved capacity of LF-g-PEI to remove drugs like AMP and NTZ, from water. The increased number of active sites on LF-g-PEI was a key factor in its superior performance compared to unmodified LF. The adsorption of both drugs, NTZ and AMP, was driven by physical interactions, including H-bonding, π - π interactions, and hydrophobic forces. Given that the adsorption of both AMP and NTZ on LF-g-PEI occurred through physical interactions, the material could be efficiently regenerated and reused over at least 8 consecutive adsorption/desorption cycles. In summary, the results of this study highlight that the modification of LF with PEI, through grafting with glutaraldehyde, is viable, and that the modification does not damage the macroporous structure of the LF and also results in a material with greater thermal stability and a greater

number of active sites to promote drug removal. The data reported in this investigation could be useful in approaching the modification of lignocellulosic fibers, similar to LF.

References

- [1] M. Kumari, A. Kumar, Can pharmaceutical drugs used to treat Covid-19 infection leads to human health risk? A hypothetical study to identify potential risk, *Sci. Total Environ.* 778 (2021) 146303, <https://doi.org/10.1016/j.scitotenv.2021.146303>.
- [2] T.J. Al-Musawi, N. Mengelizadeh, M. Taghavi, S. Mohebi, D. Balarak, Activated carbon derived from *Azolla filiculoides* fern: a high-adsorption-capacity adsorbent for residual ampicillin in pharmaceutical wastewater, *Biomass Convers. Biorefin.* 13 (2023) 12179–12191, <https://doi.org/10.1007/s13399-021-01962-4>.
- [3] R. Pashaei, R. Dzingelevičienė, A. Bradauskaitė, A. Lajevardipour, M. Mlynska-Szultka, N. Dzingelevičius, S. Raugelė, A. Razbadauskas, S. Abbasi, R.M. Rees, B. Buszewski, Pharmaceutical and microplastic pollution before and during the COVID-19 pandemic in surface water, wastewater, and groundwater, *Water* 14 (2022) 3082, <https://doi.org/10.3390/w14193082>.
- [4] J. Luo, D. Bello, S. Pagsuyoin, Long-term wastewater-based surveillance and impacts of the COVID-19 pandemic on drug use trends in a U.S. Northeast rural town, *Sci. Total Environ.* 877 (2023) 162806, <https://doi.org/10.1016/j.scitotenv.2023.162806>.
- [5] T. Raza, M. Shehzad, M. Farhan Qadir, H. Abdul Kareem, N.S. Eash, M. Sillanpää, K. Rehman Hakeem, Indirect effects of Covid-19 on water quality, *Water-Energy Nexus* 5 (2022) 29–38, <https://doi.org/10.1016/j.wen.2022.10.001>.
- [6] D. Han, M. López-Mesas, R. Boada, T. Farías, A.R. Lazo Fraga, M. Valiente, Trace cisplatin and carboplatin removal by 3-mercaptopropionic acid and L-cysteine functionalized sponges: adsorption behaviour and mechanism, *Chem. Eng. J.* 472 (2023) 144894, <https://doi.org/10.1016/j.cej.2023.144894>.
- [7] P.C. Nnaji, V.C. Anadebe, I.G. Ezemagu, O. Onukwuli, Potential of *Luffa cylindrica* seed as coagulation-flocculation (CF) agent for the treatment of dye

- wastewater: kinetic, mass transfer, optimization and CF adsorption studies, Arab. J. Chem. 15 (2022) 103629, <https://doi.org/10.1016/j.arabjc.2021.103629>.
- [8] M. Alizadeh, S.J. Peighambaroust, R. Foroutan, H. Azimi, B. Ramavandi, Surface magnetization of hydrolyzed *Luffa Cylindrica* biowaste with cobalt ferrite nanoparticles for facile Ni²⁺ removal from wastewater, Environ. Res. 212 (2022) 113242, <https://doi.org/10.1016/j.envres.2022.113242>.
- [9] M. Salimi, Z. Salehi, H. Heidari, F. Vahabzadeh, Production of activated biochar from *Luffa cylindrica* and its application for adsorption of 4-Nitrophenol, J. Environ. Chem. Eng. 9 (2021) 105403, <https://doi.org/10.1016/j.jece.2021.105403>.
- [10] L.C. Maia, L.C. Soares, L.V. Alves Gurgel, A review on the use of lignocellulosic materials for arsenic adsorption, J. Environ. Manag. 288 (2021) 112397, <https://doi.org/10.1016/j.jenvman.2021.112397>.
- [11] J.B. Neris, F.H.M. Luzardo, E.G.P. da Silva, F.G. Velasco, Evaluation of adsorption processes of metal ions in multi-element aqueous systems by lignocellulosic adsorbents applying different isotherms: a critical review, Chem. Eng. J. 357 (2019) 404–420, <https://doi.org/10.1016/j.cej.2018.09.125>.
- [12] O. Akay, C. Altinkok, G. Acik, H. Yuce, G.K. Ege, G. Genc, Preparation of a sustainable bio-copolymer based on *Luffa cylindrica* cellulose and poly (ϵ -caprolactone) for bioplastic applications, Int. J. Biol. Macromol. 196 (2022) 98–106, <https://doi.org/10.1016/j.ijbiomac.2021.12.051>.
- [13] Z. Sasan Narkesabad, R. Rafiee, E. Jalilnejad, Experimental study on evaluation and optimization of heavy metals adsorption on a novel amidoximated silane functionalized *Luffa cylindrica*, Sci. Rep. 13 (2023) 3670, <https://doi.org/10.1038/s41598-023-30634-8>.
- [14] S. Maher, L.A. Smith, C.A. El-Khoury, H. Kalil, K. Sossey-Alaoui, M. Bayachou, Inducible nitric oxide synthase embedded in alginate/polyethyleneimine hydrogel as a new platform to explore NO-driven modulation of biological function, Molecules 28 (2023) 1612, <https://doi.org/10.3390/molecules28041612>.
- [15] J. Zhang, C. Ma, H. Li, X. Wang, F. Ning, M. Kang, Z. Qiu, Polyethyleneimine modified magnetic microcrystalline cellulose for effective removal of congo red: adsorption properties and mechanisms, Fibers Polym. 22 (2021) 1580–1593, <https://doi.org/10.1007/s12221-021-0543-7>.

- [16] M. Chen, G. Yang, Y. Liu, Y. Lv, S. Sun, M. Liu, Preparation of amino-modified cellulose aerogels and adsorption on typical diclofenac sodium contaminant, *Environ. Sci. Pollut. Res.* 29 (2022) 19790–19802, <https://doi.org/10.1007/s11356-021-17214-x>.
- [17] S.A. Ali, M. Abid, A. Ahmed, A. Wadood, S. Ahmed, Nitazoxanide and azithromycin for the early treatment of COVID-19: a multi-spectroscopic, biochemical and computational drug–drug interaction study, *J. Chin. Chem. Soc.* 70 (2023) 1568–1579, <https://doi.org/10.1002/jccs.202350075>.
- [18] H.M. Al-kuraishy, A.I. Al-Gareeb, E. Elekhawy, G.E.-S. Batiha, Nitazoxanide and COVID-19: a review, *Mol. Biol. Rep.* 49 (2022) 11169–11176, <https://doi.org/10.1007/s11033-022-07822-2>.
- [19] G. Navarrete-Vazquez, F. Ch´avez-Silva, R. Argotte-Ramos, M. del C. Rodríguez- Guti´errez, M.J. Chan-Bacab, R. Cedillo-Rivera, R. Moo-Puc, E. Hern´andez-Nuñez, Synthesis of benzologues of nitazoxanide and tizoxanide: a comparative study of their in vitro broad-spectrum antiprotozoal activity, *Bioorg. Med. Chem. Lett.* 21 (2011) 3168–3171, <https://doi.org/10.1016/j.bmcl.2011.02.100>.
- [20] L.M. Fox, L.D. Saravolatz, Nitazoxanide: a new thiazolide antiparasitic agent, *Clin. Infect. Dis.* 40 (2005) 1173–1180, <https://doi.org/10.1086/428839>.
- [21] F. Sanches-Neto, N. Coutinho, V. Aquilanti, W. Silva, V. Carvalho-Silva, Mechanism and kinetics of the degradation of nitazoxanide and hydroxychloroquine drugs by hydroxyl radicals: theoretical approach to ecotoxicity, *J. Braz. Chem. Soc.* (2023), <https://doi.org/10.21577/0103-5053.20230025>.
- [22] R. Hirsch, T. Ternes, K. Haberer, K.-L. Kratz, Occurrence of antibiotics in the aquatic environment, *Sci. Total Environ.* 225 (1999) 109–118, [https://doi.org/10.1016/S0048-9697\(98\)00337-4](https://doi.org/10.1016/S0048-9697(98)00337-4).
- [23] N. Xu, C. Hu, Z. Zhu, W. Wang, H. Peng, B. Liu, Establishment of a novel system for photothermal removal of ampicillin under near-infrared irradiation: persulfate activation, mechanism, pathways and bio-toxicology, *J. Colloid Interface Sci.* 640 (2023) 472–486, <https://doi.org/10.1016/j.jcis.2023.02.131>.
- [24] A. Batool, S. Valiyaveetil, Surface functionalized cellulose fibers – a renewable adsorbent for removal of plastic nanoparticles from water, *J. Hazard. Mater.* 413 (2021), <https://doi.org/10.1016/j.jhazmat.2021.125301>.

- [25] S. Larous, A.H. Meniai, Adsorption of Diclofenac from aqueous solution using activated carbon prepared from olive stones, *Int. J. Hydrog. Energy* 41 (2016) 10380–10390, <https://doi.org/10.1016/j.ijhydene.2016.01.096>.
- [26] S. Singh, R. Jelinek, Solar-mediated oil-spill cleanup by a carbon dot-polyurethane sponge, *Carbon* 160 (2020) 196–203, <https://doi.org/10.1016/j.carbon.2020.01.016>.
- [27] T. Avcu, O. Üner, Ü. Geçgel, Adsorptive removal of diclofenac sodium from aqueous solution onto sycamore ball activated carbon – isotherms, kinetics, and thermodynamic study, *Surf. Interfaces* 24 (2021) 101097, <https://doi.org/10.1016/j.surfin.2021.101097>.
- [28] J.S. da Costa, A.R. Fajardo, Polypyrrole/stearic acid-coated *Luffa cylindrica* for enhanced removal of sodium diclofenac from water: batch and continuous adsorption studies, *J. Clean. Prod.* 389 (2023) 136084, <https://doi.org/10.1016/j.jclepro.2023.136084>.
- [29] A. Hijazi, B. Azambre, G. Finqueneisel, F. Vibert, J.L. Blin, High iodine adsorption by polyethyleneimine impregnated nanosilica sorbents, *Microporous Mesoporous Mater.* 288 (2019) 109586, <https://doi.org/10.1016/j.micromeso.2019.109586>.
- [30] J. Zhang, Y. Li, Y. Dai, T. Lin, H. Shao, Y. Liu, X. Liu, Three-dimensional porous hydrogel based on hyperbranched polyethyleneimine functionalized apple pomace derived cellulose for efficient removal of methyl orange, *Chem. Eng. J.* 456 (2023) 140995, <https://doi.org/10.1016/j.cej.2022.140995>.
- [31] D.-M. Guo, Q.-D. An, R. Li, Z.-Y. Xiao, S.-R. Zhai, Ultrahigh selective and efficient removal of anionic dyes by recyclable polyethylenimine-modified cellulose aerogels in batch and fixed-bed systems, *Colloids Surf. A Physicochem. Eng. Asp.* 555 (2018) 150–160, <https://doi.org/10.1016/j.colsurfa.2018.06.081>.
- [32] X. Chen, L. Liu, Z. Luo, J. Shen, Q. Ni, J. Yao, Facile preparation of a cellulose-based bioadsorbent modified by hPEI in heterogeneous system for high-efficiency removal of multiple types of dyes, *React. Funct. Polym.* 125 (2018) 77–83, <https://doi.org/10.1016/j.reactfunctpolym.2018.02.009>.
- [33] C. Zhang, X. Lin, N. Zhang, Y. Lu, Z. Wu, G. Liu, S. Nie, Chemically functionalized cellulose nanofibrils-based gear-like triboelectric nanogenerator for energy harvesting and sensing, *Nano Energy* 66 (2019) 104126, <https://doi.org/10.1016/j.nanoen.2019.104126>.

- [34] N. Zhang, G.-L. Zang, C. Shi, H.-Q. Yu, G.-P. Sheng, A novel adsorbent TEMPO-mediated oxidized cellulose nanofibrils modified with PEI: preparation, characterization, and application for Cu(II) removal, *J. Hazard. Mater.* 316 (2016) 11–18, <https://doi.org/10.1016/j.jhazmat.2016.05.018>.
- [35] D. Kim, D.-S. Lim, H.-J. Lee, I.-C. Kim, Y.-N. Kwon, S. Myung, Hollow-fiber mixed-matrix membrane impregnated with glutaraldehyde-crosslinked polyethyleneimine for the removal of lead from aqueous solutions, *J. Memb. Sci.* 663 (2022) 121031, <https://doi.org/10.1016/j.memsci.2022.121031>.
- [36] J.G. Jeon, H.C. Kim, R.R. Palem, J. Kim, T.J. Kang, Cross-linking of cellulose nanofiber films with glutaraldehyde for improved mechanical properties, *Mater. Lett.* 250 (2019) 99–102, <https://doi.org/10.1016/j.matlet.2019.05.002>.
- [37] T. Hou, K. Guo, Z. Wang, X.-F. Zhang, Y. Feng, M. He, J. Yao, Glutaraldehyde and polyvinyl alcohol crosslinked cellulose membranes for efficient methyl orange and Congo red removal, *Cellulose* 26 (2019) 5065–5074, <https://doi.org/10.1007/s10570-019-02433-w>.
- [38] F.D. Guerra, M.L. Campbell, M.F. Attia, D.C. Whitehead, F. Alexis, Capture of aldehyde VOCs using a series of amine-functionalized cellulose nanocrystals, *ChemistrySelect* 3 (2018) 5495–5501, <https://doi.org/10.1002/slct.201703149>.
- [39] N. Premalatha, S.S. Saravanakumar, M.R. Sanjay, S. Siengchin, A. Khan, Structural and thermal properties of chemically modified luffa cylindrica fibers, *J. Nat. Fibers* 18 (2021) 1038–1044, <https://doi.org/10.1080/15440478.2019.1678546>.
- [40] X. Huang, B. Li, S. Wang, X. Yue, Y. Zhengguo, X. Deng, J. Ma, Facile in-situ synthesis of PEI-Pt modified bacterial cellulose bio-adsorbent and its distinctly selective adsorption of anionic dyes, *Colloids Surf. A Physicochem. Eng. Asp.* 586 (2020) 124163, <https://doi.org/10.1016/j.colsurfa.2019.124163>.
- [41] H. Sehaqui, M.E. Gálvez, V. Becatinni, Y. cheng Ng, A. Steinfeld, T. Zimmermann, P. Tingaut, Fast and reversible direct CO₂ capture from air onto all-polymer nanofibrillated cellulose—polyethylenimine foams, *Environ. Sci. Technol.* 49 (2015) 3167–3174, <https://doi.org/10.1021/es504396v>.
- [42] A. Shen, X. Liao, Y. Li, Polyamine functionalized cotton fibers selectively capture negatively charged dye pollutants, *Colloids Surf. A Physicochem. Eng. Asp.* 623 (2021) 126666, <https://doi.org/10.1016/j.colsurfa.2021.126666>.

- [43] M.B. Martinez-Pavetti, L. Medina, M. Espínola, M. Monteiro, Study on two eco-friendly surface treatments on *Luffa cylindrica* for development of reinforcement and processing materials, *J. Mater. Res. Technol.* 14 (2021) 2420–2427, <https://doi.org/10.1016/j.jmrt.2021.07.141>.
- [44] A. Khadir, M. Negarestani, A. Mollahosseini, Sequestration of a non-steroidal anti-inflammatory drug from aquatic media by lignocellulosic material (*Luffa cylindrica*) reinforced with polypyrrole: study of parameters, kinetics, and equilibrium, *J. Environ. Chem. Eng.* 8 (2020) 103734, <https://doi.org/10.1016/j.jece.2020.103734>.
- [45] S. Wang, X. Du, S. Deng, X. Fu, Z. Du, X. Cheng, H. Wang, A polydopamine-bridged hierarchical design for fabricating flame-retarded, superhydrophobic, and durable cotton fabric, *Cellulose* 26 (2019) 7009–7023, <https://doi.org/10.1007/s10570-019-02586-8>.
- [46] Y. Ding, C. Song, W. Gong, L. Liu, M. Wu, L. Li, J. Yao, Robust, sustainable, hierarchical multi-porous cellulose beads via pre-crosslinking strategy for efficient dye adsorption, *Cellulose* 28 (2021) 7227–7241, <https://doi.org/10.1007/s10570-021-03979-4>.
- [47] Y. Meng, T. Ju, F. Meng, S. Han, M. Song, J. Jiang, Insights into the critical role of abundant-porosity supports in polyethylenimine functionalization as efficient and stable CO₂ adsorbents, *ACS Appl. Mater. Interfaces* 13 (2021) 54018–54031, <https://doi.org/10.1021/acsami.1c17132>.
- [48] A. Maged, P.D. Dissanayake, X. Yang, C. Pathirannahalage, A. Bhatnagar, Y.S. Ok, New mechanistic insight into rapid adsorption of pharmaceuticals from water utilizing activated biochar, *Environ. Res.* 202 (2021), <https://doi.org/10.1016/j.envres.2021.111693>.
- [49] B. Qiu, X. Tao, H. Wang, W. Li, X. Ding, H. Chu, Biochar as a low-cost adsorbent for aqueous heavy metal removal: a review, *J. Anal. Appl. Pyrolysis* 155 (2021) 105081, <https://doi.org/10.1016/j.jaap.2021.105081>.
- [50] A.S. Eltaweil, H. Ali Mohamed, E.M. Abd El-Monaem, G.M. El-Subruiti, Mesoporous magnetic biochar composite for enhanced adsorption of malachite green dye: characterization, adsorption kinetics, thermodynamics and isotherms, *Adv. Powder Technol.* 31 (2020) 1253–1263, <https://doi.org/10.1016/j.appt.2020.01.005>.

- [51] A.K. Sakr, M.M. Abdel Aal, K.A. Abd El-Rahem, E.M. Allam, S.M. Abdel Dayem, E. A. Elshehy, M.Y. Hanfi, M.S. Alqahtani, M.F. Cheira, Characteristic aspects of uranium(VI) adsorption utilizing nano-silica/chitosan from wastewater solution, *Nanomaterials* 12 (2022) 3866, <https://doi.org/10.3390/nano12213866>.
- [52] T.L. Tan, P.A. Krusnamurthy, H. Nakajima, S.A. Rashid, Adsorptive, kinetics and regeneration studies of fluoride removal from water using zirconium-based metal organic frameworks, *RSC Adv.* 10 (2020) 18740–18752, <https://doi.org/10.1039/D0RA01268H>.
- [53] A.G. Al Lafi, J. Al Abdullah, Y. Amin, G. Alsayes, N. Al-Kafri, The effects of pH on the structure of polystyrene-nano manganese dioxide composites, *J. Mol. Struct.* 1237 (2021) 130315, <https://doi.org/10.1016/j.molstruc.2021.130315>.
- [54] C.B. de Carvalho, I.R. Rosa, P. Del Vecchio, I.V.J. D´avila, K.G.P. Nunes, N. R. Marcilio, L.A. F´eris, Degradation of ampicillin by combined process: adsorption and Fenton reaction, *Environ. Technol. Innov.* 26 (2022) 102365, <https://doi.org/10.1016/j.eti.2022.102365>.
- [55] Y. Lu, Z. Wang, X. Ouyang, C. Ji, Y. Liu, F. Huang, L.-Y. Yang, Fabrication of cross-linked chitosan beads grafted by polyethylenimine for efficient adsorption of diclofenac sodium from water, *Int. J. Biol. Macromol.* 145 (2020) 1180–1188, <https://doi.org/10.1016/j.ijbiomac.2019.10.044>.
- [56] Y.S. Ho, G. McKay, Application of kinetic models to the sorption of copper(II) on to peat, *Adsorpt. Sci. Technol.* 20 (2002) 797–815, <https://doi.org/10.1260/026361702321104282>.
- [57] C.M. Kerkhoff, K. da Boit Martinello, D.S.P. Franco, M.S. Netto, J. Georgin, E. L. Foletto, D.G.A. Piccilli, L.F.O. Silva, G.L. Dotto, Adsorption of ketoprofen and paracetamol and treatment of a synthetic mixture by novel porous carbon derived from *Butia capitata* endocarp, *J. Mol. Liq.* 339 (2021) 117184, <https://doi.org/10.1016/j.molliq.2021.117184>.
- [58] X. Geng, S. Lv, J. Yang, S. Cui, Z. Zhao, Carboxyl-functionalized biochar derived from walnut shells with enhanced aqueous adsorption of sulfonamide antibiotics, *J. Environ. Manag.* 280 (2021) 111749, <https://doi.org/10.1016/j.jenvman.2020.111749>.
- [59] S.K. Low, M.C. Tan, Dye adsorption characteristic of ultrasound pre-treated pomelo peel, *J. Environ. Chem. Eng.* 6 (2018) 3502–3509, <https://doi.org/10.1016/j.jece.2018.05.013>.

- [60] Q. Hu, Z. Zhang, Application of Dubinin–Radushkevich isotherm model at the solid/solution interface: a theoretical analysis, *J. Mol. Liq.* 277 (2019) 646–648, <https://doi.org/10.1016/j.molliq.2019.01.005>.
- [61] V. Choudhary, L. Philip, Sustainability assessment of acid-modified biochar as adsorbent for the removal of pharmaceuticals and personal care products from secondary treated wastewater, *J. Environ. Chem. Eng.* 10 (2022) 107592, <https://doi.org/10.1016/j.jece.2022.107592>.
- [62] K.G.P. Nunes, I.V.J. Davila, D. Arnold, C.H.R. Moura, D.C. Estumano, L.A. F'eris, Kinetics and thermodynamic study of laponite application in caffeine removal by adsorption, *Environ. Process.* 9 (2022) 47, <https://doi.org/10.1007/s40710-022-00598-4>.
- [63] Asranudin, A.S. Purnomo, D. Prasetyoko, H. Bahruji, Holilah, Single-step synthesis and modification of CTAB-hectorite for efficient adsorption of methyl orange dye, *Mater. Chem. Phys.* 291 (2022) 126749, <https://doi.org/10.1016/j.matchemphys.2022.126749>.
- [64] E.D.S. Filho, E.L. Brito, D.O. Nogueira, J.L.C. Fonseca, Thermal degradation and drug sorption in hybrid interpolyelectrolyte particles, *Colloids Surf. A Physicochem. Eng. Asp.* 610 (2021) 125894, <https://doi.org/10.1016/j.colsurfa.2020.125894>.
- [65] J. Ouyang, L. Zhou, Z. Liu, J.Y.Y. Heng, W. Chen, Biomass-derived activated carbons for the removal of pharmaceutical micropollutants from wastewater: a review, *Sep. Purif. Technol.* 253 (2020) 117536, <https://doi.org/10.1016/j.seppur.2020.117536>.
- [66] J.A. Kumar, T. Krithiga, G. Narendrakumar, P. Prakash, K. Balasankar, S. Sathish, D. Prabu, D.P. Pushkala, N. Marraiki, A.G. Ramu, D. Choi, Effect of Ca²⁺ ions on naphthalene adsorption/desorption onto calcium oxide nanoparticle: adsorption isotherm, kinetics and regeneration studies, *Environ. Res.* 204 (2022) 112070, <https://doi.org/10.1016/j.envres.2021.112070>.
- [67] C. Bai, L. Wang, Z. Zhu, Adsorption of Cr(III) and Pb(II) by graphene oxide/alginate hydrogel membrane: characterization, adsorption kinetics, isotherm and thermodynamics studies, *Int. J. Biol. Macromol.* 147 (2020) 898–910, <https://doi.org/10.1016/j.ijbiomac.2019.09.249>.
- [68] D.D. Eslek Koyuncu, M. Okur, Removal of AV 90 dye using ordered mesoporous carbon materials prepared via nanocasting of KIT-6: adsorption

- isotherms, kinetics and thermodynamic analysis, *Sep. Purif. Technol.* 257 (2021) 117657, <https://doi.org/10.1016/j.seppur.2020.117657>.
- [69] A.I.A. Sherlala, A.A.A. Raman, M.M. Bello, A. Buthiyappan, Adsorption of arsenic using chitosan magnetic graphene oxide nanocomposite, *J. Environ. Manag.* 246 (2019) 547–556, <https://doi.org/10.1016/j.jenvman.2019.05.117>.
- [70] D. Balarak, M. Zafariyan, C.A. Igwegbe, K.K. Onyechi, J.O. Ighalo, Adsorption of acid blue 92 dye from aqueous solutions by single-walled carbon nanotubes: isothermal, kinetic, and thermodynamic studies, *Environ. Process.* 8 (2021) 869–888, <https://doi.org/10.1007/s40710-021-00505-3>.
- [71] H.-J. Kang, J.-H. Kim, Adsorption kinetics, mechanism, isotherm, and thermodynamic analysis of paclitaxel from extracts of *taxus chinensis* cell cultures onto sylopute, *Biotechnol. Bioprocess Eng.* 24 (2019) 513–521, <https://doi.org/10.1007/s12257-019-0001-1>.
- [72] A. Topsakal, S. Midha, E. Yuca, A. Tukay, H.T. Sasmazel, D.M. Kalaskar, O. Gunduz, Study on the cytocompatibility, mechanical and antimicrobial properties of 3D printed composite scaffolds based on PVA/ Gold nanoparticles (AuNP)/ Ampicillin (AMP) for bone tissue engineering, *Mater. Today Commun.* 28 (2021) 102458, <https://doi.org/10.1016/j.mtcomm.2021.102458>.
- [73] M. Shirani, B. Akbari-adergani, H. Rashidi Nodeh, S. Shahabuddin, Ultrasonication-facilitated synthesis of functionalized graphene oxide for ultrasound-assisted magnetic dispersive solid-phase extraction of amoxicillin, ampicillin, and penicillin G, *Microchim. Acta* 187 (2020) 634, <https://doi.org/10.1007/s00604-020-04605-z>.
- [74] A. Rogowska, V. Railean-Plugaru, P. Pomastowski, J. Walczak-Skierska, A. Król- Górnaiak, A. Gołębiowski, B. Buszewski, The study on molecular profile changes of pathogens via zinc nanocomposites immobilization approach, *Int. J. Mol. Sci.* 22 (2021) 5395, <https://doi.org/10.3390/ijms22105395>.
- [75] Y. Gao, K. Liu, R. Kang, J. Xia, G. Yu, S. Deng, A comparative study of rigid and flexible MOFs for the adsorption of pharmaceuticals: kinetics, isotherms and mechanisms, *J. Hazard. Mater.* 359 (2018) 248–257, <https://doi.org/10.1016/j.jhazmat.2018.07.054>.
- [76] S.N. Oba, J.O. Ighalo, C.O. Aniagor, C.A. Igwegbe, Removal of ibuprofen from aqueous media by adsorption: a comprehensive review, *Sci. Total Environ.* 780 (2021) 146608, <https://doi.org/10.1016/j.scitotenv.2021.146608>.

- [77] H. Khalid, S. Batool, F. ud Din, S. Khan, G.M. Khan, Macrophage targeting of nitazoxanide-loaded transethosomal gel in cutaneous leishmaniasis, R. Soc. Open Sci. 9 (2022), <https://doi.org/10.1098/rsos.220428>.
- [78] K. Fan, T. Zhang, S. Xiao, H. He, J. Yang, Z. Qin, Preparation and adsorption performance of functionalization cellulose-based composite aerogel, Int. J. Biol. Macromol. 211 (2022) 1–14, <https://doi.org/10.1016/j.ijbiomac.2022.05.042>.
- [79] L.A. Rohen, A.C.C. Neves, D. de P. Mantovani, F. V. Carlos Maurício, J. da Silva Vieira, L. de A. Pontes, F.M. Margem, S. Monteiro, Hemp Fiber Density Using the Pycnometry Technique, in: 2017: p. 423–428. https://doi.org/10.1007/978-3-319-51382-9_46.

Supporting information for: Synthesis and characterization of polyethyleneimine grafted lignocellulosic fibers for improved removal of nitazoxanide and ampicillin from water

1. Results

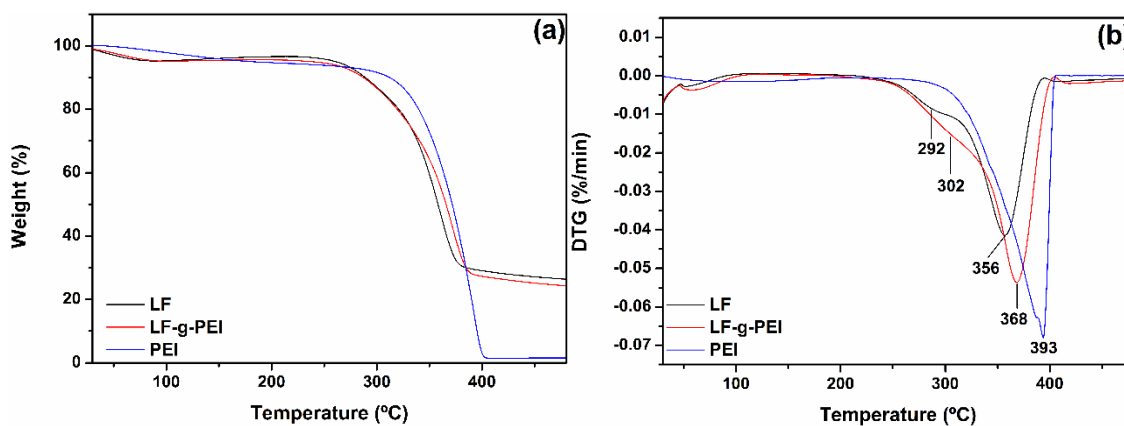


Figure 3-1.S1: (a) TGA and (b) DTG curves for LF, LF-g-PEI, and PEI.

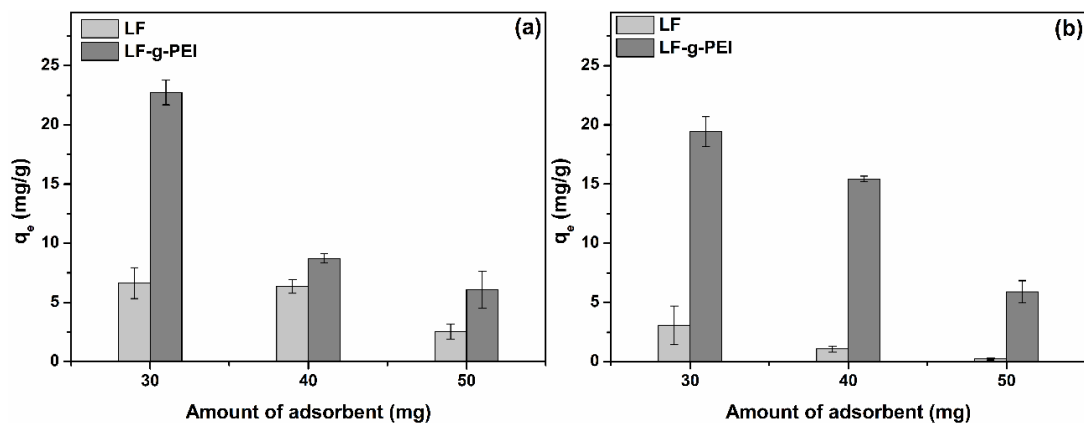


Figure 3-1.S2: Effect of the amount of adsorbent on the adsorption of (a) NTZ and (b) AMP (Other experimental conditions: C_0 50 mg/L, volume 30 mL, r.t., pH not adjusted, stirring 100 rpm).

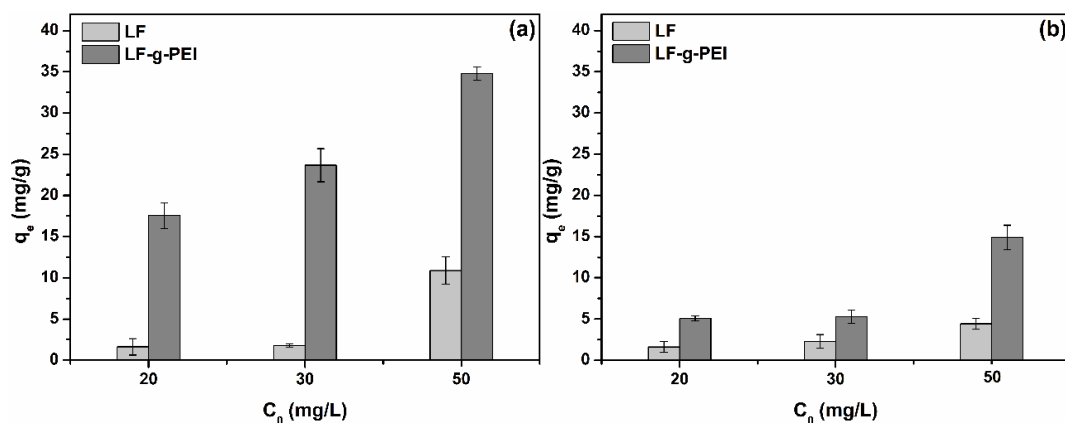


Figure 3-1.S3: Effect of initial concentration on the adsorption of (a) NTZ and (b) AMP (Other experimental conditions: Amount of adsorbent 30 mg, volume 30 mL, r.t., pH not adjusted, stirring 100 rpm).

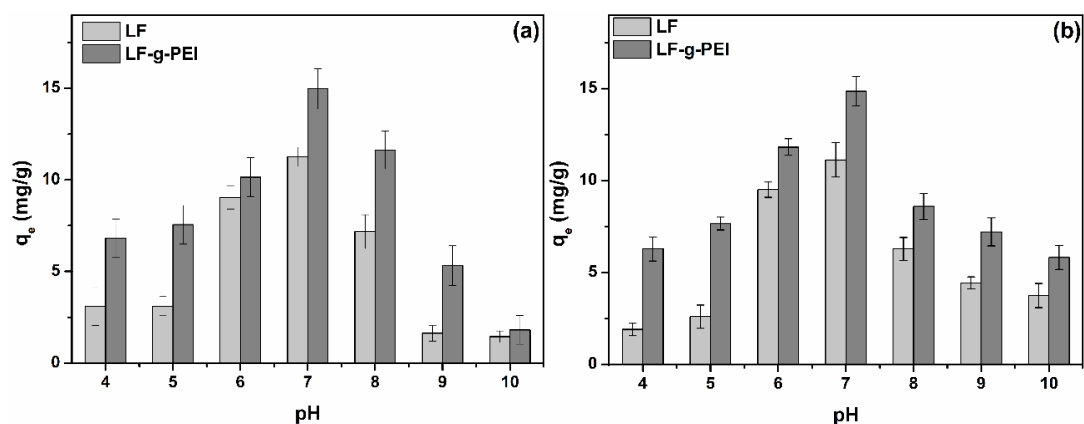


Figure 3-1.S4: Effect of the pH on the adsorption of (a) NTZ and (b) AMP (Other experimental conditions: Amount of adsorbent 30 mg, C_0 50 mg/L, volume 30 mL, r.t., stirring 100 rpm).

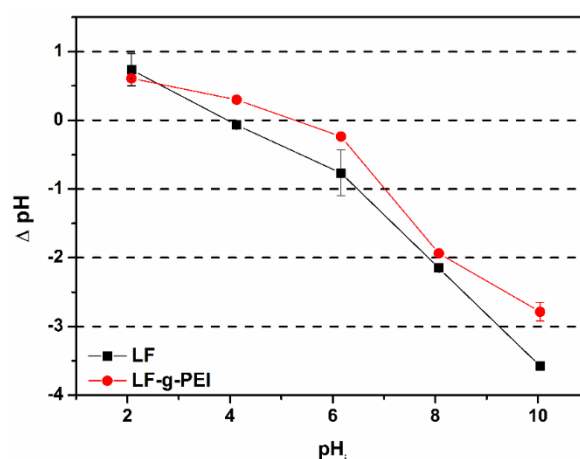


Figure 3-1.S5: ΔpH vs pH_i curves for LF and LF-g-PEI.

Table 3-1.S1: Kinetic and isotherm mathematical models and error-function.

Kinetic models		
Pseudo-first order (PFO)	$q_t = q_{e(theo)}e^{-k_1t}$	q_t – Adsorption capacity at time t (mg/g) $q_{e(theo)}$ – Theoretical adsorption capacity (mg/g) k_1 – Pseudo-first-order constant (1/min)
Pseudo-second order (PSO)	$q_t = \frac{q_{e(theo)}^2 k_2 t}{1 + q_{e(theo)} k_2 t}$	k_2 – Pseudo-second-order constant (mg/g)
Isotherm models		
Langmuir	$q_e = \frac{q_m K_L C_e}{1 + K_L C_e}$	q_m – Maximum adsorption capacity (theoretical) (mg/g) C_e – Pharmaceutical concentration remaining equilibrium (mg/L) K_L – Langmuir isotherm constant (L/mg)
Freundlich	$q_e = K_F C_e^{1/n}$	K_F – Freundlich isotherm constant (mg/g(L/mg) ^{1/n}) $1/n$ – Heterogeneous factor (dimensionless)

Dubinin-Radushkevich (DR)	$q_e = q_{mDR} e^{-K_{DR} \varepsilon^2}$ $\varepsilon = RT \ln \left(1 + \frac{1}{C_e} \right)$ $E = (2K_{DR})^{-1/2}$	q_{mDR} – Maximum adsorption capacity (theoretical) (mg/g) ε – Adsorption potential K_{DR} – DR isotherm constant (mol^2/J^2) R – Universal gas constant (8.314 J/K mol) T – Absolute temperature (K) E – Mean free energy (KJ/mol)
Sips	$q_e = \frac{K_S C_e^{n_S}}{1 + K_S C_e^{n_S}}$	K_S – Sips isotherm constant (L/mg) n_S – Sips model exponent
Error function		
Chi-square (χ^2)	$\chi^2 = \sum \frac{(q_e - q_{e(theo)})^2}{q_{e(theo)}}$	

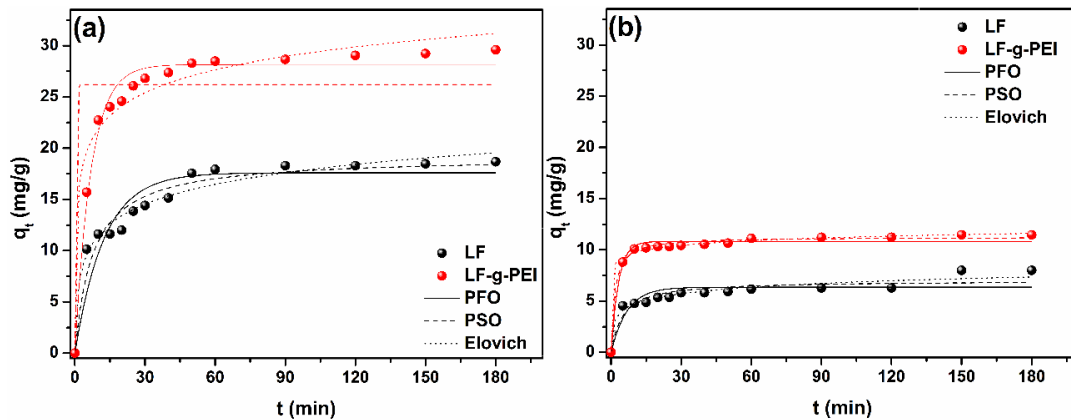


Figure 3-1.S6: Kinetic plots for the adsorption of (a) NTZ and (b) AMP on LF and LF-g-PEI.

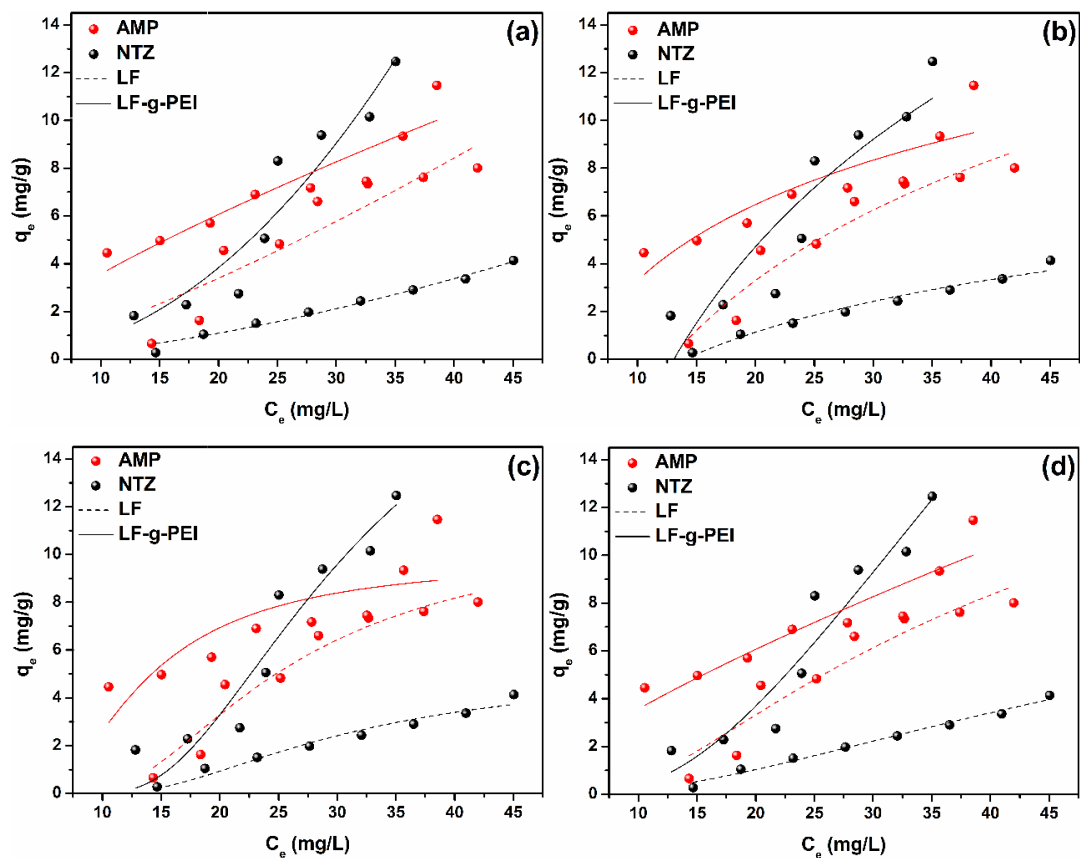


Figure 3-1.S7: (a) Freundlich, (b) Temkin, (c) DR, and (d) Sips isotherm plots for the adsorption of NTZ and AMP on LF and LF-g-PEI at 25 °C.

Table 3-1.S2: Thermodynamic parameters for NTZ and AMP adsorption on LF and LF-g-PEI.

Adsorbent	Temperature (K)	ΔG° (kJ/mol)	ΔH° (kJ/mol)	ΔS° (kJ/K mol)
NTZ				
LF	293	-1.61	-48.49	-0.16
	308	0.79		
	318	2.39		
	328	3.99		
LF-g-PEI	293	-4.24	-15.96	-0.04
	308	-3.64		
	318	-3.24		
	328	-2.84		
AMP				
LF	293	4.34	-54.26	-0.20
	308	7.34		
	318	9.34		

	328	11.34		
	293	3.71		
	308	4.64		
LF-g-PEI	318	5.26	-14.45	-0.06
	328	5.88		

3.2. Article – Polypyrrole/stearic acid-coated *Luffa cylindrica* for enhanced removal of sodium diclofenac from water: Batch and continuous adsorption studies

The results of this chapter of the thesis were published in the Journal of Cleaner Production, v. 389, p. 136084, fev. 2023.

Polypyrrole/stearic acid-coated *Luffa cylindrica* for enhanced removal of sodium diclofenac from water: Batch and continuous adsorption studies

Juliê S. da Costa and André R. Fajardo*

Abstract

Vegetal biomasses are prominent adsorbents; however, their hydrophilicity is a limitation in removing some emerging contaminants from water. As an approach to overcome this, in this study, *Luffa cylindrica* (LF), a 3D natural fiber array biomass, was coated with polypyrrole/stearic acid (PPy/SAc) (LF-PPySAc) to increase its adsorption capacity towards sodium diclofenac (DCF). Characterization analyses demonstrated that the physicochemical, morphological, and wettability properties of LF changed due to the PPy/SAc coating. As a result, LF-PPySAc becomes hydrophobic (water contact angle $>124^\circ$) benefiting the interaction with DCF. Experimentally, it was verified that the PPy/SAc coating enhances the adsorption of DCF by 234% (batch process) and 80% (continuous process) compared to raw LF. Kinetic, isothermal, and thermodynamics analyses indicated that the DCF adsorption is mediated mainly

by physical forces (H-bonding, π - π interaction, and hydrophobic forces), and intraparticle diffusional processes are involved. The high stability of LF-PPySAC allowed its reuse at least five times without losing adsorption performance in both batch and continuous processes. Thus, the coating of LF with PPy/SAC is ranked as a promising approach to obtaining an adsorbent material with an enhanced capacity to remove hydrophobic contaminants from the aqueous media.

Keywords: Adsorption; sponge gourd; emerging contaminants; pharmaceuticals; water treatment.

1. Introduction

As well-reported, many human activities (urban, industrial, agricultural, and health-related) generate pollutants that are discharged into the aqueous environment harming its quality (Araujo et al., 2021; Shamsudin et al., 2022a). Recently, spread attention has been given to a particular group of pollutants known as emerging contaminants (ECs) mainly due to the environmental risks associated with them. Some examples of ECs that can be detected in the aqueous environment are pesticides, hormones, flame retardants, pharmaceuticals, and personal care products (Rigueto et al., 2021). Khadir et al. (2020) warn that pharmaceuticals are the most dangerous ECs because these compounds are metabolized by human or animal organisms partially. Hence, unmetabolized fractions of pharmaceuticals are excreted into the environment (Araujo et al., 2021). Moreover, some physicochemical properties of the pharmaceuticals (such as polarity, high water-solubility, persistence, microbial resistance, and bioaccumulation potential) increase the risk associated with these pollutants (Khadir et al., 2020; Pap et al., 2021).

Diclofenac sodium (DCF) is one of the non-steroidal anti-inflammatory drugs (NSAIDs) most commonly used in the world (Huang et al., 2020; Li et al., 2021). It is widely used in the treatment of human and animal conditions, including inflammation and fever (Li et al., 2021). Rigueto et al. (2021) and Shamsudin et al. (2022b) reported that the annual global consumption of this drug exceeds hundred tons. This estimative increased with the pandemic coronavirus crisis (Younes et al., 2022). The overconsumption of this DCF (with and without prescription) has a straight relationship to the appearance of this drug and its metabolites in water and wastewater (Acuña et al., 2015). Since DCF has a hydrophobic nature, conventional treatment plants are unable to remove it from aquatic environments (Shamsudin et al., 2022a).

To deal with this, different techniques and processes such as sonophotocatalytic degradation (Meroni et al., 2020), photo and electro-Fenton processes (Rehman et al., 2021), and advanced oxidative processes (Jang et al., 2020) have been applied to promote the removal of DCF from wastewater. Although these techniques have shown varying levels of success in this task, they have disadvantages (e.g., high operating and maintenance costs, generation of a toxic secondary pollutant, and complicated procedures involved in treatment) (de Gisi et al., 2016). Alternatively, adsorption is exploited as a promising methodology for removing ECs, including pharmaceuticals, from water. Unlike other methods, the adsorption process has advantages such as high removal efficiency, no toxic secondary pollutants, operational simplicity, and low-cost (Huang et al., 2021; Rigueto et al., 2021). The efficiency of the adsorption process depends on the chemical properties of the pollutant to be removed from the water and on the properties of the adsorbent. These factors determine the adsorption

mechanism and the interactions that occur between the adsorbent and the pollutant (Shamsudin et al., 2022b). In this sense, several adsorbents have been developed to adsorb DCF such as metal-organic frameworks or MOFs (Younes et al., 2022), carbon-based materials (Larous and Meniai, 2016; Pedrosa et al., 2022), aerogels (Lv et al., 2021), and modified magnetic cellulose nanocrystal (Zhu et al., 2022). In contrast to these sophisticated and expensive materials, agricultural biomass products raise as alternative adsorbents to remove pharmaceuticals from water, including DCF (De Gisi et al., 2016; Shearer et al., 2022). Among these alternative adsorbents, *Luffa cylindrica* (LF), a subtropical plant that belongs to the *Cucurbitaceae* family, has attracted widespread attention due to its eco-friendly, structural, and morphological properties (e.g., natural availability, biodegradability, non-toxic, low-cost, high porosity, toughness, strength, lightness, and rigidity) (Khadir et al., 2021). LF is also known as sponge gourd, loofah, vegetable sponge, bath sponge, or dishcloth gourd (Akay et al., 2022). In terms of chemical composition, LF is composed of 60% cellulose, 30% hemicellulose, and 10% lignin; however, this composition may vary depending on the region, plant age, and also its nature (Khadir et al., 2020). This lignocellulosic material has a micro sponge structure with 200–500 microcellular fibers, which makes it a promising adsorbent material (Khadir et al., 2021). Nevertheless, the applicability of LF in the adsorption of hydrophobic pollutants, like DCF, is restricted due to its hydrophilic nature (Akay et al., 2022).

In this study, the fibers of LF were coated with polypyrrole and stearic acid to increase the adsorption performance of this material towards DCF. Polypyrrole (PPy) is a conductive polymer with unique characteristics, such as high conductivity, good environmental and chemical stability, high porosity, easy

synthesis, non-toxicity, and low-cost (Parit et al., 2020). This polymer is often tested in adsorption studies because it can reversibly transform between its charged and neutral forms, allowing it to adsorb different types of contaminants (Pires et al., 2017). Together with PPy, stearic acid (SAC) was also utilized to coat the fibers of LF. This fatty acid is formed by a monofunctional molecule with a long hydrophobic chain and a large amount of -COOH groups (Chen et al., 2020). Among the various uses of SAC, its ability to modify the surface of different materials is highly appreciated since it significantly reduces the surface energy and increases the hydrophobicity of the material (Zeng et al., 2022). Based on the properties of PPy and mainly on the properties of SAC, it is expected that LF coated by them shows an enhanced capacity to adsorb DCF from water. This approach has not been exploited yet as a strategy to increase the physical-chemical compatibility of LF with the DCF in the aqueous media and to improve its removal efficiency. To investigate this, a series of batch and continuous adsorption experiments were conducted. Furthermore, the experimental data were rationalized using different kinetic and isothermal models. Also, the reusability of the PPy/SAC-coated LF sponge was examined through consecutive adsorption/desorption experiments and adsorption experiments using tap water were done as proof of concept.

2. Materials and methods

2.1. Materials

The materials employed in this study are described in the Supporting information file.

2.2. Coating of LF with PPy and SAc

Firstly, the raw LF sponge was cut into small pieces (cubic shape, 1 cm³), thoroughly washed with an ethanol/H₂O solution (70:30 v/v) three times, and oven-dried at 50 °C for 24 h. The coating process of LF was done in two steps. For the first, clean LF (3 g) was added to a beaker filled with isopropyl alcohol (300 mL) and FeCl₃ solution (0.1 mol/L, 50 mL) and kept under vigorous stirring for 30 min. Then, pyrrole (3 mL) was gently added to the reaction media, which was cooled down to 4 °C using an ice bath (Dashairya et al., 2019). The reaction mixture was kept under stirring overnight to ensure an adequate polymerization of PPy on the LF fibers. Next, the PPy-coated LF (LF-PPy) was recovered and washed with isopropyl alcohol and distilled water. The second step encompassed the coating with SAc. Herein, LF-PPy (3.5 g) was added to a beaker filled with SAc solution in isopropyl alcohol (0.1 mol/L, 300 mL) and kept under stirring at r.t. for 2 h. Afterward, the SAc-coated sponge (LF-PPySAc) was recovered, washed with isopropyl alcohol and distilled water, oven-dried at 50 °C for 24 h, and stored for later characterization and use. Scheme S1 in the Supporting information summarizes the experimental steps done to prepare LF-PPySAc.

2.3. Characterization

All characterization analyses and experiments are described in the Supporting information.

2.4. Batch adsorption experiments

Batch experiments were performed to evaluate the ability of LF (coated or not) to adsorb DCF from the aqueous media. For these adsorption experiments,

the following general protocol was utilized: 40 mg of each sample (raw LF, LF-PPy, or LF-PPySAc) were added to Erlenmeyer flasks filled with DCF aqueous solutions (20 mL) at fixed initial concentrations (C_0) (10–50 mg/L). The flasks were kept under orbital stirring (100 rpm) at r.t. during the experiment. At pre-determined time intervals, aliquots were withdrawn from the Erlenmeyer flasks and immediately analyzed by UV–Vis spectroscopy (PerkinElmer Lambda 25 spectrometer, USA) at the wavelength (λ) of 275 nm. After UV–Vis measurements, the aliquots were returned to the flasks, and the absorption data were converted to concentration using previously built calibration curves ($R^2 > 0.998$). The amount of DCF adsorbed per gram of sponge at equilibrium (q_e) was calculated per Equation (1):

$$q_e = \frac{(C_0 - C_e)}{m} \times V \quad (1)$$

where C_0 (mg/L) is the initial DCF concentration, C_e (mg/L) is the concentration at equilibrium, m (g) is the mass of the sponge, and V (L) is the volume of the solution. Equation (1) was also utilized to calculate the amount of DCF adsorbed at different time intervals (q_t). In this case, C_e was replaced by C_t (i.e., the concentration of DCF at time t).

2.5. Continuous adsorption experiments

Additional experiments were performed to evaluate the ability of the LF samples to adsorb DCF from the aqueous media in continuous adsorption. To simulate an adsorption column, a syringe pump (New Era NE-300 Pump Systems, USA) was adapted vertically and a 20 mL syringe (inner diameter 19.13

mm) was utilized (Scheme S2). Specific amounts of LF-PPySAC, LF-PPy, or LF were put into the syringe and then, a DCF solution (100 mL, at fixed C_0) flowed through them. Aliquots of the solution passing through the sample were collected in a beaker after different time intervals and were immediately analyzed by UV–Vis spectroscopy (PerkinElmer, model Lambda 25, USA) in wavelengths (λ) of 275 nm. After UV–Vis measurements, aliquots were discarded into a pharmaceutical waste vial and absorption data were converted to concentration using previously constructed calibration curves ($R^2 > 0.998$). The total amount (q_{total}) of DCF adsorbed in the continuous adsorption was calculated per Equation (2) (Salman et al., 2011):

$$q_{total} = \frac{Q}{1000} \int_{t=0}^{t=t_{total}} C_{ad} dt \quad (2)$$

$$q_t = \frac{q_{total}}{m} \quad (3)$$

where Q (mL/min) is the volumetric flow rate, and C_{ad} (mg/L) is the difference between the initial and final concentrations of DCF at the end of the total flow time. The amount of DCF adsorbed per gram of adsorbent at time t (q_t (mg/g)) was computed per Equation (3). Under equilibrium conditions, q_t was replaced by q_e in Equation (3). All these experiments were done in triplicate.

2.6. Reuse experiments

After the adsorption experiments, the post-utilized LF-PPySAC samples were collected and immersed in an HCl/ethanol mixture (50:50 v/v %, 20 mL) for 1 h at r.t. for desorption. Next, the regenerated samples were oven-dried at 50 °C for 24 h and then reused in new adsorption experiments. The following

experimental conditions were utilized for adsorption: C_0 of DCF was set to 50 mg/L, the volume of solution was 20 mL, pH \sim 5.5, and the temperature at 25 °C. Based on previous results, the maximum adsorption time was fixed at 1 h for the batch experiments, and the maximum adsorption rate was fixed at 0.5 mL/min for the continuous adsorption experiments. Just after batch and continuous adsorption, q_e values were calculated according to the previous sections. The adsorption/desorption processes were repeated five times. Each reuse experiment was conducted in duplicate, and the results are expressed as mean \pm standard deviation.

3. Results and discussion

3.1 Characterization of the coated LF

FTIR analyses were used to characterize the chemical nature of raw LF, LF-PPy, and LF-PPySAc (Figure 1a). As seen, the spectrum of LF exhibited characteristic bands ascribed to its major components (i.e., cellulose and lignin). The broadband centered at 3447 cm^{-1} is attributed to the O–H stretching (–OH groups) of cellulose, hemicellulose, and lignin, while bands at 2925 and 2855 cm^{-1} are attributed to the C–H stretching of CH_x groups of cellulose, lignin, and hemicellulose (Khadir et al., 2021). Bands in the range of 1650 – 1550 cm^{-1} are due to the combination of C=O stretching and C=C aromatic stretching of the lignin moiety (Ighalo et al., 2020). The lignocellulosic nature of LF is also characterized by the presence of two bands at 1419 and 1254 cm^{-1} , attributable to the C–H stretching of –CH₃ groups and C–O stretching of –OCH₃ groups present in the lignin structure. The band at 1050 cm^{-1} is due to the C–O–C stretching of pyranose rings, typically observed for polysaccharides like cellulose

and hemicellulose (Mohana Krishnudu et al., 2019). All these bands are consistent with previous studies (Kesraoui et al., 2019). After the PPy-coating, the spectrum of LF-PPy exhibited the characteristic bands of LF combined with new bands as observed. Due to the higher amount of LF compared to PPy, some characteristic bands of this polymer were not observed. For example, the band around $3447\text{--}3363\text{ cm}^{-1}$ referring to the N–H stretching of the PPy ring, and the band around 1586 cm^{-1} due to the C–C/C=C stretching of the five-membered heterocyclic ring were not observed (Stejskal et al., 2021; Hamam et al., 2022). However, bands attributable to PPy were observed at 1459 , 924 , and 672 cm^{-1} due to C–N stretching and C–H out-of-plane deformation vibrations of the PPy ring. Other authors mention the appearance of these bands to confirm the successful polymerization of PPy (Dey and Kar, 2019). The observance of the LF bands in the spectrum of LF-PPy suggests that the coating process occurred by the physical deposition of PPy on the surface of the LF fibers. Indeed, the PPy chains may interact with the lignocellulose structure of LF through physical interaction forces (H-bonding, hydrophobic forces, etc.) (Yang et al., 2022). The spectrum of LF-PPySAC exhibited the same bands observed for LF-PPy. However, can be seen an increase in the intensity of the bands at 2925 and 2855 cm^{-1} , which be caused by the contribution of the asymmetric and symmetrical C–H stretching of CH_2 groups of SAC (Al-Shirawi et al., 2021). Moreover, the band observed at 1459 cm^{-1} is due to C–H bending of CH_2 groups confirming the presence of this second coating on the LF fibers (Patti et al., 2021; Zeng et al., 2022). The SAC-coating was expected to be deposited on LF-PPy fibers due to intermolecular H-bond interaction between the –COOH groups of SAC and the

N–H groups of the PPy ring. According to Tsumura et al. (2022), hydrophobic forces are also involved in this interaction.

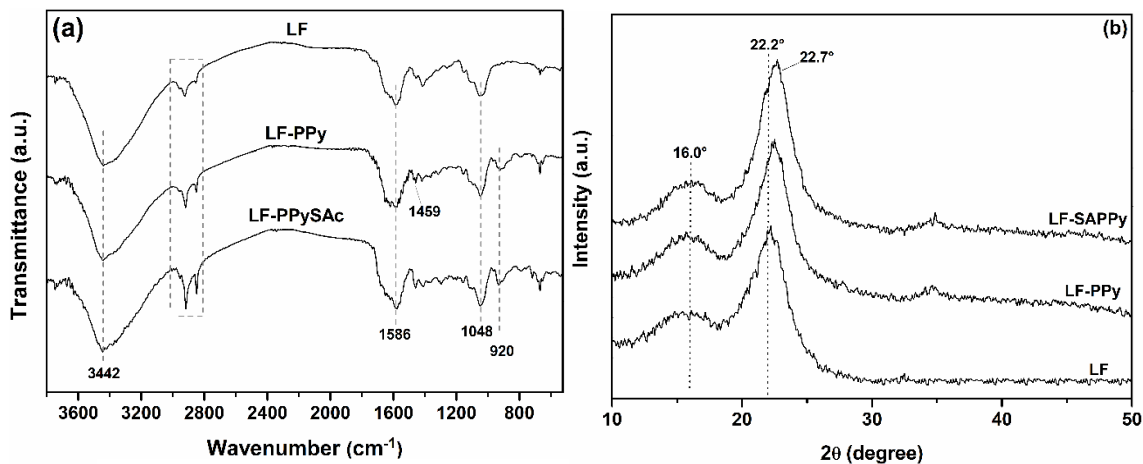


Figure 3-2.1: (a) FTIR spectra and (b) XRD pattern of raw LF, LF-PPy, and LF-PPySAC.

The XRD patterns of LF, LF-PPy, and LF-PPySAC (Figure 1b) are useful to investigate the structure and crystallinity of these materials before and after coating. The XRD pattern of LF exhibited two diffraction peaks at $2\theta \approx 16.0^\circ$ and 22.2° corresponding to the reflection from the (101) and (200) planes of the amorphous and crystalline moieties of cellulose Park et al. (2019). As seen, the XRD patterns obtained for the coated samples (LF-PPy and LF-PPySAC) were similar compared to the raw LF and among themselves. Both patterns exhibited the diffraction peaks associated with the cellulosic nature of LF (at $2\theta \approx 16.0^\circ$ and 22.2°) and a new peak at $2\theta \approx 22.7^\circ$, which indicates the presence of amorphous PPy (Pirsa and Asadzadeh, 2021). By comparing the patterns of the coated-LF samples, no changes were noticed after the PPy and SAC-coating, suggesting that the deposition of PPy and SAC on the LF fibers did not generate ordered structures on this material. The XRD data are consonant with FTIR analyses that showed that only physical interactions occur between the LF fibers and the

coating agents (PPy and SAc). Moreover, the coating process did not affect the chemical and structural nature of LF.

TGA/DTGA analyses demonstrated that LF and LF-PPy exhibit three main weight-loss stages, while LF-PPySAc exhibited four stages within the temperature range of 25–600 °C (Figure S1). For all samples, the first stage (from 30 to 100 °C) refers to the evaporation of water molecules adsorbed on the LF fibers. The second weight-loss stage of LF (from 230 to 300 °C) is attributed to the thermal depolymerization of its hemicellulose moieties. The last weight-loss stage (from 320 to 400 °C) of LF is related to the depolymerization of cellulose (Premalatha et al., 2021). LF-PPy showed similar TGA/DTG curves compared to LF; however, the PPy-coating decreased the temperature ranges associated with the thermal degradation of the lignocellulose structure of LF. This data indicates that the thermal stability of the LF fibers decreases due to the coating process. PPy chains deposited on the fibers limit the ordered alignment of the cellulose chains, weakening the thermal stability of LF-PPy (Akay et al., 2022). This limited alignment can be assigned to a probable interaction between PPy and the oxygen-rich groups on the surface of the fibers by H-bonding. Indeed, this interaction altered the diffraction pattern of the amorphous component of LF as demonstrated by XRD analyses. The TGA/DTG curves of LF-PPySAc exhibit an additional weight-loss stage (from 148 to 225 °C) attributable to SAc volatilization (Xianfeng et al., 2019). As seen, the SAc-coating impaired the thermal stability of LF-PPy since the weight-loss stages associated with the decomposition of the LF components were shifted to lower temperature ranges. According to Fan et al. (2022), the physical interactions between SAc and PPy by H-bonding, can also

affect the inter and intramolecular interactions of the lignocellulosic structure of LF, decreasing its thermal stability.

Photographic images taken before and after the coating processes revealed remarkable visual discrepancies among the LF samples. As observed, raw LF exhibits a typical yellowish color (Figure 2a), while the LF-PPy sample is dark black (Figure 2b), which results from the PPy polymerization (Fan et al., 2022). The dark LF-PPy becomes grayish after the SAc coating (Figure 2c). Images obtained by SEM show small embedded particles and some membranes on the surface of the raw LF fibers, which may be due to waxy and gummy substances that were not completely removed by the cleaning step (Martinez-Pavetti et al., 2021). Moreover, it is noted that the surface of the raw LF fibers is rough and dense without porosity, corroborating the previous description (Khadir et al., 2020). After the PPy-coating, the roughness of the LF fibers decreased, and a granular-like microstructure is observed (Mohd Tarmizi et al., 2018). Due to the *in situ* polymerization, the PPy particles form an interconnected network heterogeneously distributed on the surface of the fibers, which results in agglomerates with high density (Velhal et al., 2018). The lower thermal stability of the LF noticed from TGA/DTA analysis can also be related to the changes in the microstructure of the fibers caused by the coating process. After the SAc-coating, the surface of the fibers became markedly rough and uneven (Liu et al., 2020). Lu et al. (2021) explain that this kind of structure behaves like the Cassie model, where the contact area between water and sponge can be reduced. Together, this morphology and the low surface energy properties of SAc endow the LF-PPySAc with a hydrophobic property (Lu et al., 2021). Complementary to

this discussion, the total porosity of the LF samples was determined and discussed in the Supporting information.

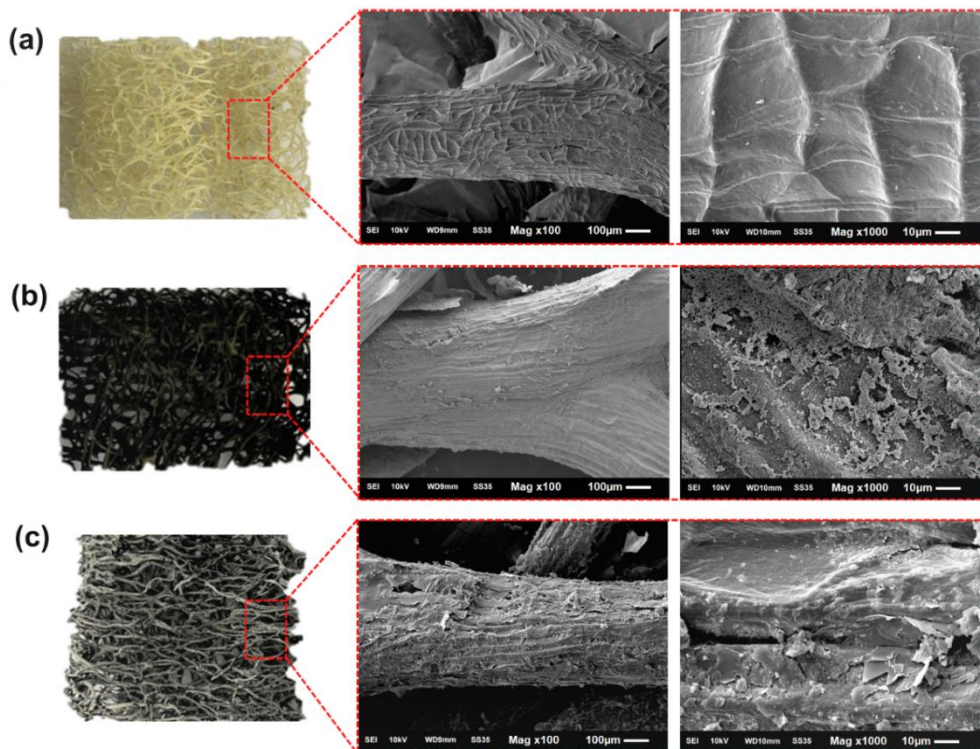


Figure 3-2.2: Photographic and SEM images (at different magnifications) obtained for (a) raw LF, (b) LF-PPy, and (c) LF-PPySAc.

Beyond the color change, the coating process made the LF samples rigid during handling. Compressive tests were done to verify this aspect. After compression using a load, the height variation was computed for each sample. As seen in Figure S2, raw LF presented the lowest mechanical compression strength with a height variation of 4 mm (~33% strain) concerning its initial height. The height variation for LF-PPy was determined to be 3 mm (~25% strain), indicating that this sample is slightly more rigid than LF. These results contrast with some studies that demonstrated that the mechanical compressive strength of cellulose fibers decreases after coating by PPy. According to these studies, this occurs due to the reduction of intramolecular H-bonding into the fibers (Parit

et al., 2020). On the other hand, in this study, SEM analyses showed that PPy was distributed over the entire surface of the LF fibers and its particles formed an interconnected and dense network that might contribute to an increase in the rigidity of LF-PPy. The LF-PPySAC sample exhibited the lowest height variation (2 mm, ~13% strain), suggesting that it is the more rigid sample. As demonstrated by the previous data, new physical interactions were formed on the surface of LF-PPy after SAC-coating, which may explain this result.

3.2. WCA measurements

One of the limitations of the adsorptive processes for the removal of drugs from water lies in the incompatibility (or low affinity) between the hydrophilic adsorbents and hydrophobic adsorbates or vice-versa. As a strategy to enhance the adsorption performance towards DCF, the fibers of LF were coated with PPy and PPy/SAC to increase their hydrophobicity. To evaluate the efficiency of this approach, the wettability of the coated LF samples was examined by WCA measurements. Figure 3 depicts the values of the static contact angle between the surface of the LF samples and water as well as photographic images taken from the water droplets on these samples. The WCA value for LF was determined as $76.9 \pm 11.1^\circ$, indicating that the surface of this biomass is hydrophilic since this value is lower than 90° (Derouich et al., 2020). Overall, natural fibers have a hydrophilic nature, and some factors can increase this character, like the environment in which it is grown, the number of polar hydroxy groups, surface roughness, and the number and size of pores, among others (Akay et al., 2022). Some of these characteristics were afore-discussed for LF. After the coating of the fibers by the relatively hydrophobic PPy, the WCA value increased to $90.0 \pm$

3.4° suggesting a lower wettability of LF-PPy compared to raw LF. This slight change in the hydrophilicity of the LF-PPy sample corroborates the morphological change observed on its surface after the deposition of PPy (Parit et al., 2020). Finally, the LF-PPySAC sample exhibited a WCA value of $124.2 \pm 8.3^\circ$, demonstrating that the SAc-coating endowed this sample with a high hydrophobic character. The second coating consisting of SAc reduced the surface energy of the fibers and increased their roughness (as observed by SEM) and, thereby, hydrophobicity. This last aspect can be associated with the long carbon layer formed by the SAc molecules (Lu et al., 2020). The results presented here confirmed that the dual coating of LF-PPySAC fibers becomes this material hydrophobic, which may potentize its adsorption towards hydrophobic adsorbates, such as DCF.

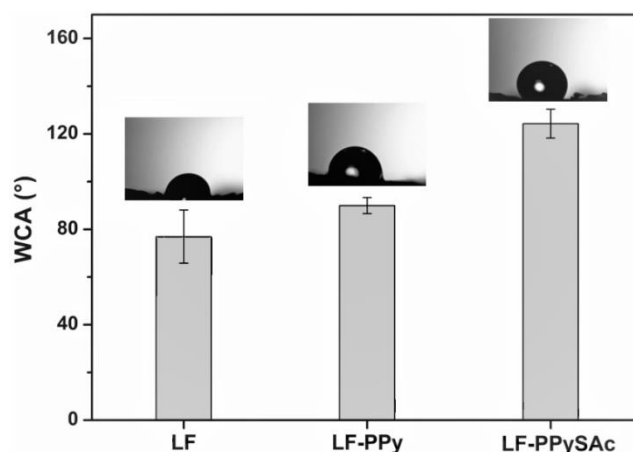


Figure 3-2.3: WCA measurements for raw LF, LF-PPy, and LF-PPySAC. Inset: Water droplet photographs on each sample.

3.4. Batch adsorption of DCF

3.4.1. Kinetics analysis

Batch experiments were conducted to estimate the adsorption capacity of the LF samples towards DCF concerning time. The data collected from these

experiments allow for gaining insights into the kinetics of this process. Herein, kinetic analysis was done for different DCF concentrations, since this parameter is directly related to the driving force at the solid-liquid interface and affects the adsorption capacity (Shamsudin et al., 2022b). Moreover, it is relevant informing the reader that the adsorbent dosage (40 mg) and initial pH (~5.5) were selected from a previous study detailed in the Supporting information (Figs. S3 and S4).

By comparing the data determined for the three LF samples (raw LF, LF-PPy, and LF-PPySAc), it is observed from a kinetic viewpoint that the adsorption of DCF behaves differently for each adsorbent (Figure 4). However, the increase of DCF concentration to values higher than 30 mg/L accelerated the adsorption kinetics for all adsorbents. This trend occurs because the concentration gradient at high DCF concentrations acts as a driving force favoring the mass transfer of drug molecules between the liquid and solid phases (Hiew et al., 2019). For the LF sample (Figure 4a) exposed to high DCF concentrations (>30 mg/L), the q_t values increased fast at the beginning of the experiment, then slowed down showing low variation with the increase of contact time. The higher adsorption rates up to 10 min can be associated with the great availability of binding sites on LF and the high concentration of DCF molecules in the liquid phase. After the saturation of these sites, the kinetics of the adsorption process decreases. As observed in Figure 4a, the equilibrium condition was not achieved at 60 min independently of the DCF concentration, this probably occurred because the contact time was not sufficient for the adsorption. This behavior may also indicate that the adsorption/desorption rates of DCF on LF are equal (Khadir et al., 2020).

Compared to LF, the kinetic behavior of LF-PPy was quite different, especially because for this adsorbent the adsorption equilibrium was achieved at

around 30 min for DCF solutions with concentration ≥ 30 mg/L (Figure 4b). Before this time, the q_t values increased fast up to 15 min, and then, the process slowed down, likely due to the saturation of the binding sites on LF-PPy. In terms of performance, at the highest DCF concentration, the maximum adsorption capacity computed for LF-PPy showed to be 188% higher than that computed for raw LF. Indeed, this enhancement trend for LF-PPy was also observed for the DCF solutions with 10 and 30 mg/L, respectively. This finding suggests that the PPy-coating increased the interaction affinity between DCF molecules and the adsorbent, benefiting the adsorption process.

The enhancement tendency for the DCF adsorption was kept for the experiments done with the LF-PPySAC sample; however, the process followed completely different kinetics compared to the other adsorbents (Figure 4c). For the experiments performed in high concentrations of DCF (>30 mg/L), the q_t values increased up to 5 min, and, after this while, their variation was low. However, as time goes on, the q_t values increased again, which typically denotes a multi-step adsorption process (Chang et al., 2021). Overall, multi-step adsorption involves surface interaction and diffusion of the adsorbate into the adsorbent. Considering the hydrophobic nature of the LF-PPySAC surface, the liquid-adsorbent interface may be affected by altering the mass transfer, which affects the whole process. Despite this, the adsorption performance computed for LF-PPySAC in the solution with the highest concentration of DCF increased by 16% compared to LF-PPy and 234% compared to raw LF. This data confirms that the dual-coating of LF with PPy/SAC is an effective strategy to increase the adsorption ability of LF towards this kind of contaminant. Beyond the morphology and textural discrepancies between the three LF samples, the presence of PPy

of PPy/SAc on the LF fibers also increased the hydrophobicity of the coated materials. As explained in the literature, DCF has an high octanol-water partition coefficient ($\log K_{ow} \approx 4.75$) and, therefore, it is considered a hydrophobic molecule (Ahsaie et al., 2021). Therefore, endowing the fibers of LF with a hydrophobic property allowed to increase in the affinity with DCF molecules.

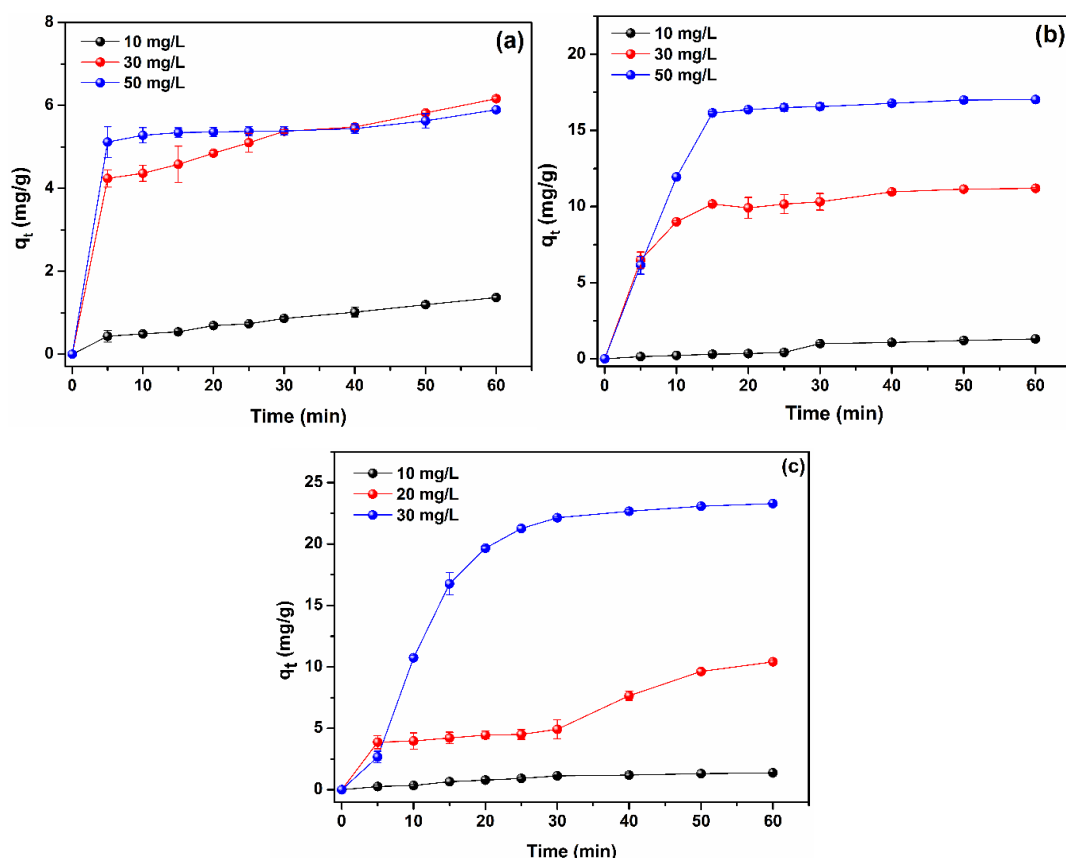


Figure 3-2.4: Batch adsorption kinetics of DCF on (a) raw LF, (b) LF-PPy, and (c) LF-PPySAc (Experimental conditions: $C_0 = 10\text{--}50$ mg/L, adsorbent dosage 40 mg, pH ~ 5.5 , r.t., stirring 100 rpm, contact time 60 min).

The adsorption data summarized in Figure 4 were fitted using the pseudo-first-order (PFO) and pseudo-second-order (PSO) kinetic models, which are expressed in the Supporting information (Equations S5 and S6). The kinetic parameters were determined from the non-linear regression of the data depicted

in the plot of q_t versus t plot (Figs. S5 and S6). Beyond the correlation coefficient (R^2) values, an error function, the non-linear Chi-square (χ^2) distribution (Equation S7), was employed to evaluate the best-fitting model.

Table 3-2.1: Kinetic parameters calculated for DCF adsorption on LF, LF-PPy, and LF-PPySAC.

PFO model						
Samples	C_0	q_e^a	$q_{e(calc)}$	k_1 ($\times 10^{-2}$)	R^2	χ^2
LF	10	1.36	1.55	2.94	0.941	0.03
	30	6.16	5.38	23.30	0.914	0.11
	50	5.89	5.47	53.41	0.988	0.03
LF-PPy	10	1.30	8.49	0.29	0.916	6.08
	30	11.19	10.74	17.90	0.988	0.01
	50	17.03	17.30	12.00	0.976	<0.01
LF-PPySAC	10	1.37	1.60	3.40	0.986	0.03
	30	10.40	15.21	1.81	0.862	1.51
	50	23.29	24.71	6.60	0.955	0.08
PSO model						
Sample	C_0	q_e^a	$q_{e(calc)}$	k_2 ($\times 10^{-4}$)	R^2	χ^2
LF	10	1.37	2.19	106.70	0.949	0.30
	30	6.16	5.92	579.90	0.962	<0.01
	50	5.89	5.61	3093.00	0.992	0.01
LF-PPy	10	1.30	17.19	0.85	0.916	14.68
	30	11.19	11.91	226.60	0.991	0.04
	50	17.03	20.14	73.60	0.945	0.48
LF-PPySAC	10	1.37	2.36	105.40	0.982	0.41
	30	10.40	22.36	6.00	0.837	6.39
	50	23.29	32.23	18.60	0.931	2.47

Units: C_0 (mg/L); q_e (mg/g); $q_{e(calc)}$ (mg/g); k_1 (1/min); k_2 (g mg/min).

^a Experimental data.

The kinetic parameters determined from the tested models, including R^2 and χ^2 values, are summarized in Table 1. As seen, the adsorption data collected for LF were well-fitted by the PSO model, which showed the highest R^2 and the lowest χ^2 values compared to the PFO model. Theoretically, the low χ^2 values calculated for the PSO model indicate that there is a good correlation between the experimental and theoretical q_e data. The data summarized in Table 1 also demonstrated that adsorption rate (k_2 values) on LF increases as the initial DCF concentration increases. Due to the high DCF concentration, more vacant sites on LF will probably be occupied as a function of time.

The kinetic analysis for the coated LF samples showed that the DCF adsorption on these adsorbents is well-fitted by the PFO model. For LF-PPy and LF-PPySAC, the R^2 values were relatively higher, while the χ^2 values were lower compared to the PSO model. This finding suggests that the coating of LF fibers with PPy or PPy/SAC alters the adsorption kinetics for DCF. Overall, the PFO model is useful to describe adsorption processes in liquid-solid systems considering the adsorption capacity of the solids (Wang et al., 2015). The coating of LF fibers with PPy and PPy/SAC may alter the interaction forces between the adsorbents and DCF, which explains this change in the kinetics. Regarding the PFO model, our finds corroborate other studies that investigated the adsorption of DCF on hydrophobic adsorbents (Suriyanon et al., 2013; De Oliveira et al., 2017). Finally, the analysis of the k_1 values determined for LF-PPy and LF-PPySAC indicates that the adsorption rate tends to decrease as the DCF concentration increase. Yang and Al-Duri (2005) related that this occurs because a longer time is required for a large initial solute concentration.

According to the literature, adsorption processes that follows PFO kinetics are preceded by the diffusion of the adsorbent molecules through a boundary layer to the surface of the adsorbent (Wang et al., 2014). However, this kinetic model is not able to provide information about the diffusion mechanism and the rate-limiting step. To investigate these aspects, the intraparticle diffusion model (Equation S8) was also utilized to fit the experimental data (Weber e Morris, 1963).

As seen in Figure S7, the intraparticle diffusion of DCF molecules into the adsorbents occurs in three steps, and the increase of the drug concentration increases the K_{diff} values determined for all tested LF samples. This behavior is attributable to the higher drug concentration, which increases the driving force. The first step (Region 1), which corresponds to the contact time between 5 and 15 min, represents the external mass transfer, that is, the transport of the DCF molecules from the solution to the surface of the adsorbent (Tran et al., 2020). The second step (Region 2), between 20 and 30 min, represents the intraparticle diffusion process, which is when the adsorbate molecules on the surface enter the adsorbent pores (Pires et al., 2017). The third and last step (Region 3) is the final equilibrium at which intraparticle diffusion starts to slow down (Puga et al., 2021). By analyzing the data summarized in Table S1, it can be suggested that for each adsorbent (LF, LF-PPy, and LF-PPySAc) there is a dominant region for intraparticle diffusion. For LF, Region 3 (the last step) seems to be the dominant independent of the DCF concentration since. As determined, this region showed the highest K_{diff} and the lowest C values. On the other hand, Region 1 was dominant for LF-PPy since it showed low resistance and, hence, the highest transport of the DCF molecules from the solution to the external surface of the

adsorbent. Finally, it was observed for LF-PPySAC that the region dominant was dependent on the DCF concentration. For instance, when the DCF concentration was 10 mg/L, Region 2 dominates the adsorption process on this adsorbent. This means that an intraparticle diffusion occurs quickly, and there is low resistance to DCF transport from the surface to inside the adsorbent. In this case, the adsorption kinetics is controlled by intraparticle diffusion, which is the rate-limiting step. By increasing the DCF concentration to 30 mg/L, Region 3 dominates the adsorption process. At the highest concentration of DCF (50 mg/L), Region 1 is dominant; however, the other regions showed a good correlation considering the value of R^2 .

3.4.2. Isothermal analysis

To understand the mechanism associated with the adsorption of DCF on LF, LF-PPy, and LF-PPySAC, the experimental data depicted in Figure 4 were fitted using isotherm models. For this, the non-linear forms of Langmuir (Equation S9) (Langmuir, 1917), Freundlich (Equation S10) (Freundlich, 1906), Temkin (Equation S11) (Temkin e Pyzhev, 1940), and Dubinin-Radushkevich (D-R) (Equation S12) (Dubinin e Radushkevich, 1947) isotherm were employed.

The non-linear regression of the data arranged in the q_e versus C_e plots (Figure S8) was used to estimate all these isotherm parameters and constants. Table 2 summarizes the computed data.

Table 3-2.2: Isotherms parameters calculated for DCF adsorption LF, LF-PPy, and LF-PPySAC at 25 °C.

Isotherm	Parameter	LF	LF-PPy	LF-PPySAC
Langmuir	q_m (mg/g)	104791.988	93908.379	91335.641
	K_L (L/mg)	7.003×10^{-6}	9.586×10^{-6}	1.135×10^{-5}
	R^2	0.693	0.621	0.701
	χ^2	12.194	17.357	26.231
Freundlich	$1/n$	2.016	1.623	5.291
	n	0.496	0.616	0.189
	K_F (mg/g(L/mg) $^{1/n}$)	0.053	0.199	6.164×10^{-5}
	R^2	0.895	0.732	0.937
	χ^2	4.168	12.26	3.286
Temkin	K_T (L/mg)	0.444	0.456	0.620
	b_T (J/mol)	506.660	430.134	476.456
	R^2	0.456	0.445	0.352
	χ^2	21.597	25.447	33.779
D-R	q_{mDR} (mg/g)	27.580	26.22	197.780
	E (kJ/mol)	0.002	0.003	0.002
	K_{DR} (mol 2 /J 2)	0.066	0.042	0.124
	R^2	0.963	0.827	0.952
	χ^2	1.438	7.915	2.463

Based on the calculated R^2 values, it is suggested that the D-R isotherm is the most suitable compared to the other isotherms to describe the adsorption mechanism. The low χ^2 values calculated for this isotherm corroborate this statement. According to the D-R isotherm, adsorption processes occur through

the formation of multilayers on the surface of the adsorbent (Cuccarese et al., 2021). Furthermore, this model expresses how the adsorption process occurs on homogeneous and heterogeneous surfaces and explains the average distribution of the free energy of the adsorbate that will be adsorbed on a heterogeneous surface (Rashid et al., 2021). Theoretically, the parameter E calculated from the D-R isotherm describes whether the adsorption occurs via chemical or physical processes (Khadir et al., 2020). As seen in Table 2, the estimated values of E were noticeably low (<0.003 kJ/mol) for all LF samples, confirming that the adsorption of DCF on these adsorbents is purely physical. Additionally, the q_{mDR} values calculated from this isotherm (27.58, 26.22, and 197.78 mg/g) are closer to the q_e values (16.16, 16.82, and 19.41 mg/g) experimentally determined for LF, LF-PPy, and LF-PPySAc, which strengthens the robustness of this isotherm to explain the experimental data.

3.6. Continuous adsorption of DCF

The continuous adsorption process has the same physicochemical nature as batch adsorption; however, it involves characteristics that will influence the mass transfer process (Danish et al., 2022). Herein, continuous experiments were done to verify the scalable potential of this process and to evaluate the applicability of LF samples in practical uses. These experiments utilized the ideal adsorbent dosage and solution flow rate conditions (i.e., 40 mg and 0.5 mL/min) determined from previous experiments. Moreover, the concentration of DCF was set to 50 mg/L based on the results from the batch experiments.

As observed in Figure 5, for all LF samples, the adsorption process occurs faster in the first 60 min and reaches equilibrium at 122 min of continuous

adsorption. By comparing the adsorption performance of the LF samples, the highest q_t value was computed to LF-PPySAC (0.40 mg/g), which showed to be 25% higher than that determined for LF-PPy and 80% higher than raw LF. Indeed, the q_t values determined for the dual-coated LF sample were higher than that determined for the other adsorbents in all tested conditions. This finding highlights the superior adsorption performance of LF-PPySAC, which can be attributed to the PPy/SAC coating. The superiority of this sample corroborates the data obtained from the batch adsorption experiments. On the other hand, it is worth mentioning that the adsorption results in the continuous adsorption mode were quite different from those obtained in the batch conditions, which corroborates previous studies that also investigate these two operation modes (Wojnicki et al., 2020). Together, these results suggest that the adsorbents tested in this study (especially LF-PPySAC) exhibit the potential to be used in continuous adsorption processes, which are close to real treatment processes.

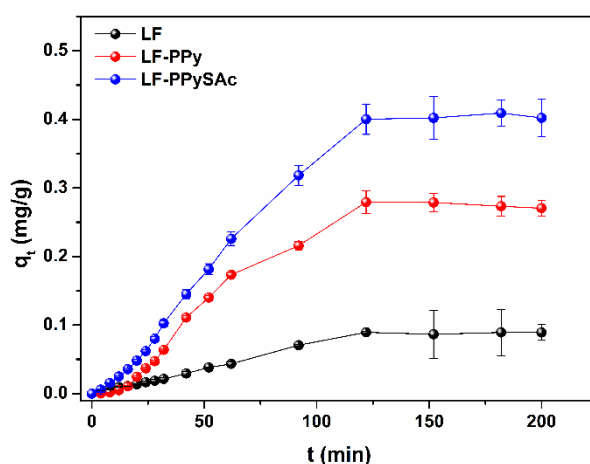


Figure 3-2.5: Continuous adsorption kinetics of DCF on (a) raw LF, (b) LF-PPy, and (c) LF-PPySAC (Experimental conditions: $C_0 = 50$ mg/L, flow rate 0.5 mL/min, adsorbent dosage 40 mg, pH ~5.5, r.t.).

3.7. Adsorption mechanism

The complete description of the mechanism associated with DCF adsorption can be a complex task due to the influence of several factors, such as physicochemical properties, operational conditions, and surface chemistry of the adsorbent, among others (Darryle et al., 2021). Based on the previous discussion, it was suggested that the adsorption of DCF on the LF samples depends mainly on physical interactions. FTIR analyses were conducted with the LF-PPySAC sample before and after DCF adsorption to investigate the main interactions and functional groups involved in this process. This investigation effort was done only for LF-PPySAC, which showed the highest adsorption performance towards DCF. Comparing the FTIR spectra shown in Figure 6, it is noted that after adsorption of DCF, the broadband associated with the combination of O–H and N–H stretching ($3650\text{--}3050\text{ cm}^{-1}$) of LF-PPySAC is broadened and shifted to lower wavenumber region, which suggests a probable H-bonding interaction between the adsorbent and DCF. Changes were also observed in the range of $1180\text{--}990\text{ cm}^{-1}$ due to the C–O stretching, the strength of this suggestion. Indeed, oxygen-containing groups of LF and –NH– groups of the PPy ring may interact with DCF by H-bonding (Shamsudin et al., 2022b; Hu et al., 2019). Moreover, some bands attributable to the elongation of C–C bonds of aromatic rings ($1600\text{--}1400\text{ cm}^{-1}$) were shifted compared to LF-PPySAC before the adsorption. This change indicates the π - π interaction between the aromatic rings of DCF and LF-PPySAC (Tomul et al., 2019). Finally, the band associated with the rocking vibration of $\text{--}(\text{CH}_2)_n\text{--}$ groups of long chains (around 720 cm^{-1}) in the LF-PPySAC spectra disappears after DCF adsorption, probably because of the hydrophobic interaction between the SAC moieties and the drug. The increase

in the intensity of the bands observed in the range of 3000–2800 cm^{-1} (C–H stretching) and the broadening of the band in the range of 1700–1500 cm^{-1} (C=O and C=C stretching) confirms the presence of DCF on LF-PPySAc. Also, the LF-PPySAc/DCF spectrum exhibited a band centered at 2500 cm^{-1} ascribed to the primary H-bonding between $-\text{COO}-$ and H–N (heterocycle) groups of DCF (Aakeröy et al., 2011). The observance of this band suggests the interaction among the DCF molecules after adsorption. Indeed, the multi-layer deposition of DCF on the adsorbent may favor this kind of interaction.

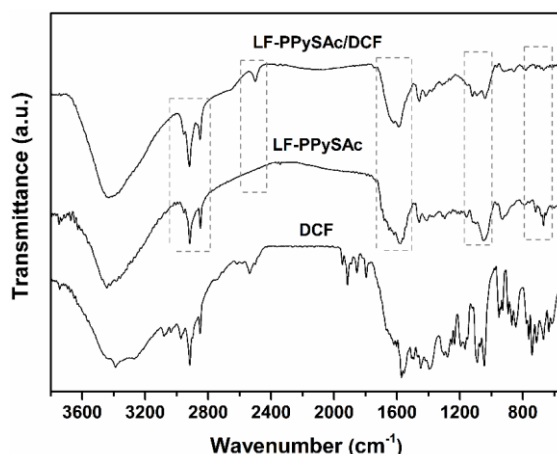


Figure 3-2.6: FTIR spectra of DCF, LF-PPySAc (before adsorption) and LF-PPySAc/DCF (after adsorption).

Figure 7 brings a schematic illustration of the possible interactions that must occur between LF-PPySAc and DCF after adsorption. As illustrated, H-bonding and π - π interactions are the main forces involved here, which is coherent with previous studies that investigated the adsorption of DCF (Tomul et al., 2019; Wu et al., 2020). The absence of electrostatic interactions mediating the adsorption process is strengthened based on the pH of the solution (~ 5.5), in which both adsorbent and adsorbate are negatively charged. Indeed, after the adsorption process, the pH of the DCF solution decreased to 4.7 ± 0.1 .

Considering the initial pH (5.5), the adsorption of DCF became the medium more acidic, which can be attributable to the release of H^+ due to the ionization of DCF molecules.

Czech et al. (2021) reported that a less hydrophilic surface enhances the adsorption of DCF. Moreover, the carbon portions on the surface of the adsorbent are pivotal for the adsorption process and its efficiency. Based on this, the hydrophobic nature of the LF-PPySAC ascribed to the long carbon chain of SAC on the surface of the adsorbent should influence the adsorption process. Thus, beyond H-bonding and π - π interactions, hydrophobic forces are also involved in the adsorption mechanism. Isothermal and thermodynamic data corroborate this discussion since they have indicated that the adsorption of DCF on LF-PPySAC is a physical process. A survey covering the recent literature was done to compare the performance and the adsorption mechanism reported for different materials tested in the adsorption of DCF from water (Table 3).

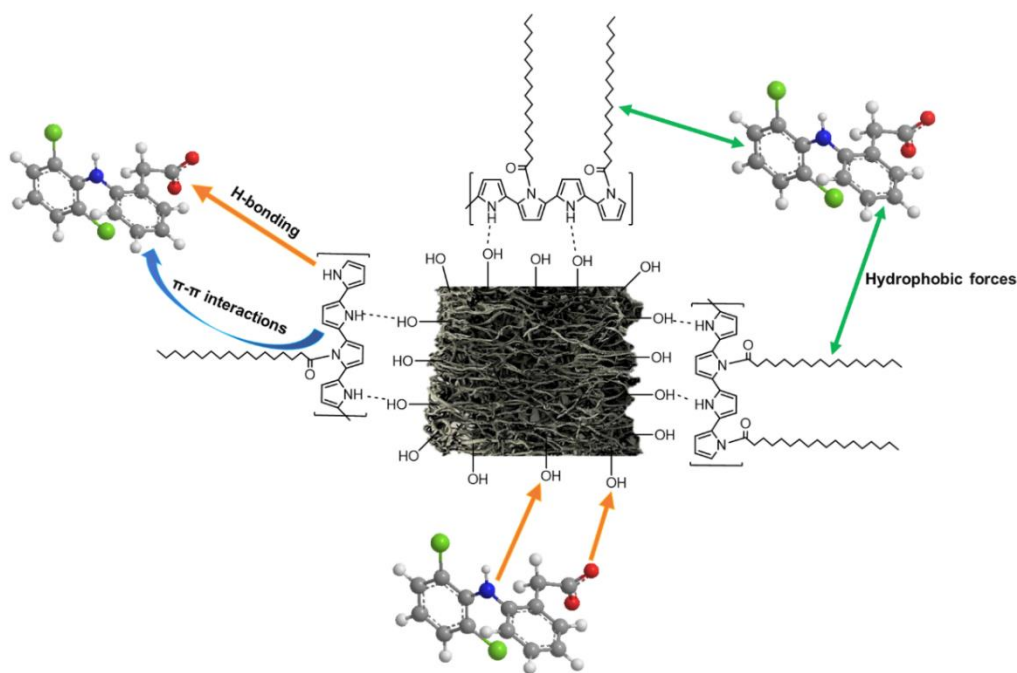


Figure 3-2.7: Schematic illustration of the adsorption mechanism of DCF on LF-PPySAC.

Table 3-2.3: Comparison between adsorption capacities (q_e) of some adsorbents tested in the removal of DCF from aqueous media.

Adsorbent	Dosage (mg)	C_0 (mg/L)	Equilibrium time (min)	q_e (mg/g)	Adsorption mechanism	Ref.
CNC-ED@CS-ED	20	100	50	444.44	Electrostatic	(HU et al., 2019)
<i>G. ulmifolia</i> Lam. fruits	50	100	1440	27.80	H-bonding and π - π interactions	(ARAUJO et al., 2021)
LAC-2	10	35	30	224.00	H-bonding, π - π interactions, and electrostatic	(WU et al., 2020)
BCSLWN ₂ 700	50	10	1440	92.70	π -Stacking	(CZECH et al., 2021)
CBW ₅₀₀ ^{HPO} (continuous adsorption)	50	10	455	53.84	Electrostatic, π - π interactions and hydrophobic forces	(MAGED et al., 2021)
MCNC-PEI	10	200	90	299.93	H-bonding and electrostatic	(ZHU et al., 2022)
LF-PPySAc	40	50	40	23.29	H-bonding, π - π interactions and hydrophobic forces	<i>this study</i>
LF-PPySAc (continuous adsorption)	40	50	122	0.40	H-bonding, π - π interactions and hydrophobic forces	<i>this study</i>

3.8. Reuse experiments

Among the characteristics that an adsorbent material must fulfill to assure its practical application, the ability to be recyclable and reusable is one of the most important (Azam et al., 2021). Herein, the regeneration/reuse capacity of the dual-coated LF sponge (LF-PPySAc) was examined, since it exhibited the best adsorption performance compared to the raw LF and LF-PPy. The maximum adsorption capacity at equilibrium (q_e) was determined for LF-PPySAc after consecutive adsorption/desorption cycles and compared. Reuse experiments were performed in batch and continuous adsorption processes, and the results are depicted in Figure 8a and b.

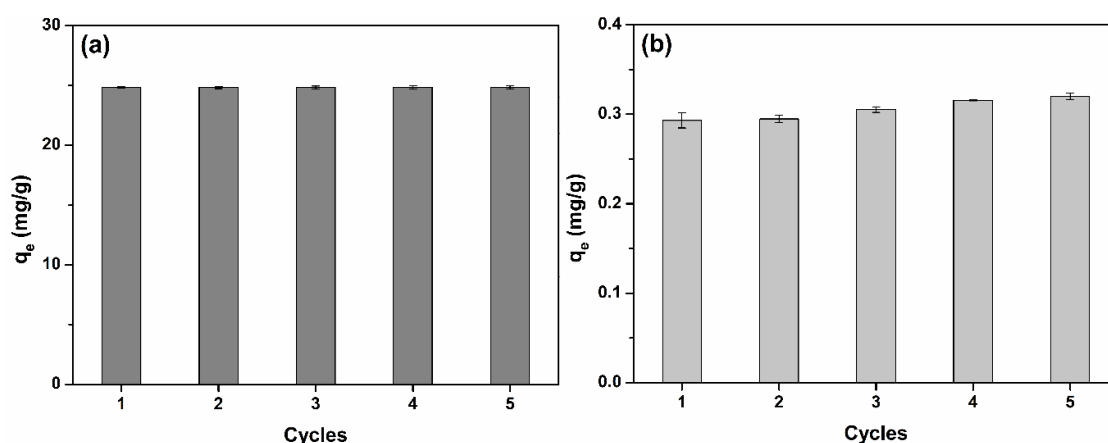


Figure 3-2.8: Adsorption capacity of LF-PPySAc as a function of the reuse cycles. (a) Batch adsorption (Experimental conditions: $C_0 = 50$ mg/L, adsorbent dosage 40 mg, pH ~ 5.5 , r.t., stirring 100 rpm, contact time 60 min) and (b) continuous adsorption (Experimental conditions: $C_0 = 50$ mg/L, flow rate 0.5 mL/min, adsorbent dosage 40 mg, pH ~ 5.5 , r.t.).

As verified, the adsorption capacity of LF-PPySAc for DCF is minimally affected even after five cycles of adsorption/desorption, both in batch and continuous adsorption. In the batch mode (Figure 8a), the q_e values exhibited a variation below 0.1% between the first to the last cycle, and in the continuous adsorption (Figure 8b), the q_e values varied by 8.7%. Indeed, the q_e values determined in the continuous adsorption increased as the reuse cycles increased, which may be due to the regeneration process. The acidic solution used to regenerate the post-utilized LF-PPySAc adsorbent might protonate the N–H groups of the PPy ring, facilitating the adsorption of the negatively charged DCF (Khadir et al., 2020). The (re)characterization of the surface portion of LF-PPySAc after the last cycle showed that this material has notorious stability, which aids in explaining its great reuse potential. Images obtained by SEM (Figure S11) confirmed that the texture and morphology of the post-used adsorbent still show characteristics comparable to the as-prepared material.

Besides, the WCA determined for the LF-PPySAC after the last cycle decreased by 2.6% compared to the as-prepared sample, which confirms that the hydrophobic character of this material remains after consecutive reuses. This finding suggests the permanence of the SAc-coating on the LF-PPySAC fibers and that the regeneration medium imparts low changes on this material. Complementary, TGA/DTG analysis of the post-utilized LF-PPySAC (not shown) suggested that the adsorption process does not affect the thermal stability of the adsorbent, which confirms that the adsorption process was restricted to the surface portion of the adsorbent. Besides, the maintenance of this property is an additional indication that only physical interaction forces are established between LF-PPySAC and DCF, corroborating the previous discussion. Given these characterization and adsorption results, it can be said that LF-PPySAC is a stable and recyclable adsorbent with a promising potential to treat DCF-contaminated aqueous media. Indeed, this statement is corroborated by the results obtained from adsorption experiments conducted in tap water as a proof of concept to validate the potential application of LF-PPySAC in the practical adsorption of DCF. As discussed in the Supporting information, this original adsorbent demonstrates high adsorption capacity toward DCF even in tap water.

4. Conclusions

In the present work, the fibers of LF were coated with PPy and SAc. This dual-coating process changed the physicochemical and morphological properties of LF and decreased its hydrophilicity. As a result, the ability of LF-PPySAC to adsorb DCF from water (using the batch or continuous processes) increased considerably. The higher affinity between the PPy/SAC coating and the DCF molecules mediated by weak physical interactions (H-bonding, π - π interactions,

and hydrophobic forces) explains the enhanced adsorption performance compared to raw LF or the sample coated only by PPy. This simple modification (i.e., coating with PPy and SAc) can be useful to other researchers that use vegetal biomasses in the adsorption of hydrophobic molecules from the aqueous media. The nature of the physical interactions between the LF-PPySAc and DCF allowed regenerating and reusing of the adsorbent in consecutive adsorption/desorption cycles even. The appreciable chemical and mechanical stability of LF-PPy/SAc is also a relevant characteristic of this original adsorbent. Together, the results indicated that LF-PPySAc can serve as an efficient adsorbent for DCF removal from aqueous solutions in scalable and practical processes.

References

- Aakeröy, C.B., Grommet, A.B., Desper, J., 2011. Co-crystal screening of diclofenac. *Pharmaceutics* 3, 601–614. <https://doi.org/10.3390/pharmaceutics3030601>.
- Acuña, V., Ginebreda, A., Mor, J.R., Petrovic, M., Sabater, S., Sumpter, J., Barceló, D., 2015. Balancing the health benefits and environmental risks of pharmaceuticals: diclofenac as an example. *Environ. Int.* 85, 327–333. <https://doi.org/10.1016/j.envint.2015.09.023>.
- Ahsaie, F.G., Pazuki, G., Sintra, T.E., Carvalho, P., Ventura, S.P.M., 2021. Study of the partition of sodium diclofenac and norfloxacin in aqueous two-phase systems based on copolymers and dextran. *Fluid Phase Equil.* 530, 112868. <https://doi.org/10.1016/j.fluid.2020.112868>.
- Akay, O., Altinkok, C., Acik, G., Yuce, H., Ege, G.K., Genc, G., 2022. Preparation of a sustainable bio-copolymer based on *Luffa cylindrica* cellulose and poly (ϵ -caprolactone) for bioplastic applications. *Int. J. Biol. Macromol.* 196, 98–106. <https://doi.org/10.1016/j.ijbiomac.2021.12.051>.
- Al-shirawi, M., Karimi, M., Al-maamari, R.S., 2021. *Journal of Petroleum Science*

- and Engineering Impact of carbonate surface mineralogy on wettability alteration using stearic acid. *J. Pet. Sci. Eng.* 203, 108674 <https://doi.org/10.1016/j.petrol.2021.108674>.
- Araujo, L.A., Bezerra, C.O., Cusioli, L.F., Rodríguez, M.T., Gomes, R.G., Bergamasco, R., 2021. Diclofenac adsorption using a low-cost adsorbent derived from *Guazuma ulmifolia* Lam. fruit via chemical and thermal treatment. *J. Environ. Chem. Eng.* 9, 106629 <https://doi.org/10.1016/j.jece.2021.106629>.
- Azam, T., Pervaiz, E., Farrukh, S., Noor, T., 2021. Biomimetic highly hydrophobic stearic acid functionalized MOF sponge for efficient oil/water separation. *Mater. Res. Express* 8. <https://doi.org/10.1088/2053-1591/abd822>.
- Chang, J., Wang, H., Zhang, J., Xue, Q., Chen, H., 2021. New insight into adsorption and reduction of hexavalent chromium by magnetite: multi-step reaction mechanism and kinetic model developing. *Colloids Surfaces A Physicochem. Eng. Asp.* 611, 125784 <https://doi.org/10.1016/j.colsurfa.2020.125784>.
- Chen, Q., Shi, Y., Chen, G., Cai, M., 2020. Enhanced mechanical and hydrophobic properties of composite cassava starch films with stearic acid modified MCC (microcrystalline cellulose)/NCC (nanocellulose) as strength agent. *Int. J. Biol. Macromol.* 142, 846–854. <https://doi.org/10.1016/j.ijbiomac.2019.10.024>.
- Cuccarese, M., Brutti, S., De Bonis, A., Teghil, R., Mancini, I.M., Masi, S., Caniani, D., 2021. Removal of diclofenac from aqueous solutions by adsorption on thermo-plasma expanded graphite. *Sci. Rep.* 11 <https://doi.org/10.1038/s41598-021-83117-z>.
- Czech, B., Kónczak, M., Rakowska, M., Oleszczuk, P., 2021. Engineered biochars from organic wastes for the adsorption of diclofenac, naproxen and triclosan from water systems. *J. Clean. Prod.* 288 <https://doi.org/10.1016/j.jclepro.2020.125686>.
- Danish, Mohd, Ansari, K.B., Danish, Mohammad, Khatoon, A., Ali Khan Rao, R., Zaidi, S., Ahmad Aftab, R., 2022. A comprehensive investigation of external mass transfer and intraparticle diffusion for batch and continuous adsorption of heavy metals using pore volume and surface diffusion model. *Separ. Purif. Technol.* 292, 120996 <https://doi.org/10.1016/j.seppur.2022.120996>.

- Darryle, C.M., Acayanka, E., Takam, B., Line, L.N., Kamgang, G.Y., Laminsi, S., Sellaoui, L., Bonilla-Petriciolet, A., 2021. Influence of plasma-based surface functionalization of palm fibers on the adsorption of diclofenac from water: experiments, thermodynamics and removal mechanism. *J. Water Proc. Eng.* 43 <https://doi.org/10.1016/j.jwpe.2021.102254>.
- Dashairya, L., Sahu, A., Saha, P., 2019. Stearic acid treated polypyrrole-encapsulated melamine formaldehyde superhydrophobic sponge for oil recovery. *Adv. Compos. Hybrid Mater.* 2, 70–82. <https://doi.org/10.1007/s42114-019-00084-w>.
- De Gisi, S., Lofrano, G., Grassi, M., Notarnicola, M., 2016. Characteristics and adsorption capacities of low-cost sorbents for wastewater treatment: a review. *Sustain. Mater. Technol.* 9, 10–40. <https://doi.org/10.1016/j.susmat.2016.06.002>.
- De Oliveira, T., Guégan, R., Thiebault, T., Milbeau, C. Le, Muller, F., Teixeira, V., Giovanela, M., Boussafir, M., 2017. Adsorption of diclofenac onto organoclays: effects of surfactant and environmental (pH and temperature) conditions. *J. Hazard Mater.* 323, 558–566. <https://doi.org/10.1016/j.jhazmat.2016.05.001>.
- Derouich, G., Alami Younssi, S., Bennazha, J., Cody, J.A., Ouammou, M., El Rhazi, M., 2020. Development of low-cost polypyrrole/sintered pozzolan ultrafiltration membrane and its highly efficient performance for Congo red dye removal. *J. Environ. Chem. Eng.* 8, 103809. <https://doi.org/10.1016/j.jece.2020.103809>.
- Dey, S., Kar, A.K., 2019. Morphological and optical properties of polypyrrole nanoparticles synthesized by variation of monomer to oxidant ratio. *Mater. Today Proc.* 18, 1072–1076. <https://doi.org/10.1016/j.matpr.2019.06.566>.
- Dubin, M.M., Radushkevich, L.W., 1947. Equation of the characteristic curve of activated charcoal proceedings of the academy of sciences. *Phys. Chem. Sect. USSR* 55, 327.
- Fan, S., Wang, Z., Liang, P., Li, H., Zhang, Y., Fan, W., Xu, G., 2022. Fabrication of polypyrrole coated superhydrophobic surfaces for effective oil/water separation. *J. Mater. Res. Technol.* 19, 4337–4349. <https://doi.org/10.1016/j.jmrt.2022.06.170>.
- Freundlich, H.M., 1906. Over the adsorption in solution. *J. Phys. Chem.* 57,

1100–1107.

- Hamam, A., Maiza, M., Chehimi, M.M., Oukil, D., 2022. Properties of silver nanoparticle-polypyrrole composite film grown on cellulosic paper. *Cellulose* 29, 4579–4588. <https://doi.org/10.1007/s10570-022-04536-3>.
- Hiew, B.Y.Z., Lee, L.Y., Lee, X.J., Gan, S., Thangalazhy-Gopakumar, S., Lim, S.S., Pan, G. T., Yang, T.C.K., 2019. Adsorptive removal of diclofenac by graphene oxide: optimization, equilibrium, kinetic and thermodynamic studies. *J. Taiwan Inst. Chem. Eng.* 98, 150–162. <https://doi.org/10.1016/j.jtice.2018.07.034>.
- Hu, D., Huang, H., Jiang, R., Wang, N., Xu, H., Wang, Y.G., Ouyang, X. kun, 2019. Adsorption of diclofenac sodium on bilayer amino-functionalized cellulose nanocrystals/chitosan composite. *J. Hazard Mater.* 369 <https://doi.org/10.1016/j.jhazmat.2019.02.057>.
- Huang, L., Mao, N., Yan, Q., Zhang, D., Shuai, Q., 2020. Magnetic covalent organic frameworks for the removal of diclofenac sodium from water. *ACS Appl. Nano Mater.* 3, 319–326. <https://doi.org/10.1021/acsanm.9b01969>.
- Huang, L., Shen, R., Shuai, Q., 2021. Adsorptive removal of pharmaceuticals from water using metal-organic frameworks: a review. *J. Environ. Manag.* 277, 111389 <https://doi.org/10.1016/j.jenvman.2020.111389>.
- Ighalo, J.O., Adeniyi, A.G., Eletta, O.A.A., Ojetimi, N.I., Ajala, O.J., 2020. Evaluation of *Luffa cylindrica* fibres in a biomass packed bed for the treatment of fish pond effluent before environmental release. *Sustain. Water Resour. Manag.* 6, 1–11. <https://doi.org/10.1007/s40899-020-00485-6>.
- Jang, J., Shahzad, A., Woo, S.H., Lee, D.S., 2020. Magnetic $\text{Ti}_3\text{C}_2\text{Tx}$ (Mxene) for diclofenac degradation via the ultraviolet/chlorine advanced oxidation process. *Environ. Res.* 182, 108990 <https://doi.org/10.1016/j.envres.2019.108990>.
- Kesraoui, A., Bouzaabia, S., Seffen, M., 2019. The combination of *Luffa* cylindrical fibers and metal oxides offers a highly performing hybrid fiber material in water decontamination. *Environ. Sci. Pollut. Res.* 26, 11524–11534. <https://doi.org/10.1007/s11356-018-1507-3>.
- Khadir, A., Negarestani, M., Mollahosseini, A., 2020. Sequestration of a non-steroidal anti-inflammatory drug from aquatic media by lignocellulosic material (*Luffa cylindrica*) reinforced with polypyrrole: study of parameters,

- kinetics, and equilibrium. *J. Environ. Chem. Eng.* 8, 103734
<https://doi.org/10.1016/j.jece.2020.103734>.
- Khadir, A., Motamedi, M., Pakzad, E., Sillanpää, M., Mahajan, S., 2021. The prospective utilization of Luffa fibres as a lignocellulosic bio-material for environmental remediation of aqueous media: a review. *J. Environ. Chem. Eng.* 9 <https://doi.org/10.1016/j.jece.2020.104691>.
- Krishnudu, D.M., Sreeramulu, D., Reddy, P.V., 2019. Synthesis and characterization of coir and luffa cylindrica filled with CaCO_3 hybrid composites. *Int. J. Integr. Eng.* 11, 290–298.
<https://doi.org/10.30880/ijie.2019.11.01.029>.
- Langmuir, I., 1917. The constitution and fundamental properties of solids and liquids. II. Liquids. *J. Am. Chem. Soc.* 39, 1848–1906.
<https://doi.org/10.1021/ja02254a006>.
- Larous, S., Meniai, A.H., 2016. Adsorption of Diclofenac from aqueous solution using activated carbon prepared from olive stones. *Int. J. Hydrogen Energy* 41, 10380–10390. <https://doi.org/10.1016/j.ijhydene.2016.01.096>.
- Li, S., Gan, Y., Shah, S.J., Wang, R., Gong, W., Wei, R., Ji, H., Zhao, Zhongxing, Zhao, Zhenxia, 2021. Engineering NSAIDs imprinted UiO-66s for markedly enhanced adsorption of coexisting diclofenac sodium and Cu(II) and their synergistic adsorption mechanism. *Chem. Eng. J.* 426, 131440
<https://doi.org/10.1016/j.cej.2021.131440>.
- Liu, H., Su, S., Xie, J., Ma, Y., Tao, C., 2020. Preparation of superhydrophobic magnetic stearic acid polyurethane sponge for oil-water separation. *J. Mater. Res.* 35, 2925–2935. <https://doi.org/10.1557/jmr.2020.260>.
- Lu, J., Lang, J., Lan, P., Yang, H., Yang, J., Wu, X., Zhang, H., 2020. Evaluation of surface activity of hydrophobic modified nanocrystalline cellulose. *Cellulose* 27, 9299–9309. <https://doi.org/10.1007/s10570-020-03415-z>.
- Lu, J., Liu, X., Zhang, T.C., He, H., Yuan, S., 2021. Magnetic superhydrophobic polyurethane sponge modified with bioinspired stearic acid@ Fe_3O_4 @PDA nanocomposites for oil/water separation. *Colloids Surfaces A Physicochem. Eng. Asp.* 624, 126794 <https://doi.org/10.1016/j.colsurfa.2021.126794>.
- Lv, Y., Liang, Z., Li, Y., Chen, Y., Liu, K., Yang, G., Liu, Y., Lin, C., Ye, X., Shi, Y., Liu, M., 2021. Efficient adsorption of diclofenac sodium in water by a novel functionalized cellulose aerogel. *Environ. Res.* 194, 110652

- <https://doi.org/10.1016/j.envres.2020.110652>.
- Maged, A., Dissanayake, P.D., Yang, X., Pathirannahalage, C., Bhatnagar, A., Ok, Y.S., 2021. New mechanistic insight into rapid adsorption of pharmaceuticals from water utilizing activated biochar. *Environ. Res.* 202 <https://doi.org/10.1016/j.envres.2021.111693>.
- Martinez-Pavetti, M.B., Medina, L., Espínola, M., Monteiro, M., 2021. Study on two eco-friendly surface treatments on *Luffa cylindrica* for development of reinforcement and processing materials. *J. Mater. Res. Technol.* 14, 2420–2427. <https://doi.org/10.1016/j.jmrt.2021.07.141>.
- Meroni, D., Jiménez-Salcedo, M., Falletta, E., Bresolin, B.M., Kait, C.F., Boffito, D.C., Bianchi, C.L., Pirola, C., 2020. Sonophotocatalytic degradation of sodium diclofenac using low power ultrasound and micro sized TiO₂. *Ultrason. Sonochem.* 67, 105123 <https://doi.org/10.1016/j.ultsonch.2020.105123>.
- Mohd Tarmizi, E.Z., Baqiah, H., Talib, Z.A., Kamari, H.M., 2018. Preparation and physical properties of polypyrrole/zeolite composites. *Results Phys.* 11, 793–800. <https://doi.org/10.1016/j.rinp.2018.09.043>.
- Pap, S., Taggart, M.A., Shearer, L., Li, Y., Radovic, S., Turk Sekulic, M., 2021. Removal behaviour of NSAIDs from wastewater using a P-functionalised microporous carbon. *Chemosphere* 264, 128439. <https://doi.org/10.1016/j.chemosphere.2020.128439>.
- Parit, M., Du, H., Zhang, X., Prather, C., Adams, M., Jiang, Z., 2020. Polypyrrole and cellulose nanofiber based composite films with improved physical and electrical properties for electromagnetic shielding applications. *Carbohydr. Polym.* 240, 116304 <https://doi.org/10.1016/j.carbpol.2020.116304>.
- Park, N.M., Choi, S., Oh, J.E., Hwang, D.Y., 2019. Facile extraction of cellulose nanocrystals. *Carbohydr. Polym.* 223, 115114 <https://doi.org/10.1016/j.carbpol.2019.115114>.
- Patti, A., Lecocq, H., Serghei, A., Acierno, D., Cassagnau, P., 2021. The universal usefulness of stearic acid as surface modifier: applications to the polymer formulations and composite processing. *J. Ind. Eng. Chem.* 96, 1–33. <https://doi.org/10.1016/j.jiec.2021.01.024>.
- Pedrosa, M., Ribeiro, R.S., Guerra-Rodríguez, S., Rodríguez-Chueca, J., Rodríguez, E., Silva, A.M.T., Đolic, M., Rita Lado Ribeiro, A., 2022. Spirulina-

- based carbon bio-sorbent for the efficient removal of metoprolol, diclofenac and other micropollutants from wastewater. *Environ. Nanotechnol. Monit. Manag.* 18 [https://doi.org/ 10.1016/j.enmm.2022.100720](https://doi.org/10.1016/j.enmm.2022.100720).
- Pires, B.C., Dutra, F.V.A., Nascimento, T.A., Borges, K.B., 2017. Preparation of PPy/ cellulose fibre as an effective potassium diclofenac adsorbent. *React. Funct. Polym.* 113, 40–49. <https://doi.org/10.1016/j.reactfunctpolym.2017.02.002>.
- Pirsa, S., Asadzadeh, F., 2021. Synthesis of Fe₃O₄/SiO₂/Polypyrrole magnetic nanocomposite polymer powder: investigation of structural properties and ability to purify of edible sea salts. *Adv. Powder Technol.* 32, 1233–1246. [https://doi.org/ 10.1016/j.appt.2021.02.027](https://doi.org/10.1016/j.appt.2021.02.027).
- Premalatha, N., Saravanakumar, S.S., Sanjay, M.R., Siengchin, S., Khan, A., 2021. Structural and thermal properties of chemically modified *Luffa cylindrica* fibers. *J. Nat. Fibers* 18, 1038–1044. <https://doi.org/10.1080/15440478.2019.1678546>.
- Puga, A., Pazos, M., Rosales, E., Sanromán, M.A., 2021. Electro-reversible adsorption as a versatile tool for the removal of diclofenac from wastewater. *Chemosphere* 280. <https://doi.org/10.1016/j.chemosphere.2021.130778>.
- Rashid, J., Saleemi, F., Akram, B., Wang, L., Hussain, N., Xu, M., 2021. Facile synthesis of g-C₃N₄/MOO₃ nanohybrid for efficient removal of aqueous diclofenac sodium. *Nanomaterials* 11. <https://doi.org/10.3390/nano11061564>.
- Rehman, F., Ahmad, W., Sayed, M., 2021. Mechanistic investigations on the removal of diclofenac sodium by UV/S₂O₈²⁻/Fe²⁺, UV/H₂SO₅/Fe²⁺ and UV/H₂O₂/Fe²⁺-based advanced oxidation processes. *Environ. Technol.* 42, 3995–4005. [https://doi.org/ 10.1080/09593330.2020.1770869](https://doi.org/10.1080/09593330.2020.1770869).
- Rigueto, C.V.T., Rosseto, M., Nazari, M.T., Ostwald, B.E.P., Alessandretti, I., Manera, C., Piccin, J.S., Dettmer, A., 2021. Adsorption of diclofenac sodium by composite beads prepared from tannery wastes-derived gelatin and carbon nanotubes. *J. Environ. Chem. Eng.* 9, 105030. <https://doi.org/10.1016/j.jece.2021.105030>.
- Salman, J.M., Njoku, V.O., Hameed, B.H., 2011. Batch and fixed-bed adsorption of 2,4- dichlorophenoxyacetic acid onto oil palm frond activated carbon. *Chem. Eng. J.* 174 <https://doi.org/10.1016/j.cej.2011.08.024>.

- Shamsudin, M.S., Azha, S.F., Ismail, S., 2022a. A review of diclofenac occurrences, toxicology, and potential adsorption of clay-based materials with surfactant modifier. *J. Environ. Chem. Eng.* 10, 107541 <https://doi.org/10.1016/j.jece.2022.107541>.
- Shamsudin, M.S., Azha, S.F., Sellaoui, L., Badawi, M., Bonilla-Petriciolet, A., Ismail, S., 2022b. Performance and interactions of diclofenac adsorption using Alginate/ Carbon-based Films: experimental investigation and statistical physics modelling. *Chem. Eng. J.* 428, 131929 <https://doi.org/10.1016/j.cej.2021.131929>.
- Shearer, L., Pap, S., Gibb, S.W., 2022. Removal of pharmaceuticals from wastewater: a review of adsorptive approaches, modelling and mechanisms for metformin and macrolides. *J. Environ. Chem. Eng.* 10, 108106 <https://doi.org/10.1016/j.jece.2022.108106>.
- Stejskal, J., Sapurina, I., Vilčáková, J., Jurca, M., Trchová, M., Kolská, Z., Prokes, J., Krivka, I., 2021. One-pot preparation of conducting melamine/polypyrrole/magnetite ferrosponge. *ACS Appl. Polym. Mater.* 3, 1107–1115. <https://doi.org/10.1021/acsapm.0c01331>.
- Suriyanon, N., Punyapalakul, P., Ngamcharussrivichai, C., 2013. Mechanistic study of diclofenac and carbamazepine adsorption on functionalized silica-based porous materials. *Chem. Eng. J.* 214, 208–218. <https://doi.org/10.1016/j.cej.2012.10.052>.
- Temkin, M.J., Pyzhev, V., 1940. Recent modifications to Langmuir isotherms. *Acta Physiochim Ussr* 12 12, 217.
- Tomul, F., Arslan, Y., Bas,oglu, F.T., Babu,çcuoglu, Y., Tran, H.N., 2019. Efficient removal of anti-inflammatory from solution by Fe-containing activated carbon: adsorption kinetics, isotherms, and thermodynamics. *J. Environ. Manag.* 238, 296–306. <https://doi.org/10.1016/j.jenvman.2019.02.088>.
- Tran, T.V., Thi, D., Nguyen, C., Le, H.T.N., Vo, D.N., Nanda, S., Nguyen, T.D., 2020. Optimization, equilibrium, adsorption behavior and role of surface functional groups on graphene oxide-based nanocomposite towards diclofenac drug. *J. Environ. Sci.* 93, 137–150. <https://doi.org/10.1016/j.jes.2020.02.007>.
- Tsumura, Y., Oyama, K., Fameau, A.L., Seike, M., Ohtaka, A., Hirai, T., Nakamura, Y., Fujii, S., 2022. Photo/Thermo dual stimulus-responsive liquid

- marbles stabilized with polypyrrole-coated stearic acid particles. *ACS Appl. Mater. Interfaces* 14, 41618–41628. <https://doi.org/10.1021/acsami.2c12681>.
- Velhal, N., Kulkarni, G., Patil, N.D., Puri, V., 2018. Structural, electrical and microwave properties of conducting polypyrrole thin films: effect of oxidant. *Mater. Res. Express* 5. <https://doi.org/10.1088/2053-1591/aadaf7>.
- Wang, T., Kailasam, K., Xiao, P., Chen, G., Chen, L., Wang, L., Li, J., Zhu, J., 2014. Adsorption removal of organic dyes on covalent triazine framework (CTF). *Microporous Mesoporous Mater.* 187, 63–70. <https://doi.org/10.1016/j.micromeso.2013.12.016>.
- Wang, J., Liu, G., Li, T., Zhou, C., 2015. Physicochemical studies toward the removal of Zn(ii) and Pb(ii) ions through adsorption on montmorillonite-supported zero-valent iron nanoparticles. *RSC Adv.* 5, 29859–29871. <https://doi.org/10.1039/c5ra02108a>.
- Weber, W.J., Morris, J.C., 1963. Kinetics of adsorption on carbon from solution. *J. Sanit. Eng. Div.* 89 <https://doi.org/10.1061/jsedai.0000430>.
- Wojnicki, M., Nabec, P., Luty, M., Socha, R., Yang, X., Zbigniew, P., 2020. Batch reactor vs . flow column – mechanistic investigation and modeling of Au (III) ions adsorption from aqueous solutions containing Ni²⁺, Na⁺, Cl⁻ and ClO⁻4 as impurities. *Sustain. Mater. Technol.* 23, e00142 <https://doi.org/10.1016/j.susmat.2019.e00142>.
- Wu, L., Du, C., He, J., Yang, Z., Li, H., 2020. Effective adsorption of diclofenac sodium from neutral aqueous solution by low-cost lignite activated cokes. *J. Hazard Mater.* 384, 121284 <https://doi.org/10.1016/j.jhazmat.2019.121284>.
- Xianfeng, Y., Hehan, X., Qinglong, H., Zhe, Z., Xiewen, X., Li, Z., Zhipeng, X., 2019. Study of thermal degradation mechanism of binders for ceramic injection molding by TGA-FTIR. *Ceram. Int.* 45, 10707–10717. <https://doi.org/10.1016/j.ceramint.2019.02.142>.
- Yang, X., Al-Duri, B., 2005. Kinetic modeling of liquid-phase adsorption of reactive dyes on activated carbon. *J. Colloid Interface Sci.* 287, 25–34. <https://doi.org/10.1016/j.jcis.2005.01.093>.
- Yang, Y., Liu, Y., Zhao, X., 2022. Preparation and characterization of an electromagnetic composite polypyrrole/polyethylene short filament geotextile. *Textil. Res. J.* 92, 1333–1343. <https://doi.org/10.1177/00405175211053396>.

- Younes, H.A., Taha, M., Mahmoud, R., Mahmoud, H.M., Abdelhameed, R.M., 2022. High adsorption of sodium diclofenac on post-synthetic modified zirconium-based metal-organic frameworks: experimental and theoretical studies. *J. Colloid Interface Sci.* 607, 334–346. <https://doi.org/10.1016/j.jcis.2021.08.158>.
- Zeng, H., Wang, P., Liang, L., Hu, H., Peng, Y., Li, X., Liu, C., 2022. Facile preparation of superhydrophobic cotton fabric with a photothermal conversion effect via polypyrrole deposition for oil/water separation. *J. Environ. Chem. Eng.* 10, 106915 <https://doi.org/10.1016/j.jece.2021.106915>.
- Zhu, X., Tong, J., Lan, H., Pan, D., 2022. Fabrication of polyethyleneimine functionalized magnetic cellulose nanocrystals for the adsorption of diclofenac sodium from aqueous solutions. *Polymers* 14. <https://doi.org/10.3390/polym14040720>.

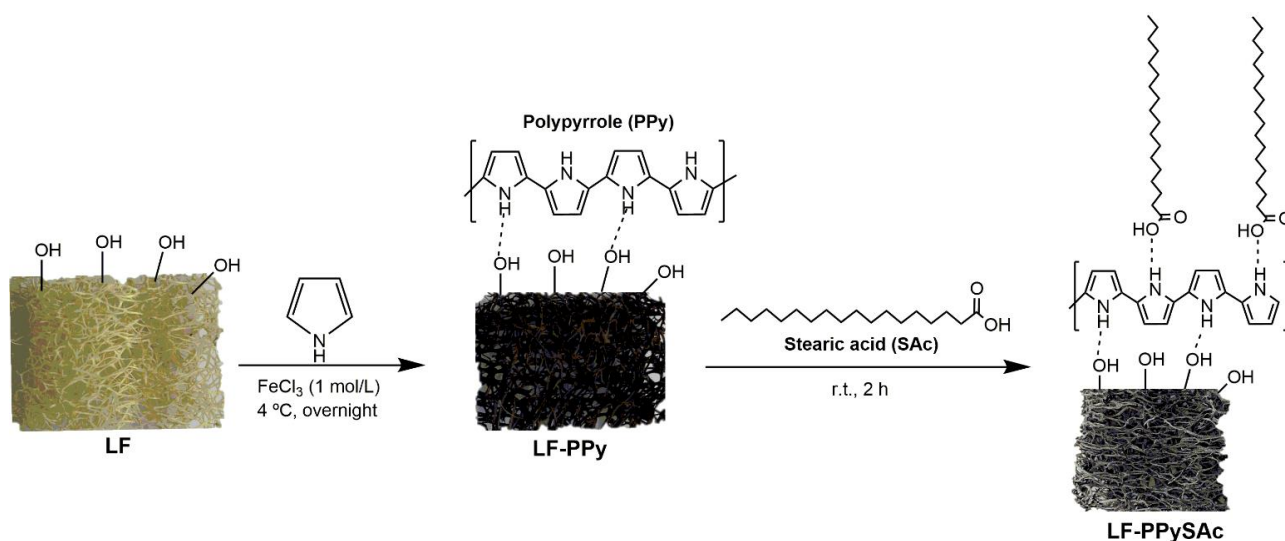
Supporting information for: Polypyrrole/stearic acid-coated Luffa cylindrica for enhanced removal of sodium diclofenac from water: Batch and continuous adsorption studies

1. Experimental

1.1. Materials

Luffa cylindrica (LF) was obtained from a plantation localized in Perola, Paraná, Brazil. Hydrochloric acid (HCl, 35%), and ethanol (EtOH, P.A.) were purchased from Synth (São Paulo, Brazil). Isopropyl alcohol and iron chloride (FeCl₃) were purchased from Êxodo Científica Química Fina (Brazil). Stearic acid (SAC, 98.5%) and pyrrole (98%) were purchased from Sigma-Aldrich (USA). Sodium diclofenac (DCF) (purity >99%) was purchased from Hebei Jiheng Company (China). All commercial chemicals of reagent grade were used as received.

1.2. Coating of LF with PPy and SAc



Scheme 1. Experimental steps to prepare LF-PPy and LF-PPySAc samples.

1.3. Characterization

Fourier-transform infrared spectroscopy (FTIR) analyses (Shimadzu IR-Affinity-1 spectrometer, Japan) were done in a wavenumber range of 4000–400 cm^{-1} with 80 scans per sample and a resolution of 4 cm^{-1} . Before the spectra acquisition, the LF samples were cut and held between two KBr pellets. Powder X-ray diffraction (XRD) analyses were performed in a diffractometer (Siemens D500, Germany) equipped with a Cu-K α source ($\lambda = 0.15418 \text{ nm}$). The XRD patterns were recorded at a 2θ angle varying from 10° to 50° (step of 1 °/min) using a voltage generator of 40 kV and an electric current of 1.75 mA. Thermogravimetry analyses (TGA) were performed in a Shimadzu DTG60 analyzer. (Japan). For this, the samples were heated at 10 °C/min under an $\text{N}_2(\text{g})$ flow rate of 20 mL/min. Before the XRD and TGA analysis, the samples were ground using a pestle and liquid nitrogen. Scanning electron microscopy (SEM) characterization was done in a JEOL JSM-6610LV microscope (USA). Before SEM visualization, the sponge samples were washed with distilled water, dried in an oven (50 °C for 24 h), and sputter-coated with gold. The sponge fibers were only sputter-coated with gold before SEM visualization. The point of zero charge (pH_{PZC}) values for the prepared beads were examined in 0.1 mol/L NaCl solutions at r.t.. For this, samples (30 mg) were put in vials filled with NaCl solution (30 mL), and, then, the initial pH value was adjusted (2–10) with 0.1 mol/L HCl or 0.1 mol/L NaOH solutions using a Hannah Instruments (model HI2211, USA)

pHmeter. All vials were stirred using an orbital shaker (100 rpm) for 24 h. Later, the final pH of each system was measured carefully. The differences between the final and the initial pH values (ΔpH) were then plotted against the initial pH values. The pH_{PZC} values were estimated from the points where the initial pH at which ΔpH is zero (Larous and Meniai, 2016). Finally, the compression resistance property was determined using cubic samples (1 cm^3) compressed by a load of 200 g.

1.4. Water contact angle measurements

The water contact angle (WCA) formed on the sponge surface was measured using an optical tensiometer (Theta Lite TL101, Biolin Scientific Inc., Finland) through the sessile drop method. Standardized drops of distilled water ($5\text{ }\mu\text{L}$) were dispensed directly onto the surface of the samples. Immediately after dispensing the drop, real-time dynamic reading of the right and left contact angles formed with the material surface was performed using the One Attension software (Biolin Scientific Inc.) used at 20 frames per second for 20 s. The WCA ($^\circ$) was recorded as the average between the right and left readings taken for 4 samples of each sponge ($n = 4$).

1.5. Total porosity

The total porosity of the LF samples was determined using a liquid displacement method (Anisha et al., 2013). Dimensions of each sample were measured using a digital vernier caliper (Lee Tools, Brazil) and, then, their volume (V) was calculated. Absolute ethanol was used as the displacing liquid. A sample of measured weight (W_i) was immersed in a vial containing 20 mL of ethanol and soaked for 24 h to allow the liquid to penetrate the pores of the sample. The final weight of the wet sponge was noted as W_f . The total porosity (%) can be calculated using Equation (S1) (Anisha et al., 2013), where ρ_{ethanol} is the ethanol density at $25\text{ }^\circ\text{C}$ (0.789 g/cm^3).

$$\%Porosity = \frac{(W_f - W_i)}{\rho_{\text{ethanol}} \times V_{\text{sample}}} \times 100 \quad (\text{S1})$$

1.5. Thermodynamics analysis

Batch adsorption experiments were done at 293, 298, 308, 318, and 323 K to investigate the thermodynamics of the adsorption of DCF on the LF samples. The other experimental conditions were set to 40 mg of adsorbent; DCF solution at 50 mg/L; 20 mL of volume; and pH 7.0, respectively. The study on the effect of temperature on adsorption will extend the knowledge of thermodynamic parameters, such as standard Gibbs free energy of adsorption (ΔG°), the heat of the adsorption (ΔH°), and standard entropy changes (ΔS°) (Avcu et al., 2021). Thermodynamic equations used for these calculations are given in Equations (S2), (S3), and (S4):

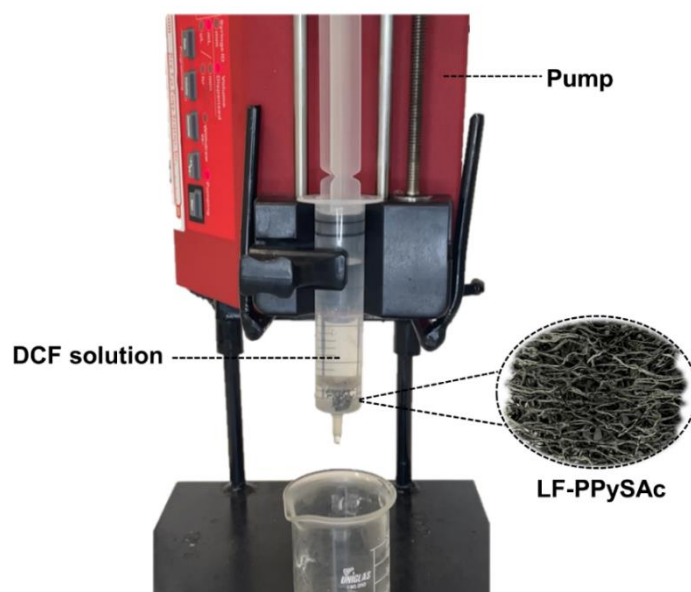
$$K = \frac{q_e}{C_e} \quad (\text{S2})$$

$$\ln K = \frac{\Delta S^\circ}{R} - \frac{\Delta H^\circ}{RT} \quad (\text{S3})$$

$$\Delta G^\circ = -RT \ln K \quad (\text{S4})$$

where K is the equilibrium constant, q_e is the amount of DCF adsorbed per gram of LF sample at equilibrium, C_e is the equilibrium concentration of DCF in the solution, R is the universal gas constant (8.314 J/mol K) and T is the absolute temperature. ΔH° and ΔS° can be determined from the slope and intercept of the plot between $\ln (q_e/C_e)$ versus $1/T$ (not shown). ΔG° can be calculated from Equation (S4).

1.6. Continuous adsorption experiments



Scheme 2. Adapted setup for continuous adsorption experiments.

1.7. Adsorption experiment in tap water

To mimic real adsorption conditions, batch experiments were done using tap water. Thus, 40 mg of the adsorbent was put in contact with a DCF solution (C_0 50 mg/L, 20 mL) prepared in tap water (pH 8.6 and conductivity 54 mV at 25 °C). The vial containing the adsorbent and solution was left on stirring at r.t. for 60 min. After that, the adsorption capacity (q_e) was calculated using Equation (1). These tests were performed in triplicate.

2. Results and Discussion

2.1. Characterization of sponges

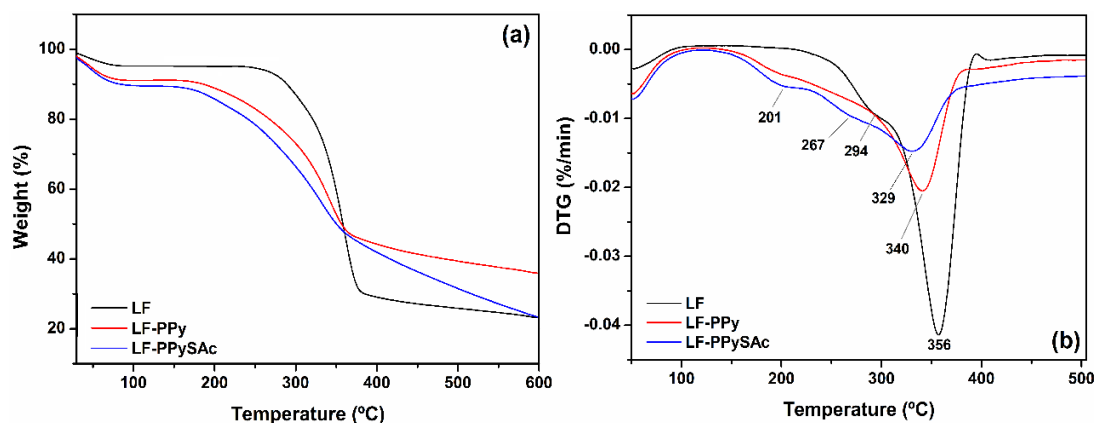


Figure 3-2.S1: (a) TGA and (b) DTG curves of LF, LF-PPy, and LF-PPySAc.

2.2. Total porosity

The total porosity of the LF samples was evaluated by the liquid displacement method as afore detailed. The total porosity of LF, LF-PPy, and LF-PPySAC was determined to be $0.09 \pm 0.01\%$, $0.03 \pm 0.01\%$, and $0.16 \pm 0.02\%$. These low values can be justified since the fibers of LF have ultra-micropores (Khadir et al., 2021). After coating with PPy, total porosity decrease because the polymerization process fills the pores previously available on the fibers with PPy. Conversely, after the second coating process, the total porosity increases compared to LF-PPy as a result of the increase in roughness caused by the SAC molecules deposition. As verified in the SEM images, after SAC-coating the surface of the fibers is rougher and irregular, which corroborates the porosity data.

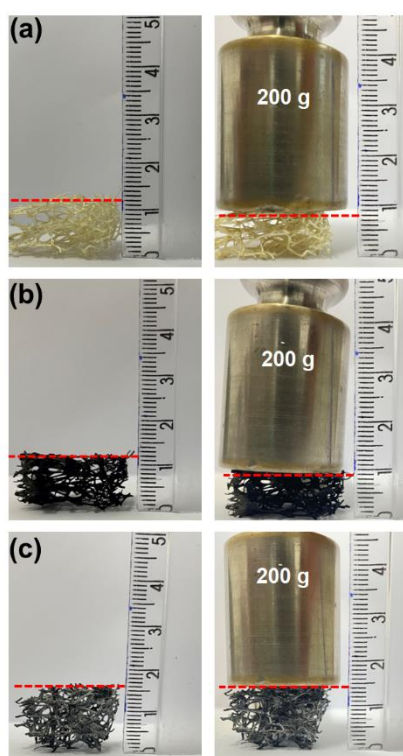


Figure 3-2.S2: Compression of the (a) LF, (b) LF-PPy, and (c) LF-PPySAC samples with a load.

2.3. Batch adsorption – Effect of adsorbent dosage

Investigating the effect of dosage adsorbent is crucial since this parameter has a critical role in the cost-effectiveness of the adsorption process (França et al., 2020). Herein, preliminary adsorption experiments were performed ranging

the adsorbents dosage from 40 to 60 mg. Overall, for all tested samples, q_e values decreased as the dose of LF (12.01 to 0.13 mg/g), LF-PPy (14.19 to 0.99 mg/g), and LF-PPySAc (15.92 to 3.21 mg/g) increased from 40 to 60 mg (Figure S3). Malhotra et al. (2018) cite two main reasons for this behavior; the first is because when the adsorbent dosage increases, the number of binding sites that remain unsaturated during adsorption increases too. Secondly, high adsorbent dosage may cause agglomeration, reducing the surface area available for adsorption (Malhotra et al., 2018). Additionally, the correlation between the adsorbent dosage and adsorption capacity revealed that the coated-LF samples (LF-PPy and LF-PPySAc) have enhanced performance for the removal of DCF from the aqueous media. Indeed, the adsorption capacity of LF-PPySAc was around 32.5% higher than the raw LF when 40 mg of these materials were tested. Based on these results, further adsorption experiments were done using the lowest dosage of LF, LF-PPy, or LF-PPySAc (i.e., 40 mg).

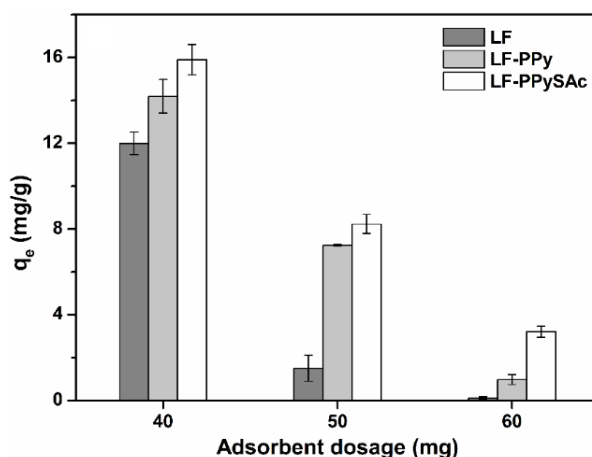


Figure 3-2.S3: Effect of adsorbent dosage on the DCF adsorption capacity (Other experimental conditions: Solution volume 20 mL, C_0 50 mg/L, pH ~5.5, r.t., stirring 100 rpm, contact time 60 min).

2.4. Batch adsorption – Effect of pH

The initial pH of the adsorbate solution is another parameter that affects the entire adsorption process because it influences the surface charge of the adsorbent, but also the ionization of the adsorbate (leamviteevanich et al., 2022). To verify this, the pH of the DCF solution was adjusted using HCl (0.1 mol/L) or NaOH (0.1 mol/L) before the adsorption experiments. As seen in Figure S4a, the

increase of solution pH from 4 to 7 caused a low effect on the adsorption capacity of the coated samples, while the raw LF was drastically affected. When the pH is moved to alkaline conditions (pH 10), the adsorption capacity of all LF samples decreases considerably. To aid in explaining these results, the pH_{PZC} values for each LF sample were determined (Figure S4b). pH_{PZC} defines the pH condition at which the components of surface charge on the solid (adsorbent) are equal to zero ($[H^+] = [OH^-]$). At pH conditions below these values ($pH < pH_{PZC}$), the surface of the LF samples is positively charged ($[H^+] > [OH^-]$), while pH conditions above pH_{PZC} denote surfaces negatively charged ($[H^+] < [OH^-]$). For LF, LF-PPy, and LF-PPySAC the pH_{PZC} values were determined to be 4.19, 3.40, and 3.54, respectively. The decrease in the pH_{PZC} values for LF-PPy and LF-PPySAC is attributable to the reduction of oxygen-containing groups on the surface of the fibers. At pH 4, only raw LF can show a positively charged surface, which may explain its high adsorption capacity since in this condition, the DCF molecules are partially ionized ($pK_a \sim 4$) (Bi et al., 2021). Under $pH > 7$, both adsorbent and adsorbate are negatively charged and the repulsive forces between them explain the impairment of the adsorption process. However, close to neutral conditions (pH 7), it is still observed a considerable adsorption performance for LF-PPy and LF-PPySAC. This result suggests that other interaction forces instead of the electrostatics are involved in the adsorption mechanism (H-bonding, π - π interaction, or hydrophobic forces) (Shamsudin et al., 2022). Furthermore, LF-PPySAC showed the lowest sensibility to the pH changes, which may suggest that this adsorbent has the highest interaction capacity towards DCF molecules. Based on these finds, further adsorption experiments were done at pH ~ 5.5 , which is the pH of the DCF solution prepared in distilled water.

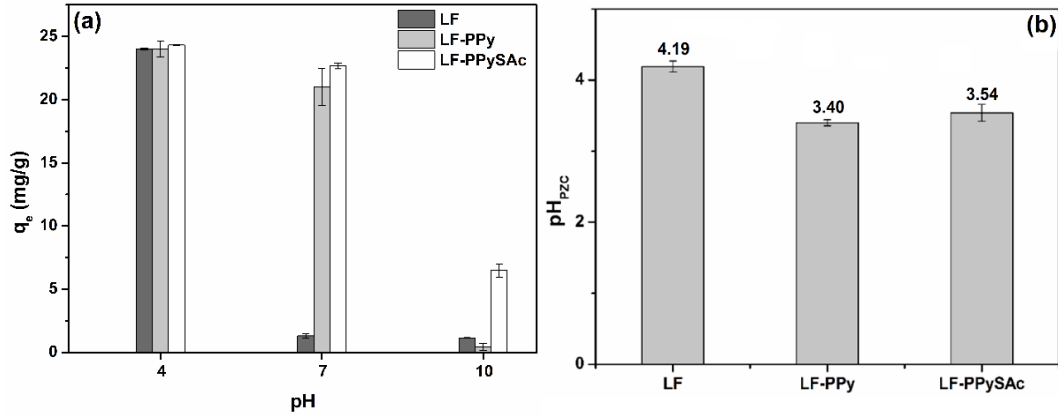


Figure 3-2.S4: (a) Effect of initial pH on the DCF adsorption capacity (Other experimental conditions: C_0 50 mg/L, adsorbent dosage 40 mg, volume 20 mL, r.t., stirring 100 rpm, contact time 60 min). (b) pH_{PZC} values determined for LF, LF-PPy, and LF-PPySAc.

2.5. Kinetic models

The non-linear forms of the PFO and PSO are expressed by Equations (S5) and (S6) as follows:

$$q_t = q_{e(cal)} (1 - e^{-k_1 t}) \quad (S5)$$

$$q_t = \frac{q_{e(cal)}^2 k_2 t}{1 + q_{e(cal)} k_2 t} \quad (S6)$$

where $q_{e(cal)}$ (mg/g) is the theoretical value of the amount of DCF adsorbed per gram of adsorbate at equilibrium, k_1 (1/min) and k_2 (g/mg min) are the rate constants for the PFO and PSO models (Lagergren, 1898; Ho e McKay, 1999)..

$$\chi^2 = \sum \frac{(q_e - q_{e(calc)})^2}{q_{e(calc)}} \quad (S7)$$

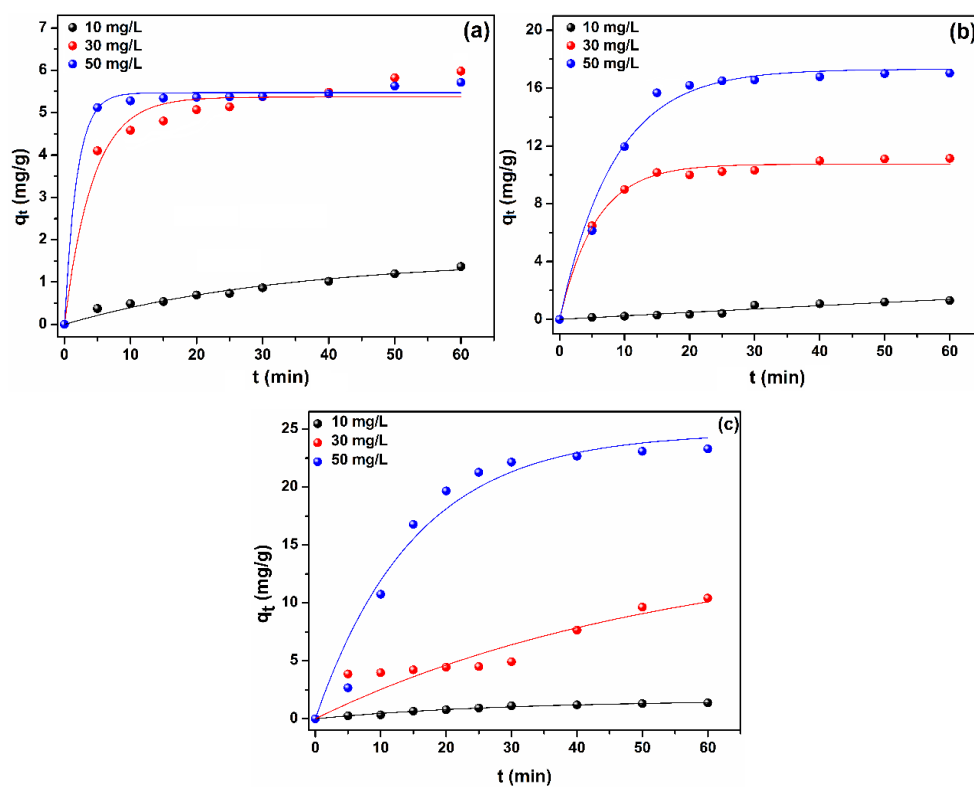


Figure 3-2.S5: PFO plots for the adsorption of DCF onto (a) LF, (b) LF-PPy, and (c) LF-PPySAc samples (Experimental conditions: C₀ = 10–50 mg/L, adsorbent dosage 40 mg, pH ~5.5, r.t., stirring 100 rpm, contact time 60 min).

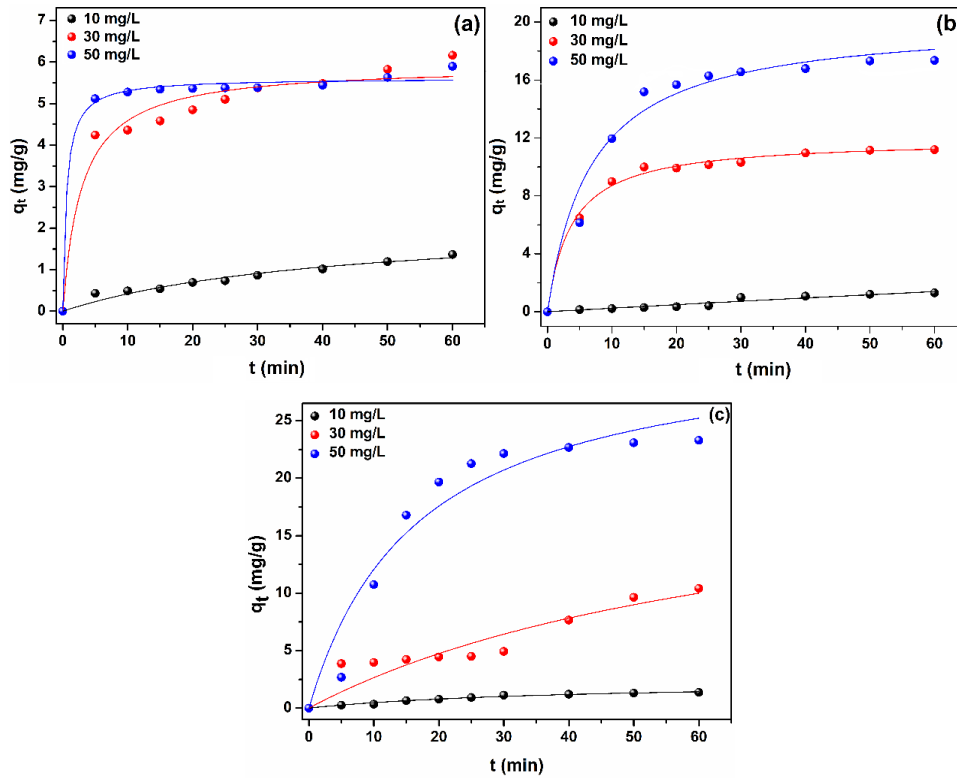


Figure 3-2.S6: PSO plots for the adsorption of DCF on (a) LF, (b) LF-PPy, and (c) LF-PPySAc samples (Experimental conditions: $C_0 = 10\text{--}50$ mg/L, adsorbent dosage 40 mg, pH ~ 5.5 , r.t., stirring 100 rpm, contact time 60 min).

2.6. Intraparticle diffusion model

$$q_t = K_{diff} t^{1/2} + C \quad (\text{S8})$$

In Equation (S8), the parameter K_{diff} ($\text{mg/g min}^{1/2}$) refers to the intraparticle diffusion rate and can be calculated from the slope of the linear segments (Regions 1 to 3) of the plot of q_t versus $t^{1/2}$ (Figure S8). C is a constant related to the thickness of the boundary layer and is determined by the intercept of the plot (Pires et al., 2017). Overall, a high K_{diff} value indicates a fast adsorption process, and the lower the C value, the lower the effect of transport resistance on the adsorbent (Pires et al., 2017).

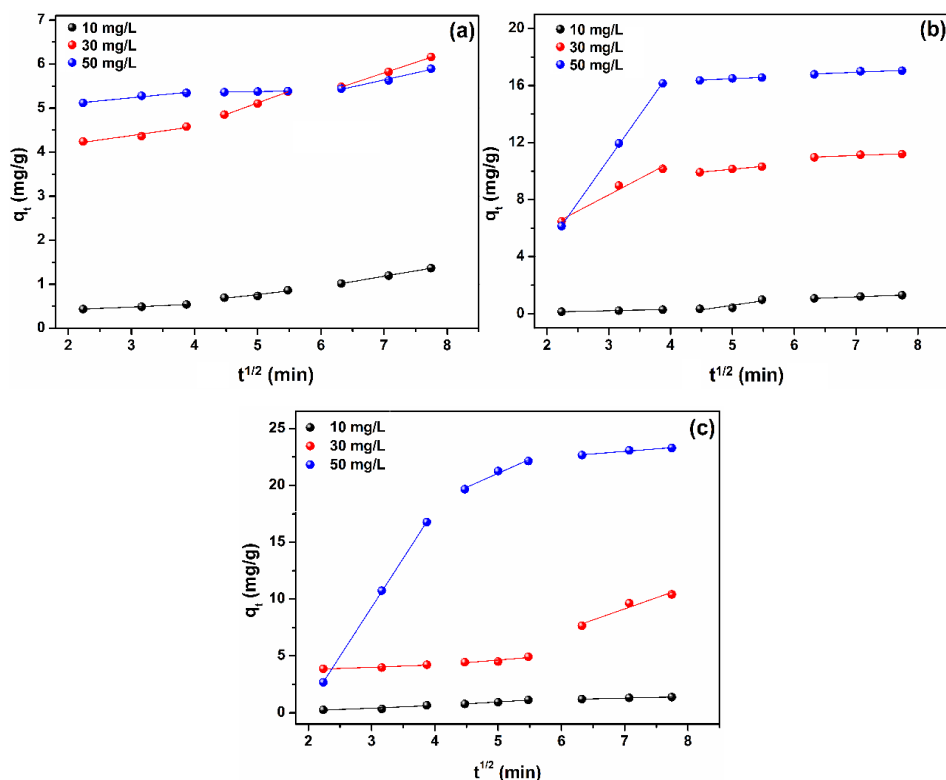


Figure 3-2.S7: Intraparticle diffusion plots for the adsorption of DCF on (a) LF, (b) LF-PPy, and (c) LF-PPySAC samples (Experimental conditions: $C_0 = 10\text{--}50$ mg/L, adsorbent dosage 40 mg, pH ~ 5.5 , r.t., stirring 100 rpm, contact time 60 min).

Table 3-2.S1: Intraparticle diffusion parameters calculated for DCF adsorption on LF, LF-PPy, and LF-PPySAC.

Sample	C_0	Region	K_{diff}	C	R^2
LF	10	1	0.064	0.289	0.998
		2	0.167	-0.072	0.798
		3	0.245	-0.533	0.999
	30	1	0.204	3.765	0.887
		2	0.523	2.502	0.993
		3	0.478	2.450	0.998
	50	1	0.140	4.813	0.944
		2	0.024	5.253	0.948
		3	0.381	3.414	0.965
LF-PPy	10	1	0.093	-0.069	0.995
		2	0.636	-2.584	0.621
		3	0.159	0.066	0.994
	30	1	2.275	1.514	0.966
		2	0.396	8.154	0.980
		3	0.161	9.968	0.836

LF-PPySAc	50	1	6.121	-7.502	0.999
		2	0.202	15.462	0.905
		3	0.178	15.675	0.730
	10	1	0.234	-0.302	0.689
		2	0.337	-0.738	0.961
		3	0.125	0.404	0.988
	30	1	0.207	3.377	0.796
		2	0.461	2.328	0.608
		3	1.950	-4.516	0.907
	50	1	8.619	-16.575	0.999
		2	2.477	8.680	0.961
		3	0.440	19.907	0.960

Units: C_0 (mg/g); K_{diff} (mg/g min^{1/2}); C (mg/g).

2.7. Isotherm models

$$q_e = \frac{q_m K_L C_e}{1 + K_L C_e} \quad (S9)$$

$$q_e = K_F \cdot C_e^{1/n} \quad (S10)$$

$$q_e = \frac{RT}{b_T} \ln(K_T C_e) \quad (S11)$$

$$q_e = q_{mDR} e^{-K_{DR} \varepsilon^2} \quad (S12)$$

$$\varepsilon = RT \ln \left(1 + \frac{1}{C_e} \right) \quad (S13) \quad E = (2K_{DR})^{-1/2} \quad (S14)$$

The parameters q_m and q_{mDR} (mg/g) are the theoretical maximum adsorption capacity of each adsorbent accordingly to the Langmuir and D-R isotherm models, while the parameters K_L , K_F , K_T , and K_{DR} are the constants of Langmuir, Freundlich, Temkin, and D-R isotherms. The parameter $1/n$ is the heterogeneity factor in the Freundlich isotherm, and b_T refers to the adsorption heat in the Temkin isotherm. In the D-R isotherm, the parameter ε is the adsorption potential (calculated by Equation S13), R is the universal gas constant (8.314 J/K mol), and T is the absolute temperature. The K_{DR} constant is related

to the adsorption energy and can be employed to calculate the mean free energy (E) involved in the adsorption process (calculated by Equation S14).

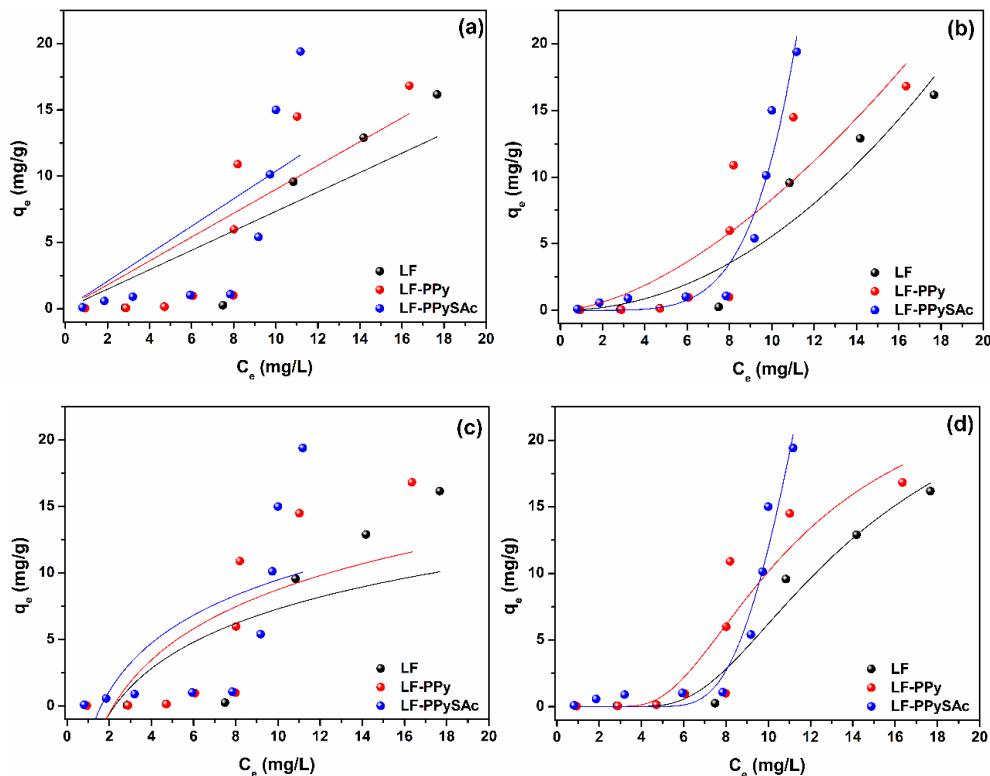


Figure 3-2.S8: (a) Langmuir, (b) Freundlich, (c) Temkin, and (d) D-R isotherm plots for the adsorption of DCF on LF, LF-PPy and LF-PPySAC at 25 °C (Experimental conditions: $C_0 = 1\text{--}50$ mg/L, adsorbent dosage 40 mg, pH ~ 5.5 , r.t., stirring 100 rpm, contact time 60 min).

2.8. Thermodynamic study

Thermodynamic parameters including standard Gibbs free energy variation (ΔG°), enthalpy variation (ΔH°), and entropy (ΔS°) for the DCF adsorption on LF samples were computed and summarized in Table S2. The adsorption of DCF on raw LF showed quite different thermodynamics than that observed for LF-PPy and LF-PPySAC. From the data in Table S2, it can be seen that the values of ΔG° for LF were positive, which indicates that the adsorption of DCF on this sample does not occur spontaneously. These finds corroborate the experimental data, which showed that raw LF has a low adsorption capacity under the experimental conditions utilized (Lonappan et al., 2018). On the other hand, after coating the fibers, the adsorption process occurs spontaneously,

considering that the ΔG° value was negative at all tested temperatures. Also, with the results obtained from ΔG° , it is observed that the process is more spontaneous at low temperatures, considering that there is an increase in ΔG° as the temperature increases. Taking into account that in a physical adsorption process the ΔG° value must be within the range of -20 to 0 kJ/mol, it can be said that the DCF molecules were physically adsorbed on LF-PPy and LF-PPySAC since the variation of their ΔG° was from -3.55 to -1.27 kJ/mol, and from -3.90 to -1.41 kJ/mol, respectively (Hiew et al., 2019a). The negative ΔH° value indicates the adsorption of DCF in the LF samples was exothermic and based on the ΔH° value < 40 kJ/mol, the adsorption of DCF occurs preferentially by physisorption (Hiew et al., 2019b). The negative ΔS° value may be associated with a decrease in randomness at the solid-solution interface during the adsorption of DCF on LF samples (Avcu et al., 2021).

Table 3-2.S2: Thermodynamic parameters for DCF adsorption on LF samples at various temperatures.

Sample	Temperature (K)	ΔG° (kJ/mol)	ΔH° (kJ/mol)	ΔS° (kJ/K mol)
LF	293	8.00	-39.08	-0.16
	298	8.96		
	308	9.72		
	318	12.15		
	323	12.87		
LF-PPy	293	-3.55	-22.23	-0.07
	298	-2.12		
	308	-2.14		
	318	-1.34		
	323	-1.28		
LF-PPySAC	293	-3.91	-22.85	-0.06
	298	-1.95		
	308	-1.5		
	318	-1.43		
	323	-1.42		

2.9. Continuous adsorption

2.9.1. Effect of adsorbent dosage and flow rate

The height of the adsorbent put into the column is one parameter that influences the efficiency of the continuous adsorption process. Herein, the effect of this parameter was not examined because a syringe was used as the adsorption column. So, the height of the LF sample changed as the plunger was pressed down, resulting in erroneous data. Therefore, we decided to investigate the effect of the adsorbent dosage placed in the syringe on the adsorption capacity of DCF. As seen in Figure S9a, the increase in the adsorbent dosage (from 40 to 60 mg) decreased the q_t values calculated for all tested adsorbents. This behavior showed to be similar to that observed in the batch experiments. High adsorbent dosages exposed to a fixed adsorbent concentration increase the number of unsaturated sites impairing the adsorption capacity. Taking into account these results, 40 mg was the optimal dosage for each adsorbent in the continuous adsorption experiments.

The effect of DCF solution flow (0.5 to 2.0 mL/min) on the adsorption capacity of LF, LF-PPy, and LF-PPySAc was also investigated (Figure S9b). As observed, the increase in the solution flow caused a decrease in the adsorption capacity of all tested adsorbents. This behavior occurs because the flow increase causes a reduction in the residence time of the adsorbate into the column. Hence, it leaves the column before the adsorption equilibrium, as explained by Gong et al. (2015). Therefore, the flow rate was set at 0.5 mL/min for the continuous adsorption experiments.

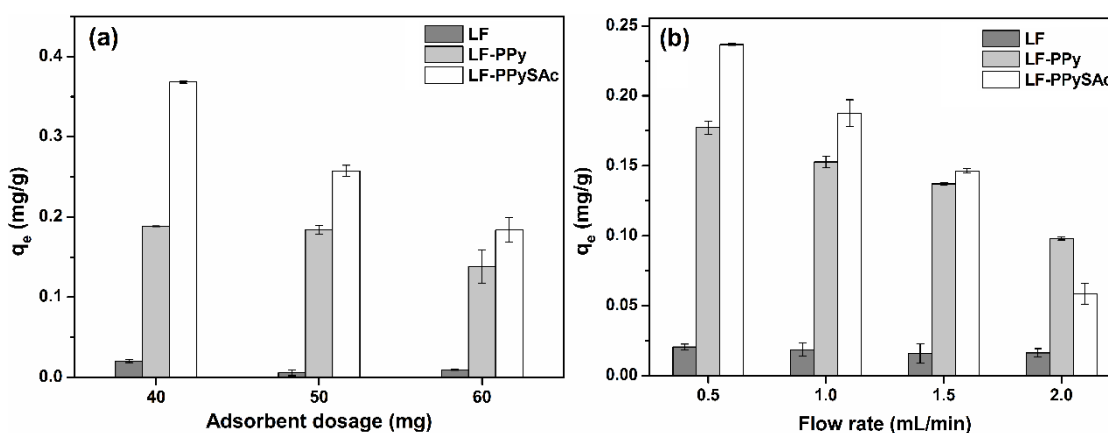


Figure 3-2.S9: (a) Effect of adsorbent dosage on the DCF adsorption capacity (Other experimental conditions: Flow rate 0.5 mL/min, C_0 50 mg/L, pH ~5.5, r.t.). (b) Effect of

flow rate on DCF adsorption capacity (Other experimental conditions: Adsorbent dosage 40 mg, C_0 50 mg/L, pH ~5.5, room temperature).

2.10. Adsorption in tap water

Figure S10 shows the q_e values determined for the adsorption of DCF on the LF samples using tap water as the medium. As seen, the PPy/SAC-coated LF showed the highest adsorption capacity followed by LF-PPy and LF. Overall, this behavior was similar to that observed in the experiments using distilled water to prepare the DCF solution. Of course, compared to that experiment, the q_e values computed in tap water showed to be slightly lower, which was expected since this medium contains interferants (ions, compounds, etc.) that impair the adsorption process. It is relevant to note that even at this non-standard condition, the sample LF-PPySAC exhibited a noticeable adsorption capacity towards DCF (15.41 mg/g). Therefore, this dual-coated material is promising for the removal of this contaminant from real water samples.

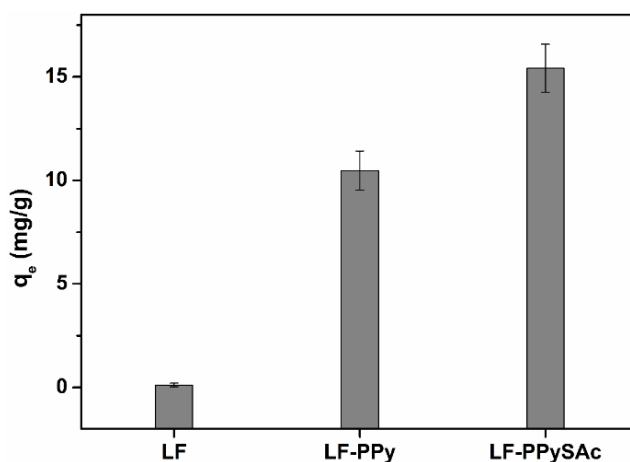


Figure 3-2.S10: Adsorption capacity at equilibrium of DCF on LF, LF-PPy, and LF-PPySAC using tap water as medium (Other experimental conditions: C_0 50 mg/L, adsorbent dosage 40 mg, volume 20 mL, room temperature, stirring 100 rpm, contact time 60 min).

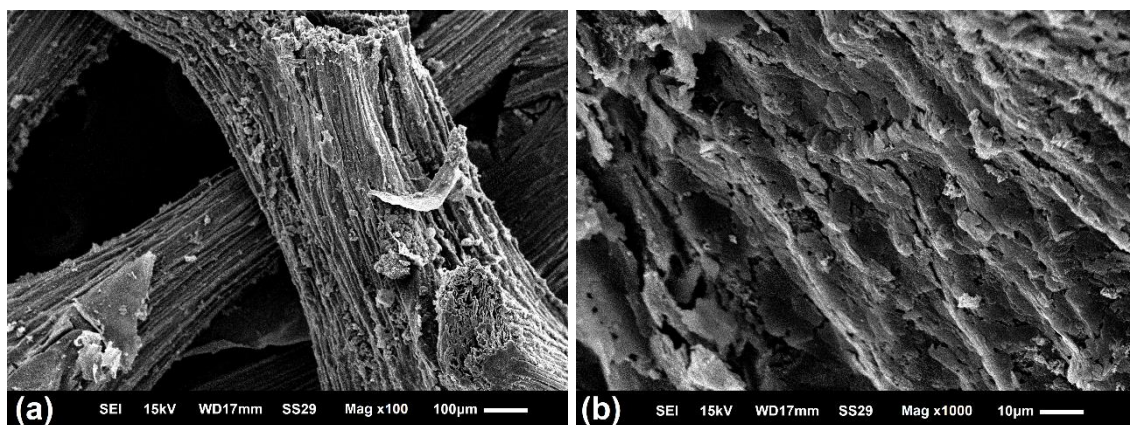


Figure 3-2.S11: Images obtained by SEM from LF-PPySAc after the 5th adsorption/desorption cycle at different magnifications. (a) Mag x100 and (b) Mag x1000.

References

- Anisha, B.S., Sankar, D., Mohandas, A., Chennazhi, K.P., Nair, S. V., Jayakumar, R., 2013. Chitosan-hyaluronan/nano chondroitin sulfate ternary composite sponges for medical use. *Carbohydr. Polym.* 92, 1470–1476. <https://doi.org/10.1016/j.carbpol.2012.10.058>
- Avcu, T., Üner, O., Geçgel, Ü., 2021. Adsorptive removal of diclofenac sodium from aqueous solution onto sycamore ball activated carbon – isotherms, kinetics, and thermodynamic study. *Surfaces and Interfaces* 24, 101097. <https://doi.org/10.1016/j.surfin.2021.101097>
- Bi, L., Chen, Z., Li, L., Kang, J., Zhao, S., Wang, B., Yan, P., Li, Y., Zhang, X., Shen, J., 2021. Selective adsorption and enhanced photodegradation of diclofenac in water by molecularly imprinted TiO₂. *J. Hazard. Mater.* 407, 124759. <https://doi.org/10.1016/j.jhazmat.2020.124759>
- França, D.B., Trigueiro, P., Silva Filho, E.C., Fonseca, M.G., Jaber, M., 2020. Monitoring diclofenac adsorption by organophilic alkylpyridinium bentonites. *Chemosphere* 242, 125109. <https://doi.org/10.1016/j.chemosphere.2019.125109>
- Gong, J.L., Zhang, Y.L., Jiang, Y., Zeng, G.M., Cui, Z.H., Liu, K., Deng, C.H., Niu, Q.Y., Deng, J.H., Huan, S.Y., 2015. Continuous adsorption of Pb(II) and methylene blue by engineered graphite oxide coated sand in fixed-bed column. *Appl. Surf. Sci.* 330. <https://doi.org/10.1016/j.apsusc.2014.11.068>
- Hiew, B.Y.Z., Lee, L.Y., Lai, K.C., Gan, S., Thangalazhy-Gopakumar, S., Pan, G.T., Yang, T.C.K., 2019a. Adsorptive decontamination of diclofenac by

- three-dimensional graphene-based adsorbent: Response surface methodology, adsorption equilibrium, kinetic and thermodynamic studies. *Environ. Res.* 168, 241–253. <https://doi.org/10.1016/j.envres.2018.09.030>
- Hiew, B.Y.Z., Lee, L.Y., Lee, X.J., Gan, S., Thangalazhy-Gopakumar, S., Lim, S.S., Pan, G.T., Yang, T.C.K., 2019b. Adsorptive removal of diclofenac by graphene oxide: Optimization, equilibrium, kinetic and thermodynamic studies. *J. Taiwan Inst. Chem. Eng.* 98, 150–162. <https://doi.org/10.1016/j.jtice.2018.07.034>
- Ho, Y.S., McKay, G., 1999. Pseudo-second order model for sorption processes. *Process Biochem.* 34, 451–465.
- Khadir, A., Motamedi, M., Pakzad, E., Sillanpää, M., Mahajan, S., 2021. The prospective utilization of Luffa fibres as a lignocellulosic bio-material for environmental remediation of aqueous media: A review. *J. Environ. Chem. Eng.* 9. <https://doi.org/10.1016/j.jece.2020.104691>
- Lagergren, S.K., 1898. About the theory of so-called adsorption of soluble substances. *Sven. Vetenskapsakad. Handlingar* 24, 1–39.
- Larous, S., Meniai, A.H., 2016. Adsorption of Diclofenac from aqueous solution using activated carbon prepared from olive stones. *Int. J. Hydrogen Energy* 41, 10380–10390. <https://doi.org/10.1016/j.ijhydene.2016.01.096>
- Lonappan, L., Rouissi, T., Kaur Brar, S., Verma, M., Surampalli, R.Y., 2018. An insight into the adsorption of diclofenac on different biochars: Mechanisms, surface chemistry, and thermodynamics. *Bioresour. Technol.* 249, 386–394. <https://doi.org/10.1016/j.biortech.2017.10.039>
- Malhotra, M., Suresh, S., Garg, A., 2018. Tea waste derived activated carbon for the adsorption of sodium diclofenac from wastewater: adsorbent characteristics, adsorption isotherms, kinetics, and thermodynamics. *Environ. Sci. Pollut. Res.* 25, 32210–32220. <https://doi.org/10.1007/s11356-018-3148-y>
- Pires, B.C., Dutra, F.V.A., Nascimento, T.A., Borges, K.B., 2017. Preparation of PPy/cellulose fibre as an effective potassium diclofenac adsorbent. *React. Funct. Polym.* 113, 40–49. <https://doi.org/10.1016/j.reactfunctpolym.2017.02.002>
- Segun Esan, O., Nurudeen Abiola, O., Owoyomi, O., Olumuyiwa Aboluwoye, C., Olubunmi Osundiya, M., 2014. Adsorption of Brilliant Green onto Luffa

Cylindrical Sponge: Equilibrium, Kinetics, and Thermodynamic Studies. ISRN Phys. Chem. 2014, 1–12. <https://doi.org/10.1155/2014/743532>

Shamsudin, M.S., Azha, S.F., Sellaoui, L., Badawi, M., Bonilla-Petriciolet, A., Ismail, S., 2022. Performance and interactions of diclofenac adsorption using Alginate/Carbon-based Films: Experimental investigation and statistical physics modelling. Chem. Eng. J. 428, 131929. <https://doi.org/10.1016/j.cej.2021.131929>

3.3. Article – Efficient fixed-bed removal of the emerging contaminant nimesulide using β -cyclodextrin-grafted *Luffa* biomass

The results of this chapter of the thesis were published in Journal Colloids and Surfaces A: Physicochemical and Engineering Aspects, v.727, part 2, p.138334, dec. 2025.

Efficient fixed-bed removal of the emerging contaminant nimesulide using β -cyclodextrin-grafted *Luffa* biomass

Juliê S. da Costa, Débora R. S. dos Santos, and André R. Fajardo*

Abstract

The widespread presence of pharmaceutical residues in water bodies, particularly non-steroidal anti-inflammatory drugs (NSAIDs), has raised significant environmental and public health concerns. Among them, nimesulide (NIM) is frequently detected in surface and drinking water, yet conventional treatments show limited efficiency in its removal. In this study, a novel bioadsorbent was developed by chemically modifying *Luffa cylindrica* (LF) fibers with β -cyclodextrin (β -CD) via citric acid-mediated esterification. The resulting LF_(NaOH)- β CD material was characterized by FTIR, SEM, TGA, and porosity analyses, confirming successful grafting and structural enhancement. Batch adsorption experiments revealed that the process was pH-dependent, endothermic, and spontaneous, with a maximum adsorption capacity of 5.37 mg/g at 25 °C. The Sips and Hill isotherm models provided the best fit to the equilibrium data, indicating heterogeneous adsorption with possible negative

cooperativity. Fixed-bed column studies under optimal conditions ($C_0 = 35$ mg/L, $Q = 1.0$ mL/min, $Z = 6$ cm) demonstrated high removal efficiency (up to 84.4%) and an adsorption capacity of 82.27 mg/g, surpassing many adsorbents reported in the literature. FTIR analysis after adsorption suggested that the primary mechanism involves inclusion complex formation between NIM and β -CD, along with hydrogen bonding and π - π interactions. Although methanol regeneration showed limited efficiency, the material maintained partial reusability over three cycles. This work presents an effective, low cost, and renewable alternative for the continuous removal of NIM from water, offering valuable insights for the design of bio-based fixed-bed adsorbents for emerging contaminants.

Keywords: Sponge gourd, emerging contaminants, bioadsorbent, breakthrough curves, environmental remediation.

1. Introduction

Pharmaceutical compounds play a crucial role in maintaining and improving human health [1]. Nevertheless, their unchecked consumption has led to increased contamination of various water bodies, as highlighted by several studies [2]. These compounds are classified as emerging pollutants due to their presence in low concentrations in the environment, coupled with limited information on their potential negative effects on both the environment and human health [3,4]. Among the pharmaceuticals commonly detected in water sources is nimesulide (NIM), a non-steroidal anti-inflammatory drug (NSAID) widely used to treat pain, fever, and inflammation [3]. Yet, the overuse of NIM can lead to a range of moderate to severe adverse effects, including nausea, gastric

damage, bronchoconstriction, and kidney and liver failure [1]. These risks have contributed to the drug ban in several countries, including the United States, Germany, Canada, Japan, and Spain [2,5]. In contrast, NIM is commercialized in Brazil and widely consumed due to its superior effectiveness compared to other anti-inflammatory drugs. Recently, Caldas et al. [2] conducted a four-year study monitoring the presence of pharmaceuticals and personal care products (PPCPs) in surface and drinking water samples. Their findings revealed that NIM concentrations ranged from 70 to 730 ng/L. Given the extensive use of this drug and its potential adverse effects on environmental and human health, there is a growing need for new, efficient, and straightforward methods to remove this drug from water [5,6], ensuring the protection of ecosystems and supporting sustainable development [4].

Considering the various approaches available to address NIM contamination in water sources [1,5], adsorption processes appear to be particularly attractive due to their operational simplicity, cost-effectiveness, and the potential for adsorbent material recyclability [7]. The adsorption process can be carried out using various adsorbent materials and techniques, including continuous moving-bed columns [8](LEUDJO TAKA et al., 2021), batch experiments [9], and fixed-bed continuous flow columns [10]. Among these, the use of fixed-bed continuous flow columns is particularly appealing due to their scalability, efficiency, and ability to minimize adsorbent consumption based on collected experimental data [11]. In this technique, the adsorbate solution is continuously passed through a column containing the adsorbent, allowing for ongoing adsorption [9]. This process is suitable for industrial applications [12], as it can handle large volumes of wastewater with high pollutant loads. Moreover,

this adsorption process becomes even more advantageous when using low cost adsorbents, such as vegetal biomass [7].

Among the various biomasses that can be effectively used for this purpose, *Luffa cylindrica* (LF) stands out as a promising candidate due to its unique macroporous three-dimensional structure, high tensile strength, and mechanical resistance [13]. Additionally, the fibrous structure of LF, primarily composed of cellulose, facilitates both chemical and physical modifications. These modifications enhance its properties, including surface characteristics [14] and adsorption capacity [15]. For example, Coutinho et al. [13] combined physical and chemical modifications to enhance the adsorption capacity of *Luffa cylindrica* (LF) for trimethoprim, an antibiotic. Abdullah et al. [16] employed a dual treatment process, involving TEMPO oxidation followed by amination with polyethyleneimine (PEI), to improve the adsorption capacity of LF for removing Cr^{6+} ions from water. Despite these and other promising examples in the literature, most studies using this biomass as an adsorbent are limited to LF in its natural or minimally processed form. Given the extensive literature on the chemical modification of cellulose [17], the primary component of LF, there is significant potential to develop adsorbent materials from this biomass with enhanced properties.

Based on this opportunity and considering the wide range of chemical compounds used to modify cellulose [18], this study explores the modification of LF with β -cyclodextrin (β -CD) as a strategy to enhance its adsorption capacity for NIM. Cyclodextrins, including β -CD, are promising molecules for modifying cellulose structures due to their unique properties, which complement those of cellulose-based materials [19]. β -CD is a cyclic oligosaccharide composed of

seven *D*-glucopyranose units. It has a distinctive structure, with a hydrophilic outer surface and a hydrophobic central cavity [20]. The hydrophobic cavity of β -CD enables the formation of inclusion complexes with a variety of molecules [21], making it suitable for diverse applications [15]. For example, Guo et al. [22] demonstrated that β -CD is an excellent adsorbent due to its ability to form host-guest complexes with organic molecules, particularly hydrophobic ones. The formation of these complexes involves multiple interactions, such as hydrogen bonds, van der Waals forces, and hydrophobic interactions [20]. This feature was exploited by Ares et al. [20], who functionalized cellulose filter paper with β -CD to enhance its capacity to remove diclofenac from water. Despite the success in improving the adsorption properties of various cellulose-based materials [23-25], the modification of LF with β -CD has not been explored for this purpose.

To validate our hypothesis, LF was chemically functionalized with β -CD, and the resulting material was tested as an adsorbent in both batch and fixed-bed continuous flow experiments to remove NIM from aqueous solutions. In addition to the experimental data, a series of theoretical investigations were conducted to provide further insights into the evaluated processes. To the best of our knowledge, this is the first study exploring this approach to address the NIM contamination in water.

2. Materials and methods

2.1. Materials

Luffa cylindrica (LF) was obtained from a plantation in Pérola, Paraná, Brazil. Ethanol (EtOH, P.A.), methanol (MeOH, P.A.), and sodium hydroxide (NaOH, $\geq 98\%$, reagent grade) were purchased from Synth (Brazil). β -

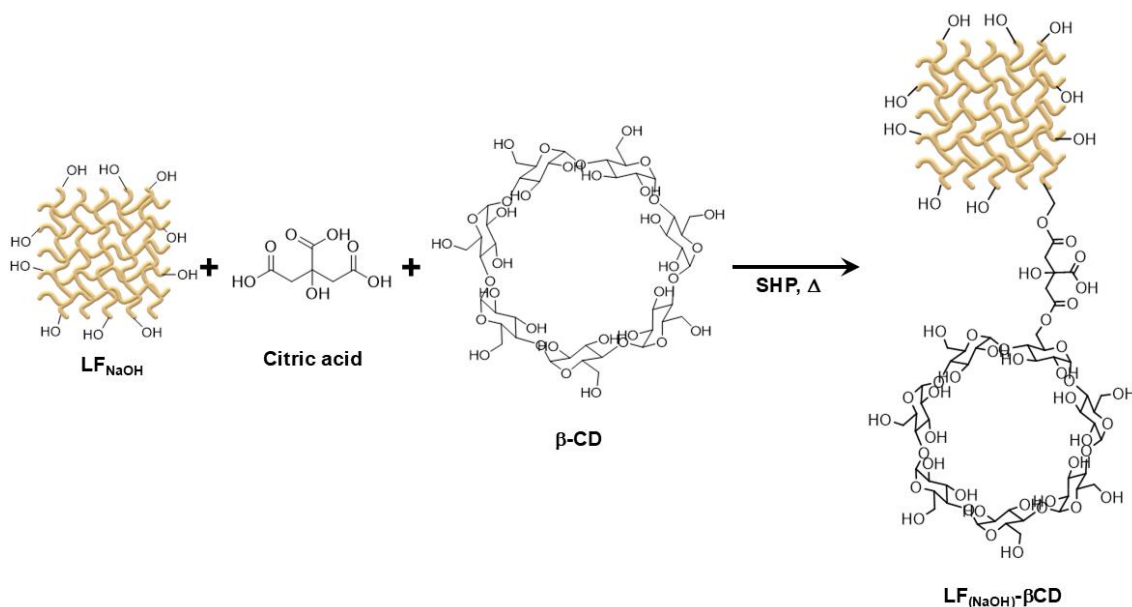
Cyclodextrin (β -CD, $\geq 97\%$ reagent grade) was obtained from Sigma-Aldrich (USA). Anhydrous citric acid (CA, P.A., $\geq 99.5\%$ analytical grade) and sodium hypophosphite (SHP, P.A., $\geq 97\%$ reagent grade) were sourced from Êxodo Científica (Brazil). Anhydrous sodium carbonate (Na_2CO_3 , P.A., $\geq 98\%$ reagent grade) was obtained from Vetec (Brazil). Phenolphthalein was acquired from Neon (Brazil). Nimesulide (NIM, $\geq 99\%$ analytical grade) was purchased from EMS® (Brazil). All commercial reagents were used as received.

2.2. Modification of LF with β -CD

Raw LF was cut into 1 cm^3 cubes, washed three times with EtOH/ H_2O (70:30 v/v), and dried at $50\text{ }^\circ\text{C}$ for 24 h. The cleaned LF (2.0 g) was then treated with NaOH (5% w/v, 200 mL) at $50\text{ }^\circ\text{C}$ for 2 h, washed to neutral pH, and dried at $50\text{ }^\circ\text{C}$ for 48 h, yielding the $\text{LF}_{(\text{NaOH})}$ sample. The alkaline treatment was applied to partially remove hemicellulose and lignin, thereby exposing the cellulose-rich fraction and increasing the availability of surface hydroxyl groups for subsequent functionalization.

For β -CD grafting, a procedure adapted from Rehan et al. [26] was followed (Scheme 1). Briefly, $\text{LF}_{(\text{NaOH})}$ (1.0 g) was immersed in an aqueous solution containing β -CD (5% w/v, 10 mL), CA (2% w/v), and SHP (2% w/v) at room temperature for 30 min. CA acted as a non-toxic, multifunctional crosslinker capable of forming ester bonds between hydroxyl groups of $\text{LF}_{(\text{NaOH})}$ and β -CD, while SHP was used as a catalyst to promote CA-mediated esterification [27]. The impregnated $\text{LF}_{(\text{NaOH})}$ was then placed in an oven at $80\text{ }^\circ\text{C}$ for approximately 5 min before increasing the temperature to $150\text{ }^\circ\text{C}$ to facilitate the esterification reaction. The thermal curing process lasted 15 min. Afterward, the modified LF

was washed with distilled water at 50 °C for 5 min, followed by a second wash at room temperature. Finally, the $\text{LF}_{(\text{NaOH})}$ - β CD sample was dried at 50 °C for 24 h and stored for later characterization and use.



Scheme 1. General reaction for β -CD grafting onto $\text{LF}_{(\text{NaOH})}$.

2.3. Quantification of grafted β -CD on $\text{LF}_{(\text{NaOH})}$ - β CD

The amount of β -CD grafted onto $\text{LF}_{(\text{NaOH})}$ - β CD was quantified using a colorimetric assay based on the phenolphthalein complexation method [28,29]. A phenolphthalein solution was prepared by adding 0.05 mL of a 1% (w/w) phenolphthalein solution in EtOH to 100 mL of an aqueous Na_2CO_3 solution (10 g/L), adjusting the pH to ~ 10 to produce the characteristic purple coloration of phenolphthalein. The solution was divided into 5 mL aliquots, placed in three vials, and mixed with increasing masses of $\text{LF}_{(\text{NaOH})}$ - β CD (10, 20, and 30 mg). The mixtures were stirred at 100 rpm at room temperature for 24 h. Afterward, the samples were removed, and the absorbance of the remaining solution was measured at 552 nm using a UV-Vis spectrophotometer (Perkin Elmer Lambda 25, USA). The β -CD concentration was determined using a previously

constructed calibration curve ($Absorbance = 0.176[conc.] - 1.410 \times 10^{-4}$, $R^2 > 0.997$, where $[conc.]$ is the β -CD concentration in mg/L), assuming a 1:1 molecular complex formation between β -CD and phenolphthalein. All tests were performed in triplicate. Finally, to evaluate the intrinsic phenolphthalein absorption capacity of $LF_{(NaOH)}-\beta CD$, a similar test was conducted with raw LF and $LF_{(NaOH)}$. In this case, a fixed sample mass of 30 mg was used, and the phenolphthalein solution volume was increased to 10 mL.

2.4. Characterization

Fourier-transform infrared spectrophotometry (FTIR) analyses were performed using a Shimadzu IR-Affinity-1 spectrometer (Japan) in the wavenumber range of $4000-400\text{ cm}^{-1}$, with 80 scans per sample and a resolution of 4 cm^{-1} . Before spectral acquisition, the LF, $LF_{(NaOH)}$, and $LF_{(NaOH)}-\beta CD$ samples were cut and placed between two KBr pellets. Thermogravimetric analysis (TGA) was carried out using a Shimadzu DTG60 analyzer (Japan). Samples were heated at $10\text{ }^{\circ}\text{C}/\text{min}$ under a N_2 (flow rate of $20\text{ mL}/\text{min}$). Prior to TGA analysis, the samples were ground using a pestle and liquid N_2 . Scanning electron microscopy (SEM) was performed using an FEI Quanta FEG 250 microscope (USA). Before SEM imaging, the dried samples were sputter-coated with gold. The pH at the point of zero charge (pH_{PZC}) was determined by placing 30 mg of each sample in 30 mL of $0.1\text{ mol}/\text{L}$ NaCl solution, adjusting the pH between 2 and 10 with $0.1\text{ mol}/\text{L}$ HCl or NaOH, and stirring at 100 rpm for 24 h. The final pH was measured, and the pH_{PZC} was determined from the point where the difference between initial and final pH (ΔpH) was zero [30].

2.5. Density and porosity measurements

The density of the LF samples was determined using the liquid pycnometer method [79]. The densities of LF samples were determined by measuring the weight of dry LF samples (m_1), of the pycnometer empty (m_2), of the pycnometer with ethylene glycol (m_3), and of the pycnometer with ethylene glycol and LF sample (m_4). The relative density (g/cm³) can be calculated using Equation (1).

$$Density = \frac{m_1/(m_3-m_2)-(m_4-m_2-m_1)}{\rho_{ethylene\ glycol}} \quad (1)$$

Where the absolute density of ethylene glycol ($\rho_{ethylene\ glycol}$) is about 1.11 g/cm³ at 18 °C.

The porosity of the LF samples were determined using a method described by Singh and Jelinek [31]. Total porosity (%) was calculated using Equation (2). For this, a sample with a known weight (m_i) was immersed in a vial containing 30 mL of EtOH and soaked for 24 h to allow the liquid to penetrate the sample pores. The final weight of the wet sample (m_f) was then recorded. The EtOH density (ρ_{EtOH}) at 25 °C is 0.789 g/cm³. Again, the measurements were done in triplicate.

$$Porosity\ (\%) = \frac{(m_f - m_i)}{\rho_{EtOH} \times lwh} \times 100 \quad (2)$$

Where l , w , and h correspond to length, width, and height, respectively. The dimensions of each sample were measured using a digital vernier caliper (Lee Tools, Brazil).

2.6. Batch adsorption experiments

Batch adsorption experiments were performed to assess the influence of solution pH on adsorption capacity and to investigate the kinetic, thermodynamic, and equilibrium characteristics of the process. For pH evaluation, 0.3 g of adsorbent was added to 30 mL of NIM solution (35 mg/L, prepared in tap water; pH 7.6, conductivity 54 mV at 25 °C), with orbital stirring at 100 rpm for 3 h. The pH was adjusted to 4, 7, or 10 using 0.1 mol/L HCl or NaOH solutions and measured with a pH meter (Hannah Instruments, model HI2211, USA). The adsorbent mass corresponded to that used in the most efficient fixed-bed column configuration in this study, ensuring direct comparability between batch and column results. The contact time of 3 h was selected based on previous reports on β -CD-modified materials for pharmaceutical removal, providing sufficient equilibration to reliably determine adsorption capacity under the experimental conditions.

After adsorption, the amount of NIM removed was determined by UV-Vis spectrophotometry using a PerkinElmer Lambda 25 spectrometer (USA) at a wavelength of 390 nm. The absorbance data were converted to concentration using previously constructed calibration curves ($Absorbance = 0.00329[conc.] + 0.01159$, $R^2 > 0.969$, where $[conc.]$ is the NIM concentration in mg/L). The adsorption capacity at equilibrium (q_e) was then calculated using Equation (3):

$$q_e = \frac{(C_0 - C_e)}{m} \times V \quad (3)$$

where C_0 is the initial drug concentration, C_e is the drug concentration remaining in the solution at equilibrium, m is the mass of the adsorbent, and V is the volume of the solution. For the kinetic analysis a similar experimental procedure was

conducted; however, aliquots were collected from the Erlenmeyers flaks at pre-determined intervals. Eq. (4) was utilized to calculate the adsorption capacity at each time interval (q_t).

$$q_t = \frac{(C_0 - C_t)}{m} \times V \quad (4)$$

In the thermodynamic analysis, the temperature of the NIM solution was varied at 308, 318, and 328 K, while the other conditions were kept the same as in the pH experiment. The effect of temperature on adsorption was evaluated using thermodynamic parameters, including the standard Gibbs free energy of adsorption (ΔG°), the heat of adsorption (ΔH°), and the standard entropy change (ΔS°) [30]. Equations (5), (6), and (7) were utilized to determine the thermodynamic parameters:

$$K = \frac{q_e}{C_e} \quad (5)$$

$$\ln K = \frac{\Delta S^\circ}{R} - \frac{\Delta H^\circ}{RT} \quad (6)$$

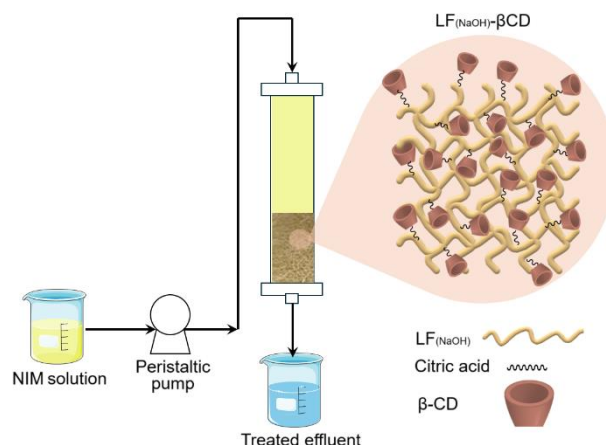
$$\Delta G^\circ = -RT \ln K \quad (7)$$

where K is the equilibrium constant, q_e is the amount of NIM adsorbed per gram of adsorbent at equilibrium, R is the universal gas constant (8.314 J/mol K) and T is the absolute temperature. ΔH° and ΔS° can be determined from the slope and intercept of the plot between $\ln(q_e/C_e)$ versus $1/T$ (not shown). ΔG° can be calculated from Equation (7).

For the isothermal analysis, similar experimental procedures were followed; however, the temperature was fixed at 298 K (room temperature), and the NIM solution concentration was varied from 5 to 35 mg/L. After 3 h, q_e values were calculated using Equation (3). The results were then fitted to three non-linear isotherm models: Sips [32], Redlich-Peterson [33], and Hill [34], which are detailed in the Supporting Information (Table S1).

2.7. Fixed bed column adsorption experiments: Optimization and operational characteristics

A 15.00 cm long glass tube with a diameter of 1.39 cm and a volume of 22.76 cm³ was used as the column for the fixed-bed experiments. Silicone tubing was connected to both ends of the column and to a peristaltic pump, which was used to circulate the NIM solution in and out of the column (Scheme 2). The LF_(NaOH)- β CD sample was placed inside the column, and the following operational parameters were tested: volumetric flow rate (Q) at 0.5, 1.0, and 1.5 mL/min, adsorbent height (Z) at 2, 4, and 6 cm, and initial NIM solution (C_0) at 25, 30, and 35 mg/L. Effluent samples were collected at different time intervals until saturation was reached and analyzed by UV-Vis spectrophotometry as detailed in the previous section. In all experiments, the NIM solution was passed through the packed bed only once in downflow mode, without recirculation. The effluent was collected at the column outlet and analyzed immediately by UV-Vis spectrophotometry to monitor NIM concentration over time.



Scheme 2: Experimental setup for fixed-bed column adsorption experiments operated in downflow single-pass mode. The NIM solution flowed through the packed bed only once, without recirculation, and the effluent was collected at the column outlet for UV-Vis analysis.

2.7.1. Breakthrough analysis

The breakthrough curves, which relate the effluent/influent concentration ratio (C_t/C_0) to the time (t) and effluent volume (V), were used to assess the performance of $\text{LF}_{(\text{NaOH})}\text{-}\beta\text{CD}$ in the column adsorption experiment. The breakthrough time (t_b), also known as usable time, is defined as the time at which the C_t reaches 10% of C_0 , whereas saturation or exhaustion corresponds to the point when the effluent concentration approaches that of the influent [10]. The exhaustion time (t_e) represents the time when the effluent reaches 95% of the influent concentration ($C_t/C_0 = 0.95$), indicating the total capacity. The column data were further evaluated by analyzing the parameters obtained from each experimental breakthrough curve [10,11,35]. The adsorption capacity of $\text{LF}_{(\text{NaOH})}\text{-}\beta\text{CD}$ in the fixed-bed column experiment was estimated by calculating the area under the breakthrough curve, as defined in Equation (8):

$$q_{total} = \frac{QA}{1000} = \frac{QC_0}{1000} \int_{t=0}^{t=total} \left(\frac{C_t}{C_0} \right) dt \quad (8)$$

where q_{total} is the amount of adsorbed NIM, C_0/C_t are the influent/effluent concentrations, Q is the flow rate, A is the area under the curve and t is the time. The amount of NIM adsorbed in the column, m_{total} , is calculated using Equation (9).

$$m_{total} = \frac{C_0 Q t_{total}}{1000} \quad (9)$$

The q_{eq} of the column is calculated per Equation (10), while the removal percentage (%) is calculated per Equation (11):

$$q_{eq} = \frac{q_{total}}{m} \quad (10) \quad Removal (\%) = \frac{q_{total}}{m_{total}} \times 100 \quad (11)$$

2.8. Regeneration and reuse experiments

The regeneration and reuse performance of $LF_{(NaOH)}-\beta CD$ were investigated under both batch and fixed-bed column configurations. For batch experiments, desorption of NIM from the post-utilized adsorbent was carried out using MeOH/HCl 0.15 mol/L (9:1 v/v) as the eluent. After each adsorption cycle, the adsorbent was recovered and immersed in 30 mL of the eluent solution for 5 h at 25 °C under orbital stirring (100 rpm). The regenerated material was then washed with distilled water, oven-dried at 50 °C for 24 h, and reused in a new adsorption run under the same conditions ($C_0 = 35$ mg/L, adsorbent mass = 0.3 g, solution volume = 30 mL). This adsorption-desorption process was repeated

for ten consecutive cycles. Desorption efficiency (%) was calculated according to Equation (12) [36]:

$$Desorption (\%) = \frac{C_d}{C_a} \times 100 \quad (12)$$

where C_d and C_a represent the concentrations of NIM desorbed and adsorbed, respectively (in mg/L). Additionally, q_e and the removal efficiency after each reuse cycle were calculated using Equations (3) and (13):

$$Removal (\%) = \frac{(C_e - C_0)}{C_0} \times 100 \quad (13)$$

For fixed-bed column experiments, desorption was performed using MeOH as the eluent. After each column run, the exhausted adsorbent was removed from the column and immersed in 50 mL of MeOH/HCl 0.15 mol/L (9:1 v/v) for 24 h at 25 °C under orbital stirring (100 rpm). The regenerated adsorbent was washed with distilled water, oven-dried at 50 °C for 24 h, and reused under identical conditions ($C_0 = 30$ mg/L, $Q = 1.0$ mL/min, $Z = 6$ cm). The adsorption-desorption cycle was repeated for three consecutive runs. All reuse experiments were performed in triplicate.

3. Results and discussion

3.1. Quantification of grafted β -CD on $LF_{(NaOH)}-\beta CD$

The quantification of β -CD grafted onto the fibers of $LF_{(NaOH)}-\beta CD$ was investigated using a spectrophotometric method based on changes in the absorption of organic probes, such as phenolphthalein. This approach is a convenient tool, as it provides insights into the shift of phenolphthalein

characteristic absorption peak at 552 nm in a basic pH environment. This shift occurs due to the formation of a complex between the hydrophobic cavities of β -CD and phenolphthalein [28]. Consequently, the decolorization of the solution is directly related to a decrease in the concentration of free phenolphthalein, which can be associated with the presence of inclusion sites, such as the cavities of β -CD [29].

As shown in Figure S1a, the characteristic absorption band of phenolphthalein decreases in the solution containing $\text{LF}_{(\text{NaOH})}$ - β CD, whereas no significant change is observed in the presence of raw LF and $\text{LF}_{(\text{NaOH})}$. This trend confirms the interaction between phenolphthalein and $\text{LF}_{(\text{NaOH})}$ - β CD, driven by the β -CD moieties forming inclusion complexes with the dye [37]. Interestingly, the alkaline-treated sample ($\text{LF}_{(\text{NaOH})}$) also induced a reduction in the UV-Vis absorption of phenolphthalein. The observed decrease ($\sim 8\%$) compared to the neat phenolphthalein solution can be attributed to interactions between phenolphthalein and $\text{LF}_{(\text{NaOH})}$, which contains functional exposed by the alkaline treatment that are available for interaction. However, this reduction was not as pronounced as that observed for $\text{LF}_{(\text{NaOH})}$ - β CD, emphasizing the crucial role of the grafted β -CD in this material. The data presented in Figure S1b further reveal that increasing the amount of $\text{LF}_{(\text{NaOH})}$ - β CD in solution (from 10 to 30 mg) results in a more pronounced decrease in the phenolphthalein absorption bands, likely due to the higher availability of inclusion sites. Based on a calibration curve, it was estimated that a 30 mg sample of $\text{LF}_{(\text{NaOH})}$ - β CD contained approximately 17.2 mg of β -CD (57% w/w). According to phenolphthalein experiments reported by Hemine et al. [38], the β -CD content in banana peel extract (BAN) crosslinked

with epichlorohydrin (EPI) and β -CD was determined to be 4.71 mmol/g, corresponding to approximately 53% β -CD in that material.

3.2. Characterization of $LF_{(NaOH)}$ and $LF_{(NaOH)}-\beta CD$

The chemical composition of LF before and after alkaline treatment was examined using FTIR analysis, and the recorded spectra are shown in Figure 1a. Notably, the FTIR spectrum of $LF_{(NaOH)}$ exhibits some differences compared to that of raw LF. The $LF_{(NaOH)}$ spectrum displays a broadband centered at 3447 cm^{-1} , attributed to the O–H stretching of hydroxyl groups present in cellulose, hemicellulose, and lignin. However, this band appears slightly more intense and broader, likely due to an increase in the number of hydroxyl groups on the $LF_{(NaOH)}$ surface. This change is attributed to the alkaline treatment, which exposed more cellulose within the fibers [39]. The bands observed at 2925 and 2855 cm^{-1} correspond to the C–H stretching of CH_x groups and show increased intensity after alkaline treatment. Although the alkaline treatment aimed to remove lignin, its characteristic bands remain visible in the FTIR spectrum of $LF_{(NaOH)}$. For instance, bands in the $1650\text{--}1550\text{ cm}^{-1}$ range correspond to the combined stretching of C=O and C=C bonds within the aromatic ring of the lignin fraction. After the alkaline treatment, these bands become more sharpened and slightly more intense compared to others that did not show changes in the same spectrum [39]. The sharpening of these bands indicates partial consumption of these groups, suggesting that while some lignin was removed, complete elimination did not occur. Additionally, Martinez-Pavetti et al. [40], reported that an increase in band intensity around 1643 cm^{-1} may be associated with water molecules absorbed by cellulose fibers. The decrease in intensity of the band at

1419 cm^{-1} , attributed to the C–H stretching of CH_3 groups in lignin, further supports lignin modification. Moreover, after alkaline treatment, the band around 1050 cm^{-1} , associated with the C–O–C stretching of pyranose and furanose rings in polysaccharides like cellulose and hemicellulose, becomes more intense. This increase in intensity suggests that alkaline treatment enhances the cellulosic fraction on the fiber surface [41].

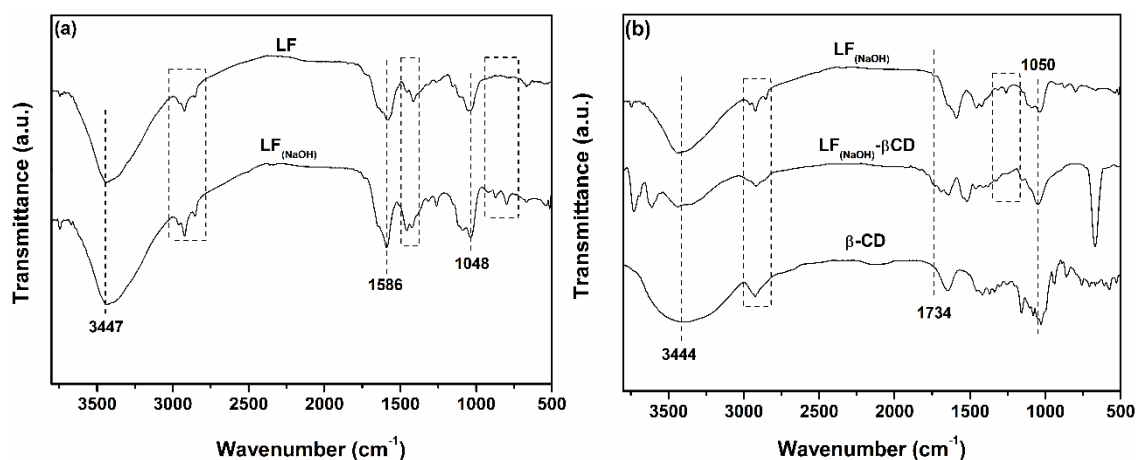


Figure 3-3.1: FTIR spectra of (a) raw LF and $\text{LF}_{(\text{NaOH})}$ and (b) $\text{LF}_{(\text{NaOH})}$, $\beta\text{-CD}$ and $\text{LF}_{(\text{NaOH})}\text{-}\beta\text{CD}$.

FTIR analysis was performed to investigate the chemical nature of $\beta\text{-CD}$ and confirm the modification of $\text{LF}_{(\text{NaOH})}$ with this macrocycle. As shown in Figure 1b, the FTIR spectrum of $\beta\text{-CD}$ exhibits a broadband centered at 3405 cm^{-1} , attributed to the O–H stretching of hydroxyl groups. The band at 2916 cm^{-1} corresponds to the asymmetric stretching of C–H bonds in CH_2 groups. Additionally, the bending vibration of the O–H bond from hydroxyl groups is observed at 1637 cm^{-1} . The bands at 1156 and 1026 cm^{-1} are assigned to the stretching of C–OH and C–O–C bonds in the $\beta\text{-CD}$ structure, respectively [42]. A characteristic band around 937 cm^{-1} , corresponding to the $\alpha(1\rightarrow4)$ bond of the glucopyranose ring, is also present in the $\beta\text{-CD}$ spectrum [43].

In the spectrum of $\text{LF}_{(\text{NaOH})}$ - β CD, characteristic bands of the starting materials are observed, along with some differences and the appearance of new bands. A decrease in the intensity of the O–H stretching band at 3444 cm^{-1} is noted, likely due to the consumption of hydroxyl groups from both the LF and β -CD during the grafting process with citric acid. Additionally, the C–H stretching bands of the $-\text{CH}_x$ groups in cellulose shift to lower wavenumbers (2916 and 2847 cm^{-1}), which may be attributed to the overlapping vibrations of CH_2 groups from β -CD. The grafting of β -CD onto the LF structure using citric acid as a crosslinking agent is confirmed by the emergence of new bands between 1740 and 1600 cm^{-1} , corresponding to the C=O stretching of ester groups formed during the grafting process. Furthermore, the increase in intensity of the C=O ester band is accompanied by a decrease in the intensity of the C–O band of cellulose (around 1300 – 1200 cm^{-1}), providing additional evidence that the grafting process occurred and corroborating to previous studies [26]. Based on these FTIR results, it can be concluded that β -CD was successfully grafted onto $\text{LF}_{(\text{NaOH})}$ using CA as the binding agent.

To evaluate the thermal effects of alkaline treatment and β -CD grafting, thermogravimetric analysis (TGA/DTG) was performed on LF, $\text{LF}_{(\text{NaOH})}$, and $\text{LF}_{(\text{NaOH})}$ - β CD samples (Figures S2a and S2b). The TGA curves reveal an initial mass loss of up to 6% in all samples, attributed to the evaporation of free water molecules adsorbed on the sponge fibers. Following alkaline treatment, the characteristic mass loss stage associated with hemicellulose depolymerization, observed in raw LF between 230 and $300\text{ }^{\circ}\text{C}$, was no longer present in $\text{LF}_{(\text{NaOH})}$, indicating its removal during treatment. The final stage of mass loss in $\text{LF}_{(\text{NaOH})}$, corresponding to the most significant thermal degradation, occurs at a lower

temperature (260–380 °C) compared to the untreated LF [44]. This shift can be attributed to the removal or reduction of hemicellulose and lignin in $\text{LF}_{(\text{NaOH})}$, which normally cover the cellulose fibers. With increased cellulose exposure, degradation occurs at lower temperatures. In this final degradation stage, $\text{LF}_{(\text{NaOH})}$ loses approximately 61% of its mass but retains a residual mass that is 9% higher than that of raw LF.

TGA/DTG curves of $\text{LF}_{(\text{NaOH})}$ - β CD exhibited three distinct mass loss stages (Figures S2a and S2b). The second stage (200–280 °C), with a peak at 248 °C, corresponds to the decomposition of CA, accounting for a 5% mass loss. As observed in the other samples, the most significant thermal degradation occurs in the final stage (290–380 °C), where $\text{LF}_{(\text{NaOH})}$ - β CD loses 54% of its mass, primarily due to cellulose depolymerization and β -CD degradation. When comparing the final degradation stages of $\text{LF}_{(\text{NaOH})}$ - β CD and $\text{LF}_{(\text{NaOH})}$, a slight increase of 5 °C in the maximum decomposition temperature is noted after grafting. Barra et al. [45] described that the 5% weight loss ($T_{5\%}$) in the principal thermal stage can be utilized to characterize the polymer thermal stability. Based on that, the thermal stability of the samples $\text{LF}_{(\text{NaOH})}$ - β CD and $\text{LF}_{(\text{NaOH})}$ was determined based on the $T_{5\%}$ value on the thermal stage at 290–380 °C. The $T_{5\%}$ value for $\text{LF}_{(\text{NaOH})}$ - β CD (307 °C) was higher than that computed for $\text{LF}_{(\text{NaOH})}$ (300 °C), confirming that the presence of β -CD increases thermal stability. Since β -CD undergoes complete degradation between 300 and 400 °C, the residual mass of $\text{LF}_{(\text{NaOH})}$ - β CD at 500 °C is 11% lower than that of $\text{LF}_{(\text{NaOH})}$, further confirming the impact of β -CD grafting on the thermal stability of the material [46].

The morphological and microstructural evaluation of $\text{LF}_{(\text{NaOH})}$ and $\text{LF}_{(\text{NaOH})}$ - βCD samples was performed using images obtained by SEM, which are shown in Figure 2. As observed, the $\text{LF}_{(\text{NaOH})}$ fibers exhibit a smoother surface morphology with fewer striations and irregularities (Figures 2a and 2b). This morphology results from the removal of hemicellulose and lignin from cellulose fibers, corroborating the observations reported by FTIR analysis [14]. Additionally, the fiber surfaces appear to form a network of coalescing structures. Although the $\text{LF}_{(\text{NaOH})}$ sample was subjected to a highly aggressive alkaline treatment that could potentially cause fiber breakage, SEM images show that the fibers maintained their structural integrity [40].

The morphology of the sample after the $\beta\text{-CD}$ grafting process was markedly different from that of the $\text{LF}_{(\text{NaOH})}$ sample. SEM images (Figures 2c and 2d) show that the $\text{LF}_{(\text{NaOH})}$ - βCD sample exhibits a rougher surface morphology, although without apparent porosity. The images reveal that after modification with $\beta\text{-CD}$, a thin film formed over the $\text{LF}_{(\text{NaOH})}$ fibers, rendering the previously visible pores less discernible [41]. Similar rough surfaces and fiber irregularities have been reported for cellulose nanofibrils grafted with $\beta\text{-CD}$ [47].

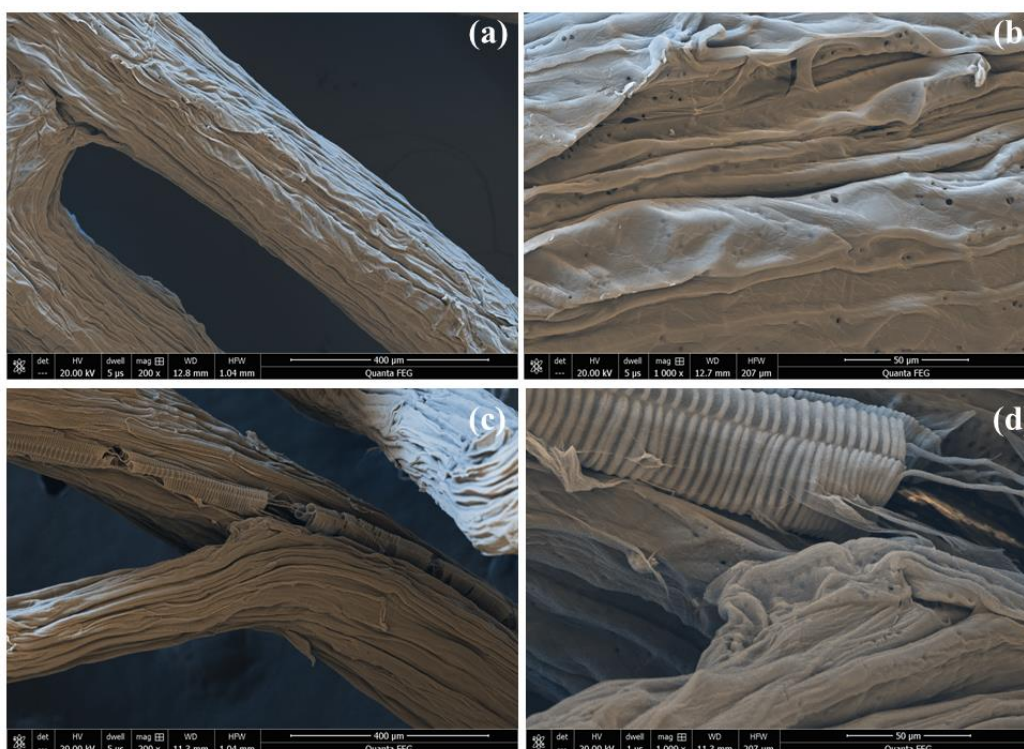


Figure 3-3.2: Images obtained by SEM from (a,b) LF_(NaOH) and (c,d) LF_(NaOH)-βCD at two different magnifications (x200 and x1000).

3.3. Density and total porosity

The density and total porosity of the LF samples are summarized in Table 1. As observed, after β-CD grafting onto LF_(NaOH) fibers, the density decreases while the total porosity increases. These results are in line with the results obtained in the quantification of β-CD, where, after the graphitization process, approximately half of the analyzed sponge mass is composed of β-CD, which has an inherent porous structure as a characteristic. The porosity values determined by the liquid displacement method indicated an increase for LF_(NaOH)-βCD compared to LF_(NaOH), consistent with the introduction of interconnected channels and voids upon β-CD grafting. These microstructural features are not directly resolved in SEM images at the magnifications used; however, the increased

surface roughness observed suggests their presence, in agreement with the porosity measurements [48].

Table 3-3.1: Density and porosity values for LF_(NaOH) and LF_(NaOH)- β CD.

Samples	Density (g/cm ³)	Porosity (%)
LF _(NaOH)	0.809 \pm 0.002	0.328 \pm 0.121
LF _(NaOH) - β CD	0.413 \pm 0.004	2.348 \pm 0.313

3.3. Batch adsorption experiments

3.3.1. Effect of pH

The pH of the medium is a critical parameter to evaluate, as changes in its value can influence the surface charges of both the adsorbent and adsorbate, thereby affecting adsorption capacity [15]. When the pH is higher than the pKa the NIM molecules are negative charged based in the dissociation that occur in the molecule in this condition, but when the pH is lower to pKa the molecule is neutral, and these differences can affect the kind of mechanism involved in the adsorption [1]. To better understand the effect of pH on the batch adsorption of NIM, the pH of the drug solution was adjusted to a range of 4–10 prior to the adsorption experiments using 0.1 mol/L HCl or NaOH. Additionally, to further support the analysis of pH-dependent adsorption behavior, the point of zero charge (pH_{PZC}) of the LF_(NaOH) and LF_(NaOH)- β CD samples was determined. The pH_{PZC} corresponds to the pH at which the total surface charge of the adsorbent is neutral ($[H^+] = [OH^-]$) [49]. At pH values below the pH_{PZC} ($pH < pH_{PZC}$), the surface of the LF samples is positively charged ($[H^+] > [OH^-]$), whereas at pH values above the pH_{PZC} ($pH > pH_{PZC}$), the surface becomes negatively charged ($[H^+] < [OH^-]$) (Figure S3a). In this study, LF_(NaOH) exhibited a pH_{PZC} of 7.18, while

LF_(NaOH)- β CD presented a significantly lower pHPZC of 2.02. This shift suggests that after grafting, the pH range in which LF_(NaOH)- β CD carries an excess of negative charges is substantially expanded compared to LF_(NaOH). The decrease in the pHPZC value following the grafting process is attributed to the introduction of additional hydroxyl groups from β -CD, which render the surface of LF_(NaOH)- β CD more negatively charged [50]. Comparable pHPZC values were previously reported by Qu et al. [19], who developed rice husk-based cellulose modified with β -CD via epichlorohydrin crosslinking.

The adsorption capacity of LF(NaOH) was evaluated in batch mode using 0.3 g of adsorbent and 30 mL of a 35 mg/L NIM solution. Although environmental NIM concentrations are typically 70–730 ng/L, higher concentrations were employed due to the limited sensitivity of UV-Vis spectrophotometry. This approach, commonly adopted in adsorption studies, allows reliable detection, robust kinetic and isotherm modeling, as well as other relevant information under controlled laboratory conditions, while still yielding mechanistic insights relevant to real scenarios.

As determined, the adsorption capacity obtained by the material without β -CD was equal to 2.37 mg/g. Considering the low performance of the material, the other adsorption analyses in the present work were carried out only with LF_(NaOH)- β CD. Overall, the adsorption capacity of LF_(NaOH)- β CD for NIM shows a slight increase as the pH rises from 4 to 7 (Figure S3b). However, at pH 10, the computed q_e value decreases considerably. At pH 4, the solution has a pH lower than the pKa of NIM (pKa = 6.7) [1], meaning that the drug is predominantly in its positively charged form. This favors electrostatic interactions between the negatively charged surface of the adsorbent and the positively charged drug

molecules. At pH 7, which is close to the pKa of NIM, the drug exists primarily in its neutral form, enhancing its interaction with the β -CD cavities and consequently increasing adsorption capacity [51]. However, at pH values above the pKa, NIM molecules become negatively charged, leading to electrostatic repulsion with the negatively charged $\text{LF}_{(\text{NaOH})}$ - β CD surface, significantly reducing adsorption capacity. These results suggest that repulsive forces play a more dominant role compared to the β -CD cavity-driven molecular capture, indicating a pH-dependent adsorption process. Based on these findings, further adsorption experiments were conducted with the solution pH 6.7 without adjustment.

3.3.2. Kinetics analysis

Batch experiments were conducted to evaluate the adsorption capacity of $\text{LF}_{(\text{NaOH})}$ - β CD for NIM over time. The experimental data are presented in Figure S4 and were fitted using the pseudo-first order (PFO) [52], pseudo-second order (PSO) [53], and Elovich [54] kinetic models, as detailed in the Supporting Information (Table S1). Kinetic parameters were determined via non-linear regression of the q_t versus t data. The best-fit model was identified based on the correlation coefficient (R^2) and chi-square (χ^2) values, which are summarized in Table 2.

Table 3-3.2: Kinetic parameters calculated for NIM adsorption onto $\text{LF}_{(\text{NaOH})}$ - β CD.

PFO				
$q_{e(\text{exp})}$ (mg/g)	$q_{e(\text{calc})}$ (mg/g)	k_1 (min^{-1})	R^2	χ^2
5.433	5.251	0.53	0.991	0.016
PSO				
$q_{e(\text{exp})}$ (mg/g)	$q_{e(\text{calc})}$ (mg/g)	k_2 (g mg/min)	R^2	χ^2
5.433	5.340	0.34	0.997	0.004
Elovich				

α	β	R^2
2.61×10^{14}	7.46	0.999

Note: Information about the equation for each model, as well as the definitions of the parameters and their units, is detailed in the Supporting Information.

The kinetic analysis indicates that NIM adsorption onto $LF_{(NaOH)}-\beta CD$ is best described by the Elovich model, which accounts for adsorption on heterogeneous surfaces with a rate that decreases exponentially as surface coverage increases [55]. Although commonly associated with chemisorption, the model can also describe systems where physisorption predominates [56], suggesting that the process involves a combination of both mechanisms. This interpretation is supported by the model constants: the high α value reflects rapid adsorption, while the lower β value relative to α indicates a progressive decrease in available adsorption sites [55].

3.3.3. Thermodynamic analysis

The effect of temperature on the adsorption of NIM on $LF_{(NaOH)}-\beta CD$ was investigated. Based on the collected data, thermodynamic parameters, including ΔG° , ΔH° , and ΔS° , were calculated and are summarized in Table S2 to assess the feasibility and nature of the adsorption process. In general lines, the negative ΔG° values at all tested temperatures indicate that the adsorption of NIM on $LF_{(NaOH)}-\beta CD$ occurs spontaneously. Furthermore, as the temperature increases, ΔG° becomes more negative, indicating that higher temperatures make the adsorption process more energetically favorable [57]. The positive ΔH° value confirms that the adsorption of NIM has an endothermic nature, meaning that elevated temperatures enhance the adsorption capacity. Additionally, since the ΔH° values are below 40 kJ/mol, the adsorption mechanism is likely physisorption

[58]. Considering the structure of NIM and the adsorbent, it is expected that the predominant interactions will be of the hydrophobic type, considering the hydrophobic cavity of β -CD and the low water solubility of NIM, as well as hydrogen interactions and p-p interactions, these possible interactions being physical [1]. The positive ΔS° value indicates an increase in randomness at the solid-liquid interface during adsorption [59]. Ravelet et al. [60] describe that water molecules in contact with nonpolar species adopt an ordered organization, and these water molecules are released when a solute is transferred from a polar phase to a nonpolar phase, increasing entropy ($\Delta S^\circ > 0$). Similar findings were reported by Pauletto et al. [58] on NIM adsorption onto activated carbon.

3.3.4. Isothermal analysis

The experimental and calculated equilibrium data for the adsorption of NIM onto $\text{LF}_{(\text{NaOH})}$ - β CD in batch experiments are presented in Figure S5. The Sips, Redlich-Peterson, and Hill isotherm models (Table S1) were employed to fit the experimental data. The mathematical parameters were estimated using the nonlinear regression method, and the results are summarized in Table 3.

Table 3-3.3: Isotherms parameters calculated for NIM adsorption onto $\text{LF}_{(\text{NaOH})}$ - β CD at 25 °C.

Sips				
q_{mS} (mg/g)	n_{S}	K_{S} (L/mg)	R^2	χ^2
5.368	0.462	2.302	0.994	0.010
Hill				
q_{mH} (mg/L)	n_{H} (J/mol)	K_{H} (mol ² /J ²)	R^2	χ^2
5.368	0.462	0.434	0.994	0.010
Redlich-Peterson				
a_{RP} (1/mg)	n_{RP}	K_{RP} (L/mg)	R^2	χ^2
83.090	0.871	301.886	0.966	0.066

Note: Information about the equation for each model, as well as the definitions of the parameters and their units, is detailed in the Supporting Information.

The analysis of the calculated data indicates that the adsorption of NIM onto $\text{LF}_{(\text{NaOH})}\text{-}\beta\text{CD}$ is well described by the Sips and Hill isotherms. Overall, these models exhibited the highest R^2 values and lowest χ^2 values [30]. The Sips model is a combination of the Langmuir and Freundlich isotherm equations, used for predicting heterogeneous adsorption systems while avoiding the drawback of continuous adsorbate increase, as seen in the Freundlich model [61]. This isotherm model becomes equivalent to the Freundlich model at low concentrations and is equivalent to the Langmuir model at high concentrations [62]. The Sips exponent (n_s), also known as the heterogeneity factor, indicates the nature of the adsorption process. A homogeneous adsorption process occurs when n_s is close to or exactly 1, while a heterogeneous adsorption process occurs when n_s is greater than 1. Herein, the value of n_s (0.462) suggests that the adsorption process occurred on a homogeneous surface and follows a pattern similar to the Langmuir model [63].

Since the Sips isotherm combines Langmuir monolayer adsorption (associated with chemisorption) and Freundlich heterogeneous surface adsorption (associated with physisorption), the coexistence of these mechanisms is consistent with the heterogeneous nature of the $\text{LF}_{(\text{NaOH})}\text{-}\beta\text{CD}$ surface and the molecular structure of NIM. The positive ΔH° value determined for the adsorption of NIM onto $\text{LF}_{(\text{NaOH})}\text{-}\beta\text{CD}$ (Table S2 indicates that the process is endothermic, suggesting that higher temperatures enhance the interactions between the adsorbent and the adsorbate. Although physisorption is typically favored at lower temperatures, the observed temperature dependence implies that the process is

not exclusively physical. Instead, the data support a mixed adsorption mechanism, where physical interactions, such as inclusion complexation within β -CD cavities [21,23], occur in parallel with chemical interactions, notably hydrogen bonding and π - π interactions, between NIM and functional groups on the bioadsorbent surface. Overall, the thermodynamic parameters are in good agreement with the adsorption behavior predicted by the Sips isotherm, reinforcing the conclusion that both physical and chemical mechanisms contribute to the overall adsorption process.

Apart from the Sips model, the Hill isotherm describes the binding of different adsorbates on a homogeneous adsorbent surface. The isotherm assumes that adsorption is a cooperative process, where the ligand binding capability at one site on a macromolecule influences other binding sites on the same macromolecule [64]. The cooperation in the adsorption process is quantified by the Hill coefficient (n_H). When $n_H = 1$, the binding is non-cooperative; when $n_H > 1$, binding exhibits positive cooperativity, and when $n_H < 1$, negative cooperativity is observed [65]. In this study, the n_H parameter is determined to be 0.462, suggesting negative cooperativity. This means that due to the complex formation between β -CD cavity and NIM, the ability of $\text{LF}_{(\text{NaOH})}$ - β CD to adsorb more drug molecules decreases. This complex relationship between the β -CD cavity and drugs via adsorptive process has been previously described by various other authors [63-65].

3.4. Fixed-bed column experiments

3.4.1. Effect of flow rate

The effect of flow rate on the adsorption of NIM on $\text{LF}_{(\text{NaOH})}\text{-}\beta\text{CD}$ is presented in Figure S6a and summarized in Table 4. In this experiment, the initial drug concentration (C_0) was fixed at 35 mg/L, and the bed height was set at 4.0 cm. The breakthrough time (t_b) varies from 87 to 183 min, while the exhaustion time (t_e) ranges from 427 to 560 min as the flow rate increases from 0.5 to 1.5 mL/min. These increases in flow rate enhance the driving force for mass transfer in the column, as well as the interaction between the NIM molecules and $\text{LF}_{(\text{NaOH})}\text{-}\beta\text{CD}$ [66]. Due to the increased driving force and influent volume, the equilibrium adsorption capacity (q_e) of NIM on $\text{LF}_{(\text{NaOH})}\text{-}\beta\text{CD}$ shows a significant increase, from 12.83 to 66.59 mg/g. However, as the flow rate rises from 1.0 to 1.5 mL/min, both t_b and t_e decrease. The higher flow rate reduces the contact time between the influent and the adsorbent bed, leading to less time for adsorption compared to lower flow rates [67]. This results in less drug capture by the adsorbent bed, causing a higher amount of NIM to pass through the column without being adsorbed. Based on that, the best flow rate for the adsorption process was 1.0 mL/min.

3.4.2. Effect of initial NIM concentration

The effect of the initial concentration (C_0) on the adsorption of NIM by $\text{LF}_{(\text{NaOH})}\text{-}\beta\text{CD}$ was studied at three concentrations (25, 30, and 35 mg/L), with a 4 cm bed height of the adsorbent and a flow rate adjusted to 0.5 mL/min. Figure S6b shows the breakthrough curve of NIM adsorption onto the tested adsorbent at different initial concentrations, and the analysis results are summarized in Table 4. The t_b decreases from 135 to 87 min, and t_e varies from 341 to 427 min as the initial NIM concentration increases from 25 to 35 mg/L. Overall, the q_e

increases from 8.71 to 12.83 mg/g with the increase in the initial NIM concentration. This can be explained by the fact that at higher concentrations, more adsorption sites become available and are occupied [10]. Additionally, the larger driving force at higher concentrations, likely due to the higher initial drug concentration, enhances the mass transfer process [68]. Conversely, lower concentrations lead to a smaller driving force, resulting in a decrease in the diffusion or mass transfer coefficient, which causes a less pronounced curve and shorter breakthrough and exhaustion times [8].

3.4.3 Effect of the adsorbent (bed) height

The effect of bed height on the adsorption of NIM is shown in Figure S6c and summarized in Table 4. For this experiment, the adsorbent (i.e., the bed) height was varied from 2 to 6 cm, the initial concentration was fixed at 35 mg/L, and the flow rate was set at 0.5 mL/min. As estimated, the t_b ranged from 42 to 439 min, while t_e varied from 184 to 901 min as the bed height increased from 2 to 6 cm. These changes in bed height directly resulted in improved equilibrium adsorption capacity (8.67 to 28.90 mg/g) and removal percentage (36.99% to 84.40%) as the bed height increased. The increase in bed height enhances the number of available adsorption sites and the time required for the drug solution to pass through the column, allowing the adsorption process to reach equilibrium more effectively [53]. Furthermore, a larger bed height provides a greater surface area, which increases the volume of solution that can be treated by the column [11]. The best bed height is 6 cm, and this height was adopted for the reuse experiments.

Table 3-3.4: Parameters of the breakthrough curve for NIM adsorption onto LF_(NaOH)- β CD.

Parameters		t_b (min)	t_e (min)	q_{total}	m_{total}	q_e (mg/g)	R (%)
Q (mL/min)	0.5	87	427	4.01	7.72	12.83	52.05
	1.0	496	773	22.54	27.41	72.03	82.27
	1.5	183	560	20.89	29.77	66.59	70.01
C₀ (mg/L)	25	135	341	2.72	4.50	8.71	60.61
	30	92	517	4.18	7.97	13.35	52.47
	35	87	427	4.01	7.72	12.83	52.05
Z (cm)	2	42	184	1.34	3.62	8.67	36.99
	4	87	427	4.02	7.72	12.83	52.05
	6	439	901	13.37	15.84	28.90	84.40

Although a formal design of experiments was not applied, the effect of each parameter (flow rate, inlet concentration, and bed height) was systematically assessed. To better visualize their combined impact on the adsorption of NIM, 3D contour plots were constructed and are presented in the Supplementary information (Figure S7).

3.5. Breakthrough curve modeling

The evaluation of breakthrough curves for the adsorption of NIM onto LF_(NaOH)- β CD was conducted using the Thomas [69], Adams-Bohart [70], and Clark [71] models (Table S1). The parameters for these breakthrough models were estimated using the nonlinear regression method, derived from fitting the experimental data to the mathematical models, and are summarized in Table 5.

Table 3-3.5: Breakthrough curve modellings calculated for NIM adsorption onto LF_(NaOH)- β CD at 25 °C.

Z (cm)	Q (mL/min)	C _o (mg/L)	Thomas model				Adams-Bohart model				Clark model			
			K _{Th} x 10 ⁻² (ml/mg min)	q _{Th} (mg/g)	R ²	χ^2	K _{AB} (mL/mg min)	N ₀ (mg/mL)	R ²	χ^2	r	A	R ²	χ^2
4	0.5	35	28.686	16.143	0.979	0.002	0.286	0.714	0.979	0.002	0.011	17.317	0.979	0.002
4	1.0	35	0.202	18570.672	0.965	0.007	0.002	822.195	0.965	0.007	0.010	2519.858	0.993	0.001
4	1.5	35	10.615	616.482	0.977	0.003	0.106	27.297	0.977	0.003	0.029	5897.593	0.989	0.001
4	0.5	25	5.591	168.017	0.979	0.003	0.055	7.438	0.979	0.003	0.023	266.491	0.980	0.003
4	0.5	30	7.535	67.889	0.972	0.002	0.075	3.005	0.972	0.002	0.010	22.792	0.972	0.002
2	0.5	35	43.113	33.827	0.985	0.002	0.431	1.478	0.985	0.002	0.061	139.034	0.989	0.001
6	0.5	35	3.218	62.490	0.916	0.010	0.032	2.725	0.916	0.010	0.004	6.349	0.916	0.010

Note: Information about the equation for each model, as well as the definitions of the parameters and their units, is detailed in the Supporting Information.

3.5.1. Thomas model

The Thomas model has two key characteristics: Langmuir adsorption-desorption kinetics, and second-order kinetics for the driving force rate, with no axial dispersion [72]. This model is widely used to evaluate column adsorption processes as it predicts the relationship between effluent concentration and time, fitting well in systems where the resistance to external and internal diffusion is negligible [73]. As shown in Table 4, the Thomas model effectively fits the experimental breakthrough curve data, as evidenced by the high correlation values obtained ($R^2 \geq 0.916$). Table 5 also presents the Thomas model constants, K_{Th} and q_{Th} , derived from the nonlinear fitting of the model to NIM removal by $LF_{(NaOH)}-\beta CD$ under various experimental conditions. The data indicate that increasing the flow rate from 0.5 to 1.0 mL/min, the initial NIM concentration from 25 to 35 mg/L, and the bed height from 2 to 6 cm result in a decrease in K_{Th} and an increase in q_{Th} [74]. The increase in bed height and NIM concentration influences the mass transfer rate. Specifically, the increase in these two parameters leads to a decrease in the mass transfer rate, prolonging the residence time between NIM molecules and $LF_{(NaOH)}-\beta CD$ [75]. Conversely, the flow rate affects the mobility of NIM molecules, and a slight increase in flow rate enhances mobility, thereby positively impacting the adsorbent performance [74].

3.5.2. Adams-Bohart model

The Adams-Bohart model was originally developed to describe adsorption processes in the gas phase and is typically applied to characterize the initial part of the breakthrough curve. This model is based on the principle that the

adsorption rate is proportional to both the remaining adsorption capacity of the adsorbent and the concentration of the adsorbate [75].

Table 4 presents the data obtained from the nonlinear fitting of the Adams-Bohart model for NIM removal by $\text{LF}_{(\text{NaOH})}\text{-}\beta\text{CD}$ under various operational conditions. As observed, the Adams-Bohart model exhibited significant correlation values ($R^2 \geq 0.916$), indicating that it also fits the experimental data well. It can be seen that by increasing the flow rate from 0.5 to 1.5 mL/min and the column height from 2 to 6 cm, the value of the Adams-Bohart kinetic constant (K_{AB}) decreases while the saturation concentration (N_0) increases. The flow rate is directly related to the mobility of the NIM molecules; thus, increasing the flow rate results in greater mobility, reducing the retention time of the molecules and lowering the value of K_{AB} [75]. The enhanced mobility of NIM molecules also leads to a rise in the saturation concentration value, as more molecules pass through the column with the increased flow rate. Additionally, increasing the column height increases the number of active sites, which boosts the transfer rate because there are more sites available to interact with the NIM molecules, leading to higher values of N_0 [74]. Moreover, increasing the NIM concentration raised the value of K_{AB} and decreased the value of N_0 . This can be explained by the fact that higher concentrations result in lower mass transfer resistance due to the greater driving force at higher concentrations. Consequently, the reduced mass transfer resistance leads to a smaller saturation concentration as the concentration increases [76].

3.5.2. Clark model

The Clark model is based on the concept of mass transfer combined with the Freundlich isotherm, and it also accounts for adsorption equilibrium to predict the nature of breakthrough curves. Additionally, this model assumes that the effluent flow through the column follows a piston-flow behavior .

The data obtained from the nonlinear fitting of the Clark model for the adsorption of NIM by $\text{LF}_{(\text{NaOH})}\text{-}\beta\text{CD}$ under various operational conditions are summarized in Table 5. The Clark model exhibited high correlation values ($R^2 \geq 0.916$), indicating that this model is also effective in fitting the experimental data. From the results, it can be observed that as the column size and NIM concentration increase, the Clark constants, r and A , decrease. In contrast, as the flow rate increases, the constants increase. The low values of the r constant suggest that rapid and efficient mass transfer occurred during the adsorption process. An increase in column size and initial NIM concentration leads to more available active sites for interaction, thus accelerating the mass transfer. However, as the flow rate increases, the contact time between the adsorbate and adsorbent decreases, resulting in a reduction in mass transfer efficiency. Based on the data present in Table 5, the Clark model is the one that presents the best fit.

3.5. Adsorption mechanism

As demonstrated by other authors [77,78], FTIR spectrophotometry is a valuable technique for investigating the chemical and physical alterations in the adsorbent structure resulting from the adsorption process. By analyzing the spectroscopic data obtained, adsorption mechanisms can be predicted at the

molecular level. Herein, FTIR spectra were recorded for the $\text{LF}_{(\text{NaOH})}\text{-}\beta\text{CD}$ sample before and after NIM flux adsorption, as well as for pure NIM (Figure 3), to gain insights into the adsorption mechanism. Upon analyzing the FTIR spectrum of the post-adsorption sample, several distinct changes were observed, confirming the presence of NIM in the post-utilized adsorbent. A broadband at 3300 cm^{-1} likely results from the overlap of N–H stretching from NIM and O–H stretching from $\beta\text{-CD}$ and LF. The band around 2900 cm^{-1} , attributed to C–H stretching, exhibited increased intensity compared to other bands in the same spectrum, reflecting a higher concentration of CH_x groups in the sample. Additionally, a new band appears at approximately 1586 cm^{-1} , corresponding to the aromatic C=C stretching vibrations in the NIM structure [79]. Another notable band, around 909 cm^{-1} , is associated with the stretching of the S–N bond present in NIM structure [80]. These newly emerging bands provide strong evidence for the adsorption of NIM onto $\text{LF}_{(\text{NaOH})}\text{-}\beta\text{CD}$.

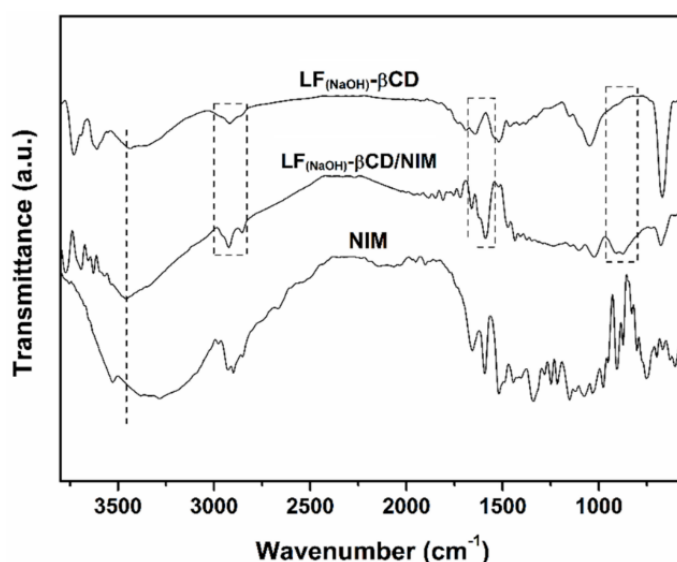
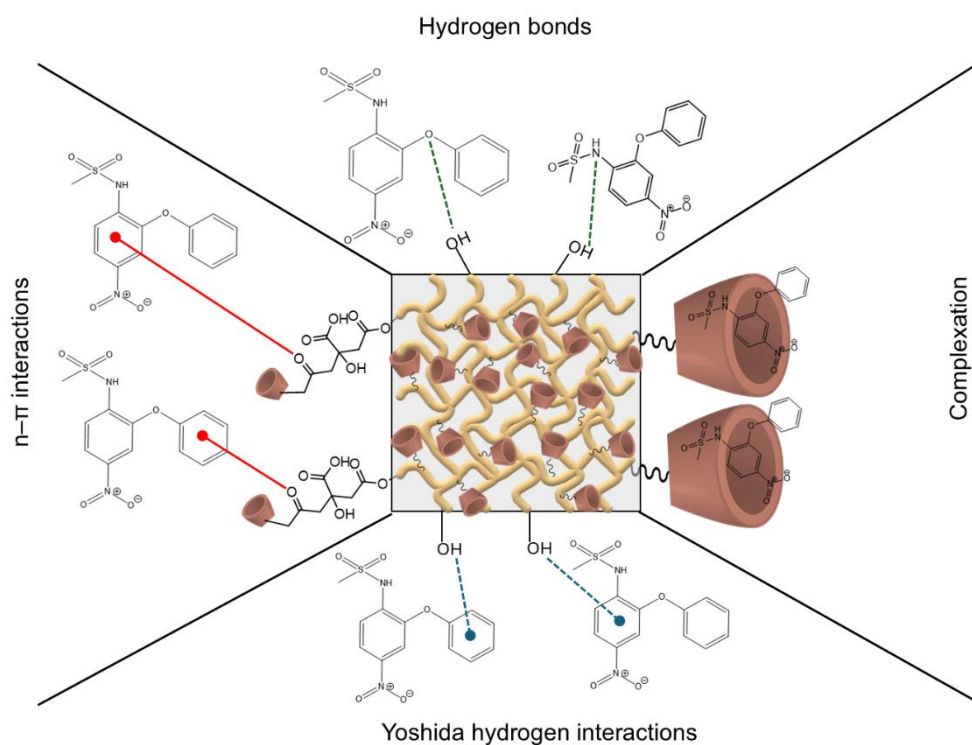


Figure 3-3.3: FTIR spectra of pure NIM, $\text{LF}_{(\text{NaOH})}\text{-}\beta\text{CD}$, and $\text{LF}_{(\text{NaOH})}\text{-}\beta\text{CD}$ after NIM adsorption (denoted as $\text{LF}_{(\text{NaOH})}\text{-}\beta\text{CD/NIM}$).

However, the absence of certain characteristic NIM bands provides insights into which portions of the molecule interacted with the internal cavity of β -CD. Specifically, the lack of bands around 1335 cm^{-1} and 1150 cm^{-1} , corresponding to the asymmetric and symmetric stretching of S=O bonds in the sulfonyl group, as well as the absence of bands around 1515 cm^{-1} and 1315 cm^{-1} , representing the asymmetric and symmetric stretching of N=O bonds in the aryl group, suggests that these functional groups are positioned within the internal cavity of β -CD [81,82]. A similar phenomenon was reported by Joudieh et al. [83], who observed that the unsubstituted aromatic ring remains exposed on the surface, whereas the substituted aromatic ring forms a complex within the β -CD cavity. Based on the FTIR results obtained in this study, an adsorption mechanism was proposed, as illustrated in Scheme 3.



Scheme 3. Schematic representation of the proposed adsorption mechanism of NIM onto LF_(NaOH)- β CD.

The adsorption of NIM onto $\text{LF}_{(\text{NaOH})}\text{-}\beta\text{CD}$ is governed by a combination of physical and chemical interactions. Host-guest inclusion complexation with $\beta\text{-CD}$ cavities plays a central role in the capture of NIM molecules, while additional interactions enhance the overall affinity. These include $n\text{--}\pi$ interactions between electron-donating oxygen-containing groups in $\text{LF}_{(\text{NaOH})}\text{-}\beta\text{CD}$ and the electron-accepting π system of the aromatic rings in NIM, as well as two types of hydrogen-related interactions: dipole–dipole hydrogen bonding, involving hydrogen atoms in the adsorbent and electronegative atoms in NIM (e.g., N, O), and Yoshida-type hydrogen bonding, which occurs between hydroxyl groups in $\text{LF}_{(\text{NaOH})}\text{-}\beta\text{CD}$ and the aromatic rings of NIM [5]. The FTIR spectra after adsorption corroborated the presence of these interactions through characteristic shifts. Thermodynamic parameters further confirmed that the adsorption process is endothermic and spontaneous, suggesting a significant contribution of chemisorption. This conclusion is consistent with the best fit of the equilibrium data to the Sips isotherm, which integrates features of Langmuir (monolayer, chemisorption) and Freundlich (heterogeneous, physisorption) models. These findings demonstrate that NIM removal by $\text{LF}_{(\text{NaOH})}\text{-}\beta\text{CD}$ arises from a synergistic combination of inclusion complexation (physisorption) and specific interactions (chemisorption), which collectively enhance the adsorption performance in fixed-bed systems. Therefore, the proposed mechanism is supported not only by FTIR spectroscopy but also by a robust dataset of adsorption experiments, providing a comprehensive understanding of the interactions driving NIM removal.

3.6. *Reuse experiments*

The regeneration ability of $\text{LF}_{(\text{NaOH})}$ - β CD was investigated under both batch and fixed-bed conditions. In batch mode, MeOH, a commonly reported eluent for β -CD-based adsorbents, did not achieve full recovery. Alternative eluents were evaluated, and while MeOH:NaOH (0.1 mol/L) promoted excessive desorption, likely due to partial material degradation, MeOH:HCl (0.15 mol/L) proved to be more effective, achieving ~73% desorption after 5 h. Jiang et al. [84] have previously demonstrated that combining MeOH with acids enhances regeneration efficiency in β -CD-containing adsorbents, supporting our findings. Using MeOH:HCl, the material was subjected to ten consecutive adsorption/desorption cycles (Figure 4a). The q_e values remained remarkably stable across all cycles, with variations below 10%, while desorption efficiencies consistently exceeded 70% (Figure 4b). These results demonstrate that $\text{LF}_{(\text{NaOH})}$ - β CD maintains its structural stability and adsorption ability after repeated use in batch systems, confirming the suitability of acidified solvents for regeneration.

In contrast, regeneration performance under dynamic fixed-bed operation was less efficient (Figure 4c). After the first cycle, the adsorbent did not reach $C_t/C_0 = 0.1$ in subsequent reuses, preventing complete breakthrough analysis. The t_e values varied across cycles, achieving 222, 264, and 173 min for the first, second, and third reuse, respectively. The increase from the first to the second cycle may be explained by cooperative adsorption effects as β -CD cavities became partially saturated, promoting adsorption in LF domains. However, by the third cycle, incomplete desorption of NIM led to faster saturation and a sharp decline in removal efficiency, which dropped from 95% to 32%. These results indicate that although acidified MeOH was highly effective in batch regeneration, its performance under flow conditions was limited. Similar decreases in

adsorption capacity due to incomplete regeneration have been reported in fixed-bed systems by Gizaw et al. [11] and Kumari et al. [35].

Taken together, these findings reveal a clear contrast between the two operational modes. While $\text{LF}_{(\text{NaOH})}$ - βCD demonstrates excellent reusability in batch mode with $\text{MeOH}:\text{HCl}$, its performance in fixed-bed systems still requires optimization, particularly in the choice of eluent and operational parameters. This highlights the importance of tailoring regeneration strategies to the operational context, especially when considering scale-up and continuous treatment applications.

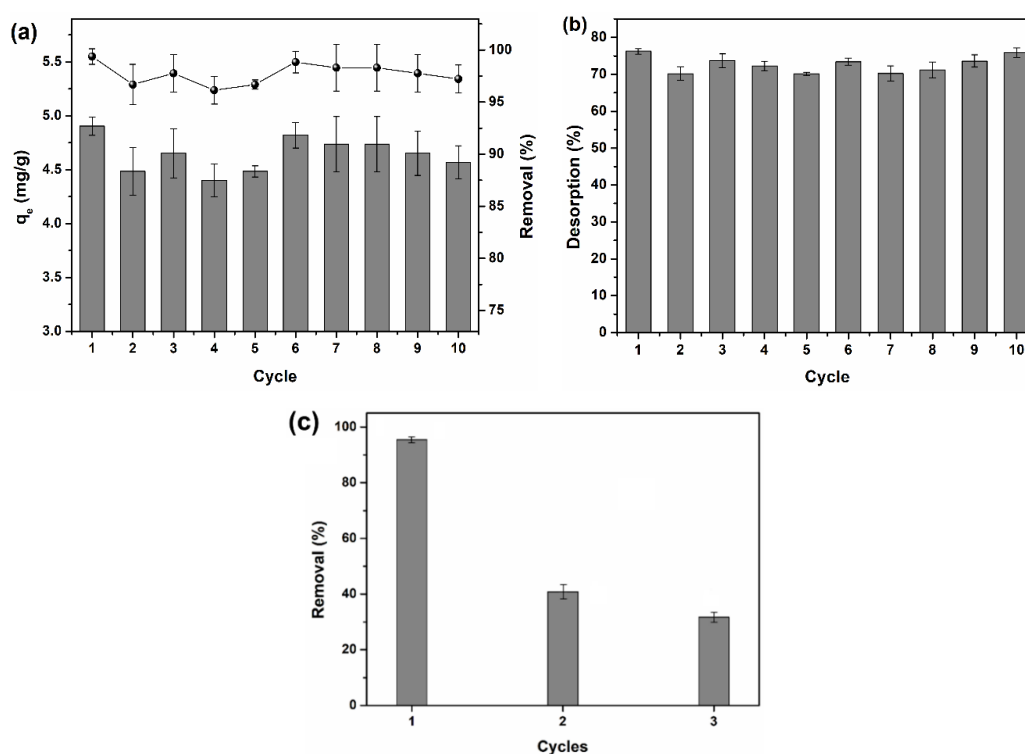


Figure 3-3.4: (a) Adsorption capacity (q_e) and removal efficiency of NIM by $\text{LF}_{(\text{NaOH})}$ - βCD during ten consecutive adsorption-desorption cycles in batch mode; (b) desorption efficiency of $\text{LF}_{(\text{NaOH})}$ - βCD in batch mode using $\text{MeOH}:\text{HCl}$ (0.15 mol/L) as eluent; (c) removal efficiency of NIM by $\text{LF}_{(\text{NaOH})}$ - βCD over three consecutive adsorption-desorption cycles in fixed-bed column experiments.

Table 6 summarizes selected NIM adsorption studies. Compared to previous work, it is evident that few studies have investigated NIM removal in fixed-bed column systems, most focusing on batch experiments. This highlights the relevance of the present study, as continuous-flow adsorption better simulates practical applications of the material as a potential filter. Furthermore, the results demonstrate that the developed adsorbent achieves a high q_e value even at a low initial adsorbent concentration, underscoring its efficiency in NIM removal.

The adsorbent developed here represents a highly promising, cost-effective, and sustainable solution for NIM removal in continuous-flow systems. It exhibits excellent adsorption capacity and is synthesized from renewable raw materials. The estimated production cost of $\text{LF}_{(\text{NaOH})}\text{-}\beta\text{CD}$ is approximately USD 1.77 per gram, which corresponds to the treatment of ~ 1 L of NIM-contaminated water under the conditions tested. This estimate includes all relevant laboratory-scale inputs, such as raw materials and chemicals, energy consumption for heating and drying, and water usage during washing and processing (see Table S3). This cost refers to bench-scale conditions and thus represents a conservative estimate. In larger and optimized production setups, where economies of scale reduce reagent and energy costs, the overall cost is expected to decrease significantly. For comparison, Patel et al. [85] reported a cost of USD 6.93 per kilogram (~ 0.007 per gram) for walnut shell biochar in ibuprofen removal, and other agro-waste-derived adsorbents for NSAIDs have consistently been described as renewable and low cost alternatives [5,85]. These comparisons reinforce the cost-effectiveness and practical scalability of $\text{LF}_{(\text{NaOH})}\text{-}\beta\text{CD}$ for the continuous treatment of emerging contaminants in water.

Table 3-3.6: Comparison between adsorption capacities (q_e) of some adsorbents tested in the removal of NIM from water.

Adsorbent	C_0 (mg/L)	Adsorption process	q_e (mg/g)	Ref.
Sludge based activated carbons	50	Batch	66.45	[86]
Cactus waste aerogel with ionic liquid (Cac/IL)	50	Batch	42.10	[5]
Reduced graphene oxide (rGO)	70	Batch	82.40	[77]
Activated carbon	30	Batch	67.83	[1]
LF _(NaOH) - β CD	35	Fixed-bed	72.03	<i>This work</i>

4. Conclusion

In this work, a novel bioadsorbent based on β -CD grafted onto alkaline-treated *Luffa cylindrica* fibers (namely, LF_(NaOH)- β CD) was successfully synthesized, characterized, and evaluated for the removal of the emerging contaminant nimesulide (NIM) from water. The central hypothesis - that β -CD grafting enhances adsorption performance through inclusion complexation and secondary interactions - was confirmed by adsorption data (batch and fixed-bed), isotherm and kinetic modeling, thermodynamic analysis, and FTIR characterization. Importantly, this study addresses two critical gaps in the literature: (i) the lack of bio-based adsorbents specifically designed for NIM removal, and (ii) the scarcity of fixed-bed column studies for NSAID elimination, which are more representative of real water treatment condition. As demonstrated, the LF_(NaOH)- β CD bioadsorbent exhibited high adsorption capacity (82.27 mg/g in fixed-bed systems), effective removal in tap water, and reusability over multiple batch cycles, demonstrating robustness and cost-effectiveness. Mechanistic insights revealed that adsorption is primarily governed by β -CD inclusion complexation, supported by hydrogen bonding and π - π interactions. While regeneration with methanol showed limited performance in column mode,

acidified MeOH improved desorption efficiency in batch studies, indicating viable optimization routes.

In summary, this work thus establishes $\text{LF}_{(\text{NaOH})}\text{-}\beta\text{CD}$ as a promising, sustainable, and scalable adsorbent for emerging contaminant removal. Future studies should optimize regeneration protocols, investigate competitive adsorption in complex matrices, and scale the system for real wastewater applications, advancing the transition of bio-based adsorbents from proof-of-concept to practical deployment.

References

- [1] P.S. Pauletto, S.F. Lütke, G.L. Dotto, N.P.G. Salau, Forecasting the multicomponent adsorption of nimesulide and paracetamol through artificial neural network, *Chem. Eng. J.* 412 (2021) 127527. <https://doi.org/10.1016/j.cej.2020.127527>.
- [2] S. Caldas, J. Arias, C. Rombaldi, L. Mello, M. Cerqueira, A. Martins, E. Primel, Occurrence of Pesticides and PPCPs in Surface and Drinking Water in Southern Brazil: Data on 4-Year Monitoring, *J. Braz. Chem. Soc.* 30 (2018) 71–80. <https://doi.org/10.21577/0103-5053.20180154>.
- [3] P.S. Pauletto, S.F. Lütke, G.L. Dotto, N.P.G. Salau, Exploring the simultaneous mass transport of nimesulide and paracetamol adsorption on activated carbon: A PVSDM approach, *Sep. Purif. Technol.* 329 (2024) 125148. <https://doi.org/10.1016/j.seppur.2023.125148>.
- [4] N.P. Shetti, S.J. Malode, S.D. Bukkitgar, G.B. Bagihalli, R.M. Kulkarni, S.B. Pujari, K.R. Reddy, Electro-oxidation and determination of nimesulide at nanosilica modified sensor, *Mater. Sci. Energy Technol.* 2 (2019) 396–400. <https://doi.org/10.1016/j.mset.2019.03.005>.
- [5] G. Viscusi, S. Mottola, Y. Boumezough, S. Arris, I. De Marco, G. Gorrasi, A novel porous adsorbentbased on cactus powder/ionic liquid for the removal of nimesulide from wastewater, *Chemosphere.* 376 (2025) 144293. <https://doi.org/10.1016/j.chemosphere.2025.144293>.

- [6] A. Medici, M. Sarakha, G. Di Fabio, M. Brigante, A. Zarrelli, Efficient Nimesulide degradation via chlorination and sun-simulated radiation: Kinetic insights, reactive species formation, and application to real wastewater, *J. Environ. Chem. Eng.* 12 (2024) 113247. <https://doi.org/10.1016/j.jece.2024.113247>.
- [7] Z. Jiang, S.-H. Ho, X. Wang, Y. Li, C. Wang, Application of biodegradable cellulose-based biomass materials in wastewater treatment, *Environ. Pollut.* 290 (2021) 118087. <https://doi.org/10.1016/j.envpol.2021.118087>.
- [8] A. Leudjo Taka, M.J. Klink, X. Yangkou Mbianda, E.B. Naidoo, Chitosan nanocomposites for water treatment by fixed-bed continuous flow column adsorption: A review, *Carbohydr. Polym.* 255 (2021) 117398. <https://doi.org/10.1016/j.carbpol.2020.117398>.
- [9] H. Patel, Comparison of batch and fixed bed column adsorption: a critical review, *Int. J. Environ. Sci. Technol.* 19 (2022) 10409–10426. <https://doi.org/10.1007/s13762-021-03492-y>.
- [10] J. Tejedor, R. Álvarez-Briceño, V.H. Guerrero, C.A. Villamar-Ayala, Removal of caffeine using agro-industrial residues in fixed-bed columns: Improving the adsorption capacity and efficiency by selecting adequate physical and operational parameters, *J. Water Process Eng.* 53 (2023) 103778. <https://doi.org/10.1016/j.jwpe.2023.103778>.
- [11] A. Gizaw, F. Zewge, Y. Chebude, A. Mekonnen, M. Tesfaye, Simultaneous nitrate and phosphate abatement using calcium silicate hydrate adsorbent: Fixed bed column adsorption study, *Surfaces and Interfaces.* 30 (2022) 101961. <https://doi.org/10.1016/j.surfin.2022.101961>.
- [12] H. Patel, Fixed-bed column adsorption study: a comprehensive review, *Appl. Water Sci.* 9 (2019) 45. <https://doi.org/10.1007/s13201-019-0927-7>.
- [13] R. Coutinho, H.Y. Hoshima, M.T.G. Vianna, M. Marques, Sustainable application of modified *Luffa cylindrica* biomass for removal of trimethoprim in water by adsorption with process optimization, *Environ. Sci. Pollut. Res.* 31 (2024) 55280–55300. <https://doi.org/10.1007/s11356-024-34797-3>.
- [14] R.R.M. de Freitas, K.P. do Carmo, J. de Souza Rodrigues, V.H. de Lima, J. Osmari da Silva, V.R. Botaro, Influence of alkaline treatment on sisal fibre applied as reinforcement agent in composites of corn starch and cellulose acetate

- matrices, *Plast. Rubber Compos.* 50 (2021) 9–17.
<https://doi.org/10.1080/14658011.2020.1816119>.
- [15] Y. Lv, J. Ma, K. Liu, Y. Jiang, G. Yang, Y. Liu, C. Lin, X. Ye, Y. Shi, M. Liu, L. Chen, Rapid elimination of trace bisphenol pollutants with porous β -cyclodextrin modified cellulose nanofibrous membrane in water: adsorption behavior and mechanism, *J. Hazard. Mater.* 403 (2021) 123666.
<https://doi.org/10.1016/j.jhazmat.2020.123666>.
- [16] H.M. Abdullah, S.S. Ahmed, B.A. Abdulghafar, S.A. Yasin, S.Y.S. Zeebaree, A.Y.S. Zeebaree, O.I.H. Zebari, Enhanced water treatment with TEMPO-modified luffa cellulose-PVA nanofiber composite for removal of hexavalent chromium, *Results Chem.* 8 (2024) 101582. <https://doi.org/10.1016/j.rechem.2024.101582>.
- [17] B.M. Ibrahim, N.A. Fakhre, M.G. Jalhoom, I.N. Qader, H.Y. Shareef, A.F. Jalal, Removal of lead ions from aqueous solutions by modified cellulose, *Environ. Technol.* 45 (2024) 2335–2347.
<https://doi.org/10.1080/09593330.2022.2056086>.
- [18] W. Ge, J. Shuai, Y. Wang, Y. Zhou, X. Wang, Progress on chemical modification of cellulose in “green” solvents, *Polym. Chem.* 13 (2022) 359–372.
<https://doi.org/10.1039/D1PY00879J>.
- [19] J. Qu, Y. Yuan, Q. Meng, G. Zhang, F. Deng, L. Wang, Y. Tao, Z. Jiang, Y. Zhang, Simultaneously enhanced removal and stepwise recovery of atrazine and Pb(II) from water using β -cyclodextrin functionalized cellulose: Characterization, adsorptive performance and mechanism exploration, *J. Hazard. Mater.* 400 (2020) 123142. <https://doi.org/10.1016/j.jhazmat.2020.123142>.
- [20] A.M. Ares, R. Muiño, A. Costoya, R.A. Lorenzo, A. Concheiro, A.M. Carro, C. Alvarez-Lorenzo, Cyclodextrin-functionalized cellulose filter paper for selective capture of diclofenac, *Carbohydr. Polym.* 220 (2019) 43–52.
<https://doi.org/10.1016/j.carbpol.2019.05.055>.
- [21] M.M. Altayan, N. Tzoupanos, M. Barjenbruch, Polymer based on beta-cyclodextrin for the removal of bisphenol A, methylene blue and lead(II): Preparation, characterization, and investigation of adsorption capacity, *J. Mol. Liq.* 390 (2023) 122822. <https://doi.org/10.1016/j.molliq.2023.122822>.
- [22] R. Guo, H. Liu, K. Yang, S. Wang, P. Sun, H. Gao, B. Wang, F. Chen, β -Cyclodextrin Polymerized in Cross-Flowing Channels of Biomass Sawdust for Rapid and Highly Efficient Pharmaceutical Pollutants Removal from Water, *ACS*

- Appl. Mater. Interfaces. 12 (2020) 32817–32826.
<https://doi.org/10.1021/acsami.0c08729>.
- [23] J. Liu, J. Zhou, Z. Wu, X. Tian, X. An, Y. Zhang, G. Zhang, F. Deng, X. Meng, J. Qu, Concurrent elimination and stepwise recovery of Pb(II) and bisphenol A from water using β -cyclodextrin modified magnetic cellulose: adsorption performance and mechanism investigation, *J. Hazard. Mater.* 432 (2022) 128758. <https://doi.org/10.1016/j.jhazmat.2022.128758>.
- [24] L.O. Mota, Y.A. de Almeida, D.F. Bispo, M.F.F. Souza, D.C. Santos, R.A.L. Sobrinho, I.F. Gimenez, Preparation of TEMPO-Oxidized Cellulose Hydrogels Modified with β -Cyclodextrin and κ -Carrageenan for Potential Adsorption Applications, *ACS Omega*. 10 (2025) 972–984. <https://doi.org/10.1021/acsomega.4c08188>.
- [25] R. Arefizadeh, A. Dadkhah Tehrani, A Dual-Functional Nano-Based Platform: Dialdehyde- β -Cyclodextrin-Modified Cellulose Nanowhiskers for Enhanced Curcumin Delivery and Efficient Dye Removal, *Fibers Polym.* 26 (2025) 2281–2296. <https://doi.org/10.1007/s12221-025-00976-3>.
- [26] M. Rehan, S.A. Mahmoud, H.M. Mashaly, B.M. Youssef, β -Cyclodextrin assisted simultaneous preparation and dyeing acid dyes onto cotton fabric, *React. Funct. Polym.* 151 (2020) 104573. <https://doi.org/10.1016/j.reactfunctpolym.2020.104573>.
- [27] X. Feng, Z. Xiao, S. Sui, Q. Wang, Y. Xie, Esterification of wood with citric acid: The catalytic effects of sodium hypophosphite (SHP), *Holzforschung*. 68 (2014) 427–433. <https://doi.org/10.1515/hf-2013-0122>.
- [28] M. Mihailiasa, F. Caldera, J. Li, R. Peila, A. Ferri, F. Trotta, Preparation of functionalized cotton fabrics by means of melatonin loaded β -cyclodextrin nanosponges, *Carbohydr. Polym.* 142 (2016) 24–30. <https://doi.org/10.1016/j.carbpol.2016.01.024>.
- [29] M.P. Moreira, G.R.S. Andrade, M.V.G. de Araujo, T. Kubota, I.F. Gimenez, Ternary cyclodextrin polyurethanes containing phosphate groups: Synthesis and complexation of ciprofloxacin, *Carbohydr. Polym.* 151 (2016) 557–564. <https://doi.org/10.1016/j.carbpol.2016.05.101>.
- [30] S. Yadav, A. Asthana, A.K. Singh, R. Chakraborty, S.S. Vidya, M.A.B.H. Susan, S.A.C. Carabineiro, Adsorption of cationic dyes, drugs and metal from aqueous solutions using a polymer composite of magnetic/ β -

- cyclodextrin/activated charcoal/Na alginate: Isotherm, kinetics and regeneration studies, *J. Hazard. Mater.* 409 (2021) 124840. <https://doi.org/10.1016/j.jhazmat.2020.124840>.
- [31] S. Singh, R. Jelinek, Solar-mediated oil-spill cleanup by a carbon dot-polyurethane sponge, *Carbon* N. Y. 160 (2020) 196–203. <https://doi.org/10.1016/j.carbon.2020.01.016>.
- [32] R. Sips, Combined form of Langmuir and Freundlich equations. , *J. Chem. Phys.* 16 (1948) 490–495.
- [33] O. Redlich, D.L. Peterson, A Useful Adsorption Isotherm, *J. Phys. Chem.* 63 (1959) 1024–1024. <https://doi.org/10.1021/j150576a611>.
- [34] T.L. Hill, Statistical Mechanics of Multimolecular Adsorption II. Localized and Mobile Adsorption and Absorption, *J. Chem. Phys.* 14 (1946) 441–453. <https://doi.org/10.1063/1.1724166>.
- [35] U. Kumari, A. Mishra, H. Siddiqi, B.C. Meikap, Effective defluoridation of industrial wastewater by using acid modified alumina in fixed-bed adsorption column: Experimental and breakthrough curves analysis, *J. Clean. Prod.* 279 (2021) 123645. <https://doi.org/10.1016/j.jclepro.2020.123645>.
- [36] O. León, A. Muñoz-Bonilla, D. Soto, D. Pérez, M. Rangel, M. Colina, M. Fernández-García, Removal of anionic and cationic dyes with bioadsorbent oxidized chitosans, *Carbohydr. Polym.* 194 (2018) 375–383. <https://doi.org/10.1016/j.carbpol.2018.04.072>.
- [37] P.G. Cadena, E.C. Oliveira, A.N. Araújo, M.C.B.S.M. Montenegro, M.C.B. Pimentel, J.L. Lima Filho, V.L. Silva, Simple Determination of Deoxycholic and Ursodeoxycholic Acids by Phenolphthalein- β -Cyclodextrin Inclusion Complex, *Lipids*. 44 (2009) 1063–1070. <https://doi.org/10.1007/s11745-009-3353-z>.
- [38] K. Hemine, N. Łukasik, M. Gazda, I. Nowak, β -cyclodextrin-containing polymer based on renewable cellulose resources for effective removal of ionic and non-ionic toxic organic pollutants from water, *J. Hazard. Mater.* 418 (2021) 126286. <https://doi.org/10.1016/j.jhazmat.2021.126286>.
- [39] C. Ye, N. Hu, Z. Wang, Experimental investigation of *Luffa cylindrica* as a natural sorbent material for the removal of a cationic surfactant, *J. Taiwan Inst. Chem. Eng.* 44 (2013) 74–80. <https://doi.org/10.1016/j.jtice.2012.08.006>.
- [40] M.B. Martinez-Pavetti, L. Medina, M. Espínola, M. Monteiro, Study on two eco-friendly surface treatments on *Luffa cylindrica* for development of

reinforcement and processing materials, *J. Mater. Res. Technol.* 14 (2021) 2420–2427. <https://doi.org/10.1016/j.jmrt.2021.07.141>.

[41] S. Noone, K. Purushothaman, R. Pradhan, An investigation on luffa cylindrica fiber reinforced epoxy composite, *Mater. Today Proc.* 33 (2020) 1026–1031. <https://doi.org/10.1016/j.matpr.2020.07.051>.

[42] A. Rukmani, M. Sundrarajan, Inclusion of antibacterial agent thymol on β -cyclodextrin-grafted organic cotton, *J. Ind. Text.* 42 (2012) 132–144. <https://doi.org/10.1177/1528083711430244>.

[43] Z. Naderi, J. Azizian, E. Moniri, N. Farhadyar, Synthesis and Characterization of Carboxymethyl Cellulose/ β -Cyclodextrin/Chitosan Hydrogels and Investigating the Effect of Magnetic Nanoparticles (Fe_3O_4) on a Novel Carrier for a Controlled Release of Methotrexate as Drug Delivery, *J. Inorg. Organomet. Polym. Mater.* 30 (2020) 1339–1351. <https://doi.org/10.1007/s10904-019-01301-1>.

[44] D. Mohana Krishnudu, D. Sreeramulu, P. Venkateshwar Reddy, Synthesis and characterization of coir and luffa cylindrica filled with CaCO_3 hybrid composites, *Int. J. Integr. Eng.* 11 (2019) 290–298. <https://doi.org/10.30880/ijie.2019.11.01.029>.

[45] G. Barra, L. Guadagno, M. Raimondo, M.G. Santonicola, E. Toto, S. Vecchio Cipriotti, A Comprehensive Review on the Thermal Stability Assessment of Polymers and Composites for Aeronautics and Space Applications, *Polymers (Basel)*. 15 (2023) 3786. <https://doi.org/10.3390/polym15183786>.

[46] H. Sadaquat, M. Akhtar, Comparative effects of β -cyclodextrin, HP- β -cyclodextrin and SBE7- β -cyclodextrin on the solubility and dissolution of docetaxel via inclusion complexation, *J. Incl. Phenom. Macrocycl. Chem.* 96 (2020) 333–351. <https://doi.org/10.1007/s10847-020-00977-0>.

[47] N.H. Abdul Manas, N.K.M.F. Kumar, N.A. Mohd Shah, G.Y. Ling, N.I.W. Azelee, S.F.Z.M. Fuzi, N. Masngut, M.A.H. Bunyamin, R.M. Illias, H.A. El Enshasy, Adsorption of Fatty Acid on Beta-Cyclodextrin Functionalized Cellulose Nanofiber, *Sustainability*. 15 (2023) 1559. <https://doi.org/10.3390/su15021559>.

[48] K.U. Khan, M.U. Minhas, S.F. Badshah, M. Sohail, R.M. Sarfraz, β -cyclodextrin modification by cross-linking polymerization as highly porous nanomatrices for olanzapine solubility improvement; synthesis, characterization and bio-compatibility evaluation, *J. Drug Deliv. Sci. Technol.* 67 (2022) 102952. <https://doi.org/10.1016/j.jddst.2021.102952>.

- [49] A.G. Al Lafi, J. Al Abdullah, Y. Amin, G. Alsayes, N. Al-Kafri, The effects of pH on the structure of polystyrene-nano manganese dioxide composites, *J. Mol. Struct.* 1237 (2021) 130315. <https://doi.org/10.1016/j.molstruc.2021.130315>.
- [50] Z. Fallah, H.N. Isfahani, M. Tajbakhsh, Removal of fluoride ion from aqueous solutions by titania-grafted β -cyclodextrin nanocomposite, *Environ. Sci. Pollut. Res.* 27 (2020) 3281–3294. <https://doi.org/10.1007/s11356-019-06948-4>.
- [51] H. Ferreira, M. Lúcio, B. de Castro, P. Gameiro, J.L.F.C. Lima, S. Reis, Partition and location of nimesulide in EPC liposomes: a spectrophotometric and fluorescence study, *Anal. Bioanal. Chem.* 377 (2003) 293–298. <https://doi.org/10.1007/s00216-003-2089-5>.
- [52] S.K. Lagergren, About the theory of so-called adsorption of soluble substances, *Sven. Vetenskapsakad. Handlingar*. 24 (1898) 1–39.
- [53] Y.. Ho, G. McKay, Pseudo-second order model for sorption processes, *Process Biochem.* 34 (1999) 451–465. [https://doi.org/10.1016/S0032-9592\(98\)00112-5](https://doi.org/10.1016/S0032-9592(98)00112-5).
- [54] Y.S. Ho, G. McKay, Application of Kinetic Models to the Sorption of Copper(II) on to Peat, *Adsorpt. Sci. Technol.* 20 (2002) 797–815. <https://doi.org/10.1260/026361702321104282>.
- [55] J. Lach, Adsorption of sulfacetamide on commercial activated carbons: statistics and kinetics of adsorption, *Desalin. Water Treat.* 274 (2022) 173–186. <https://doi.org/10.5004/dwt.2022.28913>.
- [56] M.Z. Momčilović, V. Dodevski, S. Krstić, M. Petrović, L. Suručić, A. Nešić, A.L. Bojić, Aqueous-Phase Uptake of Amlodipine Besylate by Activated Carbon Derived from Dwarf Elder, *Processes*. 13 (2025) 1483. <https://doi.org/10.3390/pr13051483>.
- [57] J.L.S. Fagundez, M.S. Netto, G.L. Dotto, N.P.G. Salau, A new method of developing ANN-isotherm hybrid models for the determination of thermodynamic parameters in the adsorption of ions Ag^+ , Co^{2+} and Cu^{2+} onto zeolites ZSM-5, HY, and 4A, *J. Environ. Chem. Eng.* 9 (2021) 106126. <https://doi.org/10.1016/j.jece.2021.106126>.
- [58] P.S. Pauletto, S.F. Lütke, G.L. Dotto, N.P.G. Salau, Adsorption mechanisms of single and simultaneous removal of pharmaceutical compounds onto activated carbon: Isotherm and thermodynamic modeling, *J. Mol. Liq.* 336 (2021) 116203. <https://doi.org/10.1016/j.molliq.2021.116203>.

- [59] M.H. Mahmoudian, A. Azari, A. Jahantigh, M. Sarkhosh, M. Yousefi, S.A. Razavinasab, M. Afsharizadeh, F. Mohammadi Shahraji, A. Pour Pasandi, A. Zeidabadi, T. Ilaghinezhad Bardsiri, M. Ghasemian, Statistical modeling and optimization of dexamethasone adsorption from aqueous solution by Fe₃O₄@NH₂-MIL88B nanorods: Isotherm, Kinetics, and Thermodynamic, *Environ. Res.* 236 (2023) 116773. <https://doi.org/10.1016/j.envres.2023.116773>.
- [60] C. Ravelet, A. Geze, A. Villet, C. Grosset, A. Ravel, D. Wouessidjewe, E. Peyrin, Chromatographic determination of the association constants between nimesulide and native and modified β -cyclodextrins, *J. Pharm. Biomed. Anal.* 29 (2002) 425–430. [https://doi.org/10.1016/S0731-7085\(02\)00088-2](https://doi.org/10.1016/S0731-7085(02)00088-2).
- [61] C.M.B. de Araujo, M.G. Ghislandi, A.G. Rios, G.R.B. da Costa, B.F. do Nascimento, A.F.P. Ferreira, M.A. da Motta Sobrinho, A.E. Rodrigues, Wastewater treatment using recyclable agar-graphene oxide biocomposite hydrogel in batch and fixed-bed adsorption column: Bench experiments and modeling for the selective removal of organics, *Colloids Surfaces A Physicochem. Eng. Asp.* 639 (2022) 128357. <https://doi.org/10.1016/j.colsurfa.2022.128357>.
- [62] D.F. dos Santos, W.M. Moreira, T.P. de Araújo, M.M.S. Bernardo, I.M. de Figueiredo Ligeiro da Fonseca, I.C. Ostroski, M.A.S.D. de Barros, Competitive adsorption of acetaminophen and caffeine onto activated Tingui biochar: characterization, modeling, and mechanisms, *Environ. Sci. Pollut. Res.* 31 (2023) 53611–53628. <https://doi.org/10.1007/s11356-023-31024-3>.
- [63] T.Z.E. Lee, J. Zhang, Y. Feng, X. Lin, J. Zhou, Adsorption of Cd(II) Ions by Coconut Copra: Isotherm and Regeneration Studies, *IOP Conf. Ser. Earth Environ. Sci.* 657 (2021) 012026. <https://doi.org/10.1088/1755-1315/657/1/012026>.
- [64] N.S. Yousef, R. Farouq, R. Hazzaa, Adsorption kinetics and isotherms for the removal of nickel ions from aqueous solutions by an ion-exchange resin: application of two and three parameter isotherm models, *Desalin. Water Treat.* 57 (2016) 21925–21938. <https://doi.org/10.1080/19443994.2015.1132474>.
- [65] M.A. Al-Ghouti, D.A. Da'ana, Guidelines for the use and interpretation of adsorption isotherm models: A review, *J. Hazard. Mater.* 393 (2020) 122383. <https://doi.org/10.1016/j.jhazmat.2020.122383>.
- [66] L. Xu, S. Wang, J. Zhou, H. Deng, R.L. Frost, Column adsorption of 2-naphthol from aqueous solution using carbon nanotube-based composite

- adsorbent, *Chem. Eng. J.* 335 (2018) 450–457.
<https://doi.org/10.1016/j.cej.2017.10.176>.
- [67] N. Fallah, M. Taghizadeh, Continuous fixed-bed adsorption of Mo(VI) from aqueous solutions by Mo(VI)-IIP: Breakthrough curves analysis and mathematical modeling, *J. Environ. Chem. Eng.* 8 (2020) 104079.
<https://doi.org/10.1016/j.jece.2020.104079>.
- [68] Z. Yang, X. Liu, X. Liu, J. Wu, X. Zhu, Z. Bai, Z. Yu, Preparation of β -cyclodextrin/graphene oxide and its adsorption properties for methylene blue, *Colloids Surfaces B Biointerfaces*. 200 (2021) 111605.
<https://doi.org/10.1016/j.colsurfb.2021.111605>.
- [69] H.C. Thomas, chromatography: a problem in kinetics, *Ann. N. Y. Acad. Sci.* 49 (1948) 161–182. <https://doi.org/10.1111/j.1749-6632.1948.tb35248.x>.
- [70] G.S. Bohart, E.Q. Adams, Some aspects of the behavior of charcoal with respect to chlorine, *J. Am. Chem. Soc.* 42 (1920) 523–544.
<https://doi.org/10.1021/ja01448a018>.
- [71] R.M. Clark, Evaluating the cost and performance of field-scale granular activated carbon systems, *Environ. Sci. Technol.* 21 (1987) 573–580.
<https://doi.org/10.1021/es00160a008>.
- [72] T.N. Ang, B.R. Young, M. Taylor, R. Burrell, M.K. Aroua, S. Baroutian, Breakthrough analysis of continuous fixed-bed adsorption of sevoflurane using activated carbons, *Chemosphere*. 239 (2020) 124839.
<https://doi.org/10.1016/j.chemosphere.2019.124839>.
- [73] O.B. Omitola, M.N. Abonyi, K.G. Akpomie, F.A. Dawodu, Adams-Bohart, Yoon-Nelson, and Thomas modeling of the fix-bed continuous column adsorption of amoxicillin onto silver nanoparticle-maize leaf composite, *Appl. Water Sci.* 12 (2022) 94. <https://doi.org/10.1007/s13201-022-01624-4>.
- [74] S.V. Manjunath, M. Kumar, Simultaneous removal of antibiotic and nutrients via *Prosopis juliflora* activated carbon column: Performance evaluation, effect of operational parameters and breakthrough modeling, *Chemosphere*. 262 (2021) 127820. <https://doi.org/10.1016/j.chemosphere.2020.127820>.
- [75] E. Salehi, M. Askari, Y. Darvishi, Novel combinatorial extensions to breakthrough curve modeling of an adsorption column — Depth filtration hybrid process, *J. Ind. Eng. Chem.* 86 (2020) 232–243.
<https://doi.org/10.1016/j.jiec.2020.03.015>.

- [76] T.C.P. Tran, T.P. Nguyen, X.C. Nguyen, X.H. Nguyen, T.A.H. Nguyen, T.T.N. Nguyen, T.Y.B. Vo, T.H.G. Nguyen, T.T.H. Nguyen, T.D.H. Vo, P. Senthil Kumar, M.-J. Um, D.D. Nguyen, Adsorptive removal of phosphate from aqueous solutions using low-cost modified biochar-packed column: Effect of operational parameters and kinetic study, *Chemosphere*. 309 (2022) 136628. <https://doi.org/10.1016/j.chemosphere.2022.136628>.
- [77] I.M. Jauris, C.F. Matos, A.J.G. Zarbin, C.S. Umpierres, C. Saucier, E.C. Lima, S.B. Fagan, I. Zanella, F.M. Machado, Adsorption of anti-inflammatory nimesulide by graphene materials: a combined theoretical and experimental study, *Phys. Chem. Chem. Phys.* 19 (2017) 22099–22110. <https://doi.org/10.1039/C7CP04272H>.
- [78] T. Kekes, C. Tzia, Adsorption of indigo carmine on functional chitosan and β -cyclodextrin/chitosan beads: Equilibrium, kinetics and mechanism studies, *J. Environ. Manage.* 262 (2020) 110372. <https://doi.org/10.1016/j.jenvman.2020.110372>.
- [79] M. Georgescu, V. Meltzer, I. Stănculescu, E. Pincu, Thermal Behavior of the Nimesulide-Salicylic Acid Eutectic Mixtures Prepared by Mechanochemistry and Recrystallization, *Materials (Basel)*. 14 (2021) 7715. <https://doi.org/10.3390/ma14247715>.
- [80] S.H. Auda, Nimesulide/Methyl β -Cyclodextrin Inclusion Complexes: Physicochemical Characterization, Solubility, Dissolution, and Biological Studies, *Drug Dev. Res.* 75 (2014) 68–75. <https://doi.org/10.1002/ddr.21156>.
- [81] A.C. de Almeida, P.O. Ferreira, M.V. Porto, J. Canotilho, R.A.E. de Castro, F.J. Caires, M.E. da Silva Eusébio, Novel nimesulide multicomponent solid forms: screening, synthesis, thermoanalytical study and characterization, *J. Therm. Anal. Calorim.* 150 (2024) 6885–6897. <https://doi.org/10.1007/s10973-024-13189-2>.
- [82] M. Rybczyńska, A. Sikorski, The synthesis, thermal behaviour, spectral and structural characterization, and in silico prediction of pharmacokinetic parameters of tetraalkylammonium salts of non-steroidal anti-inflammatory drug nimesulide, *Sci. Rep.* 13 (2023) 17268. <https://doi.org/10.1038/s41598-023-44557-x>.
- [83] S. Joudieh, M. Lahiani-Skiba, P. Bon, O. Ba, J. Le Breton, M. Skiba, Nimesulide Apparent Solubility Enhancement with Natural Cyclodextrins and

their Polymers, Lett. Drug Des. Discov. 5 (2008) 406–415.
<https://doi.org/10.2174/157018008785777270>.

[84] M. Jiang, R. Simayi, A. Sawut, J. Wang, T. Wu, X. Gong, Modified β -Cyclodextrin hydrogel for selective adsorption and desorption for cationic dyes, Colloids Surfaces A Physicochem. Eng. Asp. 661 (2023) 130912.
<https://doi.org/10.1016/j.colsurfa.2022.130912>.

[85] M. Patel, A.K. Chaubey, C.U. Pittman, D. Mohan, Aqueous ibuprofen sorption by using activated walnut shell biochar: process optimization and cost estimation, Environ. Sci. Adv. 1 (2022) 530–545.
<https://doi.org/10.1039/D2VA00015F>.

[86] G.S. dos Reis, M.K. Bin Mahbub, M. Wilhelm, E.C. Lima, C.H. Sampaio, C. Saucier, S.L. Pereira Dias, Activated carbon from sewage sludge for removal of sodium diclofenac and nimesulide from aqueous solutions, Korean J. Chem. Eng. 33 (2016) 3149–3161. <https://doi.org/10.1007/s11814-016-0194-3>.

[87] L.A. Rohen, A.C.C. Neves, D. de P. Mantovani, F. V. Carlos Maurício, J. da Silva Vieira, L. de A. Pontes, F.M. Margem, S. Monteiro, Hemp Fiber Density Using the Pycnometry Technique, in: 2017: p. 423–428.
https://doi.org/10.1007/978-3-319-51382-9_46.

Supporting information for: Efficient fixed-bed removal of the emerging contaminant nimesulide using β -cyclodextrin-grafted Luffa biomass

1. Supporting tables

Table 3-3.S1: Kinetic, isothermal, and breakthrough models, along with the associated error function used for modeling the adsorption of NIM ions on $LF_{(NaOH)}-\beta CD$.

Kinetic models		
Pseudo-first order (PFO)	$q_t = q_{e(theo)}e^{-k_1t}$	q_t – Adsorption capacity at time t (mg/g) $q_{e(theo)}$ – Theoretical adsorption capacity (mg/g) k_1 – Pseudo-first order constant (min ⁻¹)
Pseudo-second order (PSO)	$q_t = \frac{q_{e(theo)}^2k_2t}{1 + q_{e(theo)}k_2t}$	k_2 – Pseudo-second-order constant (mg/g)
Elovich	$q_t = \frac{1}{\beta}ln(\alpha\beta t + 1)$	a - Elovich constant (mg/g min) b - Elovich exponent (g/mg)
Isotherm models		
Sips	$q_e = \frac{q_mK_SC_e^{n_S}}{1 + K_SC_e^{n_S}}$	q_m – Maximum adsorption capacity (mg/g) K_S – Sips isotherm constant (L/mg) n_S – Heterogeneity parameter
Hill	$q_e = \frac{q_mC_e^{n_H}}{K_H + C_e^{n_H}}$	q_m – Maximum adsorption capacity (mg/g) K_H – Hill isotherm constant n_H – Cooperativity coefficient
Redlich-Peterson (RP)	$q_e = \frac{K_{RP}C_e}{1 + a_{RP}C_e^{n_{RP}}}$	K_{RP} – RP isotherm constant (L/mg) a_{RP} – Isotherm constant (L/mg) n_{RP} – RP exponent (dimensionless)
Error function		
Chi-square (χ^2)	$\chi^2 = \sum \frac{(q_e - q_{e(theo)})^2}{q_{e(theo)}}$	
Breakthrough models		

Thomas	$\frac{C_t}{C_0} = \frac{1}{1 + \exp\left[\left(\frac{k_{Th}}{Q}\right)(q_0 m - C_0 Q t)\right]}$	k_{Th} – Thomas rate constant (mL/mg s) Q – Flowrate (mL/s) q_0 – Maximum bed adsorption capacity (mg/g) m – Adsorbent mass (mg)
Adams-Bohart	$\frac{C_t}{C_0} = \exp(k_{AB} C_0 t - k_{AB} N_0 \frac{Z}{U_0})$	k_{AB} – Adams-Bohart rate constant (mL/mg s) Z - active bed length (cm) N_0 - saturation concentration (mg/L) U_0 - linear velocity of the inlet solution (cm/s)
Clark	$\frac{C_t}{C_0} = \left(\frac{1}{1 + A e^{-rt}}\right)^{1/(n-1)}$	n – Freundlich constant A – Clark constant r – Clark constant (min ⁻¹)

Table 3-3.S2: Thermodynamic parameters for NIM adsorption on LF_(NaOH)-βCD at various temperatures.

Adsorbent	Temperature (K)	ΔG° (kJ/mol)	ΔH° (kJ/mol)	ΔS° (kJ/K mol)
LF _(NaOH) -βCD	308	-1.362	0.783	0.006
	318	-1.432		
	328	-1.502		

Table 3-3.S3: Estimated production cost of $\text{LF}_{(\text{NaOH})}\text{-}\beta\text{CD}$ under laboratory-scale conditions.

Input	Approx. unit price (USD)	Approx. amount used per 1 g of adsorbent	Estimated cost (USD)
Raw LF fibers (washed, dried)	0.01 / g (local source, negligible cost)	1 g (before treatment)	0.01
NaOH	0.05 / g	0.6 g	0.03
$\beta\text{-CD}$	2.3 / g	0.5 g	1.15
Citric acid	0.04 / g	0.2 g	0.008
Sodium hypophosphite	0.10 / g	0.2 g	0.02
EtOH/water washing	0.003 / mL	30 mL	0.09
Energy (heating/drying)	0.12 / kWh	0.5 kWh	0.06
Water (distilled)	0.002 / L	2 L	0.004
Laboratory overhead (consumables, glassware, etc.)	—	lumped estimate	0.40
Total estimated cost			USD 1.772 / g

Note: All costs are approximate and based on commercial laboratory-scale reagent prices and local energy/water tariffs. In large-scale production, both reagent costs and energy inputs are expected to decrease substantially due to bulk purchasing, process optimization, and recovery strategies.

2. Supporting figures

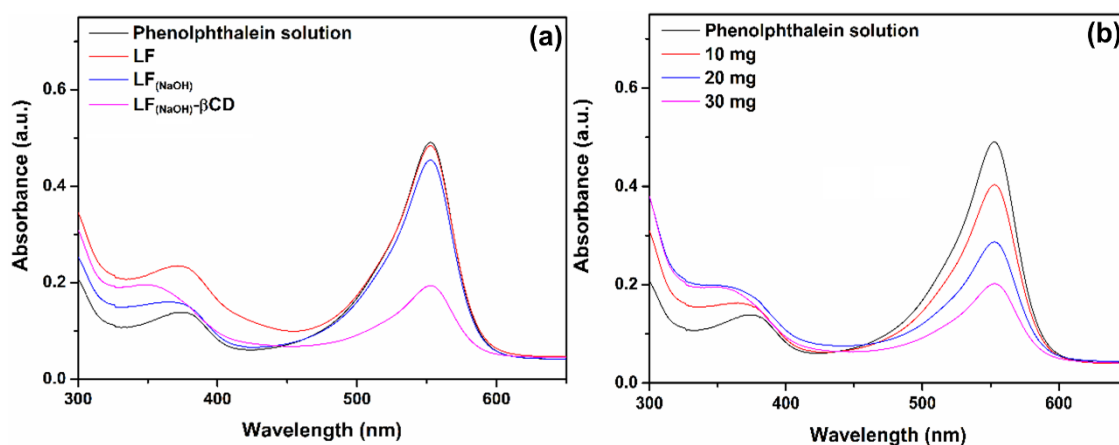


Figure 3-3.S1: UV-Vis absorption spectra of phenolphthalein in aqueous solution: (a) measured in the presence of LF, $\text{LF}_{(\text{NaOH})}$, and $\text{LF}_{(\text{NaOH})}\text{-}\beta\text{CD}$; (b) measured with varying amounts of $\text{LF}_{(\text{NaOH})}\text{-}\beta\text{CD}$.

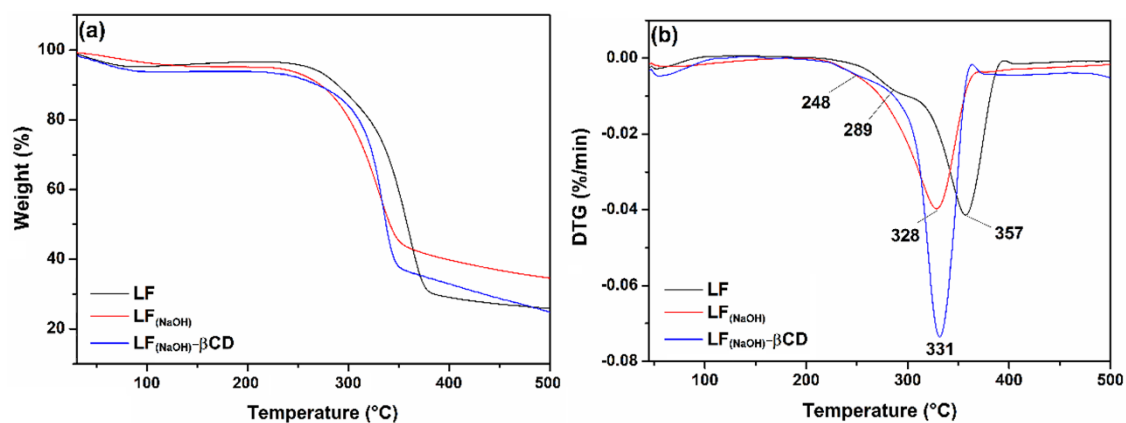


Figure 3-3.S2: (a) TGA and (b) DTG curves for raw LF, LF_(NaOH), and LF_(NaOH)-βCD.

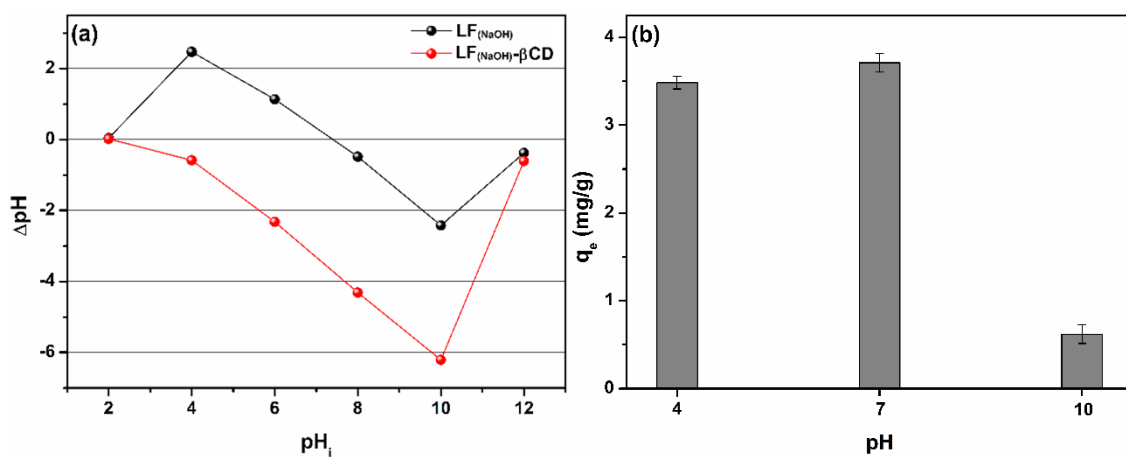


Figure 3-3.S3: (a) Variation of final pH as a function of initial pH (pH_i) for the determination of the point of zero charge (pH_{PZC}) of LF_(NaOH) and LF_(NaOH)-βCD. (b) Equilibrium adsorption capacity (q_e) of NIM onto LF_(NaOH)-βCD as a function of solution pH.

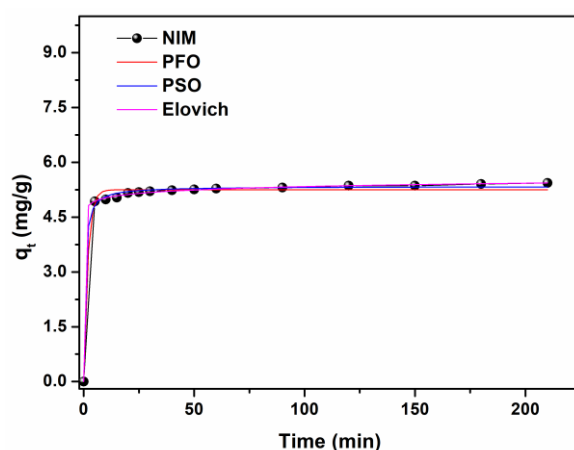


Figure 3-3.S4: Adsorption capacity (q_t) of NIM onto $LF_{(NaOH)}-\beta CD$ as a function of time. Experimental data (dots) are compared with nonlinear fits of the PFO, PSO, and Elovich kinetic models.

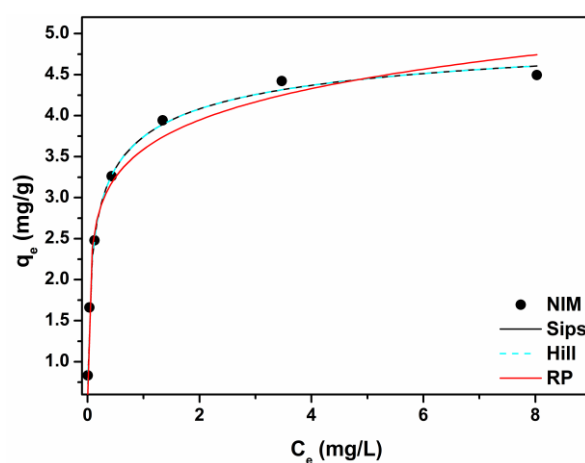


Figure 3-3.S5: Equilibrium adsorption capacity (q_e) of NIM onto $LF_{(NaOH)}-\beta CD$ as a function of initial NIM concentration. Experimental data (dots) are compared with nonlinear fits of the Sips, Hill, and Redlich-Peterson (RP) isotherm models.

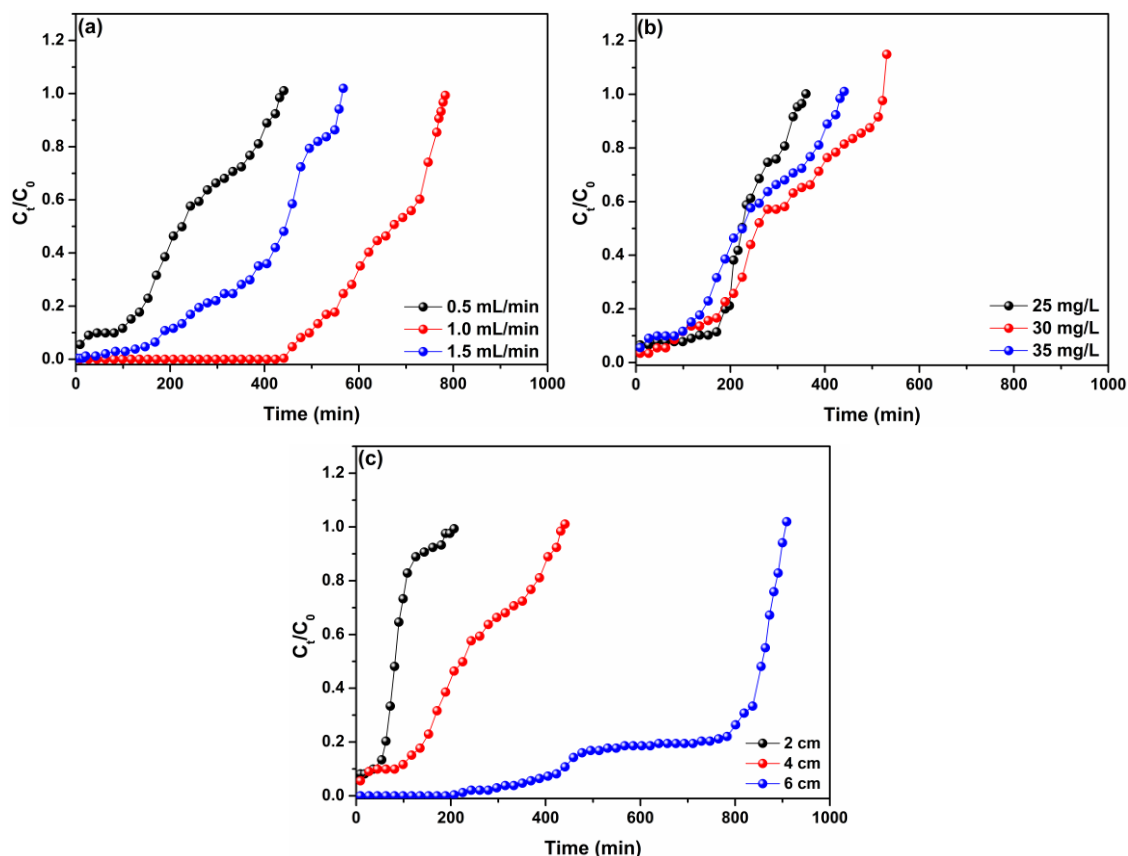


Figure 3-3.S6: Breakthrough curves for NIM adsorption onto LF_(NaOH)-βCD as a function of time, varying (a) flow rate, (b) initial NIM concentration, and (c) column height.

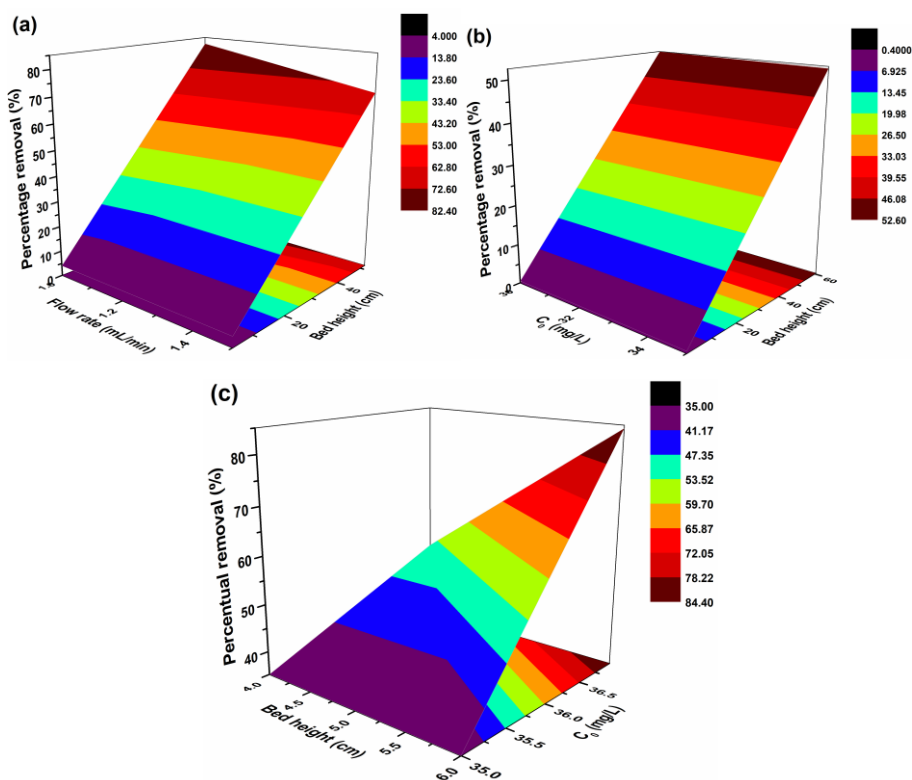


Figure 3-3.S7: 3D contour plots of NIM adsorption onto LF_(NaOH)-βCD (a) flow rate, (b) initial NIM concentration, and (c) column height; and percentage removal.

Chapter 4 – Final remarks

Luffa cylindrica (LF) is an abundant, plant-based biomass whose natural three-dimensional structure provides a versatile scaffold for chemical modification. However, strategies capable of preserving this architecture while tailoring surface chemistry for adsorption applications have been scarcely explored. This thesis addressed this gap by implementing three complementary functionalization approaches, each designed to introduce distinct chemical functionalities into the lignocellulosic network of LF without compromising its 3D architecture. **Table 4** presents a concise summary of the modifications implemented in each stage of this work, highlighting their contributions to the overall adsorption performance.

Table 4: Summary of LF modification strategies, characterization results, and adsorption performances for each study.

Study	Modification strategy	Property changes	Target PCHs	Adsorption performance
1	Grafted with PEI	An increased percentage of the element nitrogen (N), significant changes in the physicochemical and morphological properties	AMP and NTZ	Adsorption capacity increased by 59 % for NTZ and 43 % for AMP
2	Coated with PPy and SAc	Changed physicochemical and morphological properties, decreased its hydrophilicity, and enhanced the chemical and mechanical stability	DCF	Enhanced by 234% for the batch process and 80% for the continuous process
3	Grafted with β -CD	Changed physicochemical and morphological properties	NIM	High removal efficiency > 84.4% for fixed-bed column adsorption

Collectively, the results show that each modification strategy contributed to overcoming a specific limitation of raw LF while advancing the general objective of enhancing pharmaceutical adsorption. The grafting of PEI introduced nitrogen-rich groups that increased surface reactivity and enabled stable adsorption of antibiotics (AMP) and antivirals (NTZ), with confirmed reusability. The incorporation of PPy and SAc improved the hydrophobicity of LF fibers, directly enhancing interactions with less polar pharmaceuticals such as diclofenac, and further demonstrated the feasibility of adsorption under continuous flow conditions, which is essential for practical application. Finally, the grafting of β -CD provided selective host-guest complexation sites for hydrophobic drugs, resulting in a material with excellent performance in fixed-bed columns for the removal NSAIDs from water.

By correlating these strategies with the adsorption performance summarized in **Table 4**, it becomes evident that distinct modification routes can be applied to LF to expand its adsorption versatility across different classes of pharmaceuticals, while preserving its structural integrity. Beyond meeting the initial objectives, this thesis advances the understanding of how functionalization governs adsorption in lignocellulosic fibers, demonstrates the potential of LF as a reusable and scalable adsorbent, and provides a framework to guide future developments in sustainable biomass-based water treatment technologies.

As a future perspective, the developed adsorbent materials should be evaluated in systems containing mixtures of pharmaceuticals or even mixtures of different contaminants, in order to assess whether their adsorption capacity is affected, or whether they exhibit the ability to simultaneously remove multiple pollutants. Such studies may also help to identify which material modifications

enhance the removal of diverse contaminants from water. Furthermore, it is suggested that flow-through experiments be expanded and even combined with other water treatment processes, such as coagulation–flocculation, to demonstrate the feasibility of applying the developed materials in large-scale industrial water treatment.

5. References

- ABDULLAH, H. M. et al. Enhanced water treatment with TEMPO-modified luffa cellulose-PVA nanofiber composite for removal of hexavalent chromium. **Results in Chemistry**, v. 8, p. 101582, jun. 2024.
- ABU RAHIM, N. E. A. et al. Crosslinked Cyclodextrin as Potent Composite For Removal of Wastewater Pollutants. **Current Pollution Reports**, v. 9, n. 4, p. 680–693, 16 ago. 2023.
- ADENIYI, A. G. et al. Production and properties of the fibrillated plastic composite from recycled polystyrene and Luffa cylindrica. **Polymer Bulletin**, v. 80, n. 9, p. 9569–9588, 13 set. 2023.
- ADEYANJU, C. A. et al. A review on Luffa fibres and their polymer composites. **Journal of Materials Science**, v. 56, n. 4, p. 2797–2813, 26 fev. 2021.
- AHAMMAD, N. A. et al. A mini review of recent progress in the removal of emerging contaminants from pharmaceutical waste using various adsorbents. **Environmental Science and Pollution Research**, v. 30, n. 60, p. 124459–124473, 22 mar. 2022.
- AHMADI, P. et al. Current advances in the synthesis of beta-cyclodextrin-based metal organic frameworks and their potential applications in the adsorption/removal of pollutants: A comprehensive review. **Carbohydrate Polymers**, v. 353, p. 123241, abr. 2025.
- AKAY, O. et al. A bio-based and non-toxic polyurethane film derived from Luffa cylindrica cellulose and L-Lysine diisocyanate ethyl ester. **European Polymer Journal**, v. 161, n. October, p. 110856, 2021.
- AKAY, O. et al. Preparation of a sustainable bio-copolymer based on Luffa cylindrica cellulose and poly(ϵ -caprolactone) for bioplastic applications. **International Journal of Biological Macromolecules**, v. 196, n. October 2021, p. 98–106, 2022.
- AKINYEMI, B. A.; DAI, C. Luffa cylindrical fibre as a natural reinforcement for cement composites: A review. **Journal of Sustainable Cement-Based Materials**, v. 11, n. 5, p. 297–307, 3 set. 2022.
- AL-ARAJI, D. D.; AL-ANI, F. H.; ALSALHY, Q. F. Polyethyleneimine (PEI) grafted silica nanoparticles for polyethersulfone membranes modification and their outlooks for wastewater treatment - a review. **International Journal of**

Environmental Analytical Chemistry, v. 103, n. 16, p. 4752–4776, 18 dez. 2023.

AL-MASHAQBEH, O. et al. Treatment of pharmaceutical industry wastewater for water reuse in Jordan using hybrid constructed wetlands. **Science of The Total Environment**, v. 939, p. 173634, ago. 2024.

ALKHATHAMI, N. D. et al. Adsorption of pharmaceutical ibuprofen over functionalized zirconium metal-organic frameworks; Batch experiment and mechanism of interaction. **Polyhedron**, v. 235, p. 116349, maio 2023.

ALOMAR, T. et al. Recent advances on humic acid removal from wastewater using adsorption process. **Journal of Water Process Engineering**, v. 53, p. 103679, jul. 2023.

ANASTOPOULOS, I.; PASHALIDIS, I. Environmental applications of Luffa cylindrica-based adsorbents. **Journal of Molecular Liquids**, v. 319, p. 114127, dez. 2020.

ARABKHANI, P.; ASFARAM, A. The potential application of bio-based ceramic/organic xerogel derived from the plant sources: A new green adsorbent for removal of antibiotics from pharmaceutical wastewater. **Journal of Hazardous Materials**, v. 429, p. 128289, maio 2022.

ARAUJO, L. A. et al. Diclofenac adsorption using a low-cost adsorbent derived from Guazuma ulmifolia Lam. fruit via chemical and thermal treatment. **Journal of Environmental Chemical Engineering**, v. 9, n. 6, p. 106629, 2021.

ARES, A. M. et al. Cyclodextrin-functionalized cellulose filter paper for selective capture of diclofenac. **Carbohydrate Polymers**, v. 220, p. 43–52, set. 2019.

BANGAR, S. P. et al. Recent advancements in functionality, properties, and applications of starch modification with stearic acid: A review. **International Journal of Biological Macromolecules**, v. 280, p. 135782, nov. 2024.

BARRA, G. et al. A Comprehensive Review on the Thermal Stability Assessment of Polymers and Composites for Aeronautics and Space Applications. **Polymers**, v. 15, n. 18, p. 3786, 16 set. 2023.

BETTAIEB, F. et al. Polyethylenimine-grafted cellulose nanofibril composites: Adsorbents for anionic dye removal with thermodynamic insights. **International Journal of Biological Macromolecules**, v. 310, p. 143354, maio 2025.

BHATTACHARJEE, T. et al. Synthesis and characterization of exfoliated beta-cyclodextrin functionalized graphene oxide for adsorptive removal of atenolol.

Materials Chemistry and Physics, v. 288, p. 126413, set. 2022.

BHUYAN, A.; AHMARUZZAMAN, M. Recent advances in new generation nanocomposite materials for adsorption of pharmaceuticals from aqueous environment. **Environmental Science and Pollution Research**, v. 30, n. 14, p. 39377–39417, 8 fev. 2023.

CALDAS, S. et al. Occurrence of Pesticides and PPCPs in Surface and Drinking Water in Southern Brazil: Data on 4-Year Monitoring. **Journal of the Brazilian Chemical Society**, v. 30, p. 71–80, 2018.

CAO, M. et al. Loofah sponge crosslinked polyethyleneimine loaded with biochar biofilm reactor for ecological remediation of oligotrophic water: Mechanism, performance, and functional characterization. **Bioresource Technology**, v. 399, p. 130567, maio 2024.

CARAFA, R. N.; FOUCHER, D. A.; SACRIPANTE, G. G. Biobased polymers from lignocellulosic sources. **Green Chemistry Letters and Reviews**, v. 16, n. 1, 2 jan. 2023.

CHEN, Q. et al. Polyethyleneimine grafted starch nanocrystals as a novel biosorbent for efficient removal of methyl blue dye. **Carbohydrate Polymers**, v. 273, p. 118579, dez. 2021.

CHOUCHANE, T. et al. Equilibrium, kinetics, and thermodynamics of batch adsorption of Mn(II) ions on blast furnace slag (BFS) and kaolin (KGA). **Journal of Engineering and Applied Science**, v. 70, n. 1, p. 58, 6 dez. 2023.

COSTA, T. C. et al. Evaluation of the technical and environmental feasibility of adsorption process to remove water soluble organics from produced water: A review. **Journal of Petroleum Science and Engineering**, v. 208, p. 109360, jan. 2022.

COUTINHO, R. et al. Sustainable application of modified *Luffa cylindrica* biomass for removal of trimethoprim in water by adsorption with process optimization. **Environmental Science and Pollution Research**, v. 31, n. 43, p. 55280–55300, 3 set. 2024.

CZECH, B. et al. Engineered biochars from organic wastes for the adsorption of diclofenac, naproxen and triclosan from water systems. **Journal of Cleaner Production**, v. 288, 2021.

DA COSTA, J. S. et al. Synthesis and characterization of polyethyleneimine grafted lignocellulosic fibers for improved removal of nitazoxanide and ampicillin

from water. **Colloids and Surfaces A: Physicochemical and Engineering Aspects**, v. 693, p. 134063, jul. 2024.

DAI, L.; SUN, Z.; ZHOU, P. Modification of Luffa Sponge for Enrichment of Phosphopeptides. **International Journal of Molecular Sciences**, v. 21, n. 1, p. 101, 22 dez. 2019.

DONG, F.-X. et al. Simultaneous adsorption of Cr(VI) and phenol by biochar-based iron oxide composites in water: Performance, kinetics and mechanism. **Journal of Hazardous Materials**, v. 416, p. 125930, ago. 2021.

FANG, C. et al. An omniphobic membrane with macro-corrugation for the treatment of real pharmaceutical wastewater via membrane distillation. **Journal of Membrane Science**, v. 676, p. 121582, jun. 2023.

FEIZI, F.; SARMAH, A. K.; RANGSIVEK, R. Adsorption of pharmaceuticals in a fixed-bed column using tyre-based activated carbon: Experimental investigations and numerical modelling. **Journal of Hazardous Materials**, v. 417, n. April, p. 126010, 2021.

FINKBEINER, P. et al. Sonoelectrochemical degradation of the anti-inflammatory drug diclofenac in water. **Chemical Engineering Journal**, v. 273, p. 214–222, 2015.

FOROUTAN, R. et al. Generation of biodiesel from edible waste oil using ZIF-67-KOH modified Luffa cylindrica biomass catalyst. **Fuel**, v. 322, p. 124181, ago. 2022.

FRAIHA, O. et al. Comprehensive review on the adsorption of pharmaceutical products from wastewater by clay materials. **Desalination and Water Treatment**, v. 317, p. 100114, jan. 2024.

FURLAN, F. R. et al. Removal of reactive dyes from aqueous solutions using combined coagulation/flocculation and adsorption on activated carbon. **Resources, Conservation and Recycling**, v. 54, n. 5, p. 283–290, mar. 2010.

GUO, R. et al. β -Cyclodextrin Polymerized in Cross-Flowing Channels of Biomass Sawdust for Rapid and Highly Efficient Pharmaceutical Pollutants Removal from Water. **ACS Applied Materials & Interfaces**, v. 12, n. 29, p. 32817–32826, 22 jul. 2020.

HAMMAD, N. et al. **Antiviral effect of thiazolides relies on mitochondrial mild uncoupling**, 16 set. 2022. Disponível em: <<http://biorxiv.org/lookup/doi/10.1101/2022.09.16.508272>>

HE, H. et al. Flexible loofah sponge-based phase change composite for thermal protection and wearable thermal management. **Journal of Energy Storage**, v. 100, p. 113465, out. 2024.

HE, M.; XU, M.; ZHANG, L. Controllable Stearic Acid Crystal Induced High Hydrophobicity on Cellulose Film Surface. **ACS Applied Materials & Interfaces**, v. 5, n. 3, p. 585–591, 13 fev. 2013.

HU, D. et al. Adsorption of diclofenac sodium on bilayer amino-functionalized cellulose nanocrystals/chitosan composite. **Journal of Hazardous Materials**, v. 369, 2019.

HU, S. et al. Biomimetic Polylactic Acid Electrospun Fibers Grafted with Polyethyleneimine for Highly Efficient Methyl Orange and Cr(VI) Removal. **Langmuir**, v. 39, n. 10, p. 3770–3783, 14 mar. 2023.

HUANG, A. K. et al. Sequential process of coagulation/flocculation/sedimentation- adsorption - microfiltration for laundry effluent treatment. **Journal of Environmental Chemical Engineering**, v. 7, n. 4, p. 103226, ago. 2019.

HUANG, L.; SHEN, R.; SHUAI, Q. Adsorptive removal of pharmaceuticals from water using metal-organic frameworks: A review. **Journal of Environmental Management**, v. 277, n. May 2020, p. 111389, 2021.

HUSSAIN, A. et al. Pharmaceutical contaminants in aquatic systems, conventional and green strategies, recent updates, challenges and policies, and potential outcomes. **Journal of Molecular Liquids**, v. 389, p. 122905, nov. 2023.

IGHALO, J. O. et al. Evaluation of Luffa cylindrica fibres in a biomass packed bed for the treatment of fish pond effluent before environmental release. **Sustainable Water Resources Management**, v. 6, n. 6, p. 1–11, 2020.

IQBAL, J. et al. Pharmaceuticals wastewater treatment via different advanced oxidation processes: Reaction mechanism, operational factors, toxicities, and cost evaluation – A review. **Separation and Purification Technology**, v. 347, p. 127458, nov. 2024.

JAMSHIDI-ADEGANI, F. et al. Prevention of Postoperative Adhesion Bands by Alkali-treated Cellulosic Luffa Fibers. **Journal of Natural Fibers**, v. 18, n. 4, p. 559–567, 3 abr. 2021.

JANG, J. et al. Magnetic Ti₃C₂T_x (Mxene) for diclofenac degradation via the ultraviolet/chlorine advanced oxidation process. **Environmental Research**, v.

182, n. August 2019, p. 108990, 2020.

JOODAKI, S.; MOLLAHOSSEINI, A. Evaluation modified luffa with silver nanoparticles (LF/AgNPs) for removal of a nonsteroidal anti-inflammatory (IBUPROFEN) from aqueous media. **Environmental Nanotechnology, Monitoring & Management**, v. 20, p. 100823, dez. 2023.

JOUDIEH, S. et al. Nimesulide Apparent Solubility Enhancement with Natural Cyclodextrins and their Polymers. **Letters in Drug Design & Discovery**, v. 5, n. 6, p. 406–415, 1 set. 2008.

KAMRAN, M. J. et al. A review: Surface treatments, production techniques, mechanical properties and characteristics of *Luffa cylindrica* bio composites. **Journal of Industrial Textiles**, v. 51, n. 1_suppl, p. 215S-245S, 5 jun. 2022.

KANI, A. N. et al. Pollutant decontamination by polyethyleneimine-engineered agricultural waste materials: a review. **Environmental Chemistry Letters**, v. 20, n. 1, p. 705–729, 10 fev. 2022.

KAUR, H. et al. Effect of hydrophobicity of pharmaceuticals and personal care products for adsorption on activated carbon: Adsorption isotherms, kinetics and mechanism. **Environmental Science and Pollution Research**, v. 25, n. 21, p. 20473–20485, 11 jul. 2018.

KHADIR, A. et al. The prospective utilization of Luffa fibres as a lignocellulosic bio-material for environmental remediation of aqueous media: A review. **Journal of Environmental Chemical Engineering**, v. 9, n. 1, 2021.

KHADIR, A.; NEGARESTANI, M.; MOLLAHOSSEINI, A. Sequestration of a non-steroidal anti-inflammatory drug from aquatic media by lignocellulosic material (*Luffa cylindrica*) reinforced with polypyrrole: Study of parameters, kinetics, and equilibrium. **Journal of Environmental Chemical Engineering**, v. 8, n. 3, p. 103734, 2020.

KHAN, A. H. et al. Sustainable green nanoadsorbents for remediation of pharmaceuticals from water and wastewater: A critical review. **Environmental Research**, v. 204, p. 112243, mar. 2022.

KHATTAB, T. A.; MOHAMED, A. L.; HASSABO, A. G. Development of durable superhydrophobic cotton fabrics coated with silicone/stearic acid using different cross-linkers. **Materials Chemistry and Physics**, v. 249, p. 122981, jul. 2020.

KOLTSAKIDOU, A. et al. Photolysis and photocatalysis of the non-steroidal anti-inflammatory drug Nimesulide under simulated solar irradiation: Kinetic studies,

transformation products and toxicity assessment. **Science of The Total Environment**, v. 689, p. 245–257, nov. 2019.

KRASNOPEEVA, E. L.; PANOVA, G. G.; YAKIMANSKY, A. V. Agricultural Applications of Superabsorbent Polymer Hydrogels. **International Journal of Molecular Sciences**, v. 23, n. 23, p. 15134, 1 dez. 2022.

KUMAR, R. et al. A review on emerging water contaminants and the application of sustainable removal technologies. **Case Studies in Chemical and Environmental Engineering**, v. 6, p. 100219, dez. 2022.

KURODA, K.; KOBAYASHI, J. Pharmaceuticals, Personal Care Products, and Artificial Sweeteners in Asian Groundwater: A Review. In: [s.l: s.n.]. p. 3–36.

LAI, S.-M. et al. Preparation and properties of luffa fiber- and kenaf fiber-filled poly(butylene succinate-co-lactate)/starch blend-based biocomposites. **Polymer Testing**, v. 50, p. 191–199, abr. 2016.

LETSOALO, M. R. et al. Efficient detection and treatment of pharmaceutical contaminants to produce clean water for better health and environmental. **Journal of Cleaner Production**, v. 387, p. 135798, fev. 2023.

LEUDJO TAKA, A. et al. Chitosan nanocomposites for water treatment by fixed-bed continuous flow column adsorption: A review. **Carbohydrate Polymers**, v. 255, p. 117398, mar. 2021.

LIU, G. et al. Modification of agricultural wastes to improve sorption capacities for pollutant removal from water – a review. **Carbon Research**, v. 1, n. 1, p. 24, 15 nov. 2022a.

LIU, J. et al. Concurrent elimination and stepwise recovery of Pb(II) and bisphenol A from water using β -cyclodextrin modified magnetic cellulose: adsorption performance and mechanism investigation. **Journal of Hazardous Materials**, v. 432, p. 128758, jun. 2022b.

MADDELA, N. R. et al. Major contaminants of emerging concern in soils: a perspective on potential health risks. **RSC Advances**, v. 12, n. 20, p. 12396–12415, 2022.

MAGED, A. et al. New mechanistic insight into rapid adsorption of pharmaceuticals from water utilizing activated biochar. **Environmental Research**, v. 202, 2021.

MAITY, S.; DUBEY, A.; CHAKRABORTY, S. A review on polypyrrole-coated biocomposites for the removal of heavy metal traces from waste water. **Journal of**

Industrial Textiles, v. 51, n. 1, p. 152–173, 10 jul. 2021.

MARTINEZ-PAVETTI, M. B. et al. Study on two eco-friendly surface treatments on *Luffa cylindrica* for development of reinforcement and processing materials. **Journal of Materials Research and Technology**, v. 14, n. Lc, p. 2420–2427, 2021.

MOHANRASU, K. et al. Eco-friendly biopolymers and composites: a sustainable development of adsorbents for the removal of pollutants from wastewater. **npj Materials Sustainability**, v. 3, n. 1, p. 13, 17 maio 2025.

MOHAPATRA, S. et al. Photodegradation of a mixture of five pharmaceuticals commonly found in wastewater: Experimental and computational analysis. **Environmental Research**, v. 216, p. 114659, jan. 2023.

MORILLAS-ESPAÑA, A. et al. Microalgae wastewater treatment: Pharmaceutical removal and biomass valorization. **Journal of Environmental Management**, v. 380, p. 124942, abr. 2025.

MUHAMMAD EKRAMUL MAHMUD, H. N.; HUQ, A. K. O.; YAHYA, R. BINTI. The removal of heavy metal ions from wastewater/aqueous solution using polypyrrole-based adsorbents: a review. **RSC Advances**, v. 6, n. 18, p. 14778–14791, 2016.

OSUOHA, J. O.; ANYANWU, B. O.; EJILEUGHA, C. Pharmaceuticals and personal care products as emerging contaminants: Need for combined treatment strategy. **Journal of Hazardous Materials Advances**, v. 9, p. 100206, fev. 2023.

PATEL, H. Fixed-bed column adsorption study: a comprehensive review. **Applied Water Science**, v. 9, n. 3, p. 45, 16 abr. 2019.

PATEL, H. Comparison of batch and fixed bed column adsorption: a critical review. **International Journal of Environmental Science and Technology**, v. 19, n. 10, p. 10409–10426, 24 out. 2022.

PAULETTO, P. S. et al. Adsorption mechanisms of single and simultaneous removal of pharmaceutical compounds onto activated carbon: Isotherm and thermodynamic modeling. **Journal of Molecular Liquids**, v. 336, p. 116203, ago. 2021.

PÉREZ-BOTELLA, E.; VALENCIA, S.; REY, F. Zeolites in Adsorption Processes: State of the Art and Future Prospects. **Chemical Reviews**, v. 122, n. 24, p. 17647–17695, 28 dez. 2022.

PLACOVA, K. et al. **Issues of Non-Steroidal Anti-Inflammatory Drugs in**

Aquatic Environments: A Review Study. The 4th International Conference on Advances in Environmental Engineering. **Anais...**Basel Switzerland: MDPI, 1 dez. 2023

PRASETYA, N. et al. Metal-organic frameworks for the adsorptive removal of pharmaceutically active compounds (PhACs): Comparison to activated carbon. **Coordination Chemistry Reviews**, v. 475, p. 214877, jan. 2023.

PREMALATHA, N. et al. Structural and Thermal Properties of Chemically Modified Luffa Cylindrica Fibers. **Journal of Natural Fibers**, v. 18, n. 7, p. 1038–1044, 2021.

PUGA, A. et al. Continuous adsorption studies of pharmaceuticals in multicomponent mixtures by agroforestry biochar. **Journal of Environmental Chemical Engineering**, v. 10, n. 1, p. 106977, fev. 2022.

QU, J. et al. Simultaneously enhanced removal and stepwise recovery of atrazine and Pb(II) from water using β -cyclodextrin functionalized cellulose: Characterization, adsorptive performance and mechanism exploration. **Journal of Hazardous Materials**, v. 400, p. 123142, dez. 2020.

RAVELET, C. et al. Chromatographic determination of the association constants between nimesulide and native and modified β -cyclodextrins. **Journal of Pharmaceutical and Biomedical Analysis**, v. 29, n. 3, p. 425–430, jul. 2002.

RICHARD, O. et al. An Integrated Approach of ANN and CFD for Predicting and Modelling the Adsorptive Removal of Methylene Blue Dye Using Sandbox Seed as Adsorbent: A Review. **Journal of Energy, Environmental & Chemical Engineering**, v. 10, n. 2, p. 56–67, 25 jun. 2025.

RIVA, L.; FIORATI, A.; PUNTA, C. Synthesis and Application of Cellulose-Polyethyleneimine Composites and Nanocomposites: A Concise Review. **Materials**, v. 14, n. 3, p. 473, 20 jan. 2021.

SAMAL, K.; MAHAPATRA, S.; HIBZUR ALI, M. Pharmaceutical wastewater as Emerging Contaminants (EC): Treatment technologies, impact on environment and human health. **Energy Nexus**, v. 6, p. 100076, jun. 2022.

SANTOS, M. A. et al. Luffa cylindrica as a biosorbent in wastewater treatment applications: a comprehensive review. **Cellulose**, v. 31, n. 17, p. 10115–10142, 14 nov. 2024.

SASSO, C. et al. Polypyrrole and polypyrrole/wood-derived materials conducting composites: A review. **BioResources**, v. 6, n. 3, p. 3585–3620, 28 jul. 2011.

SHAMSUDIN, M. S. et al. Performance and interactions of diclofenac adsorption using Alginate/Carbon-based Films: Experimental investigation and statistical physics modelling. **Chemical Engineering Journal**, v. 428, n. June 2021, p. 131929, 2022.

SHEARER, L.; PAP, S.; GIBB, S. W. Removal of pharmaceuticals from wastewater: A review of adsorptive approaches, modelling and mechanisms for metformin and macrolides. **Journal of Environmental Chemical Engineering**, v. 10, n. 4, p. 108106, 2022.

SOARES, C. et al. Removal of diclofenac and sulfamethoxazole from aqueous solutions and wastewaters using a three-dimensional electrochemical process. **Journal of Environmental Chemical Engineering**, v. 10, n. 5, p. 108419, out. 2022.

SOKOŁOWSKI, A. et al. Plant-Waste-Derived Sorbents for Nitazoxanide Adsorption. **Molecules**, v. 28, n. 15, p. 5919, 7 ago. 2023.

SOPHIA A., C.; LIMA, E. C. Removal of emerging contaminants from the environment by adsorption. **Ecotoxicology and Environmental Safety**, v. 150, n. December 2017, p. 1–17, 2018.

SUNTISUKASEAM, U.; WESCHAYANWIWAT, P.; SABATINI, D. A. Sorption of Amphiphile Pharmaceutical Compounds onto Polar and Nonpolar Adsorbents. **Environmental Engineering Science**, v. 24, n. 10, p. 1457–1466, dez. 2007.

TAN, Y. Y. et al. A review on sustainable management of biomass: physicochemical modification and its application for the removal of recalcitrant pollutants—challenges, opportunities, and future directions. **Environmental Science and Pollution Research**, v. 31, n. 25, p. 36492–36531, 15 maio 2024.

TEE, W. T. et al. Application of 3D heteroatom-doped graphene in adsorptive removal of water pollutants: Review on hydrothermal synthesis and its influencing factors. **Separation and Purification Technology**, v. 320, p. 124072, set. 2023.

THAKUR, V. et al. Modification and management of lignocellulosic waste as an ecofriendly biosorbent for the application of heavy metal ions sorption. **Materials Today: Proceedings**, v. 32, p. 608–619, 2020.

TIAN, B. et al. Cyclodextrin-based adsorbents for the removal of pollutants from wastewater: a review. **Environmental Science and Pollution Research**, v. 28, n. 2, p. 1317–1340, 20 jan. 2021.

UROOJ, T.; MISHRA, M.; PANDEY, S. Unlocking environmental solutions: a

review of cyclodextrins in pollutant removal. **Discover Environment**, v. 2, n. 1, p. 65, 15 jun. 2024.

VIEIRA, A. M. S. et al. Use of Moringa oleifera Seed as a Natural Adsorbent for Wastewater Treatment. **Water, Air, and Soil Pollution**, v. 206, n. 1–4, p. 273–281, 5 fev. 2010.

WANG, K. M. et al. Evaluation of a modified internal circulation (MIC) anaerobic reactor for real antibiotic pharmaceutical wastewater treatment: Process performance, microbial community and antibiotic resistance genes evolutions. **Journal of Water Process Engineering**, v. 48, p. 102914, ago. 2022a.

WANG, T. et al. Application of polypyrrole-based adsorbents in the removal of fluoride: a review. **RSC Advances**, v. 12, n. 6, p. 3505–3517, 2022b.

WANG, X. et al. PEI grafted defective MOF-808 for enhanced boron removal. **Separation and Purification Technology**, v. 336, p. 126293, maio 2024.

WU, H. et al. Bifunctional porous polyethyleneimine-grafted lignin microspheres for efficient adsorption of 2,4-dichlorophenoxyacetic acid over a wide pH range and controlled release. **Chemical Engineering Journal**, v. 411, p. 128539, maio 2021.

WU, J.; WANG, J. Radiation-induced grafting of polyethyleneimine onto cellulose triacetate membrane for separation of cesium ions from aqueous solution. **Radiation Physics and Chemistry**, v. 222, p. 111832, set. 2024.

WU, L. et al. Effective adsorption of diclofenac sodium from neutral aqueous solution by low-cost lignite activated cokes. **Journal of Hazardous Materials**, v. 384, n. September 2019, p. 121284, 2020.

XIA, N. N. et al. A functionalized bio-based material with abundant mesopores and catechol groups for efficient removal of boron. **Chemosphere**, v. 263, p. 128202, jan. 2021.

XU, S. et al. Macro- and micro-algae-based carbon composite for pharmaceutical wastewater treatment: Batch adsorption and mechanism study. **Process Safety and Environmental Protection**, v. 176, p. 641–652, ago. 2023.

YUAN, Y.; LI, R.; PENG, S. Research progress on chemical modification of waste biomass cellulose to prepare heavy metal adsorbents. **Polymer Bulletin**, v. 80, n. 11, p. 11671–11700, 20 nov. 2023.

ZHANG, F. et al. Hydrophobic sponge derived from natural loofah for efficient oil/water separation. **Separation and Purification Technology**, v. 330, p.

125519, fev. 2024.

ZHU, X. et al. Fabrication of Polyethyleneimine-Functionalized Magnetic Cellulose Nanocrystals for the Adsorption of Diclofenac Sodium from Aqueous Solutions. **Polymers**, v. 14, n. 4, 2022.